



DIVISIÓN DE CIENCIAS BÁSICAS  
Departamento de Física y Geociencias  
and  
FACULTEIT WETENSCHAPPEN  
Departement Fysica

Tuning the properties of group III-As in the thinnest limit:  
A theoretical study of single layer and 2D-heterostructures  
by

Alvaro González García

Dissertation submitted to obtain the degree of *doctor in sciences:*  
*physics* at both Universidad del Norte and Antwerp University

Supervisors

Prof. Dr., William López  
Prof. Dr., Milorad Milošević  
Prof. Dr., François Peeters

June 2021

DIVISIÓN DE CIENCIAS BÁSICAS  
Departamento de Física y Geociencias  
and  
FACULTEIT WETENSCHAPPEN  
Departement Fysica

by

Alvaro González García

Tuesday 28<sup>th</sup> September, 2021 01:40

Dissertation submitted to obtain the degree of *doctor in sciences: physics* at both  
Universidad del Norte and Antwerp University

## Abstract

In this thesis, a first-principles research to tune the physical properties of group III-V materials in the thinnest limit is carried out. Among the different methods to tune the mechanical, electronic and magnetic properties of these graphene related materials, we use: two-dimensional (2D) multilayers, straintronics, hydrogen functionalization, and transition metal adsorption. The first part of this research is devoted to a complete characterization of the structural, electronic, mechanical and vibrational properties of 2D group III-As monolayers, obtained from density functional theory. Our findings are used to understand the contribution of the  $\sigma$  and  $\pi$  bonding in the most stable geometry (planar or buckled) for 2D  $h$ -III-As systems. Structural and electronic properties of  $h$ -III-As systems, as a function of the number of layers, have also been studied. In the second part of this thesis, the electronic properties of graphene and GaAs, in the graphene/GaAs bilayer heterostructure, are tuned, under both uniaxial stress along the  $c$ -axis and different planar strain distributions. Here, the tunable graphene bandgap, not only by the strength but also by the direction of the strain, enhances the potential for strain engineering of ultrathin group-III-V electronic devices hybridized by graphene. In the third part of this study, the structural and electronic properties, as well as the energy and dynamical stability of 2D hydrogenated GaAs sheets, are studied taking into account three different geometric configurations: chair, zigzag-line and boat. The hydrogenation of 2D-GaAs tunes the bandgap of pristine 2D-GaAs, which makes it a potential candidate for optoelectronic applications in the blue and violet ranges of the visible electromagnetic spectrum. Finally, the tunability of the magnetic properties by spin-orbit coupling, on both magnetic anisotropy and Dzyaloshinskii-Moriya interaction, for two-dimensional gallium arsenide when single transition metal (TM) atoms are adsorbed (Mn, Co, Mo and Os), is investigated. The obtained results

indicate novel pathways towards two-dimensional chiral magnetic materials by design, tailored for desired applications in magneto-electronics. The present work will bring new theoretical insights to the research of the thinnest materials, opening the possibility for further investigations in atomically thin III-As materials.

## Abstract – Nederlandse versie

In dit proefschrift wordt een eerste-principe onderzoek uitgevoerd om de fysische eigenschappen van atomair dunne groep III-V-materialen te beschrijven. Onder de verschillende methoden om de mechanische, elektronische en magnetische eigenschappen van deze grafeengerelateerde materialen te besturen, gebruiken we: 2D-meerlagen, straintronica, waterstoffunctionalisatie en overgangsmetaaladsorptie. Het eerste deel van dit onderzoek is gewijd aan het uitvoeren van een volledige karakterisering van de structurele, elektronische, mechanische en vibratie-eigenschappen van 2D groep III-As monolagen, met behulp van dichtheidsfunctionaaltheorie. Onze bevindingen worden gebruikt om de bijdrage van de  $\sigma$  en  $\pi$  en binding in de meest stabiele geometrie (planair of geknikt) voor 2D  $h$ -IIIAs-systemen te begrijpen. Structurele en elektronische eigenschappen van  $h$ -IIIAs-systemen, als functie van het aantal lagen, zijn ook bestudeerd. In het tweede deel van dit proefschrift worden de elektronische eigenschappen van grafeen en GaAs in de grafeen/GaAs dubbellaag heterostructuur bestudeerd, zowel onder uniaxiale spanning langs de  $c$ -as als onder verschillende vlakke vervormingsverdelingen. Hierdoor vergroot de instelbare bandkloof van grafeen, niet alleen door de sterkte maar ook door de richting van de spanning. Deze eigenschap vergroot het potentieel van de spanningstechniek bij het gebruik van ultradunne groep-III-V elektronische apparaten gehybridiseerd door grafeen. In het derde deel van deze thesis worden de structurele en elektronische eigenschappen, evenals de energie en dynamische stabiliteit van 2D gehydrogeneerde GaAs-membranen, bestudeerd rekening houdend met drie verschillende geometrische configuraties: stoel, zigzaglijn en boot. De hydrogenering van 2D-GaAs verkleint de bandafstand van ongerepte 2D-GaAs, waardoor het een potentiële kandidaat wordt voor opto-elektronische toepassingen in het blauwe en violette bereik van het zichtbare elektromagnetische spectrum. Ten slotte wordt de afstembaarheid van de magnetische eigenschappen door de spin-orbit-koppeling, zowel op magnetische anisotropie als op Dzyaloshinskii-Moriya-interactie, voor tweedimensionaal galliumarsenide onderzocht wanneer enkele transitie metaal (TM) atomen worden geabsorbeerd (Mn, Co, Mo en Os). De verkregen resultaten duiden op nieuwe wegen naar tweedimensionale chirale magnetische materialen die afgestemd kunnen worden voor gewenste toepassingen in magneto-elektronica. Het huidige werk brengt nieuwe theoretische inzichten in het onderzoek van de dunste materialen, en opent de mogelijkheid voor verder onderzoek in atomair dunne III-As-materialen.

# Publications

## Publications related to this thesis

1. **A González-García**, W López-Pérez, J Rivera-Julio, V Mendoza-Estrada, R Gonzalez-Hernandez, and FM Peeters. *Structural, mechanical and electronic properties of two-dimensional structure of III-arsenide (111) binary compounds: An ab-initio study*. Computational Materials Science, 144:285–293, 2018.
2. **A González-García**, W López-Pérez, R González-Hernández, JA Rodríguez, MV Milošević, and FM Peeters. *Tunable 2d-gallium arsenide and graphene bandgaps in a graphene/GaAs heterostructure: an ab-initio study*. Journal of Physics: Condensed Matter, 31(26):265502, 2019.
3. **A González-García**, W López-Pérez, R González-Hernández, J Rivera-Julio, C Espejo, MV Milošević, and FM Peeters. *Two-dimensional hydrogenated buckled gallium arsenide: an ab-initio study*. Journal of Physics: Condensed Matter, 32(14):145502, 2020.
4. **A González-García**, W López-Pérez, R González-Hernández, C Bacaksiz, D Šabani, MV Milošević, and FM Peeters. *Transition-metal adatoms on 2d-GaAs: a route to chiral magnetic 2d materials by design*. Journal of Physics: Condensed Matter, 33(14):145803, 2021.

## Other publications

5. J Rivera-Julio, **A González-García**, R González-Hernández, W López-Pérez, FM Peeters, and David Hernández-Nieves. Vibrational properties of germanane and fluorinated germanene in the chair, boat, and zigzag-line configurations. Journal of Physics: Condensed Matter, 31(7):075301, 2019.
6. V Mendoza-Estrada, W López-Pérez, R González-Hernández, and **A González-García**. Electronic structure and magnetic order in  $\text{Cu}_x\text{Zn}_{(1-x)}\text{O}$ : A study GGA and GGA+U. Physica B: Condensed Matter, 557:74–81, 2019.

7. R González-Ariza, O Martínez-Castro, M G Moreno-Armenta, **A González-García**, W López-Pérez, and R González-Hernández. Tuning the electronic and magnetic properties of 2d-GaN by H adsorption: An ab-initio study. *Physica B: Condensed Matter*, 569:57–61, 2019.
8. R González, W López-Pérez, **A González-García**, M G Moreno-Armenta, and González-Hernández. Vacancy charged defects in two-dimensional GaN. *Applied Surface Science*, 433:1049–1055, 2018.
9. W López-Pérez, L Ramírez-Montes, **A González-García**, C Pinilla, J Rivera-Julio, and R González-Hernández. Charged vacancy defects in an AlN nanosheet: A first-principles DFT study. *Computational Condensed Matter*, 14:153–160, 2018.
10. V Mendoza-Estrada, D Barragán-Yani, W López-Pérez, J Rivera-Julio, R González-Hernández, and **A González-García**. Ferromagnetic orderings in  $\text{Co}_x\text{Cu}_y\text{Zn}_{1-(x+y)}\text{O}$  by GGA and GGA+U formalisms within density functional theory. *Computational Materials Science*, 126:344–350, 2017.
11. V Mendoza-Estrada, **A González-García**, W López-Pérez, C Pinilla, and R González-Hernández. Structural, electronic and magnetic properties of Ti-doped polar and non polar GaN surfaces. *Journal of Crystal Growth*, 467:12–17, 2017.
12. **A González-García**, V Mendoza-Estrada, W López-Pérez, C Pinilla-Castellanos, and R González-Hernández. Ab-initio study on electronic and magnetic properties of (Ga, Co) Co-doped ZnO. In *Journal of Physics: Conference Series*, volume 743, page 012002. IOP Publishing, 2016.
13. R González-Hernández, **A González-García**, and W López-Pérez. Density functional theory study of the adsorption and incorporation of Sc and Y on the AlN (0001) surface. *Journal of Crystal Growth*, 443:1–7, 2016.
14. R González-Hernández, **A González-García**, G Martínez, and W López-Pérez. Formation of two-dimensional  $\text{SiN}_x$  layers on GaN non-polar surfaces.

Thin Solid Films, 603:238–242, 2016

15. L Ramirez-Montes, W López-Pérez, **A González-García**, and R González-Hernández. Structural, and thermodynamic properties of  $Y_xAl_{(1-x)}N$  semi-conducting alloys. *Journal of Materials Science*, 51(6):2817–2829, 2016.
16. W López-Pérez, P Castro-Diago, L Ramírez-Montes, **A González-García**, and R González-Hernández. Effects of scandium composition on the structural, electronic, and thermodynamic properties of  $Sc_xY_{(1-x)}$  metallic alloys. *Philosophical Magazine*, 96(5):498–510, 2016.
17. L Ramírez-Montes, W López-Pérez, **A González-García**, and R González-Hernández. Theoretical prediction of the electronic and thermodynamic properties of YN-ZrN solid solutions. *International Journal of Quantum Chemistry*, 116(1):13–20, 2016.
18. **A González-García**, W López-Pérez, D Barragán-Yani, and R González-Hernández. A comparative DFT and DFT+U study on magnetism in Ni-doped wurtzite AlN. *Journal of Superconductivity and Novel Magnetism*, 28(11):3185–3192, 2015.
19. **A González-García**, W López-Pérez, and R González-Hernández. Magnetism in Ni-doped AlN with N vacancy: A first-principles study. *Computational Materials Science*, 91:1–5, 2014.
20. **A González-García**, William López-Pérez, Rommel Palacio-Mozo, and Rafael González-Hernández. Thermodynamic properties of  $In_{(1-x)}B_xP$  semi-conducting alloys: A first-principles study. *Computational Materials Science*, 91:279–284, 2014.
21. **A González-García**, W López-Pérez, and R González-Hernández. First-principles LDA+U study of magnetism in  $Cu_xIn_{(1-x)}N$ . *Solid State Communications*, 156:64–68, 2013.
22. **A González-García**, W López-Pérez, and R González-Hernández. Ab initio

calculations of magnetic properties of Ag-doped GaN. *Computational Materials Science*, 55:171–174, 2012.

23. **A González-García**, W López-Pérez, and R González-Hernández. Theoretical study of magnetic ordering and electronic properties of  $\text{Ag}_x\text{Al}_{(1-x)}\text{N}$  compounds. *Solid State Communications*, 151(23):1794–1797, 2011.
24. Th Dittrich, **A González-García**, T Rada, T Rissom, E Zillner, S Sade-wasser, and M Lux-Steiner. Comparative study of Cu (In, Ga)  $\text{Se}_2/\text{CdS}$  and Cu (In, Ga) $\text{Se}_2/\text{In}_2\text{S}_3$  systems by surface photovoltage techniques. *Thin Solid Films*, 535:357–361, 2013.

*Dedicated to:*  
*the spiritual energy that has enlightened my path all my life;*  
*my parents, for teaching me the best way to go;*  
*my wife, for giving me the strength to keep fighting.*  
*And, last but not least, to my children,*  
*for being the motivation to continue improving myself.*

# Acknowledgments

Everything that exists around us vibrates with a certain frequency. When our thoughts vibrate with the correct frequency to make dreams come true, the universe will conspire to provide us with what we need to achieve them. But, once we have accomplished them with the help of others, we need to be an instrument for others to achieve their goals.

Let me thank all my supporters for being there at the precise moment of my life, sharing with me their knowledge and wise guidance to help me grow as a human being:

To Professor William López, thank you for being the first to believe in me.

To Professor Rafael González, thank you for sharing his expertise with me.

To Professor François Peeters, thank you for being the bridge that united two worlds.

To Professor Milorad Milošević, thank you for being there pushing me to always give my best.

To each Professor that has taught me, thank you for sharing your wisdom with me.

To the team of human beings from the physics research groups of both universities, Norte and Antwerp, thank you for the fruitful scientific discussions.

To all my friends, thank you for giving me the warmth of your friendship.

Special thanks to the Special Research Funds of the University of Antwerp (BOF), and the Research Foundation-Flanders (FWO). This research was supported

by a scholarship from BOF/UA (Bijzonder Onderzoeks Fonds/Universiteit Antwerpen). Part of the calculations were performed within the VSC (Flemish Supercomputer Center), funded by the FWO and the Flemish Government—department EWI.

Special thanks to the Granados Cluster from the Universidad del Norte.

To my wife Betty and my daughter Stephy, thank you for all your love and unconditional support.

A special thanks to my son Andrés for reviewing the English redaction of this manuscript.

A special thanks to my son Alvarito for always being available when I have need him.

And, last but not least, to all the administrative staff from both Universidad del Norte and Antwerp university, thank you for all your support. I apologize if I was a bit intense at times.

# Contents

<b>List of Figures</b>	<b>xiv</b>
<b>1 Introduction</b>	<b>1</b>
1.1 Two-dimensional materials . . . . .	2
1.1.1 Historical overview . . . . .	2
1.1.2 Properties of 2D graphene-like materials . . . . .	5
1.1.3 Brief summary on principal experimental methods to synthesize 2D-materials . . . . .	10
1.1.4 Tuning physical properties of 2D-materials . . . . .	14
1.1.5 Applications . . . . .	21
1.2 From 3D group III-V to 2D group III-V semiconductors. . . . .	24
1.3 Scope and organization of the thesis. . . . .	28
<b>2 Theoretical framework</b>	<b>31</b>
2.1 The quantum many-body problem . . . . .	32
2.1.1 Born-Oppenheimer approximation . . . . .	33
2.2 Density Functional Theory (DFT) . . . . .	35
2.2.1 The Hohenberg-Kohn theorems . . . . .	36
2.2.2 The Kohn-Sham auxiliary system . . . . .	37
2.2.3 DFT to spin spin-polarized system (SDFT) . . . . .	41
2.3 Exchange-correlation functionals . . . . .	42
2.3.1 Local Density Approximation (LDA) . . . . .	42
2.3.2 Generalized-gradient approximation (GGA) . . . . .	43
2.3.3 Hybrid functionals . . . . .	44
2.4 Density functional theory implementation . . . . .	45
2.4.1 Bloch's theorem . . . . .	45
2.4.2 Plane wave expansions . . . . .	46
2.4.3 First Brillouin zone . . . . .	48
2.4.4 Pseudopotentials and PAW . . . . .	50
2.4.5 Spin-Orbit Coupling . . . . .	53
2.4.6 Vienna <i>Ab-initio</i> Simulation Package (VASP) . . . . .	57
2.4.7 Phonons . . . . .	58
2.4.8 Supercell model . . . . .	64
2.5 Magnetic exchange interaction . . . . .	66
2.5.1 The four-state mapping methodology . . . . .	68

<b>3</b>	<b>Structural, mechanical and electronic properties of two-dimensional structure of III-arsenide (111) binary compounds: An <i>ab-initio</i> study</b>	<b>73</b>
3.1	Introduction . . . . .	74
3.2	Computational methods . . . . .	76
3.3	Results and discussion . . . . .	78
3.3.1	Structural Properties and phonon dynamical stability . . . . .	78
3.3.2	Electronic and mechanical properties . . . . .	81
3.3.3	Few-layer h-IIIs structures . . . . .	84
3.4	Conclusions . . . . .	89
3.5	Publication . . . . .	90
<b>4</b>	<b>Tunable 2D-Gallium Arsenide and Graphene bandgaps in Graphene/-GaAs heterostructure: an <i>ab-initio</i> study</b>	<b>91</b>
4.1	Introduction . . . . .	92
4.2	Computational and theoretical details . . . . .	94
4.3	Results and discussion . . . . .	98
4.3.1	Structural properties and dynamical stability . . . . .	98
4.3.2	Electronic structure and Mechanical properties . . . . .	101
4.3.3	Tuning Graphene and 2D-GaAs bandgaps . . . . .	103
4.4	Conclusions . . . . .	106
4.5	Publication . . . . .	108
<b>5</b>	<b>Two-dimensional hydrogenated buckled gallium arsenide: An <i>ab-initio</i> study</b>	<b>109</b>
5.1	Introduction . . . . .	110
5.2	Computational details . . . . .	113
5.3	Results and discussion . . . . .	114
5.3.1	Energetic and dynamic stability . . . . .	114
5.3.2	Structural properties . . . . .	117
5.3.3	Electronic structure and Bader charge transfer analysis . . . . .	119
5.4	Conclusions . . . . .	123
5.5	Publication . . . . .	124
<b>6</b>	<b>Transition-metal adatoms on 2D-GaAs: a route to chiral magnetic 2D materials by design</b>	<b>125</b>
6.1	Introduction . . . . .	125
6.2	Computational and theoretical details . . . . .	128
6.3	Results and discussion . . . . .	131
6.3.1	Energetic stability and structural properties . . . . .	131
6.3.2	MAE and electronic properties . . . . .	133
6.3.3	Magnetic Exchange Interaction . . . . .	138
6.4	Conclusions . . . . .	142
6.5	Publication . . . . .	143

<b>7</b>	<b>Summary and outlook</b>	<b>144</b>
7.1	Summary . . . . .	144
7.2	Outlook . . . . .	147
	<b>Bibliography</b>	<b>149</b>
<b>A</b>	<b>Abbreviations</b>	<b>172</b>
<b>B</b>	<b>Curriculum vitae</b>	<b>175</b>

# List of Figures

1-1	(a) The honeycomb lattice of graphene. (b) The Brillouin zone of a graphene unit cell. (c) Left: Electronic dispersion in the honeycomb lattice. Right: Zoom in the energy bands close to one of the Dirac points [1] . . . . .	7
1-2	Comparison between electronic band structure for (a) graphene, and (b) graphite [2] . . . . .	7
1-3	Chart summary of the layered 2D-materials family, where hBN means hexagonal boron nitride; BCN is 2D nanocomposite containing boron, carbon and nitrogen; BSCCO is bismuth strontium calcium copper oxide [3] . . . . .	8
1-4	Family of 2D materials as a function of time (horizontal axis) and their respective band gap values (vertical axis). Materials with yellow color represent the 2D metal oxides, which cover a band gap energy range from $\sim 2.3$ to 4.9 eV [3]. . . . .	9
1-5	Three principal experimental techniques to synthesize 2D materials: a) micromechanical cleavage, b) physical vapour deposition (PVD), and c) chemical vapour deposition (CVD) [4] . . . . .	11
1-6	Schematic illustration of the physical vapor deposition process (PVD) [5]. . . . .	13
1-7	Schematic illustration of (a) zigzag and (b) armchair edges in graphene nanoribbons (GNRs). Bold line indicates the edge, where the A and B-site denote the carbon atoms, respectively [6]. . . . .	16
1-8	Analogy for building van der Waals heterostructures using different set of materials as lego blocks [7] . . . . .	17
1-9	(a) Schematic representation of solar cells designed by multi layers: Graphene, BN and NbSe <sub>2</sub> [8]. (b) Introducing local strain in graphene by an atomic force microscopy tip [8] . . . . .	17
1-10	Potential applications of graphene and beyond materials [9] . . . . .	23
1-11	Graphene related materials as platform for studying physics new phenomena, and designing new technologies and applications [10] . . . . .	24
1-12	The hexagonal primitive cell (right-hand side), with one B, Ga or In atom (Blue color) and one As atom (Red color), was constructed from the zinc-blende structure (left-hand side) in the (111) plane. The hexagonal unit cell is also highlighted with a red line in the (111) plane. . . . .	25

1-13	Schematic diagram of a tunneling field-effect transistor based on a vertical heterostructure of 2D MoS <sub>2</sub> , and 3D Si and Group III-V semiconductors [11]. . . . .	27
2-1	Schematic illustration of the comparison between a real wave function $\Psi$ (Coulomb potential $V$ ) and a pseudo-wave function $\Psi_{pseudo}$ (pseudopotential $V_{pseudo}$ ). The real and the pseudo wavefunction and potentials match above a certain cutoff radius $r_c$ . . . . .	52
2-2	Orbital angular momentum of $p$ -graphene state ( $l=1$ ) with (a) no coupling, and (b) coupling with its spin intrinsic momentum. . . . .	54
2-3	Scheme of the self-consistent cycle of the Kohn–Sham equations employed by VASP [12]. . . . .	57
2-4	Phonon dispersion curves for 2D–BAs semiconductor in the hexagonal primitive cell with GGA scheme. . . . .	61
2-5	(a) The chirality of domain walls in the presence of spatial inversion asymmetry and the spin Hall effect – with a mechanism that conserves spin angular momentum, that is, Slonczewski spin-transfer torques (HSL: Slonczewski field induced by edge spin accumulation) [13]. (b) Skyrmions in a 2D ferromagnet [14]. (c) DMI at the interface between a ferromagnetic metal (grey) and a metal with a strong SOC (blue) [15]. . . . .	67
2-6	(a) Side view of interacting TM atoms on 2D-monolayer located at the nearest side (i,j) for $J_{ij}^{zz}$ magnetic interaction. (b) $\mathbf{J}_{ij}$ is a $3 \times 3$ matrix describing the magnetic exchange interaction between two magnetic sites (i,j). (c) Four spin configurations for calculating the $J_{ij}^{zz}$ component of exchange interaction matrix. . . . .	71
3-1	The hexagonal primitive cell (right figure), with one B, Ga or In atom (blue color) and one As atom (red color), was constructed from the zinc-blende structure (left figure) in the (111) plane. The hexagonal unit cell is also highlighted with a red line in the (111) plane in the middle figure. . . . .	79
3-2	Phonon dispersion curves for 2D BAs, GaAs and InAs semiconductors in the hexagonal primitive cell with GGA scheme. . . . .	80
3-3	The band structures and the majority density of states for 2D BAs, GaAs and InAs semiconductors in the hexagonal primitive cell with GGA scheme. The dashed line indicates the Fermi level, which is taken to be zero. . . . .	81
3-4	The majority density of states for 2D BAs, GaAs and InAs semiconductors in the hexagonal primitive cell with GGA-HSE approach. The dashed line indicates the Fermi level, which is taken to be zero. . . . .	82
3-5	Top view of five possible stacking sequences for $h$ -IIIs bilayer. Blue atoms are B, Ga or In, and red atoms refer to As. . . . .	85
3-6	Comparison of the band structures for 2, 3 and 4-layer $h$ -BAs, $h$ -GAs and $h$ -InAs structures in their most energetic favorable stacking sequence with GGA approach. . . . .	87

4-1	Orbital angular momentum of $p$ -graphene state ( $l=1$ ) with (a) no coupling and (b) coupling with its spin intrinsic momentum . . . . .	97
4-2	Honeycomb unit cells for (a) Graphene, (b) 2D-GaAs monolayers, and (c) 551-Graphene/331 GaAs bilayer crystal heterostructure. . . . .	99
4-3	Phonon dispersion curves for the 551-Graphene/331-GaAs bilayer heterostructure . . . . .	101
4-4	Electronic band structure for the 551-Graphene/331-GaAs bilayer crystal heterostructure without strain. The brown lines represent the contributions of Ga-4s and As-4 $p_z$ orbitals, while the green one the contribution of C-2 $p_z$ orbitals. . . . .	101
4-5	Electronic structures for i) uniaxial stress along $c$ -axis, ii) biaxial symmetrical strain, and iii) uniaxial asymmetrical strain along perpendicular C-C bond for $x = -6.0\%$ , $-4.0\%$ , $-2.0\%$ , $+2.0\%$ , $+4.0\%$ and $+6.0\%$ configurations of 551-Graphene/331 GaAs bilayer crystal heterostructure. . . . .	104
5-1	Schematic representation for : (a) 2D-GaAs hexagonal unit cell, (b) 2D H-GaAs chair configuration, (c) 2D H-GaAs rectangular unit cell, (d) 2D H-GaAs boat configuration, (e) 2D H-GaAs zigzag-line configuration, and (f) high symmetry points in the Brillouin zone for the rectangular unit cell of 2D H-GaAs. . . . .	111
5-2	Phonon dispersion curves for (a) pristine 2D-GaAs, (b) 2D H-GaAs chair configuration, (c) 2D H-GaAs boat configuration, and (d) 2D H-GaAs zigzag-line configurations with DFT-PBE functional. . . . .	117
5-3	Electronic band structure for (a) the pristine 2D-GaAs sheet, and (b) chair, (c) boat, and (d) zigzag-line configurations for 2D H-GaAs, with DFT-PBE functional. The red lines represent the contributions of GaAs-4 $p_z$ orbitals, the black lines the contributions of GaAs-4 $p_{xy}$ mixed orbitals, and the yellow lines represent the contributions either of the GaAs-4s orbitals (pristine 2D-GaAs) or GaAs-4s and H-1s mixed orbitals (2D H-GaAs). . . . .	120
6-1	Oblique view of the considered systems: (a) top view of a transition-metal adatom at the hollow site of 551-GaAs supercell, and side views of the optimised placements for the adsorbed (b) Mn, (c) Co, (e) Mo, and (f) Os atoms at such a site. For comparison, panel (d) shows relaxed buckling of 551-GaAs at the hollow site in absence of an adatom. . . . .	129
6-2	Parametric orbital projected band structure of pristine 2D-GaAs. The colour intensity corresponds to the degree of overlap of $sp$ orbitals between Ga and As atoms. Fermi energy is set to 0 eV. . . . .	134
6-3	Parametric orbital projected band structure of TM on 2D-GaAs, calculated with SOC included. The colour intensity corresponds to the degree of contribution of the $d$ orbital of a TM adatom. Fermi energy is set to 0 eV. . . . .	135

- 
- 6-4 Calculated electronic spin-charge density for systems with the easy magnetisation axis in-plane ((a) Os and (b) Co) or out-of-plane ((c) Mn and (d) Mo) to the surface of the 2D structure. The colour intensity represents the spin-charge density, where blue and red indicate high and low electronic spin-charge density, respectively. . . . . 137
- 6-5 Top and side view of interacting TM adatoms on 2D-GaAs: Mn (a,b), Co (c,d), and Mo (e,f) atoms, located at the hollow sites of a  $\sqrt{3}\times\sqrt{3}$ -GaAs supercell. DMI vector  $\mathbf{D}_{12}$  (blue), showing non-trivial magnetic exchange interaction between the two TM adatoms is also shown, together with their spins (vectors in gold) at ground state for facilitated sense of orientation. . . . . 138

"There are great hopes that the exceptional properties of graphene can be utilised in many areas"

Physics Nobel award ceremony  
speech, 2010

# Chapter 1

## Introduction

The influence of 3D group III-V materials in the development of the current technology, and the emergent research in two-dimensional graphene related materials, which will determine the roadmap for future technology, led us to question not only about the physical properties of new atomically thin materials based on group III-V materials, but also of those ones of hybrid materials using III-V group materials and graphene. The answer is this thesis, which focuses on **the study of the tunability properties of III-As materials (III = B, Ga and In) in the thinnest limit: single layer and 2D-heterostructures**, using Density Functional Theory (DFT).

To give clarity and insight to the reader about what this thesis covers, this section will be divided in three main topics: Two-dimensional materials overview, relevance of the design of new atomically thin materials based on group III-V materials, and the scope and organization of the thesis. The first topic is initially devoted to acknowledge the efforts of the giant scientists, whose previous research paved the way and motivated others to continue exploring the atomically thin world. Afterwards, the astonishing properties of two-dimensional materials will be highlighted, following with a brief summary of principal experimental methods to synthesize them. Lastly, the main methods to tune the properties of graphene related materials, and their applications, will be described. The second part will be aimed at highlighting the impact of designing thin layer semiconductors using 3D group III-V semiconductors. In the last part of this section, the scope and the organization of the thesis will be presented.

## 1.1 Two-dimensional materials

### 1.1.1 Historical overview

Even though graphene was worldwide known in 2004 when it was isolated by exfoliation from graphite by Andre Geim and Konstantin Novoselov [16], who in 2010 were awarded the Physics Nobel Prize for this transcendental discovery, there are some earlier pioneering theoretical and experimental researches regarding graphene [17]. In 1947, Phil Russell Wallace first calculated theoretically its band structure as a first approximation to understand the electronic properties of 3D graphite [18]. The earliest experimental observation of few-layer graphite was made by G. Ruess and F. Vogt in 1948 using transmission electron microscopy (TEM) [19]. In 1962, Hanns-Peter Boehm and Hofmann were the first to isolate and identify single graphene sheets by TEM [20]. Later, in 1986, Boehm *et al* authored the term graphene [21]. In a 2007 paper titled: "Citation errors concerning the first report on exfoliated graphite" [22], Boehm attributes the discovery of exfoliation of graphite to Schafhaeutl in 1840 [23].

Between 1970 and 1992 there were several studies on epitaxial growth of graphitic films on metal substrates [24, 25, 26, 27, 28], as described below:

In 1970, Blakely *et al* and Grant *et al* reported, almost simultaneously, graphitic films on Ni(100) [24], and Ru(0001) and Rh(111) surfaces [25], respectively, by using low energy electron diffraction (LEED) and Auger electron spectroscopy (AES).

In 1983 Rosei *et al* [26] determined experimentally the structural parameters of the graphitic carbon overlayer on a Ni(111) substrate. They also found that graphite overlayer floats at 2.80 Å above the Ni(111) face, and the substrate is not affected by the growth of the graphitic overlayer.

In 1986, McConville *et al* [27] compared the results of Angle-resolved ultraviolet photoelectron spectroscopy (ARUPS) measurements of the valence-electronic structure of the Ni [100](2x2)C structure with the ones of self-consistent density-functional calculations of the two-dimensional band structure for a (2x2)C overlayer on Ni[100]. They found excellent qualitative agreement for the dispersion energies of the C-2s and C-2p states between experiment and calculation results, although the

absolute magnitude of these dispersions appears to be somewhat overestimated in the calculation results. This is attributed to the difficulty to describe the Ni *d*-band width.

In 1992, Land *et al* [28] determined by scanning tunneling microscopy (STM) studies that hydrocarbon (ethylene) decomposition at elevated temperatures results in the formation of a single layer of graphite on the Pt(111) surface.

Graphite has also been grown epitaxially on insulating substrates (SiC). The most important researches using this technique are described below:

In 1975, van Bommel *et al* [29] were the first to grow epitaxially a monolayer of graphite on SiC (0001) surface. The grown film was analyzed by LEED and AES.

In 1993, Nagashima *et al* [30] investigated the electronic structure of monolayer graphite formed on TiC(111), TiC(100), and TaC(100) surfaces by X-ray photoelectron spectroscopy (XPS), ultraviolet photoelectron spectroscopy (UPS), and LEED. They revealed that monolayer graphite on the (111) surfaces of transition-metal carbides differs substantially from bulk graphite in its lattice constant and phonon dispersion, while those of monolayer graphite on (100) surfaces are hardly modified. These large changes are caused not by charge transfer but mainly by orbital hybridization between the graphite overlayer and the (111) surface.

Monolayer micrographite (200nm) was grown by chemical vapor deposition on TiC(111) surface in 1998 by Terai *et al* [31]. Its electronic structure was studied by LEED, XPS and ARUPS. They found no differences in the observed spectra of micrographite on TiC(111) surface from the bulk one, which can be explained by the size of the micrographite.

In addition to the TEM observations and the epitaxial growth of graphene, between 1990 and 2003 there were some attempts to obtain ultra-thin films of graphite by cleavage [32, 33, 34, 35], similar to what Geim and Novoselov did in 2004.

In 1990, free-standing films obtained by peeling optically thin layers from a master sample with transparent tape was used by Seibert *et al* to study carrier dynamics in graphite [32].

In 1995, Ebbesen *et al* [33] reported nano graphite origami obtained by scanning tunneling microscope (STM) and atomic force microscopy (AFM) on top of highly

oriented pyrolytic graphite (HOPG). They observed that the folding and bends in the graphite sheet should be separated by angles that are multiples of  $30^\circ$ .

In 1999, Lu *et al* [34] gave an important step towards manufacturing graphene single sheets by nanofabrication techniques. Nanometred-size graphene sheets were obtained by peeling graphite islands from HOPG, and then manipulated with AFM tips.

In 1999, Beyer *et al* [36] were the first to report STM results on monolayers of graphene spread on a graphite surface and rotated by a known angle. In order to do this, a monolayer of HOPG on HOPG at a known rotation angle was prepared.

In 2003, Yang Gan *et al* [35] reported graphene monolayers by using STM for their cleavage on top of HOPG.

Theoretically, graphene has been studied since 1947, when, as mentioned beforehand, Phil Wallace first calculated its band structure using the tight binding method as a first approximation in the study of graphite [18].

In 1956 McClure calculated the conduction-electron magnetic susceptibility of graphite using the Wallace two-dimensional band structure by the method of Luttinger and Kohn[37].

In 1958, JC Slonczewski and PR Weiss studied the band structure of graphite using tight-binding calculations and a two-dimensional model of the graphite lattice [38].

In 1984, G. W. Semenoff, using tight binding model, was the first to describe the electrons of a graphite monolayer by an equation that is formally equivalent to the massless Dirac equation, where the electrons and holes are called Dirac fermions [39].

In 1988, F. D. M. Haldane proposed the first model of the anomalous quantum Hall effect (AQHE) in two-dimensional (2D) electron systems using the model presented by Semenoff. In this effect the Hall conductance becomes quantized in unit of  $e^2/h$ , in the absence of an external magnetic field, which is known as the Haldane model [40].

In 1992, Saito *et al* predicted the electronic structure for graphene monolayer tubules as a function of the diameter and helicity of the constituent graphene tubules

[41].

In 2002, Gorbar *et al* developed a theory of the magnetic-field driven metal-insulator phase transition in planar systems, based on reduced Quantum Electrodynamics (QED) [42].

So far, we have highlighted the most relevant experimental and theoretical works on graphene before 2004. In the next section, we will review the current state of the art related to: the unique crystal and electronic structure properties of graphene-like materials, the drawbacks of graphene, as well as a description of 2D-materials beyond graphene.

### 1.1.2 Properties of 2D graphene-like materials

Two-dimensional (2D) materials present exceptionally different physical and chemical properties compared with conventional bulk materials. Bonding in the latter can be mainly metallic, covalent, ionic and vdW, while 2D-materials are characterized by intralayer covalent ( $\sim 200\text{-}6000$  meV) [43] and interlayer weak vdW bonding ( $\sim 40\text{-}70$  meV) [43]. The unique crystal structure and electronic structure enable 2D materials to possess ultralow weight, high Young's modulus, high strength, high anisotropy between the in-plane and out-of-plane mechanical properties, as well as outstanding electrical properties compared with their 3D counterparts [44].

Graphene, one of the most representative 2D materials, stands out in the flexible electronics field due to its combination of high electron mobility, high thermal conductivity, high specific surface area, high optical transparency, excellent mechanical flexibility, and environmental stability [45]. It is a semimetal whose conduction and valence bands, in neutral graphene, meet at the Dirac points (the K point in the Brillouin zone), see [Figure 1-2\(a\)](#). In the vicinity of the K-points the energy depends linearly on the wave vector, similar to an ultra-relativistic particle [39]. As a result, around the Dirac point K (K'), at low energies near the Fermi level, the electrons can be described by an equation that is formally equivalent to the relativistic massless Dirac equation:

$$\hat{H} = \hbar v_F \begin{pmatrix} 0 & k_x - ik_y \\ k_x + ik_y & 0 \end{pmatrix} = \hbar v_F \vec{\sigma} \cdot \vec{k}, \quad (1.1)$$

and around the K' as

$$\hat{H} = \hbar v_F \begin{pmatrix} 0 & k_x + ik_y \\ k_x - ik_y & 0 \end{pmatrix} = \hbar v_F \vec{\sigma} \cdot \vec{k}, \quad (1.2)$$

Where  $\vec{k}$  is the wave vector,  $\vec{\sigma}$  the 2D Pauli matrix, and  $v_F$  is the Fermi velocity, which replaces the speed of light in the Dirac theory. For this reason, the electrons are called massless Dirac fermions [39], except for the fact that in graphene the Dirac fermions move with a speed  $v_F$ , which is 300 times smaller than the speed of light  $c$  ( $v_F \sim 10^6$  m/s). Therefore, many of the unusual properties of quantum electrodynamics (QED) can show up in graphene but at much smaller speeds [1]. The Dirac equation is a direct consequence of graphene's crystal symmetry. Its carbon atoms are tightly packed into a flat two-dimensional (2D) honeycomb lattice. Its honeycomb lattice is made up of two equivalent carbon sublattices A and B, as shown in Figure 1-1 [16]. Figure 1-2 displays the electronic band structure for 2D-graphene and bulk graphite for comparison. We can notice the notable difference between them, especially around the K point.

Even though graphene exhibits interesting physical properties such as high charge carrier mobility, high thermal conductivity, infrared optical adsorption and total impermeability to any gas [46], which makes it desirable for technological applications, the absence of bandgap limits its use in the manufacture of electronic devices [8]. This bandgap limitation has motivated scientists to look for new 2D-materials beyond graphene [47]. Among the literature about the study of the large family of 2D-materials beyond graphene, we find monolayers: X-enes (X=B, Si, Ge, Sn, P, Bi), X-anes (Graphane, Silicane, Germanane, Stanane), fluorinated X-enes [48]; few layers crystal: hexagonal boron nitride (*h*-BN), transition metal oxides (TMOs: LaVO<sub>3</sub>, LaMnO<sub>3</sub>), transition metal chalcogenides (NbSe<sub>3</sub>, TaSe<sub>3</sub>), transition metal dichalcogenides, which are compounds composed of transition metal elements and elements of group-VI, also called chalcogen elements (S, Se, or Te), e.g., MoS<sub>2</sub>, MoSe<sub>2</sub>,

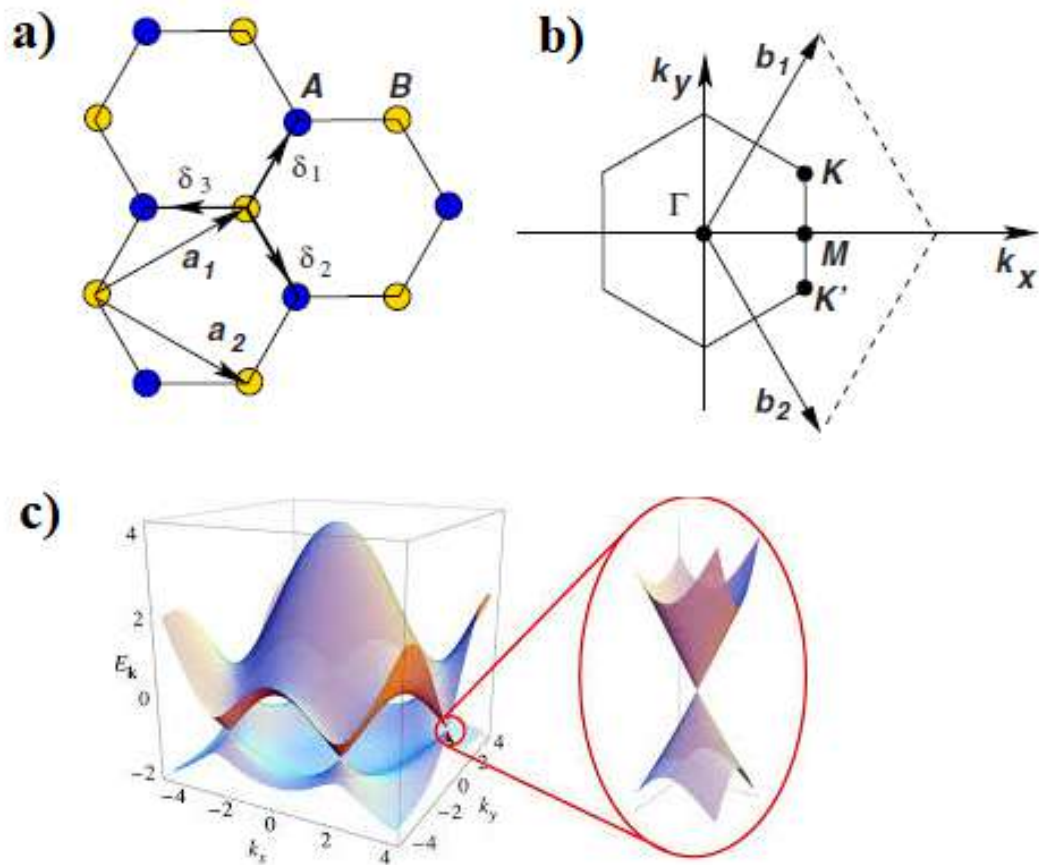


Figure 1-1: (a) The honeycomb lattice of graphene. (b) The Brillouin zone of a graphene unit cell. (c) Left: Electronic dispersion in the honeycomb lattice. Right: Zoom in the energy bands close to one of the Dirac points [1]

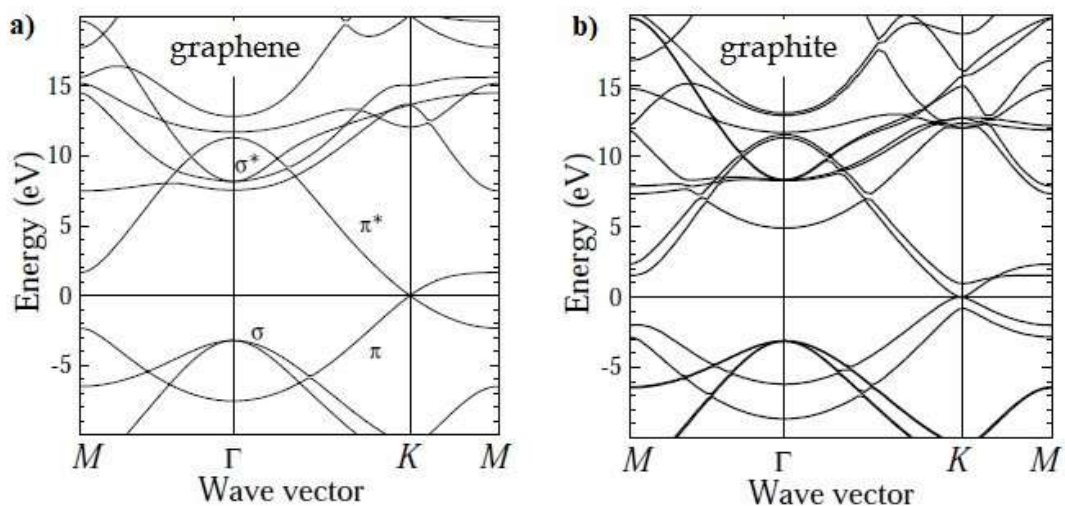


Figure 1-2: Comparison between electronic band structure for (a) graphene, and (b) graphite [2]

WS<sub>2</sub>, WSe<sub>2</sub>, among others; as well as 2D-heterostructures [3, 7, 9, 49, 50]. The family of the layered 2D-materials library is summarized in the chart of Figure 1-3. In the X-ene systems, the atoms are arranged in a honeycomb structure similar to graphene [48, 51, 52, 53, 54, 55, 56, 57]. When in the X-ene system is added hydrogen or fluor, the new configuration is labeled as X-ane (Graphane, Silicane, Germanane, Stanane), and fluorinated X-enes (fluro-X-enes or X-enes fluoride), respectively [48].

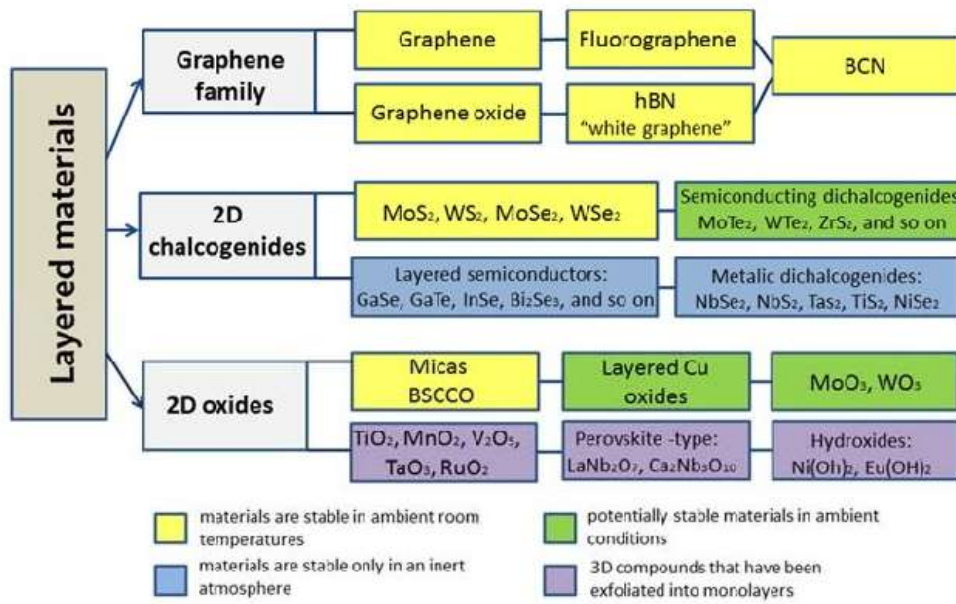


Figure 1-3: Chart summary of the layered 2D-materials family, where hBN means hexagonal boron nitride; BCN is 2D nanocomposite containing boron, carbon and nitrogen; BSCCO is bismuth strontium calcium copper oxide [3]

Importantly, the 2D materials family exhibits a wide spectrum of electronic properties covering metals, semimetals, semiconductors with various energy band gaps, and also insulators. Figure 1-4 illustrates the evolution of the family of 2D materials as a function of time (horizontal axis) and their respective band gap values (vertical axis). Materials with yellow color represent the 2D metal oxides, which cover a band gap energy range from  $\sim 2.3$  to 4.9 eV [3].

Regarding the experimental or theoretical studies of III-V (111)-binary compounds in the thinnest limit, the literature is scarce, even though the materials in question are rather accessible and readily used in technological applications. In

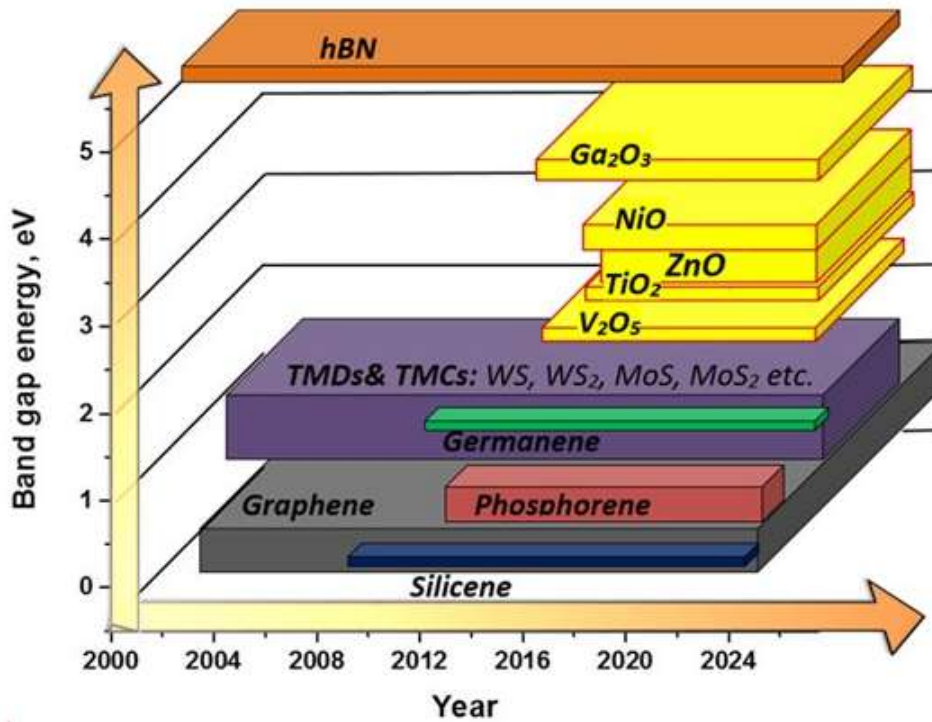


Figure 1-4: Family of 2D materials as a function of time (horizontal axis) and their respective band gap values (vertical axis). Materials with yellow color represent the 2D metal oxides, which cover a band gap energy range from  $\sim 2.3$  to  $4.9$  eV) [3].

**section 1.2** and **chapter 3** of this thesis, we will focus on the study of the main properties of group III-V materials.

Another important field that has stimulated immense interest in the scientific community for application of 2D-materials beyond graphene is spintronics. Nanomagnetic materials are potential candidates for next-generation devices having faster processing, large data storage capacity, and nanometric size. Although most 2D-materials are nonmagnetic in their pristine form, which restricts their applications in magneto-electronics, magnetism can be tuned in them through defects like vacancies, adatoms, doping, and dangling bonds. Other mechanisms to tune magnetism are strain, layered compounds, and application of an external magnetic field. The main source of magnetism in 2D-materials is magnetic anisotropy (MA), and the spin-orbit coupling (SOC) is the microscopic source of magnetic anisotropy. Hence, tuning the orbital and spin moment of a crystal is fundamental; as an illustration,

the magnetic anisotropy in a 2D material can be induced by doping with transition metals, among other ways of manipulating the SOC of a crystal [58, 59, 60, 61]. In **Chapter 6** of this thesis we will get back with this fundamental topic, such as the study of magnetism in 2D-materials. We will also investigate both the magnetic anisotropy and Dzyaloshinskii-Moriya interaction induced by transition metal adsorbed on two-dimensional gallium arsenide (TM= Mn, Co, Mo and Os).

The outstanding properties of 2D-materials, beforehand mentioned, make them attractive materials with potential industrial applications, often different from their 3D counterpart, and for studying unexplored fundamental science. These applications will be treated in **section 1.1.5**. In the next section, we will briefly review the main experimental methods to synthesize 2D-materials.

### 1.1.3 Brief summary on principal experimental methods to synthesize 2D-materials

In this section we will provide a brief summary on principal experimental methods to synthesize 2D-materials. The reliable synthesis of single- and few-layer 2D materials is an essential first step for characterizing the layer dependent changes in their properties, as well as providing pathways for their integration into a multitude of applications [43]. According to the type of chemical bonds, there are three main classification of crystalline structures that can be synthesized as a single- and few-layer 2D materials: van der Waals solids, layered ionic solids and nonlayered materials [43]. They are mainly obtained by two methodologies: top-down synthesis from bulk solids, i.e., micromechanical cleavage and liquid-phase exfoliation; and bottom-up synthesis, such as physical vapour deposition (PVD) and chemical vapour deposition (CVD), as shown in [Figure 1-5](#) [4]. The former is limited to materials derived from layered structures; the latter is not.

#### Micromechanical cleavage

This was the original method by which Andre Geim and Konstantin Novoselov isolated one carbon atom thick graphene sheets in 2004. They used Scotch tape to

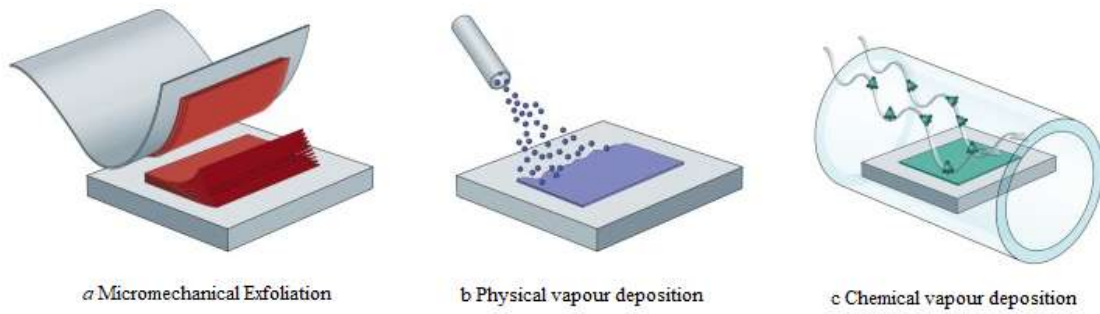


Figure 1-5: Three principal experimental techniques to synthesize 2D materials: a) micromechanical cleavage, b) physical vapour deposition (PVD), and c) chemical vapour deposition (CVD) [4]

separate the graphene sheets from graphite flakes. Thus, the mechanical exfoliation technique is used to separate single and few-layer sheets from bulk crystals by exfoliation. This method is limited to materials with a layered, bulk allotrope, which exhibit weak van der Waals (vdW) interactions between layers, with binding energies of  $\sim 40\text{--}70$  meV, facilitating the exfoliation of these layers e.g., graphite exfoliation into graphene, *h*-BN, MoS<sub>2</sub>, NbSe<sub>2</sub> [4].

This method requires repeatedly peeling of layered materials followed by the transfer of the peeled sample on top of a surface. The main features of this technique are [62]:

- It is an easy and fast way of obtaining highly crystalline atomically thin nanosheets.
- The resulting 2D sheets are stable under ambient conditions
- The peeled samples exhibit high crystal quality, and are continuous on a macroscopic scale
- The reported thickness of nanosheets obtained from their layered phases ranging from 1 to 10 atomic layers.

Although this method has been successful in isolating some thin nanosheets e.g., BN and MoS<sub>2</sub>, its usage has been limited due to its excessively low efficiency. In addition, this technique produces a larger quantity of thicker sheets in comparison

to those of monolayer ones. Thus, this method is not scalable to mass production for potential engineering applications [62].

### Chemical exfoliation

The scalability of mechanical exfoliation is enhanced by chemically derived exfoliations, also regarded as wet methods, such as liquid-phase exfoliation.

Liquid-phase exfoliation refers to a group of approaches that exfoliate single layer or few layers from those layered crystals directly in the liquid media; i.e., exfoliation in organic solvents and exfoliation in aqueous solutions. This method sonicates the layered bulk materials either in solvents, whose surface energy matches that of the energy required to overcome the vdW forces of bulk materials, or in water with surfactants, and then exfoliating the resultant dispersions into separated thin layers with assistance of centrifugation. The quality of yielded materials depends heavily on solution-processing parameters such as sonication time and centrifugation rate [62].

In the case of exfoliation in aqueous solutions, it is necessary to add surfactants, e.g., Sodium dodecylbenzene sulfonate (SDBS). This is because the surface tension of water is too high to exfoliate laminated materials alone. Therefore, the use of surfactants is essential to lower the surface tension of water and allow the exfoliation, and for the single layers to be stable in solution. The surfactant technique has been used for the production of graphene by exfoliation of graphite [63]. The drawbacks of this method are the difficulty to wash away the surfactants and the low yield of single layers [63, 64]. Even though exfoliation in organic solvents has been demonstrated to effectively isolate single layer and few layers from those thicker structures in large quantities e.g., N-Methyl-2-pyrrolidone (NMP) and Dimethylformamide (DMF) have been selected as good solvents for exfoliation, organic solvents can be toxic, expensive and difficult to remove once exfoliation has occurred [64].

### Physical vapour deposition

Physical vapor deposition (PVD) is a vaporization coating technique, where thermal energy is imparted to atoms in a liquid or solid source such that their temperature

is raised to the point where they either efficiently evaporate or sublime. The most common physical vapor deposition processes are sputtering and evaporation. In sputtering, atoms are ejected from source surfaces usually maintained at room temperature, through the impact of gaseous ions [65].

The PVD process involves the following sequence of steps. (i) The material to be deposited is converted into a vapor by physical means, e.g. evaporation (high-temperature vacuum), or collisional impact (gaseous plasma), (ii) the vapor is transported to a region of low pressure from its source to the substrate, and (iii) the vapor undergoes condensation on the substrate to form a thin film [5]. Typically, PVD processes are used to deposit films with thicknesses in the range of a few nanometers to thousands of nanometers. However, they can also be used to form multilayer coatings, graded composition deposits, very thick deposits, and freestanding structures [45]. A typical PVD process is shown in Figure 1-6 [5].

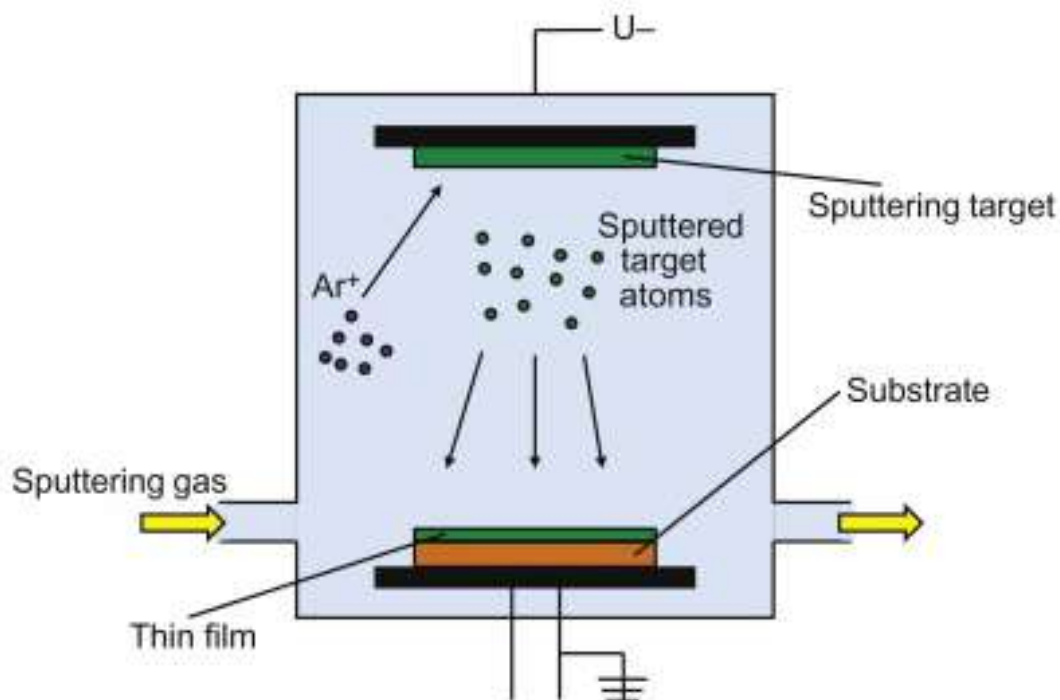


Figure 1-6: Schematic illustration of the physical vapor deposition process (PVD) [5].

PVD has several advantages including: (i) coatings formed by PVD may have improved properties compared to the substrate material; (ii) all types of inorganic

materials and some types of organic materials can be used; (iii) the process is environmentally friendly. However, PVD has also some disadvantages including: (i) problems with coating complex shapes; (ii) high process cost and low output; (iii) complexity of the process [66].

### **Chemical vapour deposition**

Chemical vapour deposition (CVD) is a coating process that uses thermally induced chemical reactions at the surface of a heated substrate, with reagents supplied in gaseous form. The main difference between CVD and PVD is the way by which the material to be deposited (precursors) is introduced to the reaction chamber. In CVD the precursors are in gaseous form, whereas in PVD, the precursors start out in solid form.

When comparing the final products obtained by mechanical exfoliation and chemical exfoliation methods, the former ones present higher quality but lower efficiency than those of the latter. CVD, on the other hand, presents much higher efficiency than for mechanical exfoliation, and the quality control is better than liquid phase routes. This method offers a compromise between quality, efficiency consistency, and control over the process. Hence, CVD has been recognized recently as a reliable route for preparing high quality two-dimensional (2D) materials [67]. The CVD is able to synthesize mono- or few-layered graphene with superior quality. For instance, in 2009, the synthesis of single layer graphene was achieved by low-pressure CVD on copper foils with methane as the carbon source [68]. In addition, single- and few-layer 2D TMD and BN nanosheets can be obtained by chemical vapor deposition (CVD) [67]. The drawback of this method is the high cost of its manufacturing conditions. This method requires high vacuum and high temperature.

#### **1.1.4 Tuning physical properties of 2D-materials**

Tuning method provides new pathways to yield novel properties in two-dimensional materials by design, e.g., mechanical, electronic and magnetic properties, tailored for desired applications in electronics devices. The physical and chemical properties of

2D Materials can be tuned by *Size Control, Heterostructuring, Strain Engineering, Electric Field Modulation, Doping, and Functionalization*. As mentioned in **section 1.1.2**, most of 2D-materials are nonmagnetic in their pristine form, which restricts their applications in magneto-electronics. However, magnetism can be tuned by applying strain, in layered compounds, and by application of an (even tiny) external magnetic field [69, 70]. It can also be induced by defects like vacancy, adatom, doping, and dangling bonds [58, 59, 60, 61].

As discussed in **section 1.1.2**, graphene presents technological restriction due to the absence of a band gap. A crucial point for the graphene band gap tailoring is to break the inversion symmetry of the equivalent sublattice of pristine graphene. There are several ways to achieve this: Cutting the 2D graphene into one-dimensional (1D) graphene nanoribbons (GNRs), doping, and functionalization. Theoretical and computational approaches such as density functional theory (DFT) are invaluable in determining the electronic band structure of 2D materials and its dependence on factors such as the number of layers, doping, electric field, or strain [71].

Now, some of the main methods to tune the physical and chemical properties of 2D Materials, such as: *Size Control, Heterostructuring, Strain Engineering, Electric Field Modulation, Doping, and Functionalization*, will be briefly discuss.

### **Size Control: Graphene Nanoribbons**

One of the most effective ways to achieve a sizable bandgap in graphene, is to decrease the dimension of graphene into one-dimensional nanoribbons by cutting the exfoliated graphene [72]. Cutting the 2D graphene into one-dimensional (1D) graphene nanoribbons (GNRs) can open a band gap in graphene due to electron confinement and the presence of edge states. The electronic properties of GNRs are highly dependent on their width and edge topologies, varying from metals to semiconductors as their widths decrease, especially below 10 nm. Depending on the atomic arrangement along their edges, GNRs can be classified as armchair or zigzag, as shown in [Figure 1-7](#). Armchair and zigzag edges can be stabilized by hydrogen saturation. The electronic and magnetic properties of armchair and zigzag

edges are sensitive to the modulation of an external field and the orientation of the spins of hydrogen [62, 73, 74, 75].

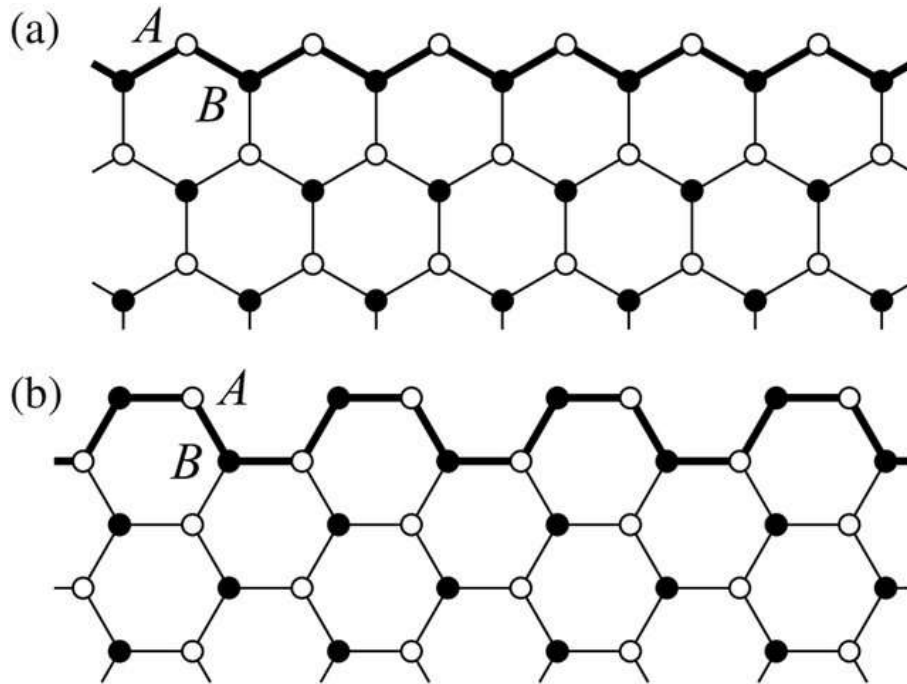


Figure 1-7: Schematic illustration of (a) zigzag and (b) armchair edges in graphene nanoribbons (GNRs). Bold line indicates the edge, where the A and B-site denote the carbon atoms, respectively [6].

## Heterostructures

Heterostructures are designed by stacking one monolayer on top of another monolayer, assembled in a chosen sequence, as Lego blocks, as shown in Figure 1-8. By these stacking combinations, new hybrid materials with different properties to those of their individuals' constituents can be manufactured, revealing unusual properties and new phenomena. The in-plane stability of these structures comes from their strong in-plane bond ( $\sigma$ ), while the weak van-der-Waals-like forces, keep the stack together [7].

2D-heterostructures have attracted the attention to tune the band gap width of semiconductors [7, 49, 50], which make them promising candidates for the manufacture of solar cells due to the complete adsorption of light by successive layers [8, 76, 77]. Figure 1-9 (a) depicts a solar cells device designed by multilayers of Graphene, BN and NbSe<sub>2</sub>. From the top down, we can see one layer of graphene,

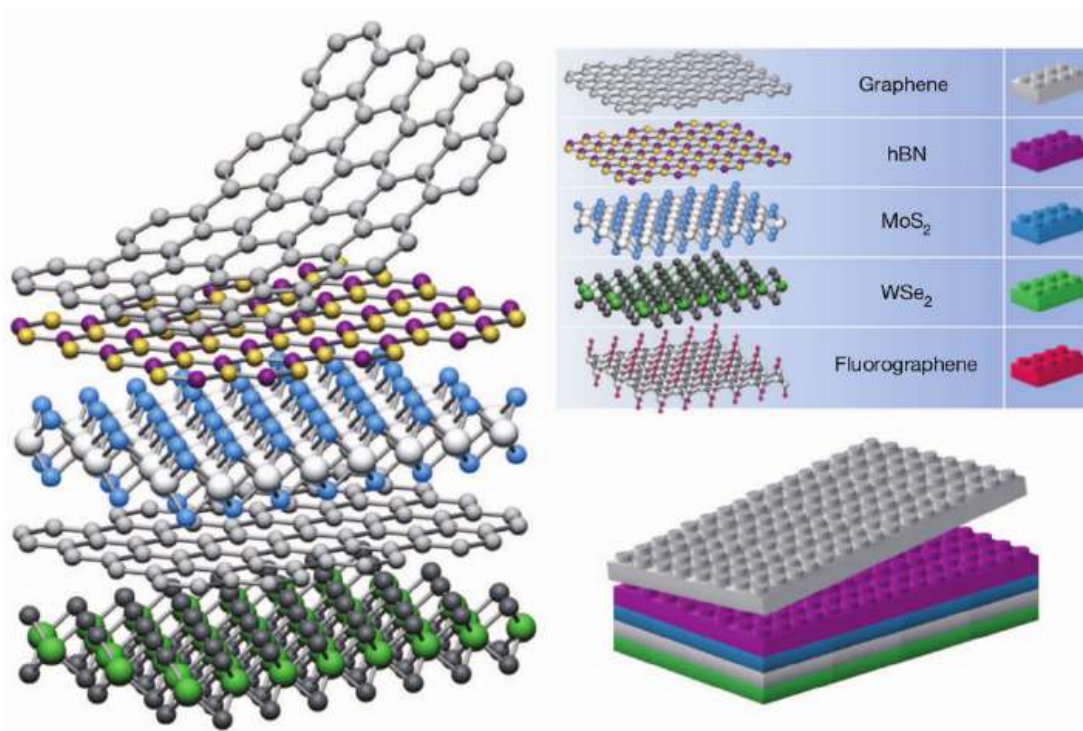


Figure 1-8: Analogy for building van der Waals heterostructures using different set of materials as lego blocks [7]

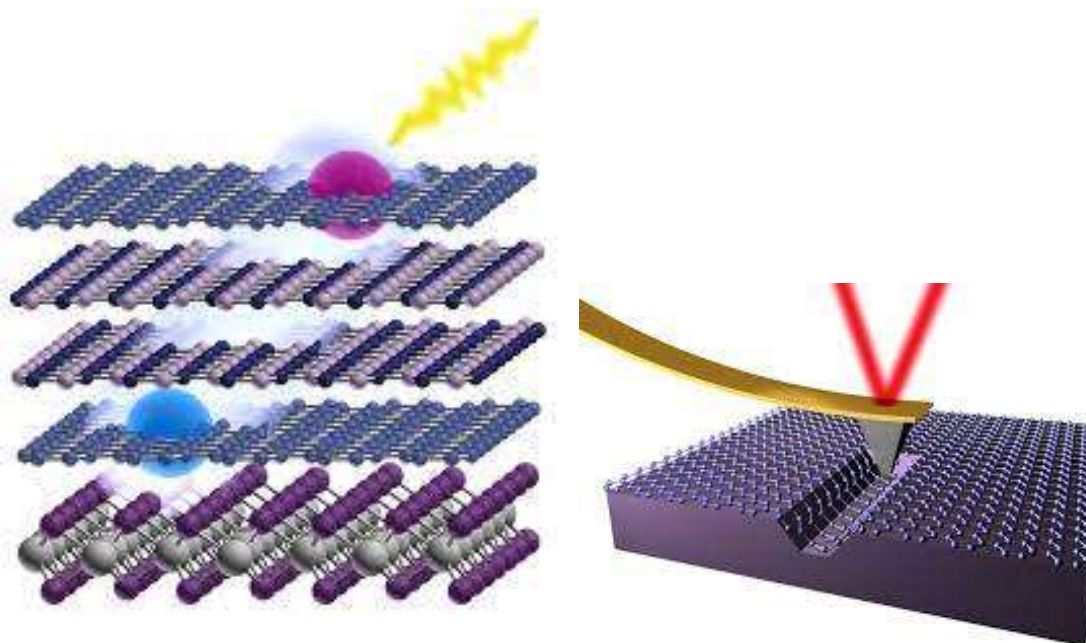


Figure 1-9: (a) Schematic representation of solar cells designed by multi layers: Graphene, BN and NbSe<sub>2</sub> [8]. (b) Introducing local strain in graphene by an atomic force microscopy tip [8]

two layers of BN, another layer of graphene, and a TMDC ( $\text{NbSe}_2$ ). The sandwiched BN layers serve as a tunneling barrier to graphene. The graphene layer next to TMDC gets doped due to the difference between their work functions. Thus, a built-in electric field is created between the two graphene layers. Because of the electron-hole pair induced by the electric field and an incoming photon, a photocurrent is created [8].

Zhang *et al* tuned the bandgap of graphene bilayer from 0 to 250 meV by applying an electrical field perpendicular to the layers. This perpendicularly applied electric field breaks the symmetry in graphene, which generates a band gap. The electrostatic band gap control suggests novel nanoelectronic and nanophotonic device applications based on graphene. This findings could be used for infrared light sources and sensors for biological measurements [78]. It has also been found that heterostructures based on graphene can improve the optoelectronic, mechanical and electrical properties of their constituent [8]. For instance, it has been found that layering sheets of graphene and hexagonal boron nitride ( $h\text{-BN}$ ), molybdenum disulfide ( $\text{MoS}_2$ ), or tungsten disulfide ( $\text{WS}_2$ ) allows operation of tunneling transistors [79].

## Strain Engineering

Strain engineering is an effective method used in semiconductor device manufacturing to tune their physical properties and improve their performance.

Most 2D materials display a remarkable strain limit due to both their strong in-plane bonding ( $\sigma$ ) and flexibility produced by the out-plane bonds ( $\pi$ ), which provides a straightforward, effective means of tuning electronic, mechanical, optical and magnetic properties. The strains can be either intrinsic, such as corrugations, distortion, lattice mismatch with substrates [80, 81, 82] ; or external, which can be induced by different techniques, e.g., by an atomic force microscope tip [83], as shown in Figure 1-9 (a) [8], by transferring the material to a piezoelectric substrate and then the substrate can be shrank or elongated by applying a bias voltage [84]. In addition, uniform strains can be applied to the layered materials from flexible substrate, on which the layered materials are fabricated [85], and the mismatch gen-

erated by thermal expansion effect of the substrate in layered materials [86]. The latter method is useful for applying strain to graphene, because it has a negative thermal expansion coefficient. Thus, by selecting a substrate with a positive thermal expansion coefficient, such as  $\text{SiO}_2$ , the graphene will experience a tensile or compressive biaxial strain when heating or cooling the substrate [87].

Strain can be induced in graphene by the methods mentioned above. It has been reported that strain can modify the electronic structure of graphene and soften the optical-phonon branches [88]. Uniaxial and shear strains shift the Dirac cones away from K and K' below different threshold strain values:  $\sim 20\%$  and  $\sim 16\%$ , respectively. Above these values both methods open a gap in graphene, the maximum value obtained is 0.72 meV [89]. In contrast, bilayer strain neither shifts the Dirac points nor opens a gap. It keeps the crystal symmetry of graphene; however, it changes the slope of the Dirac cones and hence the Fermi velocity [87].

Among the amazing physical phenomena induced by strain in graphene, we can highlight the shifting of the Dirac cones, the red shift and splitting of characteristic Raman modes, the enhancement of the electron–phonon (e–ph) coupling, superconductivity, quantizing pseudomagnetic field and the zero-field quantum hall effect [87].

### Electric Field Modulation

The application of an external electric field offers an effective way of tuning the electronic properties of 2D-materials. The applied electric field not only affects the bandgaps of 2D multilayers but also leads to the charge redistribution because of the induced potential difference. The bandgaps of most 1D nanoribbons and 2D hetrostructures can be reduced by the external electric field, and after a threshold value the materials can be metallic [72]. For instance, theoretical calculations predict that electric fields larger than  $2 \text{ V}/\text{\AA}$  decrease the band gap in monolayer group 6 TMDCs, and for values larger than  $4.5 \text{ V}/\text{\AA}$ , the material becomes metallic [71]. The effect on tuning the bandgap of applied electric field on graphene is less than in TMDCs, and even varies from one TMDC to another. This effect depends on the direction of the electric field and the number of layers [90].

On the other hand, it has been theoretically reported that the in-plane and out-of-plane dielectric constants of graphene are tunable by the value of applied electric field. The dielectric constant of a material is used to characterize its electrostatic properties such as capacitance, charge screening, and energy storage capability [91]. They reported that both the in-plane and out-of-plane dielectric constants are almost constant ( $\sim 1.8$  and  $\sim 3$ , respectively) at a low field strength of less than  $0.01 \text{ V}/\text{\AA}$ , but increase and become dependent on the number of layers under higher electric field. It has also been reported that  $\text{MoS}_2$  multilayer is more electrically polarizable than graphene [72].

## Doping

The electronic properties of low-dimensional nanomaterials can also be tuned by doping. Graphene can be doped by using substrates, electrical gating, and chemical species such as atoms and molecules [62]. The electronic coupling between the underlying substrate and graphene modifies its electronic properties; e.g., when graphene is grown epitaxially on SiC, a small gap of  $0.26 \text{ eV}$  is opened. For the case of  $\text{SiO}_2$  substrate, the type of doped graphene charge is controlled by the contact potential difference at the interface, and the charge transfer between them depends strongly on the interface geometry. In the case of metal substrate (Al, Ag, Cu, Au, and Pt), the work function difference and the chemical interaction between graphene and the metal, shift the Fermi level with respect to the conical point by  $\sim 0.5 \text{ eV}$  [62, 92, 93]. Graphene band gap can be experimentally induced from zero to  $250 \text{ meV}$  when a gapless bilayer graphene is subjected to an external electric field [78].

Substitutional doping such as B, N, and transition metal [94, 95, 96]; and surface metal adsorption with higher electron affinities (Bi, Sb and Au) [97], are other ways to tune the electronic structure of graphene.

## Functionalization

Band gap in graphene can be tuned by functionalization with H (graphane or hydrogenated graphene) and F (fluorographene or fluorinated graphene). *Ab-initio* calculations predicted graphene to be a wide bandgap material when doped with

H and F [98]. Furthermore, scanning tunneling microscopy (STM) experiments, complemented by first-principles calculations, show that isolated hydrogen atoms adsorbed on graphene are predicted to induce magnetic moments [99].

The surface of 2D group III-V materials could be chemically modified by hydrogenation [48, 100, 101]. It has been found both theoretically and experimentally that hydrogen passivation stabilizes two dimensional buckled III-V sheets [102]. Recently, two-dimensional buckled gallium nitride was synthesized by hydrogen surface passivation and graphene encapsulation [102]. Chen *et al* reported that surface hydrogenation tunes the electronic and magnetic properties of 2D-BN [103]. Hydrogenization causes the 2D-BN sheet to have a smaller energy bandgap than the pristine one, while semihydrogenated BN is a ferromagnetic metal [104]. The configuration in which the hydrogen atoms are adsorbed on III-V devices plays an important role in their electronic properties.

According to our results, see **chapter 5**, two-dimensional buckled gallium arsenide is a good candidate to be synthesized by hydrogen surface passivation as its group III–V partners two-dimensional buckled gallium nitride and boron nitride.

### 1.1.5 Applications

Technology based on semiconductor devices plays a transcendental role in our modern society. Since scientists, such as Shockley, Brattain and Bardeen, Nobel Prize in physics in 1956, invented the transistor [105, 106], a large effort has been devoted by the manufacturing industry to develop new semiconductor materials with enhanced electronic features. Therefore, the challenge has been not only to reduce the size and price of these electronic devices but also to increase their performance to obtain characteristics such as high speed and low power dissipation. Moore’s law establishes a limit for the future implementation of the current technology based on traditional 3D semiconductor materials. Moore’s law states that the number of transistors on a microchip will double roughly every two years, which means that next technological generation will be led by electronic devices manufactured by atomically thin materials.

The remarkable properties of 2D materials, beforehand mentioned, together with

the experimental and computational methods available today, which allow their synthesis and characterization, as well as tuning their physical and chemical properties, makes them attractive materials, not only limited for developing new physics and materials science, but with potential technological and industrial applications. For instance, the combination of high breaking strain, low thickness, and semiconducting properties of TMDCs ( $\text{MoS}_2$ ,  $\text{WS}_2$ ,  $\text{WSe}_2$ ) and BP allow them to be used in flexible transistors [107].

A sequential logical roadmap, since the identification of new 2D-materials until their application, could be as follows [10]:

- Identification and assessment of the potential application of new layered materials: synthesis and characterization; Engineering Science to tune the desired physical and chemical properties by: Straintronics, size control, multilayered materials, among others.
- Large scale production of 2DM attending the needs of a specific application field, e.g., component technologies, electronic, spintronic, optoelectronic, sensors, energy application, medical application.
- The identification of 2DM for the design of technological electronic components, and the integration of these 2DM to the new system, in order to develop enhanced and novelty electronic devices.

The outstanding physical properties of graphene make them suitable for diverse technological applications. It is well known that the absence of a band gap limits its applications in electronics. However, as mentioned in **section 1.1.4**, there are numerous methods that allow the improvement of this graphene drawback. In addition, materials engineering allows its layering assembly with other materials, which improves the properties of the heterostructure constituent materials. Thus, nowadays, the scientist community interest is focused on developing new materials based on graphene, it means 2D hybrid systems, with enhanced properties beyond graphene. Among the potential application areas of these hybrid systems we can highlight [10]: Fundamental research, information and communications technology, health and environment, electronic devices, spintronics, photonics and optoelectronics, sensors,

flexible electronics, energy storage and generation, biomedical applications, new functional light-weight composites to be applied in new airplanes, buses, cars, etc. Figure 1-10 depicts some potential applications of graphene related materials.

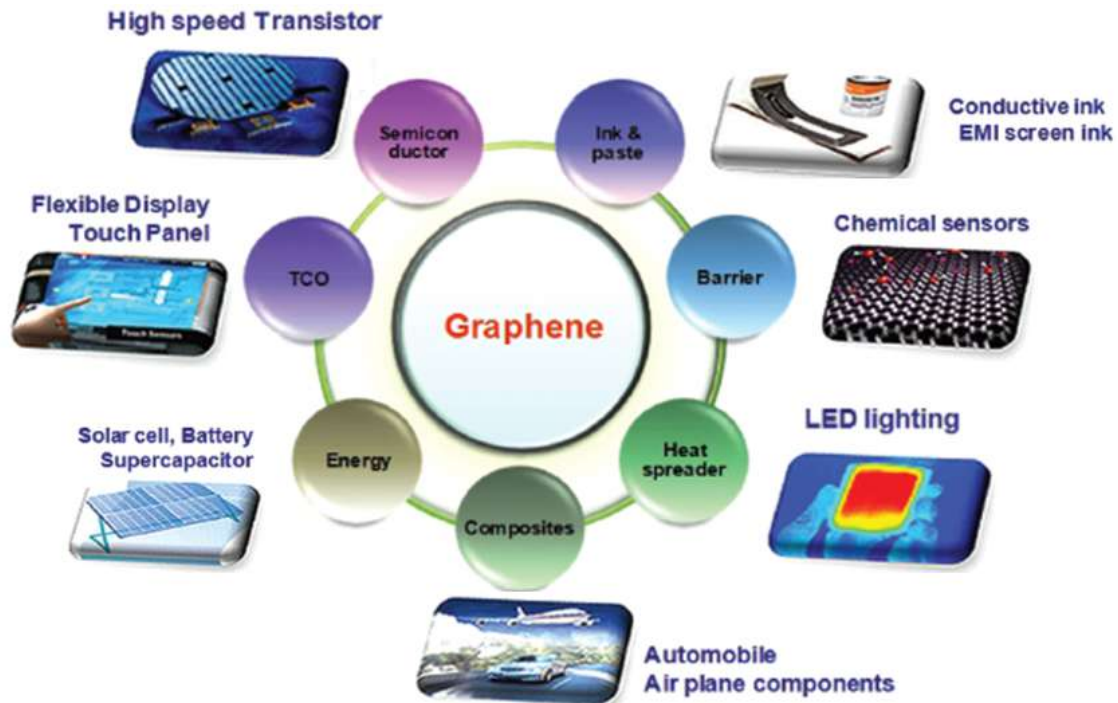


Figure 1-10: Potential applications of graphene and beyond materials [9]

Among many other applications of 2D-materials, we can highlight its application in field-effect transistors, valleytronics, chiral magnetic materials, Janus materials, thermoelectrics, and topological insulators [43].

Finally, it is expected that the next generation of atomically thin materials will disrupt the industry and technology in the upcoming years, since scientist community is using the obtained theoretical and experimental knowledge in atomically thin materials during the last years as platform to explore areas less studied, such as unconventional superconductivity in small-angle twisted heterostructures [108, 109], and unconventional tunability of two-dimensional quantum materials, e.g., electronic properties of moiré heterostructures [110, 111, 112, 113], phonon modes of few-layered structures [114]. Figure 1-11 summarizes a chart highlighting graphene related materials as platform for studying physics' new phenomena, and designing new technologies and applications, as well as the social impact [10].

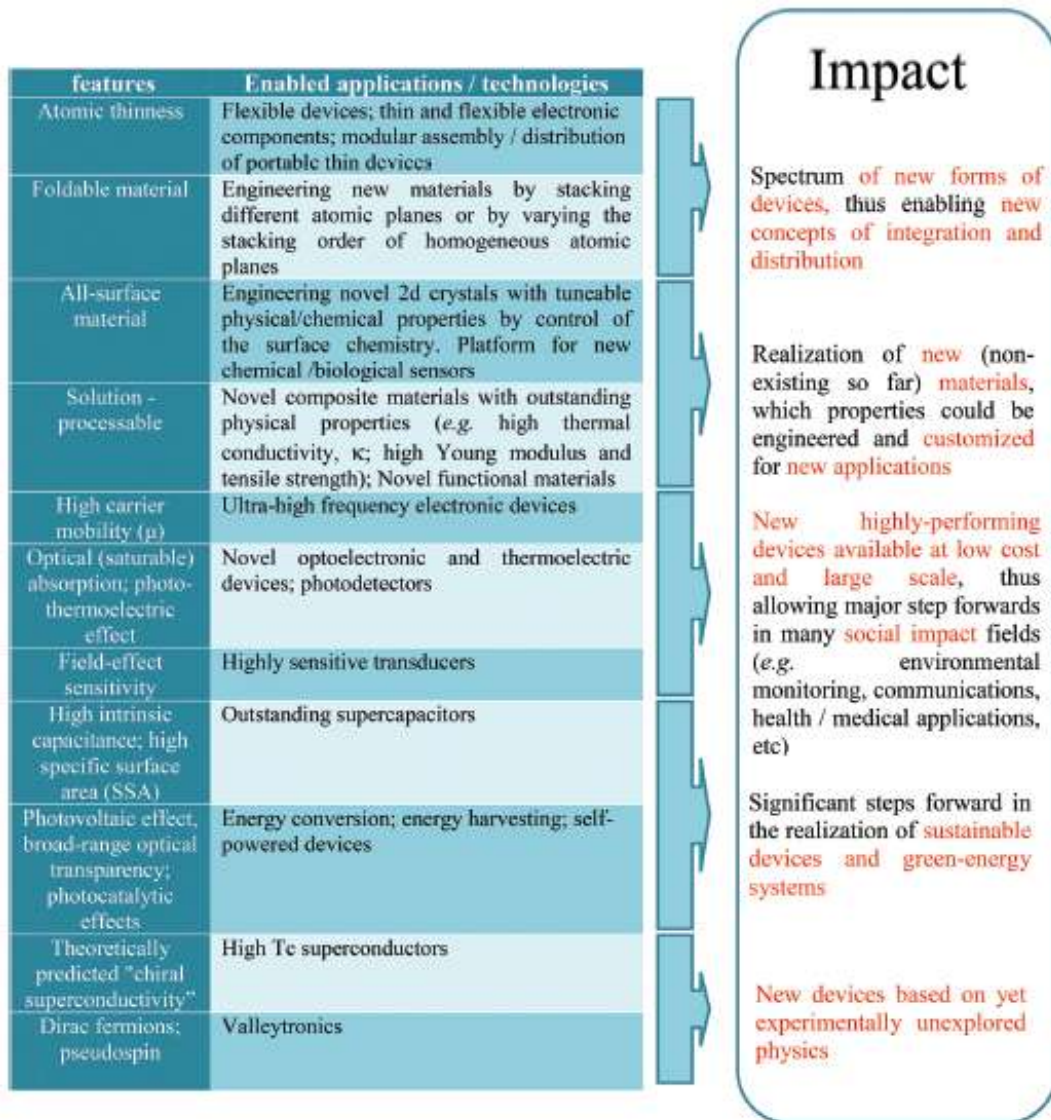


Figure 1-11: Graphene related materials as platform for studying physics new phenomena, and designing new technologies and applications [10]

## 1.2 From 3D group III-V to 2D group III-V semiconductors.

The electronic properties of group III-V semiconductors such as BAs, GaAs and InAs, have been widely studied in the bulk both theoretically and experimentally due to their interesting physical properties, such as high carrier transport, direct and wide band gap, good thermal conductivity, relative hardness, high resistivity and high melting point, which makes them promising materials in manufacturing

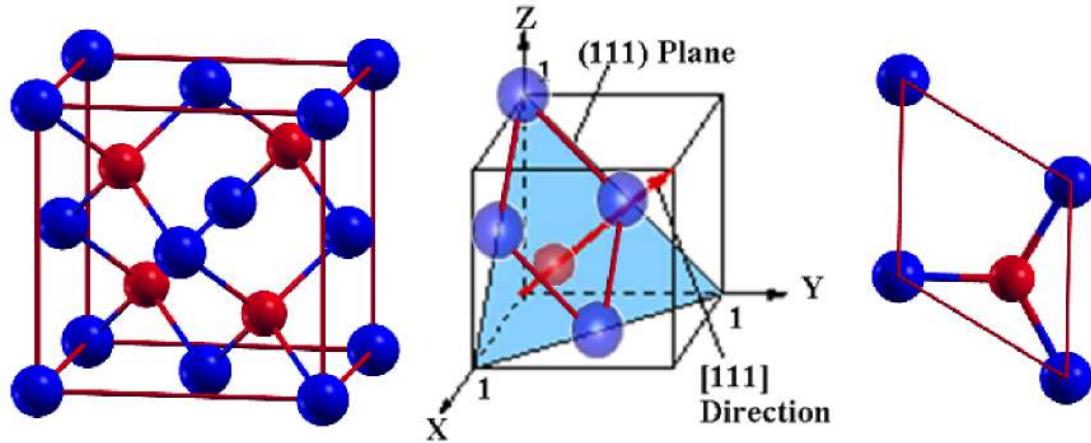


Figure 1-12: The hexagonal primitive cell (right-hand side), with one B, Ga or In atom (Blue color) and one As atom (Red color), was constructed from the zinc-blende structure (left-hand side) in the (111) plane. The hexagonal unit cell is also highlighted with a red line in the (111) plane.

of optoelectronic devices that can perform at high temperature and high power [115, 116, 117, 118, 119, 120, 121]. As illustration, they are suitable materials for fabrication of optical (lasers, diodes) and ultra-high frequency analog devices, and their integration on a Si platform will add new functionalities for optical networks, communication and microelectronic applications [122]. Because of the aforementioned reasons, and the great interest shown by the scientist community in the research of 2D materials during the last decade, it is worth asking not only if group III-V based-two-dimensional materials are dynamically and mechanically stable, but also about their potential application in engineering science.

The fact that zinc-blende III-As structures are semiconductors, display a hexagonal structure in the (111) surface and exhibit melting point above  $1000^{\circ}\text{C}$ , makes them potential candidates to be stable in their 2D hexagonal structure counterpart [7]. Indeed, the 2D hexagonal primitive cell, with one III-group atom (B, Ga or In) and one As atom, can be constructed from the zinc-blende structure in the (111) plane, as illustrated in Figure 1-12. Regarding the stability of 2D single layer of group III-V with large ionicity, there are theoretical [123, 124] and experimental [102] studies that have predicted and validated it. H. Sahin *et al.* predicted the stability of III-As and III-N binary compounds by first-principles calculations. Z. Y. Al Balushi *et al.* reported the synthesis of 2D gallium nitride (GaN) by experimental

technique utilizing epitaxial graphene.

On the other hand, it has been found that 3D III-V semiconductors and 2D III-V materials can improve the optoelectronic properties of heterostructures based on 2D MoS<sub>2</sub> [11] and graphene [8], respectively. As mentioned beforehand, 2D-heterostructures [7, 49, 50] have attracted the attention to tune the band gap width of semiconductors, which is desirable for diverse optoelectronic applications [8, 76, 77]. Furthermore, the fact that the industry of electronic devices based on 3D conventional materials, such as Si and group III-V semiconductors is stable and well-known, and the remarkable physical properties of 2D materials, offers an excellent opportunity to combine 3D group III-V semiconductors with 2D nanolayers to explore fundamental charge-transport phenomena at their interfaces, and exploit them for manufacturing new and enhanced electronic devices [125]. This approach could be applied to design field effect transistors. Moreover, this scheme presents the advantages of passivating the surface of bulk semiconductors and using the properties of 2D integrated materials to design gate-tunable diode in van der Waals heterostructure [126]. Miao *et al* manufactured a p-n heterojunction consisting of a 2D/3D (III-V) vdW heterostructure between a 2D MoS<sub>2</sub> (n-type) laid upon Si (p-doped) and GaN. They reported that this device exhibits over 7 orders of magnitude modulation in rectification ratios and conductance [11]. The authors suggest that this 2D/3D (III-V) vdW opens up possibilities for novel heterojunction device architectures, which can exceed the performance of “all-2D” vdW heterojunctions. Figure 1-13 displays a schematic illustration of this tunneling field-effect transistor designed by Miao *et al*.

III-V hexagonal structures have also been reported suitable as substrates for two dimensional materials such as graphene, MoS<sub>2</sub> and GaN based devices [127, 128]. C. R. Dean *et al* [127] reported the fabrication and characterization of high-quality exfoliated mono- and bilayer graphene devices on single-crystal *h*-BN substrates, by using a mechanical transfer process.

There is a lack of information in the literature about experimental and theoretical studies of 2D III-V (111)-binary compounds. Even though there is a theoretical research about the electronic properties of two-dimensional III-As (BAs, GaAs and

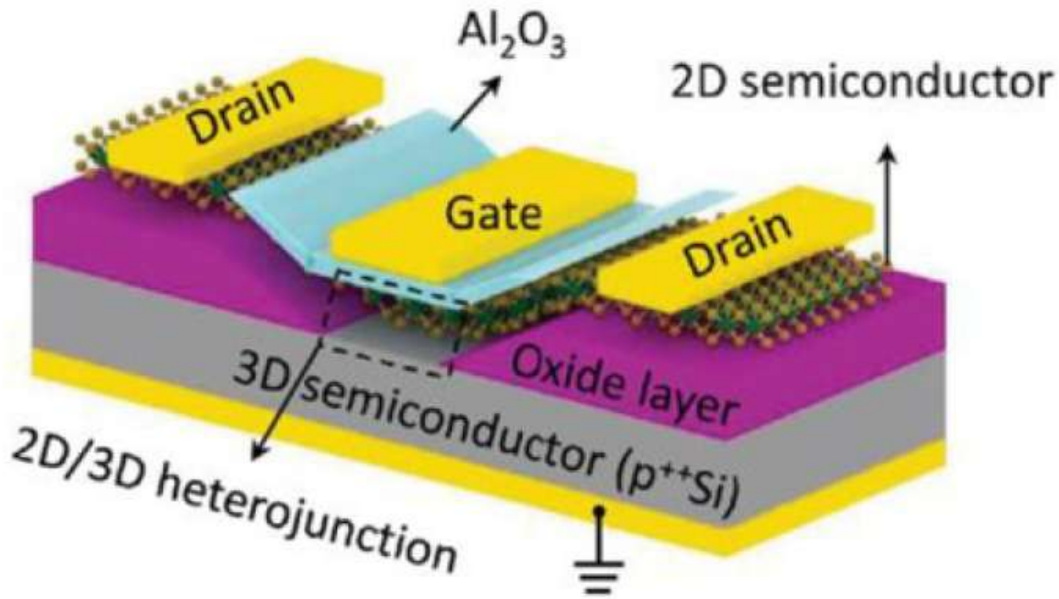


Figure 1-13: Schematic diagram of a tunneling field-effect transistor based on a vertical heterostructure of 2D MoS<sub>2</sub>, and 3D Si and Group III-V semiconductors [11].

InAs) graphene-like structures [123], authors did not take into account  $d$  orbitals of Ga, In and As atoms. It is important to know the physical interactions of  $p$ - $d$  orbitals in order to understand the magnetic nature when these 2D III-As systems are doped with metal transition impurities. They also used the Local Density Approximation (LDA) to study these  $d$  depending systems. It is well known that the LDA approach can not accurately describe strongly correlated systems.

Experimental or theoretical studies of 2D III-V (111)-binary compounds are scarce. Even though the materials in question are rather accessible and readily used in technological applications. In that sense, the present work will bring new theoretical insights to the research of 2D materials, opening the possibility for further investigations in 2D  $h$ -IIIs materials.

### 1.3 Scope and organization of the thesis.

Despite the interest devoted by the scientific community during the last decade to find and characterize new two-dimensional materials has increased exponentially, the research of 2D group III-As materials is scarce. This is in contrast with the application of 3D group III-V materials in the engineering science. The target of this research on studying the physical properties of 2D group III-As materials is to bring new theoretical insights to the research of 2D group III-V semiconductors and their potential for future electronic applications.

Since the main focus of this thesis is to tune the physical properties of the materials of group III-As in the thinnest limit, it is important to carry out a complete characterization of the structural, electronic, mechanical and vibrational properties of pristine monolayers as a benchmark for evaluating the tuning properties. Therefore, **the first objective of this thesis is to study theoretically, by Density Functional theory (DFT), the dynamical and mechanical stability of two-dimensional group III-V semiconductors (BAs, GaAs, and InAs), as well as their structural, electronic and mechanical properties.** Here, the unit hexagonal cell for our three 2D systems will be first constructed. Then, the dynamical and mechanical stability of our systems will be tested. Next, their structural, electronic and mechanical properties will be analyzed. Lastly, the structural and electronic properties of few-layer *h*-IIIs structures will be studied in order to compare them with those of the pristine ones. Because the study of these three materials is too ambitious, and taking into account the relevance of technological applications of 3D-GaAs semiconductor in engineering science, we decided to focus our research on 2D-GaAs (from chapter four on). The study carried out on 2D BAs and InAs in chapter 3, will be the basis for future research once the study of 2D GaAs is finished, as will be discussed in the **outlook** section.

Taking into account that Graphene-group III-V heterostructures have been studied in bilayer [129] and multilayer systems [130, 131] in order to tune the graphene band gap for optoelectronic applications, our **second objective is to investigate the stability, and the structural, electronic and mechanical properties of**

**graphene and GaAs in a graphene/GaAs bilayer heterostructure under both uniaxial stress along  $c$  axis and different planar strain distributions.**

On the other hand, it has been reported that the adsorption of hydrogen on 2D materials modifies their structural, optical, magnetic and mechanical properties [48, 100], generating other new crystals with different geometries and different physical properties from their pristine parent material. It has also been found both theoretically and experimentally that hydrogen passivation stabilizes two dimensional buckled III-V sheets [102]. Recently, 2D buckled gallium nitride was synthesized by hydrogen surface passivation and graphene encapsulation [102]. Therefore, **the third objective of our research is to investigate the stability, structural and electronic properties of two-dimensional (2D) hydrogenated GaAs sheets with three possible geometries: chair, zigzag-line and boat configurations.**

The recent experimental confirmation of magnetism in atomically thin magnetic crystals, which took place in 2017 [69, 132], paved the way in the search for promising 2D materials for low-dimensional magneto-electronic applications. Therefore, **the final aim of our research is to investigate the physical effect of the spin-orbit coupling on both magnetic anisotropy and Dzyaloshinskii-Moriya interaction for two-dimensional gallium arsenide when single and pair TMs are adsorbed (Mn, Co, Mo and Os).**

The central question of this thesis can thus be summarized as:

**Are 2D group III-As binary systems, and their combination with graphene, hydrogen and transition metal, stable materials with physical properties suitable for technological applications?**

To address this central question, the thesis is organized as follows:

**Chapter 2: Theoretical Framework.** The theoretical framework of first principles electronic structure theory is detailed. The most important topics dealt in this section are: the quantum many-body problem and the foundations of density functional theory, i.e, Hohenberg-Kohn theorems, the exchange-correlation functionals used in this research and its practical implementation.

**Chapter 3: Single layer and heterostructures of 2D Group III-V.** Here, we first examine the structural, mechanical and electronic properties of 2D single-layer *h*-IIIAs (BAs, GaAs, and InAs) systems, and then the structural and electronic properties of few-layer *h*-IIIAs structures taking into consideration *d* orbitals of Ga, In and As atoms.

**Chapter 4: Graphene/GaAs bilayer.** In this chapter, we first study the structural properties and dynamical stability of graphene/GaAs bilayer, then its electronic and mechanical properties and, finally, the effect of both uniaxial stress along the *c* axis and different planar strain distributions on the electronic properties.

**Chapter 5: 2D hydrogenated GaAs sheets.** The structural and electronic properties, as well as the energy and dynamical stability of 2D hydrogenated GaAs sheets will be studied taking into account three different geometric configurations: chair, zigzag-line and boat.

**Chapter 6: Transition-metal adatoms on 2D-GaAs.** In this section, we will investigate the physical effect of spin-orbit coupling on both magnetic anisotropy and Dzyaloshinskii-Moriya interaction for two-dimensional gallium arsenide when single and pair TMs are adsorbed (TM: Mn, Co, Mo and Os).

**Chapter 7: Summary and outlook.** In the last chapter, a summary of the achieved results together with an outlook for future work is given.

"Nature uses only the longest threads to weave her patterns, so that each small piece of her fabric reveals the organization of the entire tapestry."

Richard P. Feynman

## Chapter 2

# Theoretical framework

The quote chosen as the epigraph to start this chapter tells us that if we want to understand why a certain material has specific physical and chemical properties, we must go down to study its quantum world. Therefore, we need to apply the theoretical principles of quantum mechanics, which is the area of the science that studies the physical laws that govern atoms and electrons.

In this research, a first-principles (or *ab-initio*) calculation method based on the Density Functional Theory (DFT) is used to investigate the properties of group III-As in the thinnest limit. This method is named first-principles because it does not use any fitting parameters from experimental data, it is based solely on the laws of quantum mechanics. Hence, this chapter is devoted to give physical insights about the theoretical backgrounds implemented in this work. To do that, the many-body quantum problem is first introduced, as well as the approximation schemes implemented to solve the Schrödinger equation. Next, the foundations of Density Functional Theory will be presented. Then, the most crucial term in DFT, the exchange-correlation functional, will be briefly introduced. Afterwards, some practical considerations in order to implement DFT in numerical computation for real systems, will be explained. Finally, the method applied in this thesis to obtain the magnetic exchange interactions between two adsorbed metal atoms will be studied.

## 2.1 The quantum many-body problem

If we are interested in knowing the physical and chemical properties of matter, e.g., our two-dimensional system based on group III-V materials, we need to study it at the atomic scale. Matter at small scale obeys the laws of quantum mechanics. Furthermore, these systems are made up of many electrons and nuclei whose motions are coupled by Coulomb interactions. Thus, this is a quantum mechanical many-body problem. A theoretical model that pretends to describe these systems must take into account the interaction of a very large number of particles, i.e., the order of Avogadro's number  $6.023 \times 10^{23}$ . This is an extremely complex task to solve, even with the current computing power available. Despite this, there are methods called first-principles (or *ab-initio*), e.g., the calculation methods based on quantum mechanics, which can describe with a very good approximation the results for these systems. They do not depend on any external parameters except the atomic numbers of the constituent atoms to be simulated. In other words, they do not use any fitting parameters from experimental data and are based solely on the basic laws of physics.

The quantum mechanical many-body problem in a solid is described by the time-independent Schrödinger equation,

$$\hat{H}\Psi(\mathbf{r}_i, \sigma_i, \mathbf{R}_I) = E\Psi(\mathbf{r}_i, \sigma_i, \mathbf{R}_I), \quad (2.1)$$

where  $\hat{H}$  is the Hamiltonian operator of the system of electrons and nuclei,  $\Psi$  is the many-body wave function, dependent on the positions of the electrons,  $\mathbf{r}_i$ , the spin of the electrons  $\sigma_i$ , and the positions of the nuclei,  $\mathbf{R}_I$ .

The Hamiltonian operator,  $\hat{H}$ , is a sum of all energy terms involved: kinetic energies of the nuclei ( $\hat{T}_n$ ) and electrons ( $\hat{T}_e$ ), and potential energies coming from nucleus-nucleus ( $\hat{V}_n$ ), electron-electron ( $\hat{V}_{int}$ ), and electron-nucleus ( $\hat{V}_{ext}$ ) Coulomb interactions:

$$\hat{H} = \hat{T}_n + \hat{T}_e + \hat{V}_n + \hat{V}_{int} + \hat{V}_{ext}, \quad (2.2)$$

or, more concrete:

$$\begin{aligned}
\hat{H} = & - \sum_{I=1}^{N_n} \frac{\hbar^2}{2M_I} \nabla_I^2 - \sum_{i=1}^{N_e} \frac{\hbar^2}{2m} \nabla_i^2 + \frac{1}{2} \frac{e^2}{4\pi\epsilon_0} \sum_{I=1}^{N_n} \sum_{J \neq I}^{N_n} \frac{Z_I Z_J}{|\mathbf{R}_I - \mathbf{R}_J|} \\
& + \frac{1}{2} \frac{e^2}{4\pi\epsilon_0} \sum_{i=1}^{N_e} \sum_{j \neq i}^{N_e} \frac{1}{|\mathbf{r}_i - \mathbf{r}_j|} - \frac{e^2}{4\pi\epsilon_0} \sum_{I=1}^{N_n} \sum_{i=1}^{N_e} \frac{Z_I}{|\mathbf{R}_I - \mathbf{r}_i|}, \quad (2.3)
\end{aligned}$$

where  $\mathbf{R}_I$  and  $\mathbf{r}_i$  are the  $N_n$  nuclear coordinates and  $N_e$  electronic coordinates, respectively;  $m$  and  $M_I$  are the masses of electrons and nuclei, respectively; and  $Z_I e$  the nuclear charges.

To reduce the notation, Equation 2.3 can be written by using atomic units, i.e.,  $4\pi\epsilon_0 = e = m_e = \hbar = 1$ , as follows:

$$\begin{aligned}
\hat{H} = & - \sum_{I=1}^{N_n} \frac{1}{2M_I} \nabla_I^2 - \sum_{i=1}^{N_e} \frac{1}{2} \nabla_i^2 + \sum_{I=1}^{N_n} \sum_{J > I}^{N_n} \frac{Z_I Z_J}{|\mathbf{R}_I - \mathbf{R}_J|} \\
& + \sum_{i=1}^{N_e} \sum_{j > i}^{N_e} \frac{1}{|\mathbf{r}_i - \mathbf{r}_j|} - \sum_{I=1}^{N_n} \sum_{i=1}^{N_e} \frac{Z_I}{|\mathbf{R}_I - \mathbf{r}_i|}. \quad (2.4)
\end{aligned}$$

This many-body problem is in fact an extremely complex one that can be solved only for hydrogen-like systems. Unless some approximations on the model are done, Equation 2.4 has no use in practice.

### 2.1.1 Born-Oppenheimer approximation

A first approximation to simplify Equation 2.4 is the Born-Oppenheimer approximation (Max Born and J. Robert Oppenheimer, 1927) (BO) [133], which decouples the electronic degrees of freedom from the nuclear degree. The argument for doing this is that the nuclei move “slowly” compared to the electrons because of its heavier mass (1836 times for hydrogen and about 10,000 times for semiconductors), i.e., the kinetic-energy contribution is negligible, and hence a classical approximation is reasonable [134]. The operators  $\hat{T}_n$  and  $\hat{V}_n$  are reduced to classical energies  $T_n$  and  $V_n$ . The BO approximation allows the decomposition of the many-body wave function  $\Psi$  into an electronic wave function  $\psi_e$  and a nuclear wave function  $\psi_n$ , as follows:

$$\Psi(\mathbf{r}_i, \sigma_i, \mathbf{R}_I) = \psi_e(\mathbf{r}_i, \sigma_i; \mathbf{R}_I) \psi_n(\mathbf{R}_I). \quad (2.5)$$

The electronic wave function depends only on the electronic positions  $\mathbf{r}_i$ , with the nuclear positions  $\mathbf{R}_I$  as parameters, since the electrons respond instantaneously as the nuclear positions are altered and always occupy the ground state of that nuclear configuration. The electrons are considered to move in the field of stationary nuclei. Thus, the electronic wave function must satisfy the time-independent Schrödinger equation for a static configuration of the nuclei:

$$\hat{H}_e \psi_e(\mathbf{r}_i, \sigma_i; \mathbf{R}_I) = E_e(\mathbf{R}_I) \psi_e(\mathbf{r}_i, \sigma_i; \mathbf{R}_I), \quad (2.6)$$

where the energy  $E_e(\mathbf{R}_I)$  only depends on the nuclear coordinates and not on the electronic ones.  $E_e(\mathbf{R}_I)$  can be found by solving Equation 2.6 for different  $\mathbf{R}_I$ , where  $\mathbf{R}_I$  varies in little steps.

The electronic Hamiltonian can be written as:

$$\hat{H}_e = \hat{T}_e + \hat{V}_{int} + \hat{V}_{ext}, \quad (2.7)$$

or, explicitly:

$$\hat{H}_e = - \sum_{i=1}^{N_e} \frac{1}{2} \nabla_i^2 + \sum_{i=1}^{N_e} \sum_{j>i}^{N_e} \frac{1}{|\mathbf{r}_i - \mathbf{r}_j|} - \sum_{I=1}^{N_n} \sum_{i=1}^{N_e} \frac{Z_I}{|\mathbf{R}_I - \mathbf{r}_i|}. \quad (2.8)$$

On the other hand, the Hamiltonian that describes the nuclei motions in the average field generated by the electrons ( $\langle E_e(\{\mathbf{R}_I\}) \rangle$ ) is:

$$\hat{H}_n = \hat{T}_n + \hat{V}_n + \langle E_e(\{\mathbf{R}_I\}) \rangle, \quad (2.9)$$

or, more concrete:

$$\hat{H}_n = - \sum_{I=1}^{N_n} \frac{1}{2M_I} \nabla_I^2 + \sum_{I=1}^{N_n} \sum_{J>I}^{N_n} \frac{Z_I Z_J}{|\mathbf{R}_I - \mathbf{R}_J|} + \langle E_e(\{\mathbf{R}_I\}) \rangle. \quad (2.10)$$

$(V_n + \langle E_e(\{\mathbf{R}_I\}) \rangle)$  is named *potential energy surface* (PES).  $\langle E_e(\{\mathbf{R}_I\}) \rangle$  is the contribution of electrons to the potential energy of ions and determines the potential energy curves necessary to describe the ion movement. It means, in the BO approximation the nuclei motion are independent from the electrons ones, following the potential energy surface of Equation 2.10 ( $V_n + \langle E_e(\{\mathbf{R}_I\}) \rangle$ ).

The total energy of the many-body system in the BO approximation is

$$E_T = E_e + E_n, \quad (2.11)$$

where,  $E_e$  represents the total energy of the electrons, and  $E_n$  represents the classical kinetic energy and the classical electrostatic energy of the nuclei.

The issue now lies in solving the electronic problem, which involves a large number of degrees of freedom and a large number of interactions between electrons, i.e., the wave equation is a partial differential equation that depends on the  $3N$  coordinates of  $n$  electrons. In this research, the solution to the electronic problem will be addressed using the Density Functional Theory (DFT), which will be studied in the next section.

## 2.2 Density Functional Theory (DFT)

Density Functional theory is considered currently the core of computational materials science. The electronic problem (Equation 2.7) is solved in DFT by using the electron density instead of  $3N$ -dimensional equation. Now, there are no single electrons but just a three-dimensional density of electrons,  $n(\mathbf{r})$ . The goal of DFT is to reformulate the quantum mechanical theory in terms of the electron density instead of the wave function. The many body problem is reduced because  $n(\mathbf{r})$  is an observable that does not depend on the number of electrons after it is constructed in a system, but only on the three spacial coordinates (x,y,z), which will reduce the computational cost.

The DFT foundations are based on the theorems formulated by Hohenberg-Kohn

(HK) (1964) [135] and Kohn-Sham (KS) (1965) [136].

### 2.2.1 The Hohenberg-Kohn theorems

**Theorem 1** *The external potential  $V_{ext}(\mathbf{r})$ , for any system of interacting electrons, is univocally determined by the ground state electronic density,  $n_0(\mathbf{r})$ , besides a trivial additive constant [135].*

As a consequence of the first HK theorem, the following corollary is stated:

**Corollary 1** *The expectation value of any observable,  $\hat{X}$ , in the ground state is a unique functional of the ground state electronic density. This is,*

$$\langle \Psi | \hat{X} | \Psi \rangle = X[n_0(\mathbf{r})]. \quad (2.12)$$

Therefore, the first HK theorem proves that the ground state properties of any electronic system are uniquely determined by an electronic density that depends on only three spatial coordinates.

**Theorem 2** *Considering  $\hat{X}$  the Hamiltonian operator  $\hat{H}$ , the total energy functional of the ground state,  $E[n(\mathbf{r})]$ , can be expressed as [135]*

$$E[n(\mathbf{r})] = \langle \Psi | \hat{H} | \Psi \rangle = \langle \Psi | (\hat{T}_e + \hat{V}_{int}) | \Psi \rangle + \langle \Psi | \hat{V}_{ext} | \Psi \rangle, \quad (2.13)$$

or, respectively:

$$E[n(\mathbf{r})] = T_e[n(\mathbf{r})] + E_{int}[n(\mathbf{r})] + E_{ext}[n(\mathbf{r})], \quad (2.14)$$

where  $\langle \hat{F}_{HK}[n(\mathbf{r})] \rangle = \langle \Psi | (\hat{T}_e + \hat{V}_{int}) | \Psi \rangle = T_e[n(\mathbf{r})] + E_{int}[n(\mathbf{r})]$ , is a universal functional for any many-electron system. The minimum of this functional,  $E[n(\mathbf{r})]$ , is the ground state energy and the density that minimizes the functional is the exact ground state density,  $n_0(\mathbf{r})$ , for the external potential  $V_{ext}$ .

The second HK theorem defines an energy functional for the system and demonstrates that the correct ground state electron density minimizes this energy functional.

Though the HK theorems give a physical frame of reference to find both the electron density and energy of the ground state of a many-body system, they tell nothing about how to calculate them. In 1965 Walter Kohn and Lu Jeu Sham established a method to simplify the many-body problem within DFT.

## 2.2.2 The Kohn-Sham auxiliary system

Kohn and Sham (KS) (1965) proposed an alternative approach in order to overcome the many body problem. In the development of KS method, the authors make the following main assumptions [136]:

*For a system of interacting electrons, exists an equivalent or auxiliary system of non-interacting electrons, with the same ground state electron density of the real system, moving in an effective potential.*

*The kinetic energy of the interacting electrons ( $T_e$ ) is replaced with that of the equivalent non-interacting system or reference system ( $T_0$ ), and all the interactions are placed in the exchange correlation energy  $E_{xc}[n(\mathbf{r})]$ .*

*Then, the total energy functional  $E[n(\mathbf{r})]$  (Equation 2.13) is rewritten by a KS total energy functional  $E_{KS}[n(\mathbf{r})]$ , as follows:*

$$E_{KS}[n(\mathbf{r})] = T_0[n(\mathbf{r})] + E_H[n(\mathbf{r})] + E_{ext}[n(\mathbf{r})] + E_{xc}[n(\mathbf{r})], \quad (2.15)$$

where,  $n(\mathbf{r})$  is the electron density that minimizes  $E_{KS}[n(\mathbf{r})]$ ,  $T_0[n(\mathbf{r})]$  is the electrons kinetic energy functional in the non-interacting system,  $E_H[n(\mathbf{r})]$  is the Hartree potential energy, the classical Coulomb repulsion between electrons,  $E_{ext}[n(\mathbf{r})]$  is the external potential, ion-electron interaction, and  $E_{xc}[n(\mathbf{r})]$  is the the exchange-correlation energy, which includes all the interaction energies not taken into account in the other terms, and can be expressed as:

$$E_{xc}[n(\mathbf{r})] = E_{int}[n(\mathbf{r})] + T_e[n(\mathbf{r})] - T_0[n(\mathbf{r})] - E_H[n(\mathbf{r})]. \quad (2.16)$$

$E_{xc}[n(\mathbf{r})]$  can also be expressed as the sum of the exchange energy functional and the correlation energy functional:

$$E_{xc}[n(\mathbf{r})] = E_x[n(\mathbf{r})] + E_c[n(\mathbf{r})]. \quad (2.17)$$

$E_c[n(\mathbf{r})]$  is the correlation energy representing the correlating part of the kinetic and electron–electron interaction terms. The correlation energy comes from the spatial separation between electrons due to the nature of their negative charges, thus the movement of an electron is always correlated to the surrounding electrons. The exchange energy,  $E_x[n(\mathbf{r})]$ , comes from the exchange interaction between spins of fermions [137]. Like-spin electrons always repel each other keeping some distance between them and thus reduce the corresponding repulsive energy (Pauli exclusion principle).

Kohn and Sham decomposed the energy of the  $n$ -electron system (interacting) into that of  $n$  one-electron systems (non-interacting) by the following one-electron KS equations [137]:

$$\widehat{\mathcal{H}}_{KS}(i)\psi_i(\mathbf{r}) = \epsilon_i\psi_i(\mathbf{r}), \quad (2.18)$$

$$\left[ -\frac{1}{2}\nabla_i^2 + v_{KS}(\mathbf{r}_i) \right] \psi_i(\mathbf{r}) = \epsilon_i\psi_i(\mathbf{r}), \quad (2.19)$$

where,  $\psi_i(\mathbf{r})$  and  $\epsilon_i$  are the KS orbitals and KS eigenvalues, respectively;  $v_{KS}$  is the KS effective potential that is felt by the non-interacting electrons due to the other electrons and ions, and can be expressed as

$$v_{KS}(\mathbf{r}_i) = v_H(\mathbf{r}_i) + v_{xc}(\mathbf{r}_i) + v_{ext}(\mathbf{r}_i). \quad (2.20)$$

The ground state density  $n_0(\mathbf{r})$  is related to the KS orbitals by

$$n_0(\mathbf{r}) = \sum_{i=1}^N |\psi_i(\mathbf{r})|^2. \quad (2.21)$$

The constraint is that the KS auxiliary system must yield the same electron density of the real system. Furthermore, the total number of electrons must be obtained when adding up all the KS electron densities over the whole space,

$$\int n(\mathbf{r})d\mathbf{r} = N. \quad (2.22)$$

The solution of the Schrödinger equation

$$\hat{H}\Psi(\mathbf{r}) = E\Psi(\mathbf{r}), \quad (2.23)$$

for a non-interacting system, is a Slater determinant  $\Psi = |\psi_1, \psi_2, \psi_3, \dots, \psi_N|$ ; where  $\psi_i$  are orbitals with the lowest eigenvalues [134]. KS method solves decoupled equations of form (Equation 2.18), instead of one coupled equation of many electrons.

The KS total energy functional (Equation 2.15) can be expressed as

$$E_{KS}[n(\mathbf{r})] = \langle \Psi | \hat{H} | \Psi \rangle = T_0[n(\mathbf{r})] + E_H[n(\mathbf{r})] + E_{ext}[n(\mathbf{r})] + E_{xc}[n(\mathbf{r})], \quad (2.24)$$

or, explicitly

$$\begin{aligned} E_{KS}[n(\mathbf{r})] = & - \frac{1}{2} \sum_{i=1}^N \int \psi_i^*(\mathbf{r}) \nabla_i^2 \psi_i(\mathbf{r}) d\mathbf{r} + \frac{1}{2} \int \int \frac{n(\mathbf{r})n(\mathbf{r}')}{|\mathbf{r} - \mathbf{r}'|} d\mathbf{r}d\mathbf{r}' \\ & + \int v_{ext}(\mathbf{r})n(\mathbf{r})d\mathbf{r} + \int \epsilon_{xc}[n(\mathbf{r})]n(\mathbf{r})d\mathbf{r}. \end{aligned} \quad (2.25)$$

$v_H[n(\mathbf{r})]$  and  $v_{xc}[n(\mathbf{r})]$  can be obtained from  $E_H[n(\mathbf{r})]$  and  $E_{xc}[n(\mathbf{r})]$ , respectively, as follows

$$v_H[n(\mathbf{r})] = \frac{\delta E_H[n(\mathbf{r})]}{\delta n(\mathbf{r})} = \int \frac{n(\mathbf{r}')}{|\mathbf{r} - \mathbf{r}'|} d\mathbf{r}', \quad (2.26)$$

$$v_{xc}[n(\mathbf{r})] = \frac{\delta E_{xc}[n(\mathbf{r})]}{\delta n(\mathbf{r})} = \epsilon_{xc}[n(\mathbf{r})] + \frac{\partial \epsilon_{xc}[n(\mathbf{r})]}{\partial n(\mathbf{r})} n(\mathbf{r}). \quad (2.27)$$

$v_H[n(\mathbf{r})]$  requires an integral on  $\mathbf{r}'$  for the evaluation of the Hartree potential at  $\mathbf{r}$ .

By comparing Equation 2.20, 2.25, 2.26 and 2.27 the following expression for the KS effective potential  $v_{KS}$  or reference potential is obtained:

$$v_{KS}[n(\mathbf{r})] = v_{ext}(\mathbf{r}) + \int \frac{n(\mathbf{r}')}{|\mathbf{r} - \mathbf{r}'|} d\mathbf{r}' + v_{xc}(\mathbf{r}). \quad (2.28)$$

In practice, the electronic density and the ground state energy are found by selfconsistent calculations: the cycle starts with an initial (trial) electron density obtained from the KS orbitals; the electron density and a given XC functional calculate the KS Hamiltonian; the KS Hamiltonian calculates the new KS orbitals, which lead to a new electron density and total energy, and so on; the cycle is repeated until selfconsistency is reached. Therefore, to achieve meaningful results, we have to find a set of KS orbitals that leads to a KS Hamiltonian whose solutions are the KS orbitals we started with. KS orbitals, electron densities, and Hamiltonian are all interrelated during the course of the calculation: This is called self-consistency [134]. Thus, in order to find  $\psi_i(\mathbf{r})$ , we need to know the Hamiltonian which depends on the electronic density, which in turn depends on  $\psi_i(\mathbf{r})$ . In real calculations, self-consistency is reached by taking into account the total energy convergence. The cycle stops when the difference between the last two calculated energies is less than a prior chosen criterion. Afterwards, total energies and forces are calculated.

The total energy of electrons cannot be expressed directly as the sum of the KS eigenvalues  $\epsilon_i$ , due to the double counting error involved in the energy terms when calculating  $\epsilon_i$ , one by one, in terms of electron density  $n(\mathbf{r})$ , any electron is included in all other electrons, and results in an unphysical self-interaction. The sum of  $\epsilon_i$  thus becomes the actual total energy after double counting terms have been subtracted [138]

$$E[n(\mathbf{r})] = \sum_{i=1}^N \epsilon_i - E_H[n] + E_{XC}[n] - \int V_{XC}n(\mathbf{r})d\mathbf{r},$$

*or,*

$$E[n(\mathbf{r})] = \sum_{i=1}^N \epsilon_i - \frac{1}{2} \int \int \frac{n(\mathbf{r})n(\mathbf{r}')}{|\mathbf{r} - \mathbf{r}'|} d\mathbf{r}d\mathbf{r}' - \int \frac{\partial \epsilon_{xc}[n(\mathbf{r})]}{\partial n(\mathbf{r})} n(\mathbf{r}) d\mathbf{r}. \quad (2.29)$$

Here, from Equation 2.27 and definition of  $E_{XC}[n]$ ,  $-\int \frac{\partial \epsilon_{xc}[n(\mathbf{r})]}{\partial n(\mathbf{r})} n(\mathbf{r}) d\mathbf{r} = \int (\epsilon_{xc}[n(\mathbf{r})] -$

$V_{XC})n(\mathbf{r})d\mathbf{r}$ . The main challenge in KS scheme is to find reliable and practical approximations for the exchange-correlation functional  $E_{XC}$  (Equation 2.17). This topic will be addressed in **section 2.3**.

### 2.2.3 DFT to spin spin-polarized system (SDFT)

Spin-polarized systems are also studied with Kohn-Sham theory. This method is known as spin density functional theory (SDFT). SDFT considers the electronic density as composed by two independent spin densities [137],

$$n(\mathbf{r}) = n_{\uparrow}(\mathbf{r}) + n_{\downarrow}(\mathbf{r}), \quad (2.30)$$

both  $n_{\uparrow}(\mathbf{r})$  and  $n_{\downarrow}(\mathbf{r})$  are built up with the KS spin orbitals, according to

$$n_s(\mathbf{r}) = \sum_{i=1}^{N_s} |\psi_{i,s}(\mathbf{r})|^2, \quad (2.31)$$

where the subindex  $s$  indicates the spin component ( $\uparrow$  or  $\downarrow$ ), and  $N_s$  represents the number of occupied spin orbitals with spin projection  $s$ .

$n_s(\mathbf{r})$  must satisfy the self-consistent KS equations

$$\left[ -\frac{1}{2}\nabla_{i,s}^2 + v_{KS,s}(\mathbf{r}_i) \right] \psi_{i,s}(\mathbf{r}) = \epsilon_{i,s}\psi_{i,s}(\mathbf{r}). \quad (2.32)$$

In SDFT the total energy is written as:

$$\begin{aligned} E_{KS}[n_{\uparrow}, n_{\downarrow}] = & -\frac{1}{2} \sum_{s=1}^2 \sum_{i=1}^{N_s} \int \psi_{i,s}^*(\mathbf{r}) \nabla_i^2 \psi_{i,s}(\mathbf{r}) d\mathbf{r} + \frac{1}{2} \int \int \frac{n(\mathbf{r})n(\mathbf{r}')}{|\mathbf{r} - \mathbf{r}'|} d\mathbf{r} d\mathbf{r}' \\ & + \int v_{ext}(\mathbf{r})n(\mathbf{r})d\mathbf{r} + E_{xc}[n_{\uparrow}, n_{\downarrow}]. \end{aligned} \quad (2.33)$$

The total electronic density  $n(\mathbf{r})$  is given by Equation 2.30, while the magnetization or spin-polarization density, by the expression

$$\zeta(\mathbf{r}) = n_{\uparrow}(\mathbf{r}) - n_{\downarrow}(\mathbf{r}). \quad (2.34)$$

As in the case of non-spin-polarized systems, double counting terms have to be subtracted from the total energy.

## 2.3 Exchange-correlation functionals

The most relevant exchange-correlation ( $E_{xc}$ ) approximations will be briefly reviewed in this section: LDA, GGA, and hybrid functionals.

### 2.3.1 Local Density Approximation (LDA)

The Local Density Approximation (LDA) assumes that the spatial distribution of the electronic density varies smoothly, so that it can be considered locally like a uniform or homogeneous electron gas (HEG) of  $n(\mathbf{r})$ , as was proposed by Kohn and Sham [136]. In this approximation the exchange-correlation energy functional is given by

$$E_{xc}^{LDA}[n(\mathbf{r})] = \int n(\mathbf{r})\varepsilon_{xc}^{HEG}(n(\mathbf{r}))d\mathbf{r}, \quad (2.35)$$

where  $\varepsilon_{xc}^{HEG}(n(\mathbf{r}))$  is the XC energy functional of an electron in a HEG of density  $(n(\mathbf{r}))$ . It depends only on the local density at point  $\mathbf{r}$ , and can be expressed as follows:

$$\varepsilon_{xc}^{HEG}[n(\mathbf{r})] = \varepsilon_x^{HEG}[n(\mathbf{r})] + \varepsilon_c^{HEG}[n(\mathbf{r})], \quad (2.36)$$

where  $x$  and  $c$  are the exchange and correlation contributions.

The exchange energy is exactly given by Dirac's expression [139]:

$$\varepsilon_x^{HEG}[n(\mathbf{r})] = -\frac{3}{4} \left( \frac{3}{\pi} \right)^{\frac{1}{3}} \rho(\mathbf{r})^{\frac{1}{3}}. \quad (2.37)$$

Within LDA the  $\varepsilon_{xc}[n(\mathbf{r})]$  is given by the Monte Carlo simulations of Ceperley and Alder [140] for a homogeneous electron gas, and parameterized by Perdew and Zunger [141] as:

$$\varepsilon_c^{HEG}[n(\mathbf{r})] = A + B \ln r_s + r_s(C + D \ln r_s), \quad (2.38)$$

where A, B, C and D are constants;  $r_s$  is the mean inter-electronic distance (Wigner–Seitz radius), and can be calculated by the radius of a sphere containing solely one electron:

$$r_s = \left( \frac{3}{4\pi n(\mathbf{r})} \right)^{\frac{1}{3}} \quad r_s \leq 1. \quad (2.39)$$

LDA works well for systems where the electronic density is rather homogeneous, e.g., bulk metals. Nonetheless, it has been found that it underestimates the lattice parameters (overbinds), bandgaps, and the spin and orbital moments. It overestimates the cohesive energy and bulk modulus of solids [134]. Furthermore, it does not work well for materials that involve weak hydrogen bonds or van der Waals attraction, e.g., atoms and molecules. LDA also fails to describe systems where the electronic density is inhomogeneous such as transition metals or strongly correlated systems. For these systems, the Generalized-Gradient Approximation (GGA) works better.

### 2.3.2 Generalized-gradient approximation (GGA)

The Generalized-gradient approximation (GGA) defines the exchange-correlation energy in the following form

$$E_{xc}^{GGA}[n, |\nabla n|] = \int n(\mathbf{r}) \varepsilon_{xc}^{GGA}(n(\mathbf{r}), |\nabla n(\mathbf{r})|, \nabla^2(\mathbf{r}), \dots) d\mathbf{r}. \quad (2.40)$$

GGA incorporates the spatial variation in the local density by including an expansion of the density in terms of the gradient and higher order derivatives in the XC functional. Perdew-Burke-Ernzerhof (PBE) functional [142] has been one of the most widely used GGA functionals. It is noticed in Equation 2.40 that only the gradient at the same coordinate is taken into account in the XC functional, thus GGA is a semi-local approximation.

Contrary to LDA, GGA overestimates (underestimates) the lattice constants and

bond length (cohesive energy) within 1 % – 3 %. Both LDA and GGA underestimate the band gaps of insulators and semiconductors. The physics reason can be traced back to the fact that, in the local and semi-local approximations, the self-interaction present in the Hartree term of the energy is not completely removed in the exchange-correlation term [137]. Furthermore, the excitation energies are not exactly described by the KS-system in the local and semi-local approximations.

The true band gap is defined as:

$$E_g = \varepsilon_{N+1}(N+1) - \varepsilon_N(N), \quad (2.41)$$

while the KS band gap is defined in terms of the eigenvalues of the same number of electrons, as:

$$E_g^{KS} = \varepsilon_{N+1}(N) - \varepsilon_N(N). \quad (2.42)$$

This DFT band gap problem is largely solved by hybrid functional method.

### 2.3.3 Hybrid functionals

Hybrid functional method ( $E_{xc}^{Hyb}$ ) combines Hartree-Fock exchange energy ( $E_x^{HF}$ ) and DFT correlation energy ( $E_c^{GGA}$ ):

$$E_{xc}^{Hyb} = CE_x^{HF} + (1 - C)E_x^{DFT} + E_c^{DFT}, \quad (2.43)$$

where the coefficient  $C$  is either chosen to assume a specific value such as 1/2, or is fitted to some properties of a molecular database [137].

The success of hybrid functional approach in describing the band gap of semiconductors and insulators lies on the cancellation of error. While HF calculations overestimate the band gap, DFT underestimates it. Therefore, to correct the band-gap values obtained by GGA in this thesis, hybrid functional Heyd-Scuseria-Ernzerhof (HSE) calculations are carried out [143].

## 2.4 Density functional theory implementation

So far, we have argued that the many body problem is a quantum mechanics problem. Solving it is an extremely difficult task, thus it is necessary to do some approximations in order to deal with it. Born-Oppenheimer approximation decouples the electron motion from the nuclear one, while DFT, based on the Hohenberg-Kohn and Kohn-Sham theorems, used the electron density to solve the electronic issue. The most crucial term in DFT is the exchange-correlation energy. In order to implement DFT in numerical computation for real systems, some practical considerations must be taken into account. These ones will be dealt in the next sections.

### 2.4.1 Bloch's theorem

The materials studied in this thesis are crystalline solids where atoms are periodically repeated. Felix Bloch took advantage of this periodic feature of crystalline solids [144], and connected the properties of the electrons in a periodic infinite system with those of the electrons in the unit cell [137].

The Bloch's theorem states :

*The wave function of an electron in an external periodic potential  $v(\mathbf{r}) = v(\mathbf{r} + \mathbf{R})$  can be written as a product of a plane wave and a periodic function with the same periodicity as the lattice [144].*

The wave function is given by

$$\psi_{i\mathbf{k}}(\mathbf{r}) = e^{i\mathbf{k}\cdot\mathbf{r}} u_{i\mathbf{k}}(\mathbf{r}), \quad (2.44)$$

where  $e^{i\mathbf{k}\cdot\mathbf{r}}$  is a plane wave with wave vector  $\mathbf{k}$ , and

$$u_{i\mathbf{k}}(\mathbf{r}) = u_{i\mathbf{k}}(\mathbf{r} + \mathbf{R}), \quad (2.45)$$

is a periodic function which is repeated from one unit cell to another. Here,  $\mathbf{R}$  is the real lattice vector defined by

$$\mathbf{R} = n_1 \mathbf{a}_1 + n_2 \mathbf{a}_2 + n_3 \mathbf{a}_3, \quad (2.46)$$

where  $n_i$  is any integer number and  $\mathbf{a}_i$  are unit cell vectors.

The wave function can also be written as

$$\psi_{i\mathbf{k}}(\mathbf{r} + \mathbf{R}) = e^{i\mathbf{k}\cdot(\mathbf{r}+\mathbf{R})}u_{i\mathbf{k}}(\mathbf{r} + \mathbf{R}) = \psi_{i\mathbf{k}}(\mathbf{r})e^{i\mathbf{k}\cdot\mathbf{R}}. \quad (2.47)$$

It means that the real electrons in a crystal can be considered as perturbed free electrons.

Therefore, the Bloch's theorem is the first consideration employed by DFT for describing electronic real systems: It reduces the infinite number of atoms (electrons) in the whole system to a small number in the unit cell using the periodic nature of solids.

### 2.4.2 Plane wave expansions

In order to solve the KS equation (Equation 2.19), it is important to find out a particular basis set that allows us to expand the KS orbital  $\psi_i(\mathbf{r})$ . As shown in the previous section, one of the best ways is using a plane wave basis set,

$$u_{i\mathbf{k}}(\mathbf{r}) = \frac{1}{\sqrt{\Omega}} \sum_{\mathbf{G}} c_{i\mathbf{k}}(\mathbf{G}) e^{i\mathbf{G}\cdot\mathbf{r}}, \quad (2.48)$$

where  $c_{i\mathbf{k}}(\mathbf{G})$  are the Fourier expansion coefficients, and  $\Omega$  is the unit cell volume

$$\Omega = \mathbf{a}_1 \cdot (\mathbf{a}_2 \times \mathbf{a}_3), \quad (2.49)$$

the summation runs over all reciprocal lattice vectors  $\mathbf{G}$

$$\mathbf{G} = m_1\mathbf{b}_1 + m_2\mathbf{b}_2 + m_3\mathbf{b}_3, \quad (2.50)$$

with  $\mathbf{a}_i$  and  $\mathbf{b}_j$  the primitive vectors of direct and reciprocal lattice, respectively, which satisfy the relation

$$\mathbf{a}_i \cdot \mathbf{b}_j = 2\pi\delta_{ij}. \quad (2.51)$$

Replacing Equation 2.48 in Bloch's theorem (Equation 2.44), the KS electronic

wave functions are

$$\psi_{n,\mathbf{k}}(\mathbf{r}) = \frac{1}{\sqrt{\Omega}} \sum_{\mathbf{G}} c_{n,\mathbf{k}}(\mathbf{G}) e^{i(\mathbf{k}+\mathbf{G})\cdot\mathbf{r}}, \quad (2.52)$$

where  $\mathbf{k}$  is a vector of the primitive cell in the reciprocal lattice space (first Brillouin zone), and the index  $n$  refers to the  $n$ -th energy band.

The reciprocal space is the Fourier transform of real space. Fast Fourier transformation (FFT) allows us to move from real (reciprocal) to reciprocal (real) space in an efficient way.

Replacing Equation 2.52 in the KS equation (Equation 2.19), transforms the KS equations into a general matrix eigenvalue problem [137]

$$\sum_{\mathbf{G}'} \left\{ \frac{1}{2} |\mathbf{k} + \mathbf{G}'|^2 \delta_{\mathbf{G},\mathbf{G}'} + V_{eff}(\mathbf{G}, \mathbf{G}') \right\} c_{n,k}(\mathbf{G}') = \epsilon_{n,k} c_{n,k}(\mathbf{G}), \quad (2.53)$$

where

$$\delta_{\mathbf{G},\mathbf{G}'} = \langle \phi_{\mathbf{G}} | \phi'_{\mathbf{G}'} \rangle, \quad (2.54)$$

and

$$\phi_{\mathbf{G}}(\mathbf{r}) = \frac{1}{\sqrt{\Omega}} e^{i\mathbf{G}\cdot\mathbf{r}}, \quad (2.55)$$

while  $V_{eff}(\mathbf{G}, \mathbf{G}')$  is the Fourier transform of the potential

$$V_{eff}(\mathbf{G}, \mathbf{G}') = \langle \phi_{\mathbf{G}}^{\mathbf{k}} | \hat{V} | \phi_{\mathbf{G}'}^{\mathbf{k}} \rangle, \quad (2.56)$$

with

$$\phi_{\mathbf{G}}^{\mathbf{k}}(\mathbf{r}) = \frac{1}{\sqrt{\Omega}} e^{i(\mathbf{k}+\mathbf{G})\cdot\mathbf{r}}. \quad (2.57)$$

The ground-state energy (the lowest energy of each KS orbital) can be found by solving the matrix eigenvalue (Equation 2.53). In practice, the PW expansion (Equation 2.52) can be adequately set at a limited number of plane waves with the constraint that their kinetic energy be lower than some energy cutoff  $E_{cut}$ :

$$\frac{1}{2}|\mathbf{k} + \mathbf{G}|^2 \leq E_{cut}. \quad (2.58)$$

The cutoff energy must be optimized for each system in order to improve the accuracy and computational cost of calculations.

### 2.4.3 First Brillouin zone

The first Brillouin zone is a primitive cell of the reciprocal lattice, like a Wigner-Seitz cell in the direct lattice. Due to the fact that the reciprocal lattice is periodic, any  $\mathbf{k}'$  point outside the first BZ can be refolded into the first BZ by the reciprocal lattice vector  $\mathbf{G}$

$$\mathbf{k} = \mathbf{k}' - \mathbf{G}, \quad (2.59)$$

which means that the solutions of the KS equations can be fully represented by the occupied states of the first BZ, or in the irreducible Brillouin zone (IBZ) when the symmetries of the system are taken into account, by the folding mechanism in the reciprocal lattice. Thus, in addition to selecting a suitable base for the expansion of the wave functions, the integration of  $\mathbf{k}$  points in the Brillouin zone (BZ) is a fundamental factor in the accuracy and computational cost of the calculations. In practice, due to finite computer resources, the integration is substituted by a summation over a finite set of  $\mathbf{k}$ -points [145], it means:

$$\frac{1}{\Omega_{BZ}} \int_{BZ} f(\mathbf{k}) d\mathbf{k} = \sum_{\mathbf{k}} w_{\mathbf{k}} f(\mathbf{k}), \quad (2.60)$$

where  $\Omega_{BZ}$  is the volume of the Brillouin zone and  $w_{\mathbf{k}}$  is the weight factor of each  $\mathbf{k}$  point that depends on the symmetry of the unit cell. Monkhorst–Pack (MP) [146] method is one of the most efficient for the generation of  $\mathbf{k}$  points and their corresponding weights. In this approach, a mesh of  $\mathbf{k}$  points is spaced evenly along each axis of the reciprocal space. The  $\mathbf{k}_{n_1, n_2, n_3}$  mesh is defined by three integer numbers  $N_i$  ( $i = 1, 2, 3$ ), where  $N_i$  ( $i = 1, 2, 3$ ) is the number of points in the mesh along each axis:

$$\mathbf{k}_{n_1, n_2, n_3} = \sum_{i=1}^3 \frac{2n_i - N_i - 1}{2N_i} \mathbf{b}_i, \quad (2.61)$$

where  $n_i$  varies from 1 to  $N_i$ , and  $\mathbf{b}_i$  are the primitive vectors of reciprocal space. For instance, it can be seen that if  $N_i = 3$  this gives  $-1/3, 0, 1/3$ , and if  $N_i = 4$  this gives  $-3/8, -1/8, 1/8$  and  $3/8$ . In these examples, the set of  $\mathbf{k}$  points are  $3 \times 3 \times 3$  and  $4 \times 4 \times 4$ , respectively.

For solid state applications, a set of coupled KS equations (Equation 2.19) has to be solved, one for each  $\mathbf{k}$ -point included in the BZ sampling [137], where the electronic density is expressed as a BZ average

$$n(\mathbf{r}) = \sum_{\mathbf{k} \in BZ} \omega_{\mathbf{k}} \sum_{i=1}^{N_{\mathbf{k}}} f_i^{(\mathbf{k})} |\psi_i^{(\mathbf{k})}(\mathbf{r})|^2, \quad (2.62)$$

where  $N_{\mathbf{k}}$  is the number of electronic states occupied at each  $\mathbf{k}$ -point, and  $f_i^{(\mathbf{k})}$  the occupation number of band  $i$  at wave vector  $\mathbf{k}$ . If the system is insulating, then  $f_i^{(\mathbf{k})} = 1$  is independently of  $i$  and  $\mathbf{k}$ , and  $N_{\mathbf{k}} = N$ . If there is spin degeneracy the sum is carried up to  $N/2$ , and then multiplied by a degeneracy factor  $f_i^{(\mathbf{k})} = 2$ .

In the case of metallic systems with Fermi surfaces of no uniform shape, the integration of the band-structure energy,

$$\sum_i \frac{1}{\Omega_{ZB}} \int_{BZ} \epsilon_i^{(\mathbf{k})} f_i^{(\mathbf{k})} (\epsilon_i^{(\mathbf{k})} - \epsilon_{E_F}) d\mathbf{k} = \sum_i w_{\mathbf{k}} \epsilon_i^{(\mathbf{k})} f_i^{(\mathbf{k})} (\epsilon_i^{(\mathbf{k})} - \epsilon_{E_F}), \quad (2.63)$$

over the Brillouin zone for the curved Fermi surface is a delicate issue due to the discontinuity of partial filling of the energy bands. In this case, the convergence is too slow due to the occupancies jump from 1 to 0 at the Fermi-level and the high number of  $\mathbf{k}$ -points included [145].

Among the methods used to solve this situation, are the finite temperature approaches or smearing methods, where the step function is replaced by a smooth function e.g. Fermi-Dirac function [147]

$$f_i^{(\mathbf{k})}\left(\frac{\epsilon_i^{(\mathbf{k})} - \epsilon_{E_F}}{\sigma}\right) = \frac{1}{\exp\frac{\epsilon_i^{(\mathbf{k})} - \epsilon_{E_F}}{\sigma} + 1}, \quad (2.64)$$

or a Gauss like function [148]

$$f_i^{(\mathbf{k})}\left(\frac{\epsilon_i^{(\mathbf{k})} - \epsilon_{E_F}}{\sigma}\right) = \frac{1}{2}\left(1 - \operatorname{erf}\left[\frac{\epsilon_i^{(\mathbf{k})} - \epsilon_{E_F}}{\sigma}\right]\right). \quad (2.65)$$

The name of these methods comes from the fact that they mimic the effect of temperature in Fermi-Dirac statistics. Here  $\sigma = K_B T_e$ , is a broadening energy parameter that is adjusted to avoid instabilities in the convergence of the self-consistent procedure. Due to the analogy with the true Fermi distribution, this parameter is sometimes called the electronic Fermi temperature, but it has to be kept in mind that this is just a technical issue [137].

There is an improved method called Methfessel-Paxton which presents a sampling method for Brillouin-zone integration in metals as well as integrals over the occupied part of the Brillouin zone precisely, using a smooth approximation to the step functions which are constructed to give the exact result when integrating Hermite polynomials [149]. This method converges exponentially with the number of sampling points.

#### 2.4.4 Pseudopotentials and PAW

The basis of the pseudopotential approach (PP) lies on substituting the strong ionic potential (valence electron wave functions) near the core region with a smoother nodeless pseudopotential (pseudo-wave functions). This is a practical way of reducing the huge number of PW produced by the rapid oscillations (nodes) of the true valence electron orbitals near the core due to the orthogonality of the valence orbitals with respect to the core orbitals. The use of nodeless pseudo-wave functions reduces the computational cost. Pseudopotential scheme is based on the frozen-core approximation which classifies electrons according to their contribution to the chemical bonding as core and valence electrons. The core electrons are tightly bound to the nucleus and do not contribute directly to the chemical bonding, while valence

electrons are responsible for chemical bonding.

The construction steps of pseudopotentials are as follows:

First, the following all-electron radial Schrödinger equation for the atom at the reference configuration is solved, usually at the fundamental state of the neutral atom, finding the energy and wave functions of electronic states :

$$-\frac{1}{r} \frac{d^2}{dr^2}(r\psi_{nl}(r)) + \frac{l(l+1)}{r^2}\psi_{nl}(r) + V_{sc}\psi_{nl}(r) = \varepsilon_{nl}(r)\psi_{nl}(r). \quad (2.66)$$

Once the KS orbitals are obtained, an arbitrary distinction between valence and core states is made, choosing a core radius ( $r_c$ ). Then a DFT precalculation for the core electrons is performed, and they are kept frozen for the remaining calculations, and are assumed to have transferable properties. The core effect is replaced by the pseudopotential obtained from the DFT precalculation in the atomic configuration. With the new potential, the valence states are made softer. Thus, the KS orbital  $\psi$  that satisfies Equation 2.19, is expressed as:

$$\psi = \phi_{Tv} + \sum_c a_c \phi_c, \quad (2.67)$$

where  $\phi_{Tv}$  is the true valence wave function outside  $r_c$ , in the zone of chemical bonds, and  $\phi_c$  represents the core states. As shown in Figure 2-1, at  $r > r_c$  the pseudo-wave function (red line) coincides with the all electron wave function (blue line), while for the  $r < r_c$ , core part, the pseudo-wave function  $\Psi_{pseudo}$  is nodeless and smoother. At  $r = r_c$  the first and second derivatives of  $\Psi_{pseudo}$  and  $\Psi$  are the same. Afterwards, the pseudopotential  $V_{sc}$  is found inverting the radial Schrödinger equation (Equation 2.66) using the constructed pseudo-wave functions. The inversion is done because of the nodeless condition. Finally, the KS equation is rewritten in terms of the pseudopotential and pseudo-wave functions.

Since Phillips and Kleinman [150] proposed for the first time the pseudopotential approach, a lot of effort has been devoted by the scientist community in developing new and more efficient ones using different theoretical frameworks. Among the methods beyond PP, the Projector Augmented Wave (PAW) [151] is one of the most accurate ones used in DFT because it preserves the AE features of the wavefunctions.

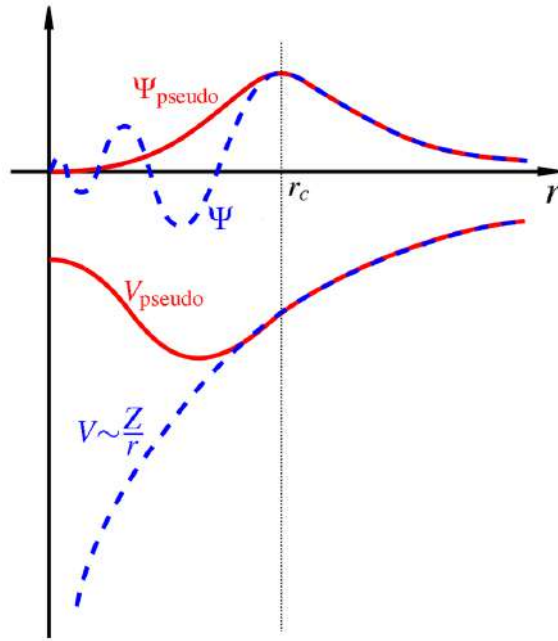


Figure 2-1: Schematic illustration of the comparison between a real wave function  $\Psi$  (Coulomb potential  $V$ ) and a pseudo-wave function  $\Psi_{pseudo}$  (pseudopotential  $V_{pseudo}$ ). The real and the pseudo wavefunction and potentials match above a certain cutoff radius  $r_c$ .

It is implemented in the Vienna Ab-initio Simulation Package (VASP) [152, 153], which is the computational program used to carry out this research.

PAW is a generalization of both the pseudopotential method and the linear augmented-plane-wave (LAPW) methods. Blöchl in his original paper [151] obtained the AE wave function  $\Psi$  from the smooth pseudo-wave function  $\tilde{\Psi}$  by the following relation

$$|\Psi\rangle = |\tilde{\Psi}\rangle + \sum_i (|\phi_i\rangle - |\tilde{\phi}_i\rangle) \langle \tilde{p}_i | \tilde{\Psi} \rangle \quad \text{with} \quad \langle \tilde{p}_i | \tilde{\phi}_j \rangle = \delta_{ij}, \quad (2.68)$$

which means that the all-electron wavefunction is rebuilt from the smooth pseudo-wave function by correcting for the differences between the AE partial orbitals  $\phi_i$  and the pseudo partial waves  $\tilde{\phi}_i$  of the atoms. The true partial orbitals  $\phi_i$  of the isolated atom are obtained from an AE calculation and coincides with the pseudo partial ones for  $r > r_c$ . They also match continuously for  $r < r_c$ . Therefore, PAW method has the efficiency of PP scheme and the accuracy of AE methods.

## 2.4.5 Spin-Orbit Coupling

Since in our study the spin-orbit interaction (SOC) for 551-Graphene/331-GaAs bilayer heterostructure has been taken into account, in this section we will review the most important concepts about the spin-orbit interaction.

Spin-orbit coupling is a relativistic interaction between moving electrons with  $\mathbf{v}=\mathbf{p}/m$  and a local electric field  $\mathbf{E}=-\frac{1}{q}\frac{dV(r)}{dr}\frac{\mathbf{r}}{r}$  in their rest frame created by the proton, where  $q$  is the charge of the moving electrons and  $V(r)=-\frac{e^2}{r}$  is the electrostatic energy of the electron. Special relativity indicates that in the electron frame, a magnetic field appears, described by [154]

$$\mathbf{B} = -\frac{1}{c^2}(\mathbf{v} \times \mathbf{E}), \quad (2.69)$$

where  $\mathbf{B}$  is equivalent to:

$$\mathbf{B} = -\left(\frac{e^2}{qm_e c^2 r^3}\right)\mathbf{L}. \quad (2.70)$$

Here,  $\mathbf{L} = \mathbf{r} \times \mathbf{P}$  represents the electron orbital angular momentum. Due to the interaction of  $\mathbf{B}$  with the electron intrinsic magnetic moment  $\mathbf{m}_s$ , given by:

$$\mathbf{m}_s = \frac{q}{m_e}\mathbf{S}, \quad (2.71)$$

and by Zeeman effect, the orbital energy levels are splitted, which can lead to different transition levels with energy:

$$H_{so} = -\mathbf{m}_s \cdot \mathbf{B}. \quad (2.72)$$

From Equation 2.70, 2.71 and 2.72,  $H_{so}$  can be rewritten as:

$$H_{so} = \xi(r)\mathbf{L} \cdot \mathbf{S}, \quad (2.73)$$

where  $\xi(r) = e^2/2m_e^2 c^2 r^3$  contains the entire radial dependence of the SOC Hamiltonian operator [155]. The factor 1/2 is due to the fact that the electron spin rotates with respect to the laboratory reference frame [154].  $\mathbf{L}$  and  $\mathbf{S}$  are the electron orbital

and spin angular momentum, respectively. The total angular momentum is  $\mathbf{J} = \mathbf{L} + \mathbf{S}$ . When the orbital angular momentum of  $p$ -graphene orbital ( $l=1$ ) interacts with its spin intrinsic momentum, the electron states can be  $j = |l \pm 1/2|$ , i.e. either  $3/2$  ( ${}^2P_{3/2}$ ) or  $1/2$  ( ${}^2P_{1/2}$ ), depending on the case if  $\mathbf{L}$  and  $\mathbf{S}$  are parallel or antiparallel, respectively, as shown in Figure 2-2.

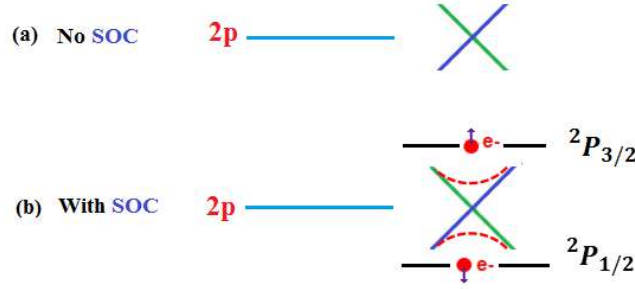


Figure 2-2: Orbital angular momentum of  $p$ -graphene state ( $l=1$ ) with (a) no coupling, and (b) coupling with its spin intrinsic momentum.

Special relativity theory states that for electrons with large average speeds the mass increases, while the radius decreases. In the weakly relativistic domain, the SOC effect is specially noticed for massive atoms of the periodic table. There are some pioneering studies [156, 157] indicating splitting of electron and hole energy bands by spin-orbit coupling (SOC) in 2D-GaAs heterostructures. Pyykkö [158] compared the relativistic (Dirac) and nonrelativistic (Schrödinger) dynamics for the valence electron in a given atomic potential, to study the importance of the direct relativistic effect on atomic orbitals. They found a relativistic radial contraction and energetic stabilization for  $s$  and  $p$  shells, spin-orbit splitting and the relativistic radial expansion and energetic destabilization of the  $d$  and all  $f$  outer shells. They also reported that all three effects were of the same order of magnitude and grow roughly like  $Z^2$ .

Dirac used quantum mechanics combined with special relativity to obtain an equation that describes the electron spin. For this purpose, the energy dispersion relation given by special relativity [159]

$$\epsilon^2 = (cp)^2 + (mc^2)^2, \quad (2.74)$$

was factorized

$$(\epsilon + c\boldsymbol{\alpha} \cdot \mathbf{p} + \beta mc^2)(\epsilon - c\boldsymbol{\alpha} \cdot \mathbf{p} - \beta mc^2) = 0, \quad (2.75)$$

to obtain a first-order time-differential equation

$$(\epsilon - c\boldsymbol{\alpha} \cdot \mathbf{p} - \beta mc^2) \Psi(\mathbf{r}, t) = 0, \quad (2.76)$$

where the coefficients  $\alpha$  and  $\beta$  should satisfy the following relations

$$\begin{aligned} \alpha_i^2 &= \beta^2 = 1 & (i = x, y, z), \\ \alpha_i \alpha_j + \alpha_j \alpha_i &= 0 & (i \neq j), \\ \alpha_i \beta + \beta \alpha_i &= 0, \end{aligned} \quad (2.77)$$

here  $\alpha$  and  $\beta$  are, at least,  $4 \times 4$  matrices. The expressions for  $\alpha$  and  $\beta$  are not unique. One possible combination of  $\alpha$  and  $\beta$ , called the Dirac representation, in terms of Pauli matrices  $\sigma_i$ , that satisfies Equation 2.76 is:

$$\begin{aligned} \sigma_x &= \begin{pmatrix} 0 & 1 \\ 1 & 0 \end{pmatrix}, \sigma_y = \begin{pmatrix} 0 & -i \\ i & 0 \end{pmatrix}, \sigma_z = \begin{pmatrix} 1 & 0 \\ 0 & -1 \end{pmatrix}, \\ \alpha_i &= \begin{pmatrix} 0 & \sigma_i \\ \sigma_i & 0 \end{pmatrix}, \beta = \begin{pmatrix} I & 0 \\ 0 & -I \end{pmatrix}, \end{aligned} \quad (2.78)$$

where  $I$  is the  $2 \times 2$  identity matrix.

Substituting the momentum operator

$$\hat{\mathbf{p}} = -i\hbar \hat{\nabla}, \quad (2.79)$$

and the energy operator

$$\hat{\epsilon} = i\hbar \frac{d}{dt}, \quad (2.80)$$

in Equation 2.74, one obtains a relativistic expansion of the Schrödinger equation for a free electron, called the Dirac equation

$$i\hbar \frac{\partial \Psi(\mathbf{r}, t)}{\partial t} + i\hbar c \boldsymbol{\alpha} \cdot \nabla \Psi(\mathbf{r}, t) - \beta m c^2 = 0. \quad (2.81)$$

Since  $\alpha$  and  $\beta$  are  $4 \times 4$  matrices, a solution  $\Psi(\mathbf{r}, t)$  that describes particles of spin  $1/2$  has four components:

$$\Psi(\mathbf{r}, t) = \begin{pmatrix} \Psi_1(\mathbf{r}, t) \\ \Psi_2(\mathbf{r}, t) \\ \Psi_3(\mathbf{r}, t) \\ \Psi_4(\mathbf{r}, t) \end{pmatrix} = \begin{pmatrix} \Psi_A(\mathbf{r}, t) \\ \Psi_B(\mathbf{r}, t) \end{pmatrix}, \quad (2.82)$$

here,  $\Psi_A(\mathbf{r}, t)$  and  $\Psi_B(\mathbf{r}, t)$  are two component spinors.

Since the total angular momentum  $\mathbf{J}$

$$\mathbf{J} = \mathbf{L} + \mathbf{S}, \quad (2.83)$$

must be conserved, where  $\mathbf{L}$  and  $\mathbf{S}$  are the electron orbital and spin angular momentum, respectively,  $\mathbf{J}$  commutes with the Hamiltonian:

$$[\mathbf{J}, \mathcal{H}] = [\mathbf{L}, \mathcal{H}] + [\mathbf{S}, \mathcal{H}] = 0. \quad (2.84)$$

Consider now an electron with charge  $-e$  placed in an electromagnetic field. The operators in Equation 2.76 are changed by replacing  $\mathbf{p}$  with  $\mathbf{p} + e\mathbf{A}$  and adding the electrostatic potential  $-e\phi$ , resulting in

$$\left[ i\hbar \frac{\partial}{\partial t} + e\phi - c\boldsymbol{\alpha} \cdot (\mathbf{p} + e\mathbf{A}) - \beta m c^2 \right] \Psi(\mathbf{r}, t) = 0, \quad (2.85)$$

here,  $\mathbf{A}$  and  $\phi$  are the vector and electric (scalar) potential, respectively.

For practical applications in DFT-calculations, the relativistic effects are incorporated directly into the PAW or pseudopotential schemes. Relativistic corrections are made only in the core region, due to the high energies of electrons of heavy atoms in the deepest shells. The exchange-correlation functional should also be modified to account for relativistic effects. This can be done by multiplying the exchange energy density and potential for quite high densities, e.g. those deep into the atomic core

by density-dependent correction factors[137].

### 2.4.6 Vienna *Ab-initio* Simulation Package (VASP)

This research has been carried out using the Vienna Ab-initio Simulation Package (VASP) because this computational program has demonstrated high efficiency and accuracy in the theoretical study of electronic systems using DFT. VASP was developed by Kresse and Furthmüller in 1996 [152, 153] and differs from others computational packages, e.g. QUANTUM-ESPRESSO, SIESTA, ABINIT, CASTEP, WIEN2K, GAUSSIAM, in the selecting basis functions, pseudopotentials, and the algorithms used for diagonalization of the KS Hamiltonian.

The following are the main features of VASP [12]:

- Needs four input files for starting running, i.e. INCAR, POSCAR, POTCAR, and KPOINTS: and gives, among others, the following output files: OUTCAR, CHGCAR, CONTCAR.

- Expands the KS orbitals and potentials with the PW basis set, and employing PP or PAW schemes for treating the electron-ion interaction for all elements. The PP or PAW information is located at the POTCAR file.

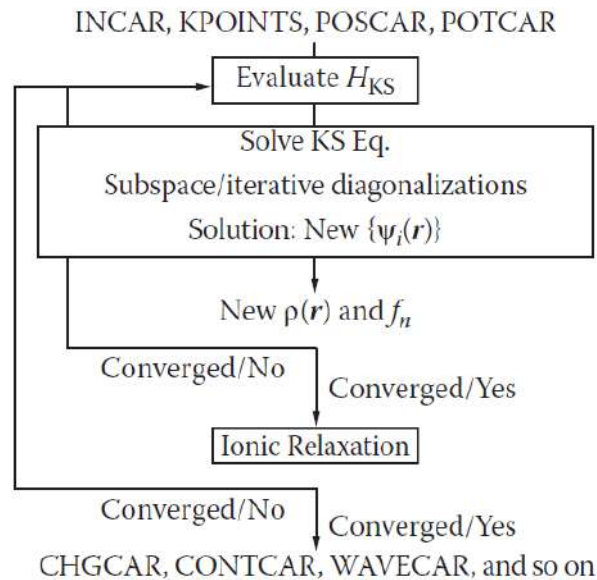


Figure 2-3: Scheme of the self-consistent cycle of the Kohn–Sham equations employed by VASP [12].

– Uses a self-consistency cycle to carry out the electronic and ionic minimization, as shown in Figure 2-3 [12]. In order to do that, first a trial  $n(r)$  is constructed from orbitals of isolated atoms, and PP or PAW. Then, from this trial  $n(r)$  and XC functional the energy terms of the KS Hamiltonian in real and reciprocal spaces, via fast Fourier transformations (FFT), are calculated. VASP provides several XC functionals for DFT, e.g. LDA, LDA+U, PW91, GGA, hybrids, and van der Waals functionals, among others. Third, the KS equations, a matrix eigenvalue equation, are solved by an iterative diagonalization in the real and reciprocal spaces. In this step new KS orbitals are calculated. The block Davidson algorithm is used for the diagonalization of the KS Hamiltonian, which is considered among the fastest methods nowadays available. Next, with the newly calculated orbitals, a new electron density is generated, and the process is repeated until self-consistency is reached. Later, after electronic minimization is achieved, the forces on atoms are calculated and the atoms are moved to new positions of lower forces. This is the ionic minimization process. The forces can be calculated using the Hellmann-Feynman theorem [137]. The electronic and ionic minimization is repeated in series until the energy-convergence criterion is achieved.

– VASP can be run in a parallel mode for any system including atoms, molecules, bulk solids, surfaces, clusters, etc.

### 2.4.7 Phonons

Just as photons are the quantized normal modes of electromagnetic waves, phonons are the quantized normal modes of the lattice vibration in a crystalline solid. Thus, the phonon energy levels (eigenvalues) are quantized for each wave vector,  $\mathbf{q}$  (lattice displacement). The dependence of the frequency,  $\omega$ , on the wave vector,  $\mathbf{q}$ , is known as the phonon dispersion, i.e.  $\omega(\mathbf{q})$ . A large number of physical properties can be understood in terms of phonons, e.g. specific heat, thermal expansion, heat conduction; and physical phenomena related to electron-phonon interactions, such as resistivity, and superconductivity.

In order to give a phonon description of lattice vibrations, some approximations are made. The harmonic approximation assumes that the amplitude of atomic

displacements is small compared to interatomic distances, and the mean equilibrium position of each ion,  $i$ , is a Bravais lattice site,  $\mathbf{R}_i$ . The results given by this theory are often in excellent agreement with experimental ones. However, for the study of physical properties of systems at elevated temperature the harmonic approximation fails. Thus, for these cases it is necessary to use the anharmonic theory [160].

In order to find a mathematical model that describes the lattice vibration, let's assume that the total potential energy of the crystal  $U$  is the sum of the potential energy contributions  $\phi(\mathbf{r})$  of all distinct pairs of ions located at  $\mathbf{r}(\mathbf{R})$  and  $\mathbf{r}(\mathbf{R}')$  [160]

$$U = \frac{1}{2} \sum_{\mathbf{R}\mathbf{R}'} \phi(\mathbf{r}(\mathbf{R}) - \mathbf{r}(\mathbf{R}')), \quad (2.86)$$

where the relation between the Bravais lattice vector  $\mathbf{R}$ , the instantaneous position  $\mathbf{r}(\mathbf{R})$  of the ion that oscillates about  $\mathbf{R}$ , and the lattice displacement  $\mathbf{u}(\mathbf{R})$ , is:

$$\mathbf{r}(\mathbf{R}) = \mathbf{R} + \mathbf{u}(\mathbf{R}), \quad (2.87)$$

and so for

$$\mathbf{r}(\mathbf{R}') = \mathbf{R}' + \mathbf{u}(\mathbf{R}'). \quad (2.88)$$

Inserting Equation 2.87 and Equation 2.88, in Equation 2.86, we obtain:

$$U = \frac{1}{2} \sum_{\mathbf{R}\mathbf{R}'} \phi(\mathbf{R} - \mathbf{R}' + \mathbf{u}(\mathbf{R}) - \mathbf{u}(\mathbf{R}')). \quad (2.89)$$

Applying now the three-dimensional form of Taylor's theorem

$$f(\mathbf{r} + \mathbf{a}) = f(\mathbf{r}) + \mathbf{a} \cdot \nabla f(\mathbf{r}) + \frac{1}{2}(\mathbf{a} \cdot \nabla)^2 f(\mathbf{r}) + \frac{1}{3!}(\mathbf{a} \cdot \nabla)^3 f(\mathbf{r}) + \dots \quad (2.90)$$

to Equation 2.89 with  $\mathbf{r} = \mathbf{R} - \mathbf{R}'$ , and  $\mathbf{a} = \mathbf{u}(\mathbf{R}) - \mathbf{u}(\mathbf{R}')$ , and vanishing the linear term because the system is in equilibrium, and there is no net force applied to any atom, the first non-vanishing correction, i.e., the quadratic term, to the equilibrium potential energy represents *the harmonic approximation*

$$U^{harm} = \frac{1}{4} \sum_{\mathbf{R}\mathbf{R}'} [(\mathbf{u}(\mathbf{R}) - \mathbf{u}(\mathbf{R}')) \cdot \nabla]^2 \phi(\mathbf{R} - \mathbf{R}'), \quad (2.91)$$

where the equilibrium potential energy is given by the first term of Equation 2.90:

$$U^{eq} = \frac{1}{2} \sum_{\mathbf{R}\mathbf{R}'} \phi(\mathbf{R} - \mathbf{R}') = \frac{N}{2} \sum_{\mathbf{R} \neq 0} \phi(\mathbf{R}). \quad (2.92)$$

The terms that represent the third and fourth corrections to  $U$  are known as *anharmonic terms*, and they are treated as small perturbations on the harmonic term.

In the Brillouin zone, at each wave vector,  $\mathbf{q}$ , there are  $3N$  vibrational modes, where three are acoustic (A) modes, and the rest ones,  $3N - 3$ , optical (O) modes. The acoustic name comes from the fact that their dispersion relation at small values, near the  $\Gamma$  point, is linear, which is the feature of sound waves. The optical modes are called in that way because they are responsible for the optical behavior of some crystals when interacting with electromagnetic radiation. Furthermore, all ions in a primitive cell move in (out of) phase in the acoustic mode (optical mode).

Lattice vibrations can be classified based on the relationship between the orientation of the polarization vector, and the propagation direction,  $\mathbf{q}$ , as longitudinal (L), in the case of parallel orientation, and transverse (T) modes, for perpendicular orientation. Therefore, phonons can be classified for acoustic (optical) modes as LA (LO) and TA (TO). For instance, in the case of 3D-GaAs ( $N=2$  atoms), there are 6 phonon modes ( $3N$ ): 3A and 3O ( $3N-3$ ). For the A modes, 1 is LA and 2 are TA; and, for the O modes, 1 is LO ( $N-1$ ) and 2 are TO ( $2N-2$ ).

On the other hand, phonons in 2D materials present different types of modes when compared to those of 3D. This is because atoms in 2D-materials are in-plane, thus they have no out-plane neighbor atoms to interact with. As we are interested in studying 2D group III–V materials, we analyze here the calculated phonon dispersion curves for 2D–BAs semiconductor in the hexagonal primitive cell with GGA scheme, as shown in Figure 2-4. We can see that the planar structure 2D *h*-BAs can be stable, because there are no imaginary frequencies in the phonon dispersion. It means, there are no soft modes and, as a consequence, there is no sign of any dynamical instability. There are six phonon dispersion bands because the unit cell

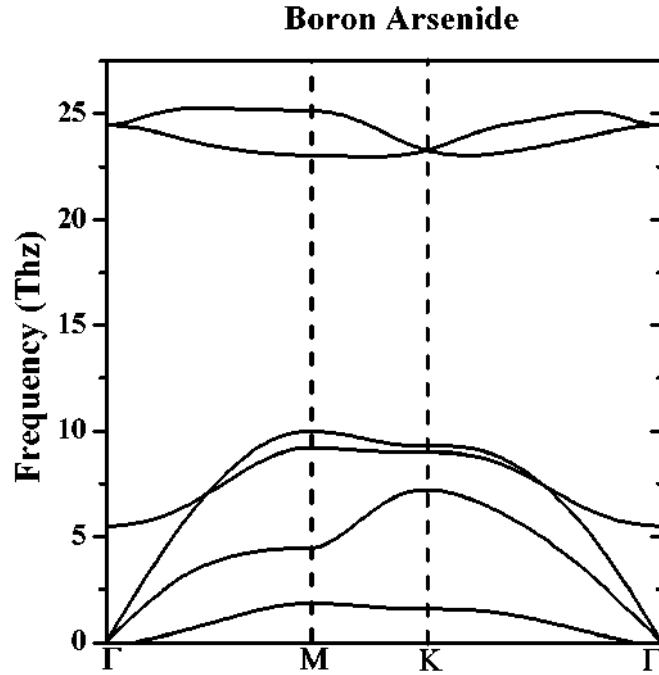


Figure 2-4: Phonon dispersion curves for 2D-BAs semiconductor in the hexagonal primitive cell with GGA scheme.

of 2D  $h$ -III-As contains two atoms, A (cation) and B (anion). The three vibrational branches, which are zero at the  $\Gamma$  point, correspond to the acoustic modes (A). The other three frequency values ( $3N-3$ ) correspond to the optical modes (O). Depending on if vibrations of cation-anion atoms directions are parallel or perpendicular, the phonon modes are classified as longitudinal (L) or transversal (T). From downward to upward modes, listed in order of increasing energy, they can be classified as: out-of plane mode (ZA), in-plane transversal mode (iT<sub>A</sub>) and in-plane longitudinal mode (iL<sub>A</sub>) for the acoustic modes. The (ZA) mode shows a  $\mathbf{q}^2$  energy dispersion relation near to the  $\Gamma$  point and the other two (iT<sub>A</sub> and iL<sub>A</sub>), a  $\mathbf{q}$  linear dependence. The remaining three branches ( $3N-3$ ) correspond to optical modes, (N-1) out-of plane mode (1 ZO), (N-1) in-plane transversal mode (1 iT<sub>O</sub>) and (N-1) in-plane longitudinal mode (1 iL<sub>O</sub>).

Phonons can be calculated by computational methods using Density functional Theory via interatomic force constants. The most common first principles phonon calculation methods are finite displacement method (FDM) [161, 162] and density functional perturbation theory (DFPT) [163]. In the linear response methods

(DFPT), the dynamical matrix is expressed in terms of the inverse dielectric matrix describing the response of the valence electron density to a periodic perturbation of the crystalline lattice [161].

In this thesis, the study of the dynamical stability of 2D group III-V semiconductors have been carried out using supercell and finite displacement approaches, because for semiconductors and transition metals, the realization of the linear-response approach is much more difficult, since the full dielectric matrix must be calculated in terms of the electronic eigenfunctions and eigenvalues of the perfect crystal [161].

The finite displacement approach uses the analysis of the forces on the atoms induced by the displacements of other atoms in the supercell to study phonon frequencies. The forces on all atoms in the supercell increase if an atom of the supercell is displaced from its equilibrium position. The difference in the energies of the perturbed and unperturbed crystal lattices is used to calculate the energy of a periodic distortion of the crystalline lattice (phonon).

The ab-initio force constant technique (FDM) is based on periodically repeated supercells. From the displacement of a single atom in each supercell, FDM calculates the forces and crystal force constants on all supercell atoms. The number of supercells, atomic displacement, depends on the crystal symmetry. For instance, cubic NiAl only needs two displacements along single direction Z, one for each Al and Ni atom. The forces are called Hellmann-Feynman forces (H-F), because they are obtained from the Hellmann–Feynman theorem [164, 165]. This theorem states that the variation of the electronic energy  $E(\lambda)$  with respect to an external parameter  $\lambda$  can be calculated as the expectation value of the variation of the Hamiltonian:

$$\frac{\partial E}{\partial \lambda} = \langle \psi | \frac{\partial \hat{H}}{\partial \lambda} | \psi \rangle, \quad (2.93)$$

here  $|\psi\rangle$  is an eigenstate of the Hamiltonian. From the Hellmann–Feynman theorem the forces acting on a given nucleus can be obtained. For instance, the  $z$ -component of the force acting on a given nucleus is equal to the negative of the derivative of the total energy with respect to that coordinate. Employing the Hellmann–Feynman theorem this is equal to

$$\mathbf{F}_z = -\frac{\partial E}{\partial \mathbf{z}} = -\langle \psi | \frac{\partial \hat{H}}{\partial \mathbf{z}} | \psi \rangle. \quad (2.94)$$

One important application of H–F is the calculation of equilibrium geometries, i.e. the nuclear coordinates where the forces acting upon the nuclei, due to the electrons and other nuclei, vanish. Thus, the derivative of the total energy with respect to the atomic position is zero

$$\mathbf{F}_I = -\frac{\partial E}{\partial \mathbf{R}_I} = -\langle \psi | \frac{\partial \hat{H}}{\partial \mathbf{R}_I} | \psi \rangle = 0. \quad (2.95)$$

As shown in **Equations (2.86–2.92)** the total crystal potential energy  $U$  is a function of the displacement and can be expanded by Taylor’s theorem. Now, we suppose that atoms  $(lk)$ , where  $l$  and  $k$  are the labels of unit cells and atoms in each unit cell, respectively, move around their equilibrium positions  $\mathbf{r}(kl)$  with displacements  $\mathbf{u}(lk)$ . Thus,  $U$  can be rewritten as follows [166]:

$$\begin{aligned} U &= U_0 + \sum_{lk} \sum_{\alpha} \phi_{\alpha}(lk) \mathbf{u}_{\alpha}(lk) + \frac{1}{2} \sum_{l'k'} \sum_{\alpha\beta} \phi_{\alpha\beta}(lk, l'k') \mathbf{u}_{\alpha}(lk) \mathbf{u}_{\beta}(l'k') \\ &+ \frac{1}{3!} \sum_{l''k''} \sum_{\alpha\beta\gamma} \phi_{\alpha\beta\gamma}(lk, l'k', l''k'') \mathbf{u}_{\alpha}(lk) \mathbf{u}_{\beta}(l'k') \mathbf{u}_{\gamma}(l''k'') + \dots \end{aligned} \quad (2.96)$$

where  $\alpha$ ,  $\beta$  and  $\gamma$  are the Cartesian indices. The coefficients of the series expansion,  $U_0$ ,  $\phi_{\alpha}(lk)$ ,  $\phi_{\alpha\beta}(lk, l'k')$ ,  $\phi_{\alpha\beta\gamma}(lk, l'k', l''k'')$  are the zeroth, first, second, and third order force constants, respectively.

The force acting on an atom  $(l, k)$  is:

$$\mathbf{F}_{\alpha}(lk) = -\frac{\partial U}{\partial \mathbf{u}_{\alpha}(lk)} = -\frac{1}{2} \sum_{l'k'} \sum_{\beta} \phi_{\alpha\beta}(lk, l'k') \mathbf{u}_{\beta}(l'k'), \quad (2.97)$$

which physically means that the displacement of a single atom  $(l'k')$  in the supercell by a vector  $\mathbf{u}_{\beta}(l'k')$  induces forces  $\mathbf{F}_{\alpha}(lk)$  acting on the surrounding atoms.

On the other hand, from [Equation 2.97](#) we can find the interatomic force constant:

$$C_{lk,l'k'}^{\alpha\beta} = -\frac{\partial \mathbf{F}_\alpha(lk)}{\partial \mathbf{u}_\beta(l'k')} = \phi_{\alpha\beta}(lk, l'k') = \frac{\partial^2 U}{\partial \mathbf{u}_\alpha(lk) \partial \mathbf{u}_\beta(l'k')} = -\frac{\partial \mathbf{F}_\beta(l'k')}{\partial \mathbf{u}_\alpha(lk)}. \quad (2.98)$$

Equation 2.97 is the key equation of the FDM, and for simplicity only a single atomic displacement is applied. This displacement  $\mathbf{u}_\beta(l'k')$  is an input for the ab-initio calculations, while the Hellmann-Feynman forces  $\mathbf{F}_\alpha(lk)$  are found as a result of a single ionic loop of optimization in ab initio calculations. The solution of Equation 2.95 is not simple, since the number of known and unknown variables is different, and the space group of the crystal requires to impose on Equation 2.97 additional symmetry constrains [162].

The Fourier transform of these interatomic force constants is the dynamical matrix,

$$D_{k,k'}^{\alpha\beta}(\mathbf{q}) = \sum_{l'} \frac{C_{0k,l'k'}^{\alpha\beta}}{\sqrt{m_k m_{k'}}} e^{i\mathbf{q} \cdot [\mathbf{r}(l'k') - \mathbf{r}(0k)]}. \quad (2.99)$$

Dynamical property of atoms in the harmonic approximation is obtained by solving the eigenvalue problem of the dynamical matrix:

$$\sum_{\beta k'} D_{k,k'}^{\alpha\beta}(\mathbf{q}) e_{\mathbf{q}\nu}^{\beta k'} = \omega_{\mathbf{q}\nu}^2 e_{\mathbf{q}\nu}^{\alpha k}, \quad (2.100)$$

where  $m_k$  is the mass of the atom  $k$ ;  $\mathbf{q}$  is the wave vector, and  $\nu$  is the band index or phonon branch.  $\omega_{\mathbf{q}\nu}$  and  $e_{\mathbf{q}\nu}$  give the phonon frequency and polarization vector of the phonon mode labeled by a set  $(\mathbf{q}, \nu)$ , respectively. Due to Equation 2.100 is an Hermitian matrix, its eigenvalues,  $\omega_{\mathbf{q}\nu}^2$ , are real.

From the eigenvalue (Equation 2.100), the phonon dispersion  $\omega_{\mathbf{q}\nu}$  and polarization vector ( $e_{\mathbf{q}\nu}$ ) can be determined.

## 2.4.8 Supercell model

The supercell model allows to study non periodic systems, e.g. surface, defects, molecules, and isolated atoms, using a set of plane waves with periodic boundary conditions (PBC) [167] in three dimensions. In this approach, the system we want

to study is simulated using a supercell which is made up of several unit cells. In the case of molecules or surfaces an optimized  $z$ -distance (vacuum region) between the adjacent supercells must be included to avoid significant interactions between initial supercell and its periodic images [137]. In the case of defects, e.g. vacancy, the supercell size must be optimized in order to be sure that interactions between the vacancy and its images in neighboring supercells are negligible [134].

Due to Bloch's theorem, the wave function has the same periodicity of the unit cell in a supercell [137] ,

$$\Psi_{\mathbf{k}}(\mathbf{r} + n\mathbf{a}_i) = e^{in\mathbf{k}\cdot\mathbf{a}_i}\Psi_{\mathbf{k}}(\mathbf{r}), \quad (2.101)$$

if

$$\mathbf{k} \cdot \mathbf{a}_i = \frac{2\pi m}{n}, \quad (2.102)$$

where  $m$  and  $n \in \mathbb{Z}$ .

The non-equivalent  $\mathbf{k}$ -vectors compatible with PBC in a supercell made of  $n$  replicas of the unit cell along the direction of the lattice vector  $\mathbf{a}_i$  are [137]

$$\mathbf{k} = \mathbf{0}, \pm \frac{\mathbf{b}_i}{n}, \pm \frac{2\mathbf{b}_i}{n}, \dots, \pm \frac{(n/2 - 1)\mathbf{b}_i}{n}, \frac{\mathbf{b}_i}{2}. \quad (2.103)$$

For instance, for  $n = 4$ , Equation 2.103, the allowed  $\mathbf{k}$ -vectors are  $\mathbf{0}$ ,  $\pm \frac{\mathbf{b}_i}{4}$ , and  $\frac{\mathbf{b}_i}{2}$ . Where the primitive vectors in reciprocal space,  $\mathbf{b}_j$ , are defined in terms of the primitive lattice vectors in real space by the relations

$$\mathbf{a}_i \cdot \mathbf{b}_j = 2\pi\delta_{ij}, \quad (2.104)$$

$$\mathbf{b}_1 = 2\pi \frac{\mathbf{a}_2 \times \mathbf{a}_3}{\Omega}, \quad \mathbf{b}_2 = 2\pi \frac{\mathbf{a}_3 \times \mathbf{a}_1}{\Omega}, \quad \mathbf{b}_3 = 2\pi \frac{\mathbf{a}_1 \times \mathbf{a}_2}{\Omega}. \quad (2.105)$$

Here,  $\Omega$  is the volume of the unit cell. The volume at the reciprocal space,  $\Omega_R$ , is called the first Brillouin zone or Brillouin zone (BZ), and is defined by

$$\Omega_R = \mathbf{b}_1 \cdot (\mathbf{b}_2 \times \mathbf{b}_3) = \frac{(2\pi)^3}{\Omega}. \quad (2.106)$$

On the other hand, the electronic density is the same in each unit cell, since the system is periodic,

$$n_{\mathbf{k}}(\mathbf{r}+\mathbf{R}) = n_{\mathbf{k}}(\mathbf{r}), \quad (2.107)$$

with  $\mathbf{R}=n_1\mathbf{a}_1 + n_2\mathbf{a}_2 + n_3\mathbf{a}_3$  ( $n_i \in \mathbb{Z}$ ).

## 2.5 Magnetic exchange interaction

Magnetic exchange interactions address the behavior of magnetic materials. Hence, the understanding of magnetic interactions on nanoscale magnetic materials, is of vital importance for tuning their magnetic properties, not only to explore new physics phenomena, but to create disruptive commercial devices based on the transport and manipulation of the electron spin [13].

In a 1966 paper titled: “Absence of Ferromagnetism or Antiferromagnetism in one- or two-dimensional isotropic Heisenberg models” [168], Mermin and Wagner claimed that thermal fluctuations strongly suppress long-range magnetic order in two-dimensional materials at any non-zero temperature, even if those materials are intrinsically magnetic in 3D bulk form. Therefore, the scientific community believed that ferromagnetism could not be an intrinsic property of two dimensional materials, although two-dimensional (2D) materials have been intensely studied theoretically and experimentally since 2004 [9, 10, 54, 169, 170, 171, 172, 173]. Fortunately for science, the first pioneering experimental confirmations of magnetism in  $\text{CrI}_3$  [132] and  $\text{CrGeTe}_3$  atomically-thin crystals were observed in 2017 [69], which opened an entirely new field of ultra-thin magnetic materials, that does not cease to surprise [70].

What are the physical reasons of this astonishing finding?

The detrimental effect of thermal fluctuations on magnetism in low-dimensional materials can be neutralized by the presence of magnetic anisotropy (MA). The spin-orbit coupling (SOC) is the microscopic source of magnetic anisotropy, e.g., in the case of monolayer  $\text{CrI}_3$ , the MA due to the SOC on I, non-magnetic atoms, removes the Mermin-Wagner constraints.

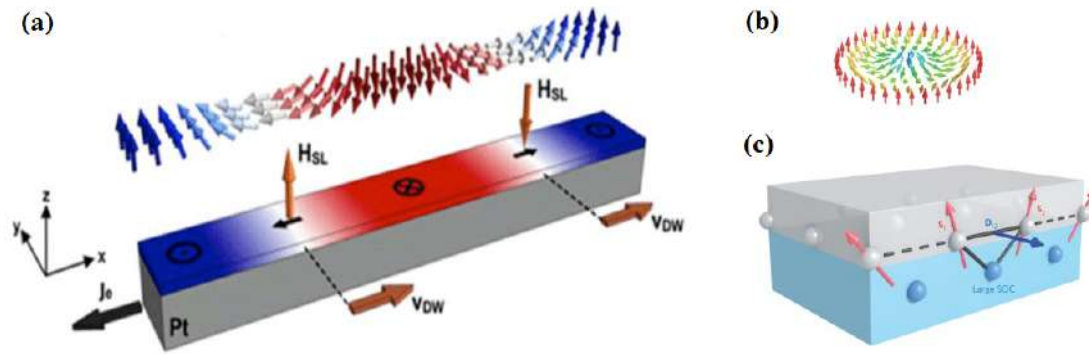


Figure 2-5: (a) The chirality of domain walls in the presence of spatial inversion asymmetry and the spin Hall effect – with a mechanism that conserves spin angular momentum, that is, Slonczewski spin-transfer torques (HSL: Slonczewski field induced by edge spin accumulation) [13]. (b) Skyrmions in a 2D ferromagnet [14]. (c) DMI at the interface between a ferromagnetic metal (grey) and a metal with a strong SOC (blue) [15].

Another important consequence of SOC, and lack of spatial inversion symmetry, is the Dzyaloshinskii-Moriya interaction (DMI) [174, 175]. DMI is an antisymmetric magnetic exchange interaction that aligns the neighbouring spins orthogonally to each other, with a unique sense of rotation, instead of the parallel or antiparallel spin alignments obtained by the usual Heisenberg exchange interaction [176]. DMI is essential for creating non-collinear long-range spin order in ultra-thin magnetic films, and is responsible for the creation, stabilisation and manipulation of skyrmions and chiral domain walls as bearers of attractive applications in novel spintronic, memory and logic devices [15, 177]. As illustration, a schematic representation of the potential effects of DMI is shown in Figure 2-5. In Figure 2-5 (a), the chirality of domain walls in ultrathin ferromagnetic films that are in contact with normal metals is depicted. This is induced by the presence of spatial inversion asymmetry and the spin Hall effect [13]. Figure 2-5 (b) depicts a special magnetic texture named skyrmions. Skyrmions are originated from chiral Dzyaloshinskii–Moriya interactions [14, 15], either due to lack of inversion symmetry in lattices; or, by the breaking of inversion symmetry at the interface of magnetic films on metals (see Figure 2-5 (c)), e.g., Fe monolayers on Ir(111) [178]. Conversely, when symmetry is preserved, for instance in pristine magnetic 2D materials, the net DMI is zero, no matter the strong spin-orbit coupling on non-magnetic atoms. DMI can only arise in systems where

the spatial inversion symmetry is broken and hold a strong SOC. Hence, tuning the orbital and spin moment of a crystal, and spatial symmetry breaking, either by doping with transition metal, or any other method, is fundamental for inducing DMI. For instance, the magnetic anisotropy in a 2D material can be induced by doping with transition metals, among other ways of manipulating the SOC of a crystal [58, 59, 60, 61].

### 2.5.1 The four-state mapping methodology

In this thesis, the four-state energy mapping methodology (4SM) [179, 180] was used in order to obtain magnetic exchange interactions between two adsorbed metal atoms. In this scheme, Heisenberg spin Hamiltonian is considered in the form:

$$H = \sum_{i<j} \mathbf{S}_i \cdot \mathbf{J}_{ij} \cdot \mathbf{S}_j, \quad (2.108)$$

where  $\mathbf{S}_i = (S_i^x, S_i^y, S_i^z)$  is a vector; and  $\mathbf{J}_{ij}$  is a  $3 \times 3$  matrix describing the magnetic exchange interaction between two magnetic sites (i,j):

$$\mathbf{J}_{ij} = \begin{bmatrix} J_{ij}^{xx} & J_{ij}^{xy} & J_{ij}^{xz} \\ J_{ij}^{yx} & J_{ij}^{yy} & J_{ij}^{yz} \\ J_{ij}^{zx} & J_{ij}^{zy} & J_{ij}^{zz} \end{bmatrix} = \mathbf{J}_{ij}^{SE} + \mathbf{J}_{ij}^{AE}, \quad (2.109)$$

where  $\mathbf{J}_{ij}^{SE}$  and  $\mathbf{J}_{ij}^{AE}$  are the symmetric exchange matrix and anti-symmetric exchange matrix, respectively. They can be obtained by the following arrays:

$$\mathbf{J}_{ij}^{SE} = \begin{bmatrix} J_{ij}^{xx} & \frac{1}{2}(J_{ij}^{xy} + J_{ij}^{yx}) & \frac{1}{2}(J_{ij}^{xz} + J_{ij}^{zx}) \\ \frac{1}{2}(J_{ij}^{xy} + J_{ij}^{yx}) & J_{ij}^{yy} & \frac{1}{2}(J_{ij}^{yz} + J_{ij}^{zy}) \\ \frac{1}{2}(J_{ij}^{xz} + J_{ij}^{zx}) & \frac{1}{2}(J_{ij}^{yz} + J_{ij}^{zy}) & J_{ij}^{zz} \end{bmatrix}, \quad (2.110)$$

$$\mathbf{J}_{ij}^{AE} = \begin{bmatrix} 0 & D_{ij}^z & -D_{ij}^y \\ -D_{ij}^z & 0 & D_{ij}^x \\ D_{ij}^y & -D_{ij}^x & 0 \end{bmatrix}, \quad (2.111)$$

$\mathbf{D}_{ij}^x$ ,  $\mathbf{D}_{ij}^y$ , and  $\mathbf{D}_{ij}^z$ , represent the DMI components, and can be calculated from the

following equations:

$$\begin{aligned}\mathbf{D}_{ij}^x &= \frac{1}{2}(J_{ij}^{yz} - J_{ij}^{zy}), \\ \mathbf{D}_{ij}^y &= \frac{1}{2}(J_{ij}^{zx} - J_{ij}^{xz}), \\ \mathbf{D}_{ij}^z &= \frac{1}{2}(J_{ij}^{xy} - J_{ij}^{yx}).\end{aligned}\tag{2.112}$$

Therefore,  $\mathbf{J}_{ij}$  may be formally decomposed into 3 components: the diagonal part, i.e. the isotropic exchange; the antisymmetric component, also known as the Dzyaloshinskii–Moriya interaction (DMI), whose vector  $\mathbf{D}$  is made from off-diagonal elements of the antisymmetric exchange, and the off-diagonal elements of the isotropic exchange.

In order to determine the magnetic exchange interaction between two neighboring spins, all nine components of the exchange interaction matrix  $\mathbf{J}_{ij}$  must be calculated. Thus, replacing  $\mathbf{S}_i = (S_i^x, S_i^y, S_i^z)$  and  $\mathbf{S}_j = (S_j^x, S_j^y, S_j^z)$  in Equation 2.108, H can be written as follows:

$$\begin{aligned}H = \sum_{i<j} \mathbf{S}_i \cdot \mathbf{J}_{ij} \cdot \mathbf{S}_j &= \sum_{i<j} [\mathbf{S}_i^x \cdot \mathbf{J}_{ij}^{xx} \cdot \mathbf{S}_j^x + \mathbf{S}_i^x \cdot \mathbf{J}_{ij}^{xy} \cdot \mathbf{S}_j^y + \mathbf{S}_i^x \cdot \mathbf{J}_{ij}^{xz} \cdot \mathbf{S}_j^z \\ &\quad + \mathbf{S}_i^y \cdot \mathbf{J}_{ij}^{yx} \cdot \mathbf{S}_j^x + \mathbf{S}_i^y \cdot \mathbf{J}_{ij}^{yy} \cdot \mathbf{S}_j^y + \mathbf{S}_i^y \cdot \mathbf{J}_{ij}^{yz} \cdot \mathbf{D}_{ij}^z \\ &\quad + \mathbf{S}_i^z \cdot \mathbf{J}_{ij}^{zx} \cdot \mathbf{S}_j^x + \mathbf{S}_i^z \cdot \mathbf{J}_{ij}^{zy} \cdot \mathbf{S}_j^y + \mathbf{S}_i^z \cdot \mathbf{J}_{ij}^{zz} \cdot \mathbf{S}_j^z].\end{aligned}\tag{2.113}$$

Then, two spin sites, labeled  $i = 1$  and  $j = 2$ , are chosen. The Hamiltonian can be written as

$$H = \mathbf{S}_1 \cdot \mathbf{J}_{12} \cdot \mathbf{S}_2 + \sum_{j \neq 2} \mathbf{S}_1 \cdot \mathbf{J}_{1j} \cdot \mathbf{S}_j + \sum_{i \neq 1} \mathbf{S}_i \cdot \mathbf{J}_{i2} \cdot \mathbf{S}_2 + \sum_{i \neq 1, j \neq 2} \mathbf{S}_i \cdot \mathbf{J}_{ij} \cdot \mathbf{S}_j.\tag{2.114}$$

If we now introduce  $\alpha$  and  $\beta = x, y, z$ ; H can be written into cartesian components as

$$\begin{aligned}
H = & \sum_{\alpha,\beta} \mathbf{S}_1^\alpha \cdot \mathbf{J}_{12}^{\alpha\beta} \cdot \mathbf{S}_2^\beta + \sum_{j \neq 2} \sum_{\alpha,\beta} \mathbf{S}_1^\alpha \cdot \mathbf{J}_{1j}^{\alpha\beta} \cdot \mathbf{S}_j^\beta \\
& + \sum_{i \neq 1} \sum_{\alpha,\beta} \mathbf{S}_i^\alpha \cdot \mathbf{J}_{i2}^{\alpha\beta} \cdot \mathbf{S}_2^\beta + \sum_{i \neq 1, j \neq 2} \sum_{\alpha,\beta} \mathbf{S}_i^\alpha \cdot \mathbf{J}_{ij}^{\alpha\beta} \cdot \mathbf{S}_j^\beta. \quad (2.115)
\end{aligned}$$

Now, a practical example of application of Equation 2.115 will be given. As illustration, the parameter  $J_{12}^{xy}$  will be calculated ( $\alpha=x$ , and  $\beta=y$ ); all other elements can be determined in the same manner

In order to isolate  $J_{12}^{xy}$ , the energies of four different magnetic configurations for the spin states need to be obtained in (x,y):  $E_1$ ,  $E_2$ ,  $E_3$ , and  $E_4$ , with the following criteria:

**Configuration 1:**  $\mathbf{S}_i = (+S, 0, 0)$        $\mathbf{S}_j = (0, +S, 0)$ ,

**Configuration 2:**  $\mathbf{S}_i = (-S, 0, 0)$        $\mathbf{S}_j = (0, +S, 0)$ ,

**Configuration 3:**  $\mathbf{S}_i = (+S, 0, 0)$        $\mathbf{S}_j = (0, -S, 0)$ ,

**Configuration 4:**  $\mathbf{S}_i = (-S, 0, 0)$        $\mathbf{S}_j = (0, 0, -S)$ ,

and for all the rest,  $\mathbf{S}_{i \neq 1,2} = (0, 0, +S)$  or  $\mathbf{S}_{i \neq 1,2} = (0, 0, -S)$  for all four states.

The four energies for each configuration will be:

$$E_1 = \mathbf{S} \cdot \mathbf{J}_{12}^{xy} \cdot \mathbf{S} + \sum_{j \neq 2} \mathbf{S} \cdot \mathbf{J}_{1j}^{xz} \cdot \mathbf{S}_j + \sum_{i \neq 1} \mathbf{S} \cdot \mathbf{J}_{i2}^{zy} \cdot \mathbf{S}_2 + \sum_{i \neq 1, j \neq 2} \mathbf{S} \cdot \mathbf{J}_{ij}^{zz} \cdot \mathbf{S}, \quad (2.116)$$

$$E_2 = -\mathbf{S} \cdot \mathbf{J}_{12}^{xy} \cdot \mathbf{S} - \sum_{j \neq 2} \mathbf{S} \cdot \mathbf{J}_{1j}^{xz} \cdot \mathbf{S}_j + \sum_{i \neq 1} \mathbf{S} \cdot \mathbf{J}_{i2}^{zy} \cdot \mathbf{S}_2 + \sum_{i \neq 1, j \neq 2} \mathbf{S} \cdot \mathbf{J}_{ij}^{zz} \cdot \mathbf{S}, \quad (2.117)$$

$$E_3 = -\mathbf{S} \cdot \mathbf{J}_{12}^{xy} \cdot \mathbf{S} + \sum_{j \neq 2} \mathbf{S} \cdot \mathbf{J}_{1j}^{xz} \cdot \mathbf{S}_j - \sum_{i \neq 1} \mathbf{S} \cdot \mathbf{J}_{i2}^{zy} \cdot \mathbf{S}_2 + \sum_{i \neq 1, j \neq 2} \mathbf{S} \cdot \mathbf{J}_{ij}^{zz} \cdot \mathbf{S}, \quad (2.118)$$

$$E_4 = \mathbf{S} \cdot \mathbf{J}_{12}^{xy} \cdot \mathbf{S} - \sum_{j \neq 2} \mathbf{S} \cdot \mathbf{J}_{1j}^{xz} \cdot \mathbf{S}_j - \sum_{i \neq 1} \mathbf{S} \cdot \mathbf{J}_{i2}^{zy} \cdot \mathbf{S}_2 + \sum_{i \neq 1, j \neq 2} \mathbf{S} \cdot \mathbf{J}_{ij}^{zz} \cdot \mathbf{S}. \quad (2.119)$$

As we are interested in determining the value of  $J_{12}^{xy}$ , if we choose the following arrangement for the energies obtained from equation Equation 2.116 to Equation 2.119

:  $(E_1 + E_4) - (E_2 + E_3)$ , we obtain  $4S^2 \cdot J_{12}^{xy}$ ; it means,

$$(E_1 + E_4) - (E_2 + E_3) = 4S^2 \cdot J_{12}^{xy}, \quad (2.120)$$

$$J_{12}^{xy} = \frac{(E_1 + E_4) - (E_2 + E_3)}{4S^2}. \quad (2.121)$$

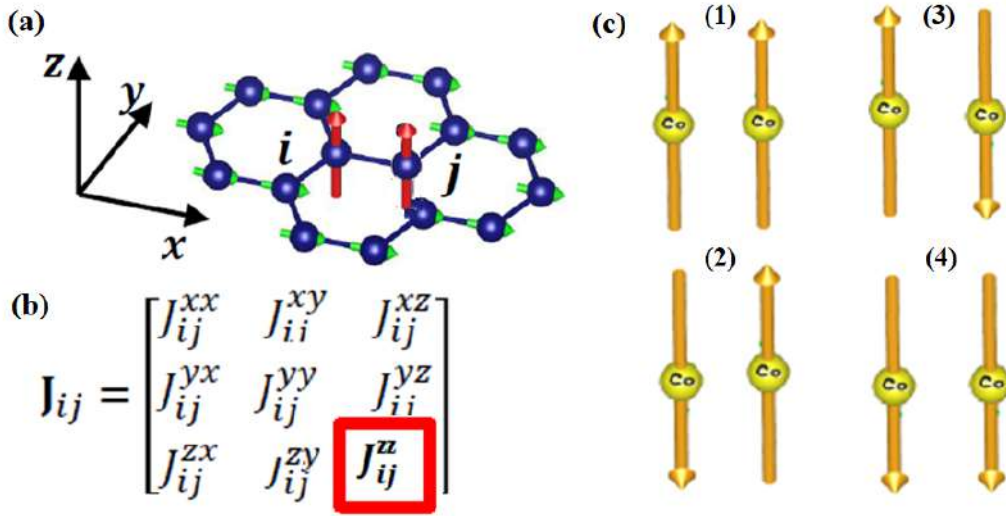


Figure 2-6: (a) Side view of interacting TM atoms on 2D-monolayer located at the nearest side ( $i, j$ ) for  $J_{ij}^{zz}$  magnetic interaction. (b)  $\mathbf{J}_{ij}$  is a  $3 \times 3$  matrix describing the magnetic exchange interaction between two magnetic sites ( $i, j$ ). (c) Four spin configurations for calculating the  $J_{ij}^{zz}$  component of exchange interaction matrix.

As illustration, see Figure 2-6, if we are interested in obtain one of the exchange interaction vector, in this case  $\mathbf{J}_{ij}^{zz}$  component of exchange interaction matrix, we need to consider 4 configurations for S vector:

- (1)  $\mathbf{S}_i = (0, 0, +S)$        $\mathbf{S}_j = (0, 0, +S)$ ,
- (2)  $\mathbf{S}_i = (0, 0, -S)$        $\mathbf{S}_j = (0, 0, +S)$ ,
- (3)  $\mathbf{S}_i = (0, 0, +S)$        $\mathbf{S}_j = (0, 0, -S)$ ,
- (4)  $\mathbf{S}_i = (0, 0, -S)$        $\mathbf{S}_j = (0, 0, -S)$ .

Where  $\mathbf{J}_{ij}^{zz}$  can be obtained from the following equation:

$$\mathbf{J}_{ij}^{zz} = \frac{((E_1 + E_4) - (E_2 + E_3))}{4S^2}. \quad (2.122)$$

The energies  $E_1$ ,  $E_2$ ,  $E_3$ , and  $E_4$ , are obtained from calculations for configurations (1), (2), (3) and (4), respectively.

The magnetocrystalline anisotropy energy (MAE) of TM on 551–GaAs was calculated using the following expression

$$MAE = E_{\parallel} - E_{\perp}, \quad (2.123)$$

where  $E_{\parallel}$  and  $E_{\perp}$  are the total energies for the in-plane and out of-plane magnetization directions with respect to the surface of the 2D crystal, respectively [61].

**In chapter 6**, we investigate the physical effect of spin-orbit coupling on both magnetic anisotropy and Dzyaloshinskii-Moriya interaction for two-dimensional gallium arsenide when single and pair TM are absorbed (TM: Mn, Co, Mo and Os).

## Chapter 3

# Structural, mechanical and electronic properties of two-dimensional structure of III-arsenide (111) binary compounds: An *ab-initio* study

*Structural, mechanical and electronic properties of two-dimensional single-layer hexagonal structures in the (111) crystal plane of IIIAs-ZnS systems (III=B, Ga and In) are studied by first-principles calculations based on density functional theory (DFT). Elastic and phonon dispersion relation display that 2D h-IIIAs systems (III=B, Ga and In) are both mechanical and dynamically stable. Electronic structures analysis show that the semiconducting nature of the 3D-IIIAs compounds is retained by their 2D single layer counterpart. Furthermore, density of states reveals the influence of  $\sigma$  and  $\pi$  bonding in the most stable geometry (planar or buckled) for 2D h-IIIAs systems. Calculations of elastic constants show that the Young's modulus, bulk modulus and shear modulus decrease for 2D h-IIIAs binary compounds as we move down on the group of elements of the periodic table. In addition, as the bond length between the neighboring cation-anion atoms increases, the 2D h-IIIAs binary compounds display less stiffness and more plasticity. Our findings can be used to understand the contribution of the  $\sigma$  and  $\pi$  bonding in the most stable geometry (planar or buckled)*

for 2D h-IIIs systems. Structural and electronic properties of h-IIIs systems as a function of the number of layers have been also studied. It is shown that h-BAs keeps its planar geometry while both h-GAs and h-InAs retained their buckled ones obtained by their single layers. Bilayer h-IIIs present the same bandgap nature of their counterpart in 3D. As the number of layers increase from 2 to 4, the bandgap width for layered h-IIIs decreases until they become semimetal or metal. Interestingly, these results are different to those found for layered h-GaN. The results presented in this study for single and few-layer h-IIIs structures could give some physical insights for further theoretical and experimental studies of 2D h-IIIV-like systems.

### 3.1 Introduction

Technology based on semiconductor devices plays a transcendental role in our modern society. Since Scientists, such as Shockley, Brattain and Bardeen, Nobel Prize in physics in 1956, invented the transistor [105, 106], a large effort has been devoted by the manufacturing industry to develop new semiconductor materials with enhanced electronic features. Therefore, the challenge has been not only to reduce the size and price of these electronic devices but also to increase their performance to obtain characteristics such as high speed and low power dissipation. Since 2004, when graphene was isolated by exfoliation from graphite [16], much attention has been given by the scientific community to find and characterize new two-dimensional (2D) materials both theoretically and experimentally. In 2010 Andre Geim and Konstantin Novoselov were awarded the Physics Nobel Prize for this transcendental discovery. The remarkable electronic and mechanical properties of these materials such as, electron mobility, covalently in-plane bonded structures, weak out-of-plane interactions and high mechanical strength make them attractive materials with potential industrial applications [4]. Even though graphene exhibits interesting physical properties such as high charge carrier mobility, high thermal conductivity, infrared optical adsorption and total impermeability to any gas [46], which makes it desirable for technological applications, the absence of bandgap limits its use in the manufacture

of electronic devices [8]. This bandgap limitation has motivated Scientists to look for new 2D-materials beyond it [47]. *Ab-initio* calculations predicted graphene to be a wide bandgap material when doped with H and F [98]. Among the literature about the study of 2D-materials beyond graphene, we find X-enes (X=B, Si, Ge, Sn, P, Bi), X-anes (graphane, silicane, germanane, stanane) [48], and fluorinated X-enes. In the X-ene systems, the atoms are arranged in a honeycomb structure similar to graphene [48, 51, 52, 53, 54, 55, 56, 57]. When hydrogen or fluor is added to the X-ene system, the new configuration is labeled as X-ane (graphane, silicane, germanane, stanane) [48], and fluorinated X-enes (fluro-X-enes or X-enes fluoride), respectively [48].

The electronic properties of group III-V semiconductors such as BAs, AlAs GaAs and InAs, have been widely studied in the bulk both theoretically and experimentally due to their applications in electronic devices [115, 116, 117, 118, 119, 120, 121]. All of them are semiconductors that crystallize in the zinc-blende structure ( $F\bar{4}3m$  space group) at ambient conditions [116]. BAs and AlAs have an indirect bandgap of 0.67 ( $\Gamma-\Delta_{min}$ ) [117, 118] and 2.24 eV ( $\Gamma-X$ ) [119], respectively. While GaAs and InAs have a direct band gap of 1.42 [120] and 0.42 eV [119], respectively, both at the  $\Gamma$  point. The fact that zinc-blende III-As structures both display a hexagonal structure in the (111) surface and exhibit melting point above 1000°C make them potential candidates to be stable in their 2D hexagonal structure counterpart [7]. H. Sahin *et al* [123] determined that two-dimensional graphene-like structure of group III-As (BAs, GaAs and InAs) are stable semiconductors using first-principles. 2D materials have been studied for their remarkable electronic properties suitable for the electronic industry, so a thorough and comprehensive study on their mechanical properties will give the physical knowledge for potential applications in engineering science [181]. Mechanical properties of 2D graphene-like materials have been researched by first principles calculations [181]. Rita *et al* [181] reported the mechanical properties of two dimensional group IV graphene-like structures by using density functional theory. 2D-heterostructures [7, 49, 50] have attracted the attention to tune the bandgap width of semiconductors which makes them promising candidates for the manufacture of solar cells due to the complete adsorption of light

by successive layers [8, 76, 77]. It has been found that 2D *h*-III V materials can improve the optoelectronic properties of heterostructures based on graphene [8]. In addition, III-V hexagonal structures have been reported suitable as substrates for two dimensional materials such as graphene, MoS<sub>2</sub> and GaN based devices [127, 128]. C. R. Dean *et al* [127] reported the fabrication and characterization of high-quality exfoliated mono- and bilayer graphene devices on single-crystal *h*-BN substrates, by using a mechanical transfer process. Experimental or theoretical studies of 2D III-V (111)-binary compounds are scarce. Even though there is theoretical research on the electronic properties of two-dimensional III-As (BAs, GaAs and InAs) graphene-like structures [123], authors did not take into account *d* orbitals of Ga, In and As atoms. It is important to know the physical interactions of *p-d* orbitals in order to understand the magnetic nature when these 2D III-As systems are doped with metal transition impurities. They also used Local Density Approximation (LDA) to study these *d* depending systems. It is well known that LDA approach can not describe well strongly correlated systems. Therefore, in this research, we first examine the structural, mechanical and electronic properties of 2D single-layer *h*-IIIAs systems and subsequently we study the structural and electronic properties of few-layer *h*-IIIAs structures taking into account the *d* orbitals of Ga, In and As atoms. In addition, we used the Generalized Gradient Approximation (GGA) as described by Perdew *et al.* [142] for the exchange and correlation potentials, which is found to correct most of the overbinding problems of LDA. It can be expected that the present work will bring new theoretical insights to the research of 2D *h*-IIIAs materials for electronic applications.

## 3.2 Computational methods

The calculations were performed using the first principles pseudo-potential method in the framework of density-functional theory. Exchange and correlation effects were treated with generalized gradient approximation (GGA) implemented in the Perdew-Burke-Ernzerhof functional (PBE) [142]. The core electrons were described by the projector augmented wave (PAW) method [151, 182] wherein the *d* states for Ga, In

and As were included as valence electrons. The valence electron configurations for B, Ga, In and As are  $2s^22p^1$ ,  $3d^{10}4s^24p^1$ ,  $4d^{10}5s^25p^1$  and  $3d^{10}4s^24p^3$ , respectively. The calculations were performed using *Vienna Ab-initio Simulation Package* (VASP) [152, 153]. The electron wave function was expanded in plane waves up to a cutoff energy of 500 eV for the structural and phonon calculations. A gamma-centered grid of  $25 \times 25 \times 1$   $k$ -point has been used to sample the irreducible Brillouin zone in the Monkhorst-Pack special scheme [146] for all calculations. Methfessel-Paxton smearing technique with a smearing width of 0.10 eV was adopted [149]. These parameters ensure a convergence better than 1 meV for the total energy. The hexagonal primitive cell, with one III-group atom (B, Ga or In) and one As atom, was constructed from the zinc-blende structure in the (111) plane, as illustrated in Figure 3-1. Phonon calculations have been performed by taking into account the interactions in  $7 \times 7 \times 1$  supercells consisting of 49 III-group atoms (B, Ga or In) and 49 As atoms. In addition, a 20 Å vacuum spacing between the adjacent supercells is kept to avoid interactions. Stress-based approach is implemented [183, 184] to study the mechanical properties. The elastic tensor is determined by performing finite distortions of the optimized lattice and deriving the elastic constants from the strain-stress relationship (Hooke's law) [183, 184]. The plane wave cutoff needs to be sufficiently large to converge the stress tensor. Thus, to find the elastic constants, the electron wave function was gradually expanded in plane waves up to a cutoff energy of 950 eV. It is well known that the exchange-correlation energy of PBE underestimates the energy gap in semiconductors [185]. Therefore, to correct the band-gap values obtained by GGA, hybrid functional Heyd-Scuseria-Ernzerhof (HSE) calculations are carried out [143].

The elastic constants for 2D  $h$ -IIIAs structures are taken from a 3D hexagonal structure. For a 3D hexagonal structure, five independent elastic constants  $C_{ij}$  are found. In Voigt notation they are:  $C_{11}$ ,  $C_{12}$ ,  $C_{13}$ ,  $C_{33}$ , and  $C_{44}$ . A 3D hexagonal structure is mechanically stable if it satisfies the Born stability criteria [186], which are given as  $C_{11} > 0$ ,  $C_{11} - C_{12} > 0$ ,  $C_{44} > 0$ ,  $(C_{11} + C_{12}) C_{33} - 2C_{13}^2 > 0$  and  $C_{66} = (C_{11} - C_{12}) / 2$ . For a 2D hexagonal structure, there are four independent elastic constants:  $C_{11}$ ,  $C_{12}$ ,  $C_{22}$  and  $C_{66}$ . For a 2D hexagonal structure the  $C_{13}$ ,  $C_{33}$  and  $C_{44}$  elastic

constants can be ignored for the following physical reasons.  $C_{33}$ , due to the interaction minimization along the z axis, which must be almost zero.  $C_{13}$  and  $C_{44}$  are also very small due to in a perfect 2D structure both elastic constants appear to fail the Born stability criteria [181]. Therefore, in the stress-strain relation for a 2D hexagonal structure only two independent elastic constants  $C_{11}$ ,  $C_{12}$  are considered. Therefore, Hooke's law ( $\sigma_i = C_{ij} \epsilon_j$ , where  $\sigma_i$  and  $\epsilon_j$ , i and j are integers, represent the stress and strain, respectively) for 2D hexagonal materials can be expressed in the following matrix form [187]:

$$\begin{bmatrix} \sigma_1 \\ \sigma_2 \\ \sigma_3 \end{bmatrix} = \begin{bmatrix} c_{11} & c_{12} & 0 \\ c_{12} & c_{11} & 0 \\ 0 & 0 & \frac{c_{11}-c_{12}}{2} \end{bmatrix} \begin{bmatrix} \epsilon_1 \\ \epsilon_2 \\ \epsilon_3 \end{bmatrix}. \quad (3.1)$$

The bulk  $B_V$  and shear  $G_V$  moduli [188], in terms of the Voigt approximation, the in-plane Young's modulus  $Y_s$  and Poison's ratio  $\nu$  [189] are obtained, respectively, from the calculated elastic constants as:

$$\begin{aligned} B_V &= (2(C_{11} + C_{12}) + 4C_{13} + C_{33})/9, \\ G_V &= (C_{11} + C_{12} + 2C_{33} - 4C_{13} + 12C_{44} + 12C_{66})/30, \\ Y_s &= (C_{11}^2 - C_{12}^2)/C_{11}, \\ \nu &= C_{12}/C_{11}. \end{aligned} \quad (3.2)$$

## 3.3 Results and discussion

### 3.3.1 Structural Properties and phonon dynamical stability

The hexagonal primitive cells, with one III-group atom (B, Ga or In) and one As atom, were constructed from the zinc-blende structure in the (111) plane, as shown in Figure 3-1. They present a threefold rotation symmetry  $C_3$ . The ideal lattice parameter ( $a_{ideal} = \sqrt{2}/2 a_{exp-3D}$  (Å) [190] for 2D *h*-BAs, GaAs and InAs (hexagonal primitive cell) are, respectively, 3.38, 4.00 and 4.27 Å. As shown in Table 3.1, the calculated lattice constant  $a$  for 2D BAs, GaAs and InAs hexagonal structures are, respectively, slightly larger than the ideal values: 3.38, 4.05 and 4.36 Å. In

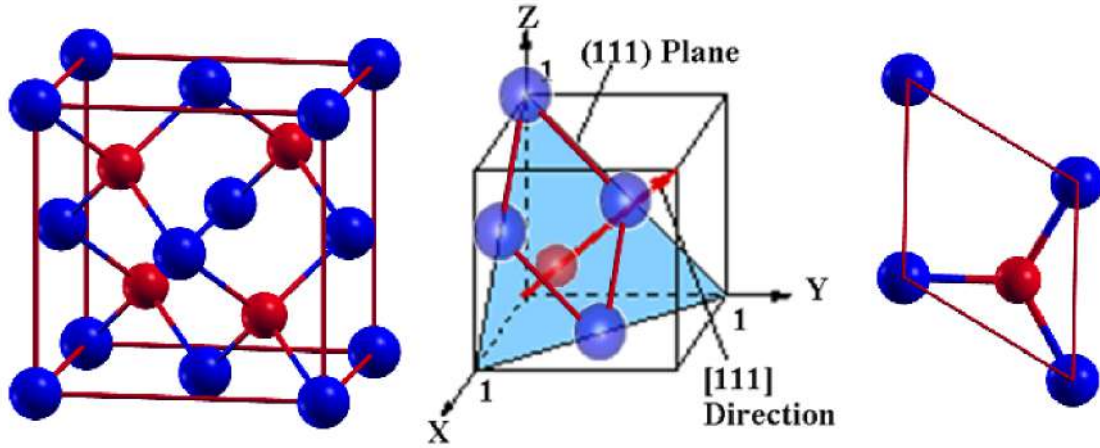


Figure 3-1: The hexagonal primitive cell (right figure), with one B, Ga or In atom (blue color) and one As atom (red color), was constructed from the zinc-blende structure (left figure) in the (111) plane. The hexagonal unit cell is also highlighted with a red line in the (111) plane in the middle figure.

Table 3.1, we also present the cohesive energy ( $E_{Coh}$  (eV)) for 2D BAs, GaAs and InAs hexagonal structures. H. Sahin *et al* [123] studied the structural properties of 2D graphene-like structure of group III-As (BAs, GaAs and InAs) by local density approximation (LDA).

Table 3.1: Calculated lattice constant ( $a$  (Å)), ideal lattice constant ( $a_{ideal} = \sqrt{2}/2 a_{exp-3D}$  (Å)), angle between neighboring bonds ( $\theta$ ), Planar (PL) or Low-Buckled (LB) geometry (G), buckling parameter ( $\Delta$  (Å)), nearest-neighbor distance ( $d$ ), interlayer distance ( $d_L$ ), cohesive energy ( $E_{Coh}$  (eV)), bandgap value ( $E_G$ ), effective charge cation/anion ( $Z_c/Z_a$ ), Poisson's ratio ( $\nu$ ); Young's ( $Y_s$ ), Bulk ( $B_v$ ) and Shear ( $G_v$ ) modules for 2D BAs, GaAs and InAs binary compounds.

	$a$ (Å)	$a_{ideal}$ (Å) $(\sqrt{2}/2)a_c$	$\theta$ (°)	G	$\Delta$ (Å)	$d$ (Å)	$E_{Coh}$ (eV)	$E_G$ (eV) (Exp-3D)	$E_G$ (eV) (GGA)	$E_G$ (eV) (HSE)	$Z_c/Z_a$	$\nu$	$Y_s$ (J/m <sup>2</sup> )	$B_v$ (J/m <sup>2</sup> )	$G_v$ (J/m <sup>2</sup> )
BAs	3.38	3.38 [115]	120.00	PL	0.00	1.95	10.70	0.67 $\Gamma\Delta_{min}$	0.76 $KK$	1.15 $KK$	2.70/15.30	0.27	117.09	35.66	23.77
[123]	3.35	-	120.00	PL	0.00	1.93	11.00	-	0.71 $KK$	-	-	0.29	119.0	-	-
GaAs	4.05	4.00 [115]	114.30	LB	0.55	2.41	7.42	1.42 $\Gamma\Gamma$	1.08 $\Gamma K$	1.87 $\Gamma K$	12.40/15.60	0.32	44.38	14.54	8.90
[123]	3.97	-	114.7	LB	0.55	2.38	8.48	-	1.29 $\Gamma K$	-	-	0.35	48.0	-	-
InAs	4.36	4.27 [115]	114.10	LB	0.65	2.60	6.86	0.42 $\Gamma\Gamma$	0.79 $\Gamma\Gamma$	1.46 $\Gamma\Gamma$	12.40/15.60	0.41	29.24	9.36	4.83
[123]	4.28	-	113.80	LB	0.62	2.55	7.85	-	0.86 $\Gamma\Gamma$	-	-	0.43	33.00	-	-

Our results with generalized gradient approximation (GGA) overestimate (underestimate) their reported lattice constant (cohesive energy) values. These results confirm that the GGA approach tends to overestimate (underestimate) the lattice constant (cohesive energy) values. The 2D structures of both  $h$ -GaAs and  $h$ -InAs exhibit buckling distortions while  $h$ -BAs presents a 2D planar one. This is due to the fact that the  $\pi$  bonds in 2D  $h$ -GaAs and  $h$ -InAs are weaker than their counterpart in 2D  $h$ -BAs [191]. The buckling parameter for 2D  $h$ -GaAs is lower than that of

$h$ -InAs. Furthermore, the bond length between the neighboring cation-anion atoms increases from 2D  $h$ -BAs to InAs in the present study, as shown in Table 3.1. On the contrary, the angle between neighboring bonds and the cohesive energy decreases. The planar atoms belong to sublattice 1 while the buckled atoms to sublattice 2. The above mentioned results follow the same qualitative trend as those reported by H. Sahin *et al* [123].

Regarding the stability of 2D single layer of group III-V with large ionicity, there are theoretical [123, 124] and experimental [102] studies that have predicted and validated it. H. Sahin *et al.* predicted the stability of III-As and III-N binary compounds by first-principles calculations. Z. Y. Al Balushi *et al.* reported the synthesis of 2D gallium nitride (GaN) by experimental technique utilizing epitaxial graphene. The calculated phonon dispersion curves for 2D BAs, GaAs and InAs semiconductors in the hexagonal primitive cell with GGA scheme are shown in Figure 3-2. We can see that the planar structure 2D  $h$ -BAs and the low buckled 2D  $h$ -GaAs and InAs can be stable, because all frequencies of the phonon dispersion are real. It means, there are no soft modes and, as consequence, there is no sign of any dynamical instability, in agreement with the theoretical result from the LDA approach, with the difference that those authors did not take into account the  $d$  orbitals of As, Ga and In atoms, while we did this in our research [123].

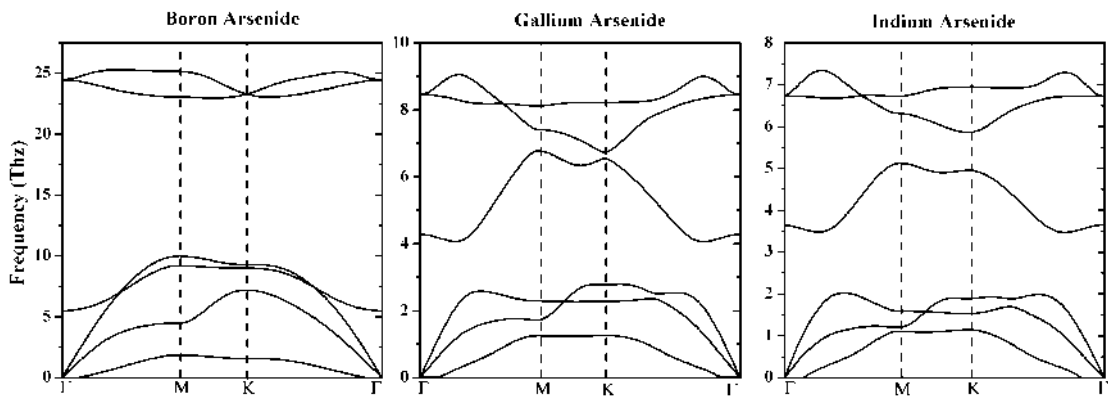


Figure 3-2: Phonon dispersion curves for 2D BAs, GaAs and InAs semiconductors in the hexagonal primitive cell with GGA scheme.

There are six phonon dispersion bands because the unit cell of 2D  $h$ -III-As contains two atoms, A (cation) and B (anion). The three vibrational branches, which

are zero at the  $\Gamma$  point, correspond to the acoustic modes (A). The other three frequency values correspond to the optical modes (O). If the vibrations of cation-anion atoms are parallel or perpendicular, the phonon modes are classified as longitudinal (L) or transversal (T). From downward to upward modes, listed in order of increasing energy, they can be classified as: out-of plane mode (ZA), in-plane transversal mode (iT<sub>A</sub>) and in-plane longitudinal mode (iL<sub>A</sub>) for the acoustic modes. The (ZA) mode shows a  $q^2$  energy dispersion relation near to the  $\Gamma$  point and the other two (iT<sub>A</sub> and iL<sub>A</sub>), a  $q$  linear dependence. The remaining three branches correspond to optical modes, out-of plane mode (ZO), in-plane transversal mode (iT<sub>O</sub>) and in-plane longitudinal mode (iL<sub>O</sub>). When comparing the phonon dispersions of BAs, GaAs and InAs systems, it is seen from Figure 3-2 that the ZO mode falls in the frequency range of acoustical vibration modes. It is also noted that the value of the high frequency mode is decreasing with increasing both atomic mass and nearest neighbor distance.

### 3.3.2 Electronic and mechanical properties

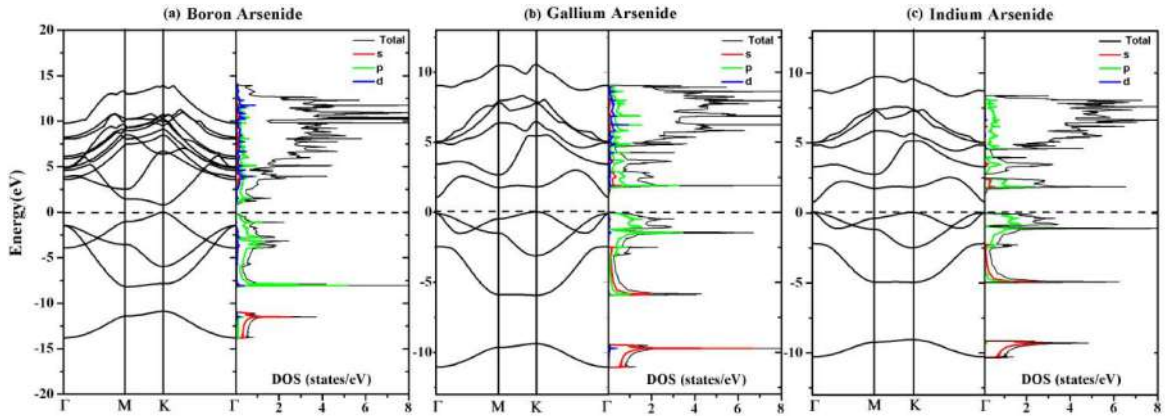


Figure 3-3: The band structures and the majority density of states for 2D BAs, GaAs and InAs semiconductors in the hexagonal primitive cell with GGA scheme. The dashed line indicates the Fermi level, which is taken to be zero.

Regarding the electronic properties, the semiconducting nature of the 3D-IIIs compounds is retained by their 2D counterpart, as illustrated in Figure 3-3 and Figure 3-4, and Table 3.1. 3D-BAs (3D-GaAs) has an  $\Gamma$ - $\Delta_{min}$  indirect ( $\Gamma$ - $\Gamma$  direct) experimental bandgap of 0.67 (1.42) eV [117, 118]. In our results, 2D *h*-BAs (*h*-

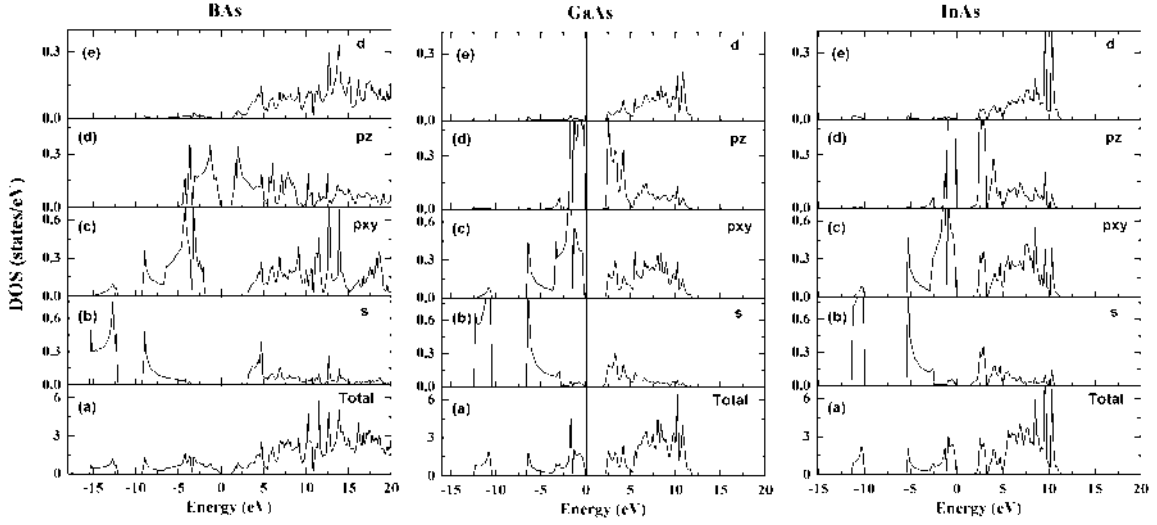


Figure 3-4: The majority density of states for 2D BAS, GaAs and InAs semiconductors in the hexagonal primitive cell with GGA-HSE approach. The dashed line indicates the Fermi level, which is taken to be zero.

GaAs) changes to a  $K$ - $K$  direct ( $\Gamma$ - $K$  indirect) bandgap of 0.76 (1.08) eV. On the other hand, the  $\Gamma$ - $\Gamma$  direct semiconducting nature of 3D-InAs (0.42 eV) is retained for its 2D counterpart (1.46 eV). As shown in Table 3.1, the corrected bandgap values for 2D  $h$ -BAS, GaAs and BAS with HSE method are higher than those ones for 3D BAS, GaAs and InAs, by 71.6, 31.7 and 247.6 % respectively. Figure 3-3 displays the electronic band structure and the density of states (DOS) along the high symmetry directions  $\Gamma$ ,  $M$ ,  $K$ ,  $\Gamma$ , in the first Brillouin zone for 2D  $h$ -BAS, GaAs and InAs, respectively. We can see in Figure 3-1(a), unhybridized  $p_z$  orbitals near the Fermi level both in the valence bands, from 0 to -1.8 eV ( $\pi$  orbitals), and in the conduction bands, from 0.8 to 2.4 eV ( $\pi^*$  orbitals). From -1.8 to -8.0 eV, some  $s$ ,  $p$  and  $d$  mixed orbitals are shown, with a major contribution of the  $p$  orbital. In the valence bands of the partial density of states, from -11.2 to -13.2 eV, localized  $s$  orbital are present. Therefore, the  $s$ ,  $p_x$  and  $p_y$  orbitals in the valence bands do not contribute to the electronic properties. In the partial density of states of the conduction bands, from 2.5 to 14.0 eV,  $s$ ,  $p$  and  $d$  mixed unoccupied orbitals are shown. These correspond to a mixture of  $\pi^*$ ,  $\sigma^*$  and  $d$  states. Contrary to what is observed in Figure 3-3(a) (BAS), Figure 3-3(b) (GaAs) and Figure 3-3(c) (InAs) display  $s$  and  $p$  mixed orbitals near the Fermi level both in the valence and in the

conduction bands. Buckling reduces (increases) the overlap between  $p_z$  ( $p_z$  and planar  $s$ ) orbitals. As a result, the  $sp^2$  hybridization becomes weaker, while the  $sp^3$  hybridization is stronger. Therefore, as the ionic radius increases, the free nature of  $p_z$  orbitals is reduced, increasing the effective mass. It is also noted from [Figure 3-3\(a\)](#), [Figure 3-3\(b\)](#) and [Figure 3-3\(c\)](#) that the energy along the  $\Gamma$  direction decreases (increases) in conduction (valence) bands as the ionic radius increases. This makes the states be more localized and, in turn, their peaks increases. Qualitative similar results were found by R. John *et al.* for two dimensional materials of IV-group by first principles study [181]. [Figure 3-4](#) depicts the majority density of states for 2D BAs, GaAs and InAs semiconductors in the hexagonal primitive cell with GGA-HSE approach. We can see a qualitative similar behavior for the  $p_z$ ,  $p_{xy}$ ,  $s$  and  $d$  orbitals as the ones displayed for the DOS in [Figure 3-3](#) with GGA approach. The main difference is the band-gap value, which is bigger for GGA-HSE approach. [Table 3.1](#) shows the band-gap values for 2D  $h$ -BAs, GaAs and InAs with both GGA and GGA-HSE schemes. An increase of 51.32, 73.15 and 86.10 % is observed for the bandgap values of 2D  $h$ -BAs, GaAs and InAs, respectively, with GGA-HSE scheme when compared to their counterpart with GGA. To date, we could not find any experimental data relating the structural and electronic properties for 2D single-layer  $h$ -IIIs. Therefore, in order to evaluate the accuracy of our research methodology, we have found both the lattice constants and bandgap size for 2D single-layer  $h$ -BN, which belongs to the group III-V, with GGA and GGA-HSE, and compared them with their experimental values. Our calculated lattice constant  $a$  and the obtained bandgap size with GGA (HSE) are 2.51 Å (2.49 Å) and  $K$ - $K$  direct 4.55 eV (5.65 eV), respectively. Their experimental values are 2.50 Å [192] and 5.97 eV [193], respectively. Hence, GGA (HSE) overestimates (underestimates) the lattice constant by  $\sim 0.4$  % and underestimates the bandgap size by  $\sim 24$  % ( $\sim 5$  %). Therefore, GGA-HSE functional improves the bandgap size by  $\sim 24$  % when compared to GGA approach. Sahin *et al* [123] reported a bandgap size for 2D  $h$ -BN of 4.61 eV (6.57 eV) by LDA ( $GW_0$ ) approach, which underestimates (overestimates) the experimental bandgap by  $\sim 23$  % ( $\sim 10$  %). Our bandgap size result for 2D  $h$ -BN with GGA-HSE is close to the experimental value.

In [Table 3.1](#) we can also find the ratio between the charge on cation and anion ( $Z_c/Z_a$ ) in order to see the charge transferred from cation to anion. This charge transfer was calculated using the Bader analysis [[194](#), [195](#), [196](#)] where we included the  $d$  orbitals of Ga, In and As. Physically, it gives insight about the direction of charge transfer and ionicity of the 2D  $h$ -III-V systems. We can see that the charge transfer increases with increasing row number, which means that ionicity increases as the atomic radii of cation increases. On the other hand, our elastic constant results satisfy the Born stability criteria [[186](#)] for mechanically stable 2D hexagonal crystals mentioned in [section 3.2](#). The calculated elastic moduli are tabulated in [Table 3.1](#). It is shown that the Young's modulus, bulk modulus and shear modulus decrease for 2D  $h$ -IIIs binary compounds as we move down on the group of elements of the periodic table. It is found that  $h$ -BAs is  $\sim 250\%$  ( $\sim 400\%$ ) times stiffer along the in-plane direction than  $h$ -GaAs ( $h$ -InAs). This can be explained by bonding features. Bond length is inversely proportional to the bond strength. On the contrary, we find that the Poisson's ratio increases with increasing row number of elements. It means, as we move down on the group of elements, the 2D  $h$ -IIIs binary compounds display less stiffness and more plasticity.

In order to study the physical effect of including  $vdW$  correction on the mechanical properties of 2D single-layer  $h$ -IIIs, we calculated their elastic constants taking into consideration the  $vdW$  interaction. When including  $vdW$ , the Young's modulus, bulk modulus, and shear modulus for BAs and GaAs (InAs) overestimate those ones without  $vdW$  interaction by 3.6 % and 2.5 % (4.50 %), 3.8 % and 8.4 % (21.9 %), 3.5 % and 11.4 % (7.1 %), respectively.

### 3.3.3 Few-layer $h$ -IIIs structures

In order to study how the structural and electronic properties of  $h$ -IIIs evolve with increasing number of layers, we first determine the optimal stacking sequence from five possible stacking types for  $h$ -BAs,  $h$ -GaAs and  $h$ -InAs bilayer ( $b$ -IIIs), as shown in [Figure 3-5](#). For AA (AB) stacking, the cation (anion) is placed above the cation, and the anion (cation) above the anion in the adjacent plane; for AC (AD) stacking, the cations (anions) are atop each other while anions (cations) are inside

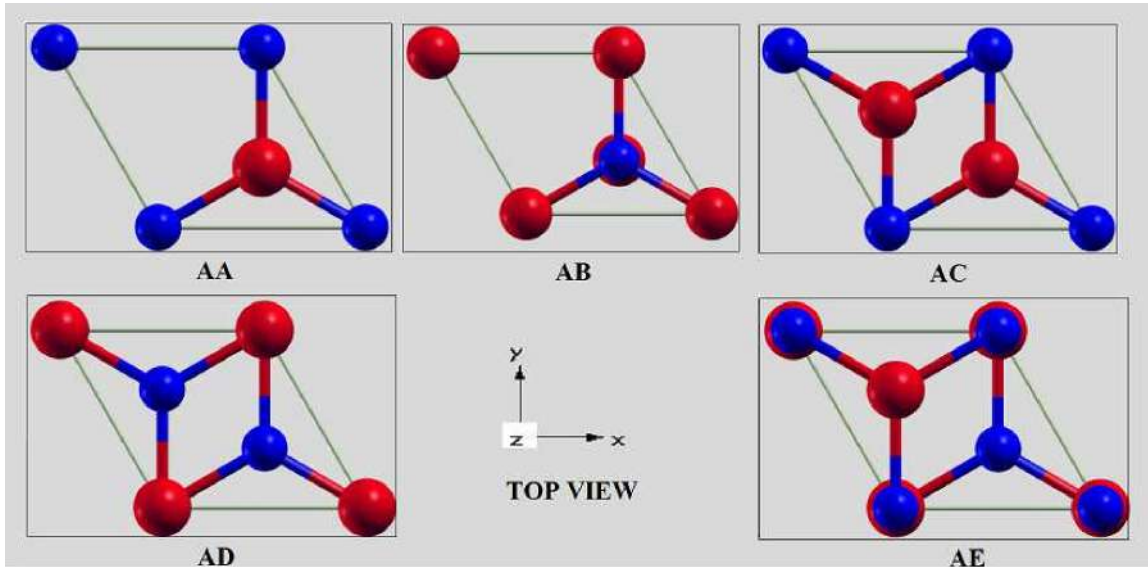


Figure 3-5: Top view of five possible stacking sequences for  $h$ -IIIs bilayer. Blue atoms are B, Ga or In, and red atoms refer to As.

the hexagonal unit cell, exchanging  $x$  and  $y$  coordinates in adjacent planes. In the case of AE stacking, the cation is atop the anion, while the other anion and cation, respectively, are inside the unit cell exchanging  $x$  and  $y$  coordinates. Next, we find the most energetic stacking sequence for three ( $t$ -IIIs) and four ( $f$ -IIIs)-layered  $h$ -BAs,  $h$ -GaAs and  $h$ -InAs structures. We expect the cohesive energy of AA to be the smallest of all stackings. This can be explained by ionic repulsion between adjacent planes. The cohesive energy takes its minimum value for AA stacking because the cation is placed above the cation and the anion above the anion in analogous adjacent planes. It is also expected the most energetic stable configuration to be either AB or AE. In AB configuration cations (anions) of one plane are directly above anions (cations) in the similar adjacent planes. This minimizes the ionic repulsion between adjacent planes, hence the system will be more stable. Besides AB, AE stacking has a high probability of being the most stable configuration. In this stacking, the fact that cations and anions are above/below the hole of the adjacent hexagonal unit cell results in a delocalization of the valence electrons. As a result, their volume increases, lowering the kinetic energy and the total energy of the system [197]. Indeed, N. Ooi *et al.* used DFT and reported that the two most likely stackings for  $h$ -BN were the AB and AE configurations. They concluded that AB maximizes

the ionic attraction between adjacent planes and AE displays both interplanar ionic attraction and delocalization as found in graphite. In addition, by first-principles calculations, C. Bacaksiz *et al.* and A. Onen *et al.* predicted that AB corresponds to the ground-state stacking order for *h*-AlN and *h*-GaN, respectively [124, 198].

Table 3.2: Calculated lattice constant ( $a(\text{\AA})$ ), interlayer distance ( $d_{LL}$  ( $\text{\AA}$ )), buckling parameter ( $\Delta$  ( $\text{\AA}$ )), cohesive energy per cation-anion pair ( $E_{Coh}$  (eV)) and band-gap value ( $E_G$ ) for 2,3 and 4-layer *h*-BAs, *h*-GAs and *h*-InAs systems with GGA approach.

	BAs-Type AC					GaAs-Type AB					InAs-Type AB				
	$a$ ( $\text{\AA}$ )	$d_{LL}$ ( $\text{\AA}$ )	$\Delta$ ( $\text{\AA}$ )	$E_{Coh}$ (eV)	$E_G$ (eV) (GGA)	$a$ ( $\text{\AA}$ )	$d_{LL}$ ( $\text{\AA}$ )	$\Delta$ ( $\text{\AA}$ )	$E_{Coh}$ (eV)	$E_G$ (eV) (GGA)	$a$ ( $\text{\AA}$ )	$d_{LL}$ ( $\text{\AA}$ )	$\Delta$ ( $\text{\AA}$ )	$E_{Coh}$ (eV)	$E_G$ (eV) (GGA)
2 Layers	3.38	3.35	0.00	10.71	0.11 $K\Lambda$	3.98	2.83	0.86	8.23	1.62 $\Gamma\Gamma$	4.31	3.15	0.88	7.83	0.12 $\Gamma\Gamma$
3 Layers	3.37	3.39	0.00	10.75	0.02 $K\Lambda$	3.99	3.26	0.77	8.18	metallic	4.33	3.35	0.79	7.81	semimetal
4 Layers	3.37	3.37	0.00	10.77	semimetal	3.98	3.13	0.85	8.34	metallic	4.32	3.30	0.86	7.98	semimetal

Table 3.2 shows that the most stable structure for *b*-BAs could be either AC or AE stacking, while for both *b*-GaAs and *b*-InAs it is AB. The different stackings can be arranged from the most energetic stacking sequence to the less one as follows:

BAs: AC(10.71 eV) > AE(10.70 eV) > AB (10.68 eV) > AD (10.66 eV) > AA (10.65 eV)

GaAs: AB(8.23 eV) > AC(7.91 eV) > AE (7.87 eV) > AD (7.80 eV) > AA (7.78 eV)

InAs: AB(7.83 eV) > AC(7.44 eV) > AE (7.41 eV) > AD (7.35 eV) > AA (7.28 eV)

From these results we can see that for all bidimensional systems, the cohesive energy of AA is the smallest of all stackings. Similar results were found for BN, AlN and GaN [124, 197, 198]. It is also noticed for *b*-BAs that cohesive energy for AC and AE configurations differs only by 10 meV, which means that any of them could be the stable configuration. The interlayer distance for AC (3.415  $\text{\AA}$ ) is almost the same as the AE (3.423  $\text{\AA}$ ) and it is the smallest one of all stackings. This latter result is followed by the most stable configurations of both *b*-GaAs and *b*-InAs. On the other hand, even though for AC and AD configurations atoms of the same nature are both atop of each other, the fact that the mass of As atoms are almost seven times larger than B atoms in *b*-BAs, causes that B atoms can be closer to each other

in AC stacking than As atoms in AD, making AC a more stable configuration.

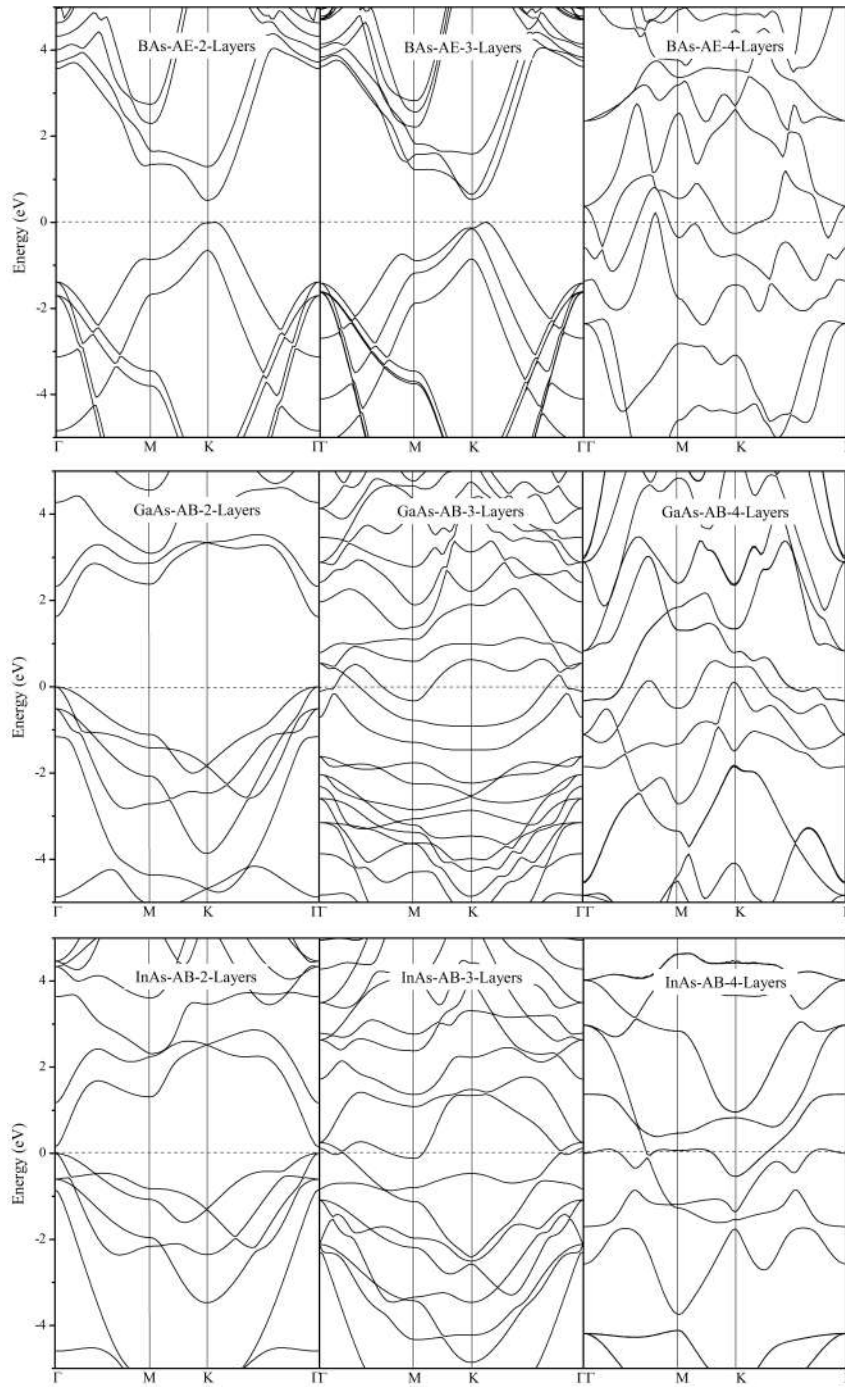


Figure 3-6: Comparison of the band structures for 2, 3 and 4-layer *h*-BAs, *h*-GAs and *h*-InAs structures in their most energetic favorable stacking sequence with GGA approach.

For both *b*-GaAs and *b*-InAs the most energetic stable configuration is AB, as was found for *b*-AlN and *b*-GaN [124, 198]. The stacking sequences (cohesive energy) that

stabilizes  $t$ -BAs and  $f$ -BAs are ACA (10.75 eV) and ACAC (10.77 eV), respectively. The energetically most favorable stackings for  $t$ -GaAs ( $t$ -InAs) and  $f$ -GaAs ( $f$ -InAs) are AB and ABAB, respectively. Their corresponding cohesive energies are shown in Table 3.2. In addition, Table 3.1 and Table 3.2 display that the buckling parameter and the lattice parameter for each layer increases as we move from  $h$ -BAs to  $h$ -InAs. Conversely, the cohesive energy decreases. When we compare results found for the bond lengths between the neighboring cation-anion atoms for each layer, from  $h$ -BAs to  $h$ -InAs, we found that these increase. Therefore, as in the monolayer case, the  $b$ - $t$ - and  $f$ -IIIs layered binary compounds display less stiffness and more plasticity as we move from  $h$ -BAs to  $h$ -InAs. On the other hand, as we move from two to four layers for each  $h$ -IIIs binary compound, it is noticed in Table 3.2 that the interlayer distance is bigger for the three layers case in comparison to two and four layered systems. It means that for the odd layered  $h$ -IIIs systems the ionic repulsion increases when compared to the even ones. Furthermore, for the  $f$ -IIIs systems the ionic repulsion is larger than that of  $b$ -IIIs.

To determine the energy vdW correction, we compared the found cohesive energy values per cation-anion pair with and without vdW interaction. It was found that the energy vdW corrections for  $b$ -BAs,  $t$ -BAs and  $f$ -BAs are 325 meV, 259 meV and 227 meV. The energy vdW corrections for  $b$ -GaAs ( $b$ -InAs),  $t$ -GaAs ( $t$ -InAs) and  $f$ -GaAs ( $f$ -InAs) are 424 meV (553 meV), 473meV (600meV), 513 meV (670 meV). It is noticed that for buckled  $h$ -GaAs and  $h$ -InAs systems the vdW correction is larger than those for planar  $h$ -BAs.

Regarding the electronic properties of 2, 3 and 4-layered  $h$ -BAs,  $h$ -GaAs and  $h$ -InAs, we can infer from Table 3.1, Table 3.2 and Figure 3-6, the following trends:

*i)*  $b$ -BAs,  $b$ -GaAs and  $b$ -InAs present the same bandgap nature of their counterpart ones in the bulk. For instance, the bandgap of  $b$ -BAs has an indirect  $K$ - $\Lambda$  nature as BAs in the bulk. *ii)* As the number of layers increase, from  $b$ -IIIs to  $f$ -IIIs systems, their bandgap decreases until they become semimetal or metal. Interestingly, these results are different to those found for  $h$ -GaN [124]. The authors reported that from two to four layered  $h$ -GaN, the systems are semiconductors and have different semiconducting nature that GaN in the bulk, even though the width

of their bandgaps decrease as the number of layers increase. *iii*) One possible reason of the difference to the tendency of *h*-GaAs to be metallic as the number of layers increases when compared to the retained semiconducting nature of *h*-GaN could be the bonding strength difference between their cations and anions. The larger the bonding strength, the larger the bandgap size. For instance, the interlayer distance and bond length for *b*-GaAs, *t*-GaAs and *f*-GaAs are, respectively, 2.83 Å and 2.45 Å, 3.26 Å and 2.43 Å, and 3.16 Å and 2.45 Å. Instead for *b*-GaN, *t*-GaN and *f*-GaN are, respectively, 2.52 Å and 1.88 Å, 2.49 Å and 1.89 Å, and 2.44 Å and 1.91 Å. The interlayer distances for each layer of *h*-GaAs are higher than the counterpart ones for *h*-GaN. As a result, the ionic repulsion between planes, the interplanar ionic bonding and the bandgap sizes are smaller for *h*-GaAs in comparison to *h*-GaN.

### 3.4 Conclusions

We have studied the mechanical and dynamic stability of the 2D single-layer *h*-IIIs (III=B, As, and Ga) by computing their elastic constants and phonon dispersion relation within density functional theory. We have found that these 2D *h*-IIIs systems are both mechanical and dynamically stable. Results show that 2D *h*-BAs is found to be a stable planar structure; while 2D *h*-GaAs and *h*-InAs exhibit a low-buckled geometry. In addition, bond length (cohesive energy) increases (decreases) from 2D *h*-BAs to 2D *h*-InAs in the present study. Calculations of elastic constants show that Young's modulus, bulk modulus and shear modulus decrease for 2D *h*-IIIs binary compounds as we move down on the group of elements of the periodic table. It is found that *h*-BAs is  $\sim 250\%$  ( $\sim 400\%$ ) times stiffer along the in-plane direction than *h*-GaAs (*h*-InAs). This can be explained by the nature of the bonding. Bond length is inversely proportional to bond strength. On the contrary, we find that the Poisson's ratio increases with increasing row number of elements. It means, as we move down on the group of elements, the 2D *h*-IIIs binary compounds display less stiffness and more plasticity. Regarding the electronic properties, the semiconducting nature of the 3D-IIIs compounds is retained by their 2D counterpart. *h*-BAs (*h*-GaAs) changes from  $\Gamma$ - $\Delta_{min}$  indirect ( $\Gamma$ - $\Gamma$  di-

rect) to  $K$ - $K$  direct ( $\Gamma$ - $K$  indirect) bandgap, while  $h$ -InAs maintains its  $\Gamma$ - $\Gamma$  direct bandgap nature. Density of states reveals the influence of  $\sigma$  and  $\pi$  bonding in the most stable geometry (planar or buckled) for 2D  $h$ -IIIs systems. In the 2D  $h$ -GaAs and InAs buckled structures, it is noted a weaker both  $\pi$  bonding and  $\sigma$  bonding than those in 2D  $h$ -BAs planar geometry. It means, buckling reduces the overlap between  $p_z$  ( $\pi$  bonding) and increases the overlap between  $p_z$  and planar  $s$  orbitals. As a result,  $sp^2$  hybridization ( $\sigma$  bonding) becomes weaker, and the  $sp^3$  one, stronger. Since graphene was isolated, the search for new 2D candidates has increased. Metallic 2D candidates are less likely to be stable due to their high reactivity. Therefore, semiconducting 2D crystals, such as 2D single-layer  $h$ -III-As, are promising materials for the design of new electronic and optoelectronic devices. We have also studied the structural and electronic properties for 2, 3 and 4 layered  $h$ -IIIs systems. For the bilayer structures,  $h$ -BAs prefers AC and AE stackings as the most energetic stable structures, while both  $h$ -GAs and  $h$ -InAs chose AB. In addition, bilayer  $h$ -IIIs present the same bandgap nature of their counterpart in 3D. As the number of layers increases from 2 to 4, the bandgap width for layered  $h$ -IIIs decreases until they become semimetal or metal. Interestingly, these results are different to those found for layered  $h$ -GaN. All of these few-layer structures for  $h$ -BAs and  $h$ -GaAs ( $h$ -InAs) retain, respectively, the planar or buckled geometries of the counterpart single-layer. We hope this study provides relevant physical knowledge for further theoretical and experimental studies of 2D  $h$ -IIIV systems.

## 3.5 Publication

**Chapter 3** was published as:

**A González-García**, W López-Pérez, J Rivera-Julio, V Mendoza-Estrada, R Gonzalez-Hernandez, and FM Peeters. *Structural, mechanical and electronic properties of two-dimensional structure of III-arsenide (111) binary compounds: An ab-initio study*. Computational Materials Science, 144:285–293, 2018.

## Chapter 4

# Tunable 2D-Gallium Arsenide and Graphene bandgaps in Graphene/GaAs heterostructure: an *ab-initio* study

*The nature of 2D-GaAs bandgap and the opening of graphene bandgap have been investigated in unexplored Graphene/GaAs bilayer van der Waals heterostructure under both uniaxial stress along  $c$  axis and different planar strain distributions using a 551/331 supercell geometry by DFT-vdW-Tkatchenko-Scheffler method and spin-orbit coupling. The 2D-GaAs bandgap nature changes from  $\Gamma$ - $K$  indirect in isolated monolayer to  $\Gamma$ - $\Gamma$  direct in Graphene/GaAs bilayer heterostructure. In the same latter physical conditions, graphene displays a bandgap of 5.0 meV. Uniaxial stress strongly influences the graphene electronic bandgap. Symmetrical in-plane strain does not open a bandgap in graphene. Nevertheless, it induces remarkable changes on the GaAs bandgap width around the Fermi level. However, when applying asymmetrical in-plane strain to graphene/GaAs, the graphene sublattice symmetry is broken, and the graphene bandgap is opened at the Fermi level to a maximum width of 814 meV. This value is much larger than that reported for graphene under asymmetrical strain. The  $\Gamma$ - $\Gamma$  direct nature of GaAs remains unchanged in Graphene/GaAs*

*under different types of applied strain. Phonon dispersion and elastic constants analysis display the dynamical and mechanical stability of Graphene/GaAs system, respectively. The calculated mechanical properties for the bilayer heterostructure are better than those of their constituent monolayers. This latter finding, together with the tunable graphene bandgap from the use and direction of the strain, feature the likelihood of enhancing the physical characteristics of potential graphene-based group-IIIV electronic devices by strain engineering.*

## 4.1 Introduction

The unique physical properties of two-dimensional graphene related materials (2D-GRM), such as low dimensionality, flexibility, high mechanical strength, lightness, in-plane covalent bonding and dangling-bond-free lattice, make them relevant for a variety of potential applications, for instance: catalysis, biomedicine, conductive ink, sensors, coating, light emitting devices, composites, storage and production of energy, touch panels and high frequency electronics, among others [9, 54, 170, 172, 192, 199, 200, 201]. Therefore, during the last ten years, the scientific community has developed an intense research on 2D nanomaterials, e.g., graphene [16], X-enes (X = B, Si, Ge, Sn, P, Bi) [51, 52, 53, 54, 55, 56, 57, 202, 203], X-anes (graphane, silicane, germanane, stanane) [48, 98], fluoro-X-enes [98], MXenes [204], IIIV systems [102, 115, 123, 124, 171, 205], transition metal dichalcogenides (TMDs) [206, 207, 208, 209], layered oxides [210], layered double hydroxides (LDHs) [211], metal-organic frameworks (MOFs) [212, 213], covalent organic frameworks (COFs) [214], polymers [215, 216, 217] and metals [218, 219, 220, 221].

Recently, theoretical and experimental research have focused on the study of van der Waals heterostructures by controlled multi-stacking of diverse layering materials such as metals, semiconductors or insulators [9, 49, 127, 222]. These novel materials will display interesting structural, electronic, optical and mechanical properties different from those of the 2D materials they are built of. Hence, they can be used to design new electronic and optoelectronic devices with unprecedented features or unique functionalities, such as tunnelling transistors, barristors, flexible electronics,

photodetectors, photovoltaics and light-emitting devices [49]. Due to the astonishing physical properties of graphene, e.g., its electrons display ballistic transport, graphene is likely the most common component in future van der Waals graphene-based electronic devices [7]. Unfortunately, graphene lacks a bandgap, which is essential for controlling the conductivity by electronic means [223].

The absence of a gap in graphene, together with the linear dispersion of the bands at the  $K$  point and the equivalence of the two carbon sublattices, restrains the Dirac fermions from getting a finite mass, which constrains the use of graphene in electronic devices. The importance of inducing a bandgap in graphene relies on generating an effective mass for the Dirac fermions, which offers the potential to improve the characteristics of graphene-based field effect transistors (FETs) [129]. This bandgap drawback has motivated scientists to look for new 2D-materials beyond graphene. It has been found in these studies that a graphene bandgap can be induced by adsorption of H and F [98, 223], and by graphene-based heterostructures [127, 222, 224, 225]. Strain can modify the interatomic distances and relative positions of atoms within a material, and consequently the electronic structure of a heterostructure can be tuned by applying strain [12]. Among these heterostructures, those with lateral graphene display higher electronic quality [127, 222, 225].

Graphene-based group IIIV heterostructures have been studied in bilayer [129] and multilayer systems [130, 131] in order to tune the graphene bandgap for optoelectronics and optics applications. Giovannetti *et al.* [129] studied graphene on top of a single layer BN by density functional calculations. They found that the presence of  $h$ -BN breaks the sublattice symmetry of graphene, inducing a bandgap of  $53\text{ meV}$ . Direct growth of graphene on  $h$ -BN and vice versa has been achieved by CVD methods [54, 196, 226]. Using first principle calculations, Kaloni *et al.* [130] predicted finite and tunable bandgaps for superlattices in which a single graphene layer alternates with  $h$ -BN slabs of variable thickness. In addition, heterostructures where one, two or more graphene (or other 2D-systems) layers sandwiched between two other 2D-systems (graphene) have been studied [131, 227, 228].

The following scientific findings motivated us to carry out this study:

- i) There are some pioneering studies [156, 157] indicating splitting of electron

and hole energy bands by spin-orbit coupling (SOC) in 2D-GaAs heterostructures. Rashba *et al.* [229] were motivated by these 2D studies to investigate the SOC contribution to the electron Hamiltonian, a term currently known as the Rashba term.

ii) Recently, 2D *h*-GaAs has been reported as a mechanical and dynamically stable semiconductor by first-principles studies [123, 171].

iii) Theoretical and experimental studies state the importance of graphene-based group III–V heterostructures to modulate the bandgap of graphene for electronic applications [54, 129, 130, 131, 196, 226, 227, 228].

iv) There is some theoretical and experimental research that highlight the importance of Graphene/GaAs systems for future practical applications in plasmonic and photonic technology [230, 231, 232, 233, 234]

v) To the best of our knowledge, there are no previous studies about tuning the bandgap in Graphene/GaAs bilayer heterostructures.

In this paper, we study first the structural properties and dynamical stability of Graphene/GaAs bilayer heterostructure. Then, its electronic and mechanical properties and, finally, the effect of both uniaxial stress along *c* axis and different planar strain distributions on the electronic properties of Graphene/GaAs. This research has been carried out using vdW-Tkatchenko-Scheffler (DFT-TS) method [235] and SOC within the DFT framework [135, 136]. Our results predict a novel 2D graphene-based heterostructure for potential electronic applications.

## 4.2 Computational and theoretical details

The calculations were performed using the *Vienna Ab-initio Simulation Package* (VASP) [152, 153] employing the first principles pseudo-potential method in the framework of the DFT [135, 136]. VdW-Tkatchenko-Scheffler (DFT-TS) method [235] and the spin-orbit coupling (SOC) have also been taken into account in our calculations. Exchange and correlation effects were treated with the generalized gradient approximation (GGA) implemented in the Perdew-Burke-Ernzerhof functional (PBE) [142]. The core electrons were described by the projector augmented

wave (PAW) method [151, 182] wherein the  $d$  states for Ga and As were included as valence electrons in their PAW pseudo-potentials. The valence electron configurations for C, Ga and As are  $2s^22p^2$ ,  $3d^{10}4s^24p^1$  and  $3d^{10}4s^24p^3$ , respectively. The hexagonal primitive cell, with one Ga atom and one As atom, see Figure 4-2(b), was constructed from the zinc-blende structure in the (111) plane [171]. In order to reduce the mismatch between graphene and 2D-GaAs hexagonal monolayers in Graphene/2D-GaAs bilayer heterostructure, a 551/331 supercell geometry was used in this study, as shown in Figure 4-2(a), Figure 4-2(b) and Figure 4-2(c), respectively. The electron wave function was expanded in plane waves up to a cutoff energy of 500 eV for all the calculations. A  $\Gamma$ -centered grid of  $25 \times 25 \times 1$   $k$ -point has been used to sample the irreducible Brillouin zone in the Monkhorst-Pack special scheme [146] for calculations, except for 551-Graphene/331-GaAs bilayer heterostructure where a  $8 \times 8 \times 1$   $k$ -point was used. Phonon calculations were performed by taking into account the interactions in a  $10 \times 10 \times 1$ -Graphene/ $6 \times 6 \times 1$ -GaAs supercell [166]. The PYPROCAR code was used to plot the electronic bands of Graphene/-GaAs bilayer heterostructure [236]. In addition, a 20 Å vacuum spacing between the adjacent supercells is kept to avoid interactions. The optimized parameters for graphene, 2D-GaAs monolayers, and 551-Graphene/331-GaAs bilayer heterostructure are depicted in Table 4.1. Stress-based approach is implemented [183, 184] to study the mechanical properties. The elastic tensor is determined by performing finite distortions of the optimized lattice and to derive the elastic constants from the strain-stress relationship (Hooke's law) [183, 184].

In our study, the spin-orbit interaction for 551-Graphene/331-GaAs bilayer heterostructure has been taken into account. Spin-orbit coupling is a relativistic interaction between moving electrons with  $\mathbf{v}=\mathbf{p}/m$  and a local electric field  $\mathbf{E}=-\frac{1}{q}\frac{dV(r)}{dr}\frac{\mathbf{r}}{r}$  in their rest frame created by the proton, where  $q$  is the charge of the moving electrons and  $V(r)=-\frac{e^2}{r}$  is the electrostatic energy of the electron. Special relativity indicates that, in the electron frame, a magnetic field appears, described by [154]

$$\mathbf{B} = -\frac{1}{c^2}(\mathbf{v} \times \mathbf{E}), \quad (4.1)$$

where  $\mathbf{B}$  is equivalent to:

$$\mathbf{B} = -\left(\frac{e^2}{qm_e c^2 r^3}\right)\mathbf{L}, \quad (4.2)$$

where  $\mathbf{L} = \mathbf{r} \times \mathbf{P}$  represents the electron orbital angular momentum. Due to the interaction of  $\mathbf{B}$  with the electron intrinsic magnetic moment  $\mathbf{Ms}$ , given by:

$$\mathbf{Ms} = \frac{q}{m_e}\mathbf{S}, \quad (4.3)$$

and by the Zeeman effect, the orbital energy levels are split, which can lead to different transition levels with energy:

$$H_{so} = -\mathbf{Ms} \cdot \mathbf{B}. \quad (4.4)$$

From **equations** (4.2), (4.3) and (4.4),  $H_{so}$  can be rewritten as:

$$H_{so} = \xi(r)\mathbf{L} \cdot \mathbf{S}, \quad (4.5)$$

where  $\xi(r) = e^2/2m_e^2 c^2 r^3$  contains the entire radial dependence of the SOC Hamiltonian operator [155]. The factor 1/2 is due to the fact that the electron spin rotates with respect to the laboratory reference frame [154].  $\mathbf{L}$  and  $\mathbf{S}$  are the electron orbital and spin angular momentum, respectively. When the orbital angular momentum of  $p$ -graphene orbital interacts with its spin intrinsic momentum, the electron states can be either 3/2 ( ${}^2P_{3/2}$ ) or 1/2 ( ${}^2P_{1/2}$ ), depending on the case if  $\mathbf{L}$  and  $\mathbf{S}$  are parallel or antiparallel, respectively, as shown in Figure 4-1(b).

The special relativity theory states that for electrons with large average speeds the mass increases, while the radius decreases. In the weakly relativistic domain, the SOC effect is specially noticed for massive atoms of the periodic table. There are some pioneering studies [156, 157] indicating splitting of electron and hole energy bands by spin-orbit coupling (SOC) in 2D-GaAs heterostructures. Pyykkö [158] compared the relativistic (Dirac) and nonrelativistic (Schrodinger) dynamics for the valence electron in a given atomic potential, and studied the importance of the direct relativistic effect on atomic orbitals. They found a relativistic radial contraction and energetic stabilization for  $s$  and  $p$  shells, spin-orbit splitting and the relativistic radial

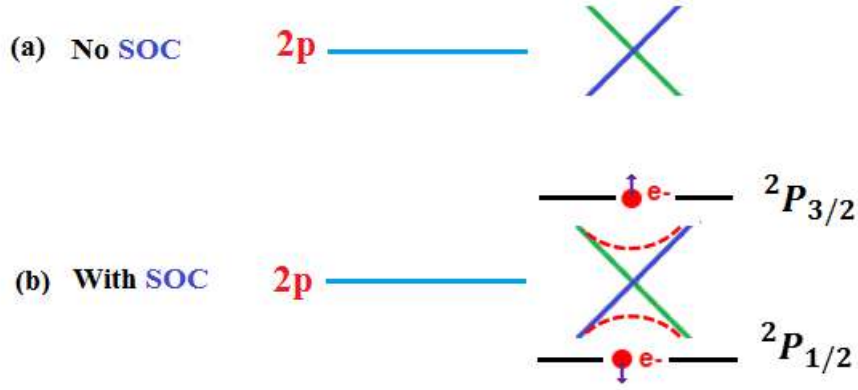


Figure 4-1: Orbital angular momentum of  $p$ -graphene state ( $l=1$ ) with (a) no coupling and (b) coupling with its spin intrinsic momentum

expansion and energetic destabilization of the  $d$  and all  $f$  outer shells. They also reported that all three effects were of the same order of magnitude and increase roughly like  $Z^2$ .

In order to study some mechanical properties that give physical insights into the potential applications of 551-Graphene/331-GaAs bilayer heterostructures in engineering science, we calculated its  $C_{11}$ ,  $C_{12}$ ,  $C_{22}$  and  $C_{66}$  elastic constants. Due to hexagonal symmetry,  $C_{11} = C_{22}$  and  $(C_{11} - C_{12})/2 = C_{66}$ , only two independent elastic constants  $C_{11}$  and  $C_{12}$  have to be calculated in the stress-strain relation for a 2D hexagonal structure. Therefore, Hooke's law ( $\sigma_i = C_{ij} \epsilon_j$ , where  $\sigma_i$  and  $\epsilon_j$ ,  $i$  and  $j$  are integers, represent the stress and strain, respectively) for 2D hexagonal materials can be expressed in the matrix form [187]:

$$\begin{bmatrix} \sigma_1 \\ \sigma_2 \\ \sigma_3 \end{bmatrix} = \begin{bmatrix} C_{11} & C_{12} & 0 \\ C_{12} & C_{11} & 0 \\ 0 & 0 & \frac{C_{11}-C_{12}}{2} \end{bmatrix} \begin{bmatrix} \epsilon_1 \\ \epsilon_2 \\ \epsilon_3 \end{bmatrix}. \quad (4.6)$$

The Poisson's ratio  $\nu$ , the in-plane Young's modulus  $Y_s$ , the 2D layer modulus  $B_{2D}$  and shear  $G_V$  modulus are obtained, from the calculated  $C_{11}$  and  $C_{12}$  elastic constants, and multiplied later by the corresponding optimized unit-cell  $z$  distance. Their respective equations are [189, 237]:

$$\nu = C_{12}/C_{11}, \quad (4.7)$$

$$Y_s = (C_{11}^2 - C_{12}^2)/C_{11}, \quad (4.8)$$

$$B_{2D} = (C_{11} + C_{12})/2, \quad (4.9)$$

$$G = (C_{11} - C_{12})/2. \quad (4.10)$$

The calculated elastic constants and the above mentioned mechanical properties for graphene and 2D-GaAs monolayers, and 551-Graphene/331-GaAs bilayer heterostructure are depicted in [Table 4.2](#). The Poisson's ratio represents the plasticity of the material, the 2D layer modulus gives physical insight on the resilience of a material to stretching, and the shear and in-plane Young's moduli indicate the 2D structure stiffness. Gonzalez *et al* [171] reported for 2D *h*-IIIAs binary compounds that as one moved down on the group of elements of the periodic table, the bond length between the neighboring cation-anion atoms increases and the materials display less stiffness and more plasticity.

## 4.3 Results and discussion

### 4.3.1 Structural properties and dynamical stability

Honeycomb unit cells for graphene and 2D-GaAs monolayers are shown in [Figure 4-2\(a\)](#) and [Figure 4-2\(b\)](#). Graphene monolayer displays a planar geometry while 2D-GaAs presents a buckled one. The TS-vdW optimized parameters for graphene and 2D-GaAs hexagonal monolayers, as well as for graphene and 2D-GaAs in 551-Graphene/331-GaAs bilayer heterostructures ([Figure 4-2\(c\)](#)), are shown for comparison in [Table 4.1](#). Our results for 2D-GaAs and graphene monolayers are in good agreement with previous theoretical DFT studies. The lattice parameter value of graphene monolayer is 39.1 % shorter than that of 2D-GaAs monolayer. Using a

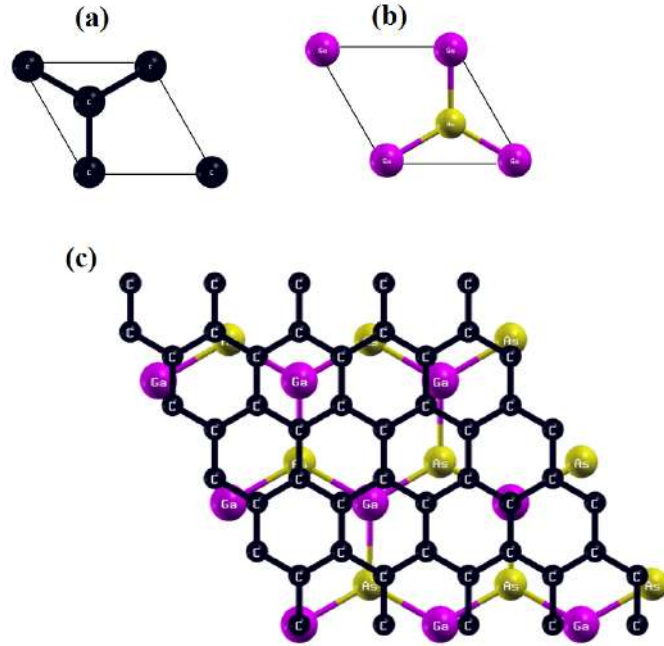


Figure 4-2: Honeycomb unit cells for (a) Graphene, (b) 2D-GaAs monolayers, and (c) 551-Graphene/331 GaAs bilayer crystal heterostructure.

computational method Kumar *et al* reported that lattice mismatch between two different bilayers causes elastic strains, which significantly affects their electronic properties [238]. In order to reduce this mismatch, 551-Graphene and 331-GaAs geometries were chosen. These selected geometries reduced the mismatch to 1.49 % between 551-Graphene and 331-GaAs sheets.

The vdW interlayer interaction between 551-graphene and 331-GaAs layers reduces the lattice constant of graphene by 0.24 % and increases that of GaAs by 1.01 % compared to the respective ones from their pristine monolayers. As a result, the initial mismatch between 551-Graphene and 331-GaAs is reduced from 1.49 % to 0.18 %, which increases the mechanical and dynamical stability of our system, as will be shown in the next sections. The optimized DFT-TS interlayer spacing ( $d_L$ ) between 551-graphene and 331-GaAs sheets is 3.476 Å. This value is higher than that found for graphene-BN bilayer, 3.34 Å [129], and reasonably comparable to that of 551-graphene/441-MoS<sub>2</sub> heterostructures, 3.40 Å [239]. The interlayer distance is sensible to the vdW flavour used in the calculations. So, it is of vital importance

Table 4.1: Calculated lattice constant ( $a$  (Å)), angle between neighboring bonds ( $\theta$ ), Planar (PL) or Low-Buckled (LB) geometry (G), buckling parameter ( $\Delta$  (Å)), nearest-neighbor distance ( $d$ ), interlayer distance ( $d_L$ ), and bandgap value ( $E_G$ ) for 2D graphene and GaAs monolayers, and graphene and GaAs in 551-Graphene/331-GaAs bilayer heterostructure.

	$a$ (Å)	$\theta$	G	$\Delta$ (Å)	$d$ (Å)	$d_L$ (Å)	$E_G$ (eV)
<b>Graphene</b>	2.465	120	PL	0	1.423	-	0
	2.460 [123]	120 [123]	PL [123]	0 [123]	1.420 [123]	-	0 [123]
<b>2D-GaAs</b>	4.048	114.4	LB	0.577	2.407	-	1.03 $\Gamma K$
	4.050 [171]	114.3 [171]	LB [171]	0.550 [171]	2.410 [171]	-	1.08 $\Gamma K$ [171]
	3.970 [123]	114.7 [123]	LB [123]	0.550 [123]	2.380 [123]	-	1.29 $\Gamma K$ [123]
<b>551-Graphene/ 331-GaAs</b>							
<b>Graphene</b>	2.459	120	PL	0.001	1.419	3.476	0.049 $KK$ height
<b>GaAs</b>	4.091	115.8	L.B	0.501	2.427	-	0.729 $\Gamma\Gamma$

the correct vdW flavour choice [239]. Singh *et al.* reported that the Tkatchenko-Scheffler method efficiently evaluates the long-range vdW interactions and accurately predicts interlayer spacing between 551-graphene and 441-MoS<sub>2</sub> sheets [239]. Their reported interlayer distance agrees with the experimental one (3.40 Å) [240]. On the other hand, theoretical [123, 124] and experimental [102] research has predicted and validated the stability of 2D buckled single layer of group III–V with ionicity. Balushi *et al.* experimentally reported that graphene plays a critical role in stabilizing ionic 2D buckled group III–V structure. Their results provide a foundation for the discovery and stabilization of 2D group III–V materials that are difficult to prepare via traditional synthesis [102]. Using Bader analysis [194], we found a charge transfer of 5.3 electrons from Ga to As for 551-Graphene/331-GaAs bilayer heterostructure, indicating a significant ionicity in the interplanar binding. However, no charge transfer from Ga to C atoms was found.

Figure 4-3 depicts the calculated phonon dispersion curves for the 551-Graphene/331-GaAs bilayer heterostructure. We see that the 551-Graphene/331-GaAs system is stable, because there are no imaginary frequencies in the phonon dispersion. Some few imaginary frequencies plotted as negative frequencies near the  $\Gamma$  point are shown. This feature has been found in other 2D-systems [239, 241, 242, 243] and highlights the flexural acoustic mode of 2D-systems. They are often present in theoretical calculations due to inadequate numerical convergence close to the  $\Gamma$  point [239].

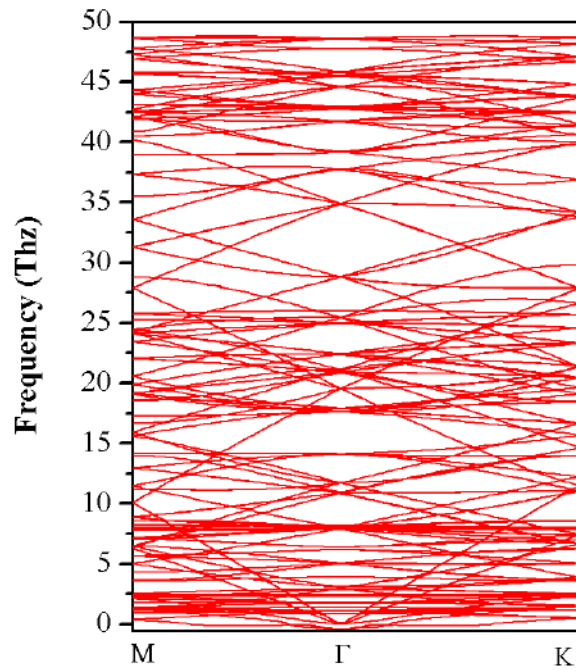


Figure 4-3: Phonon dispersion curves for the 551-Graphene/331-GaAs bilayer heterostructure

### 4.3.2 Electronic structure and Mechanical properties

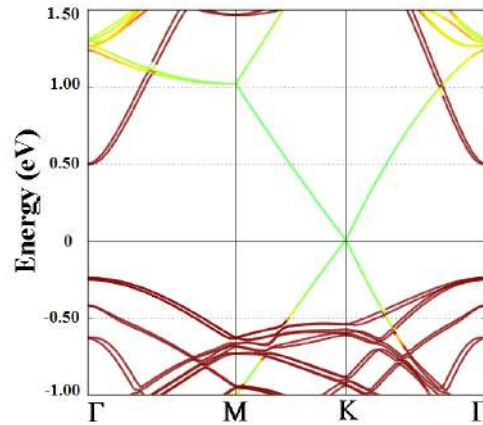


Figure 4-4: Electronic band structure for the 551-Graphene/331-GaAs bilayer crystal heterostructure without strain. The brown lines represent the contributions of Ga-4s and As-4 $p_z$  orbitals, while the green one the contribution of C-2 $p_z$  orbitals.

The TS-vdW + SOC electronic band structure for the 551-graphene/331-GaAs bilayer crystal heterostructure without strain is displayed in [Figure 4-4](#). The brown lines represent the contributions of Ga-4s and As-4 $p_z$  orbitals, while the green one

Table 4.2: Calculated 2D Poissons ratio ( $\nu$ ); Young's ( $Y_s$ ), layer ( $B_v$ ) and Shear ( $G_v$ ) moduli for 2D graphene and GaAs monolayers, and 551-Graphene/331-GaAs bilayer heterostructure.

	$C_{11}$ (J/m <sup>2</sup> )	$C_{12}$ (J/m <sup>2</sup> )	$\nu$	$Y_S$ (J/m <sup>2</sup> )	$B_{2D}$ (J/m <sup>2</sup> )	$G_V$ (J/m <sup>2</sup> )
<b>Graphene</b>	352.8	62.8	0.18	341.7	207.8	145.0
	352.7 [237]	60.9 [237]	0.17 [237]	342.2 [237]	206.6 [237]	145.9 [237]
<b>2D-GaAs</b>	49.6	16.1	0.32	44.4	32.9	17.1
	-	-	0.35[123]	48.0 [123]	-	-
<b>551-Graphene/ 331-GaAs</b>	384.7	70.0	0.18	372.1	227.4	157.0

the contribution of C- $2p_z$  orbitals. We can see the semiconductor  $\Gamma$ - $\Gamma$  direct bandgap nature for 331-GaAs layer, with a bandgap size of 0.72 eV, and a near semimetallic nature of 5.0 meV at the K point for 551-graphene layer. This electronic behavior for 331-GaAs ( $\Gamma$ - $\Gamma$  direct) is different from that one reported for 2D-GaAs monolayer ( $\Gamma$ - $K$  indirect) [123, 171]. Thus, the presence of graphene on GaAs layer induces an indirect to direct bandgap transition of the GaAs layer, which makes it potential candidate for optoelectronic applications and field-effect transistors. This bandgap transition can be physically explained by the vdW interaction between the localized C- $2p_z$  and As- $4p_z$  orbitals at the  $K$  point, which shifts this latter orbital downward in the VBM. Singh *et al.* [239] reported that MoS<sub>2</sub> undergoes a direct to indirect (direct) bandgap transition in 441-graphene/331-MoS<sub>2</sub> (551-graphene/441-MoS<sub>2</sub>) bilayer heterostructure. Authors state that these bandgap transitions, when changing the layer geometries, are imposed by the strain between the layers. Lattice mismatch between two different bilayers causes elastic strains, which significantly affects their electronic properties [238]. The change from indirect to direct of 2D-GaAs bandgap nature is physically important because heterostructures can present high photoluminescence [239]. On the other hand, we found that the proximity effects of GaAs with SOC open a bandgap of 5.0 meV at the Dirac point in graphene for the Graphene/GaAs heterostructure. Our result agrees with those found for graphene/BN. It has been reported that strain opens the graphene/BN bandgap in the range of 4 meV to 14 meV [244, 245]. Sing *et al.* found that the SOC and proximity effects of MoS<sub>2</sub> open a direct bandgap in graphene of 0.4 meV and 1.1 meV for different Graphene/MoS<sub>2</sub> geometries [239].

The elastic constants for graphene and 2D-GaAs monolayers, as well as for 551-Graphene/331-GaAs bilayer system, are tabulated in Table 4.2. Our results for the monolayer constituents of Graphene/GaAs are in excellent agreement with those reported in previous theoretical and experimental studies. It is noteworthy that  $C_{11} > 0$  and  $C_{11} - C_{12} > 0$ , which means that all our systems satisfy the Born stability criteria [186] for mechanically stable 2D hexagonal structures. The calculated Poisson's ratio for 551-Graphene/331-GaAs bilayer system is less (equal) than that of 2D-GaAs (graphene) monolayer. On the contrary, the 2D Young's ( $Y_s$ ), layer ( $B_{2D}$ ) and Shear ( $G_V$ ) moduli for the bilayer heterostructure are larger when compared to those of their constituent monolayer. Therefore, 551-graphene/331-GaAs is a stronger material than graphene but with the same plasticity, which makes it attractive for potential applications in engineering science.

### 4.3.3 Tuning Graphene and 2D-GaAs bandgaps

Stress applied on heterostructure materials changes the interatomic distances and the relative positions of the atoms, which influences the electronic structure with potential optical applications [246]. Therefore, we have investigated the impact on the electronic properties of graphene and GaAs in graphene/GaAs bilayer heterostructure under uniaxial stress along  $c$  axis and different planar strain distributions.

In order to study the effect of uniaxial stress along  $c$  axis on the electronic properties of 551-Graphene/331-GaAs bilayer crystal heterostructure, the equilibrium interlayer distance between 551-Graphene and 331-GaAs layers was modified by  $X = -6.0\%$ ,  $-4.0\%$ ,  $-2.0\%$ ,  $+2.0\%$ ,  $+4.0\%$  and  $+6.0\%$ . During each expansion ( $X > 0$ ) and compression ( $X < 0$ ) process, the vertical coordinate was kept fixed at each separation while atoms were allowed to relax in the plane of the layers. Figure 4-5(i) displays the electronic structures for all these configurations. For  $X = +2.0\%$ ,  $+4.0\%$  and  $+6.0\%$  expansion cases, the 551-Graphene bandgap (331-GaAs) is opened by 26.0% (4.2%), 68.0% (8.3%) and 68.0% (5.6%).

For the uniaxial compression along  $c$  axis, the graphene (GaAs) bandgap increases from 7.3 meV (0.75 eV) to 9.4 meV (0.78 eV) as the strain increases from  $-2.0\%$  to  $-4.0\%$  before decreasing to 5.2 meV (0.67 eV) for  $-6.0\%$ . From the results

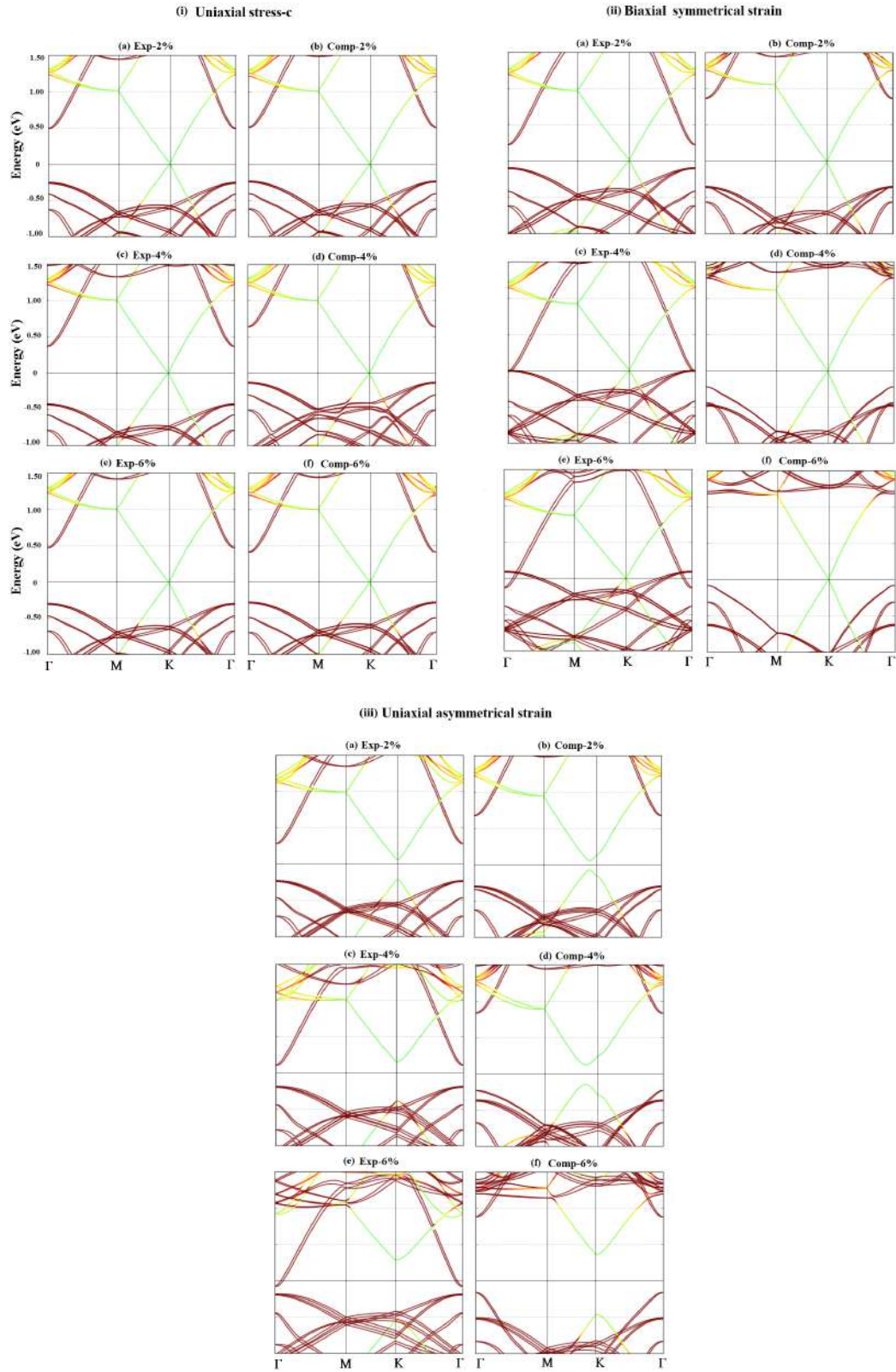


Figure 4-5: Electronic structures for i) uniaxial stress along  $c$ -axis, ii) biaxial symmetrical strain, and iii) uniaxial asymmetrical strain along perpendicular C-C bond for  $x = -6.0\%$ ,  $-4.0\%$ ,  $-2.0\%$ ,  $+2.0\%$ ,  $+4.0\%$  and  $+6.0\%$  configurations of 551-Graphene/331 GaAs bilayer crystal heterostructure.

found for the uniaxial strain along  $c$  axis, we can infer that interlayer distance plays an important role for tuning both the graphene and GaAs bandgap in Graphene/-GaAs bilayer heterostructure. The graphene bandgap opening could be attributed to the enhanced SOC of graphene due to the proximity of the GaAs-buckled effective potential. Using first-principles method, Youngbin *et al.* [12] studied the effect of strain on the bandgap characteristics of MXene semiconductors for useful optical devices. They reported that this material experiences an indirect to direct bandgap transition with variation of the bandgap size at a relatively small critical strain of about 2%.

For symmetrical strain distribution, the system undergoes in-plane biaxial stretching and compression of 2.0%, 4.0% and 6.0% from its optimized lattice parameter value. Then, the lattice structure was optimized, the lattice vectors were set to be fixed at their strained values while only the atomic coordinates were allowed to relax. Figure 4-5(ii) shows the band structure of the graphene/GaAs systems with  $X = -6.0\%$ ,  $-4.0\%$ ,  $-2.0\%$ ,  $+2.0\%$ ,  $+4.0\%$  and  $+6.0\%$  for symmetrical strain. We find that there is no bandgap opening around the Fermi level for graphene for any strength of symmetrical tensile or compressive strain. Nevertheless, strain results in a remarkable change of the GaAs bandgap width around the Fermi level. As shown in Figure 4-5(iii), strain results in a decrease in the GaAs bandgap width until becoming metallic, while compressive strain leads to an increase in the GaAs bandgap width.

In the asymmetrical strain distribution, graphene/GaAs bilayer supercell undergoes uniaxial stretching and compression in one direction, perpendicular to C–C bonds, of 2%, 4% and 6% from its optimized lattice parameter value, and unstrained along the other direction. Figure 4-5(iii) displays the electronic structures for  $X = -6.0\%$ ,  $-4.0\%$ ,  $-2.0\%$ ,  $+2.0\%$ ,  $+4.0\%$  and  $+6.0\%$  configurations. For  $X = +2.0\%$  and  $+4.0\%$ , the 551-Graphene bandgap (331-GaAs) is opened (narrowed) by 267 and 541 meV (0.502 and 0.286 eV). As the expansion is increased to  $+6.0\%$  the system becomes slightly metallic. For  $X = +2\%$  and  $+4\%$ , graphene has a bandgap located at the left side of the K point; while for 6%, at the K point. Gui *et al.* found similar results for asymmetrical strain distributions in graphene, though they

reported direct and indirect graphene bandgap nature depending on the compression value [247]. On the other hand, Figure 4-5(iii) displays that the graphene (GaAs) bandgap width increases to 91 (0.95), 248 (1.05) and 814 (1.04 eV) meV for X= -2.0% , -4.0% and -6.0%, respectively. Notice that GaAs bandgap keeps its direct nature at the  $\Gamma$  point. Gui *et al.* reported that for the asymmetrical strain distribution perpendicular to C–C bonds in graphene, the bandgap increases from 0 to 170 meV as the strain increases to 4.91% before decreasing [247]. The authors reported that lattice symmetry breaking results in the opening of graphene bandgap at the Fermi level. From Figure 4-5(iii) we notice that the valence-band maximum for GaAs is shifted upward, closer to the Fermi level as compression increases, while the graphene valence-band maximum is shifted downward, farther from the Fermi level. One physical reason for this is that as the compression reaches a value larger than 4%, the repulsion between the charge accumulation around the C atoms becomes stronger so the *p*-C orbitals are shifted downward farther from the Fermi level. For the case of GaAs, as compression increases, due to the electronegative difference between their atoms, the attraction between the charge accumulation around the Ga and As atoms becomes stronger which shifts the GaAs orbitals near each other.

From the above mentioned results, obtained for the symmetrical and asymmetrical strain applied to graphene/GaAs system, we can conclude that the nature for both GaAs and graphene electronic band structures depends on its lattice symmetry. The lattice symmetry breaking results in a bandgap opening of graphene at the Fermi level. Our findings are important to tune the electronic properties of 551-graphene/331-GaAs heterostructure by strain engineering for potential optical applications.

## 4.4 Conclusions

DFT-vdW-Tkatchenko-Scheffler method and spin-orbit coupling have been used to investigate the physical effects on the electronic band structures of 2D-GaAs and graphene monolayer constituents in Graphene/GaAs bilayer heterostructure using a 551/331 supercell geometry. It was found that the bandgap nature of 2D-GaAs

changes from  $\Gamma-K$  indirect in isolated monolayer to  $\Gamma-\Gamma$  direct in bilayer heterostructure. This bandgap transition can be physically explained by the vdW interaction between the localized C- $2p_z$  and As- $4p_z$  orbitals at the  $K$  point, which shifts this latter orbital downward of the VBM. The uniaxial stress along the c-axis strongly influences the graphene electronic bandgap. The interlayer distance plays an important role for tuning both the graphene and GaAs bandgap in Graphene/-GaAs bilayer heterostructure. The bandgap opening of graphene could be attributed to the enhanced SOC of graphene due to proximity of the GaAs-buckled effective potential.  $\Gamma-\Gamma$  direct bandgap of 2D-GaAs in 551-Graphene/331-GaAs is not altered with varying interlayer distance. These are extremely important findings for potential optical applications by strain engineering. Symmetrical in-plane strain does not open the graphene bandgap. Nevertheless, it induces remarkable changes on the GaAs bandgap width around the Fermi level. When applying asymmetrical in-plane strain to graphene/GaAs, the graphene sublattice symmetry is broken, and the graphene bandgap is opened at the Fermi level to a maximum width of 814 meV. We can conclude that the nature for both GaAs and graphene electronic band structures depends on its lattice symmetry. The lattice symmetry breaking results in a bandgap opening of graphene at the Fermi level. Our findings are important to tune the electronic properties of 551-graphene/331-GaAs heterostructure by strain engineering for potential optical applications. Phonon dispersion and elastic constants analysis display, respectively, the dynamical and mechanical stability of 551-Graphene/331-GaAs bilayer vdW-heterostructure. The calculated 2D Young's ( $Y_s$ ), layer ( $B_{2D}$ ) and Shear ( $G_V$ ) moduli for bilayer heterostructure are higher than those of its monolayer constituents, which indicates that our studied bilayer material displays more in-plane stiffness than its monolayer constituents. Our findings feature the likelihood of enhancing the physical characteristics of potential graphene-based group-IIIIV optoelectronic devices by strain engineering.

## 4.5 Publication

Chapter 4 was published as:

A González-García, W López-Pérez, R González-Hernández, JA Rodríguez, MV Milošević, and FM Peeters. *Tunable 2d-gallium arsenide and graphene bandgaps in a graphene/GaAs heterostructure: an ab-initio study*. Journal of Physics: Condensed Matter, 31(26):265502, 2019.

## Chapter 5

# Two-dimensional hydrogenated buckled gallium arsenide:

## An *ab-initio* study

*First-principles calculations have been carried out to investigate the stability, structural and electronic properties of two-dimensional hydrogenated GaAs with three possible geometries: chair, zigzag-line and boat configurations. The effect of van der Waals interactions on 2D H-GaAs systems has also been studied. These configurations were found to be energetic and dynamic stable, as well as having a semiconducting character. Although two-dimensional GaAs adsorbed with H tends to form a zigzag-line configuration, the energy differences between chair, zigzag-line and boat are very small which implies the metastability of the system. Chair and boat configurations display a  $\Gamma$ - $\Gamma$  direct bandgap nature, while pristine 2D-GaAs and zigzag-line are indirect semiconductors. The bandgap sizes of all configurations are also hydrogen dependent, and wider than that of pristine 2D-GaAs with both PBE and HSE functionals. Even though DFT-vdW interactions increase the adsorption energies and reduce the equilibrium distances of H-GaAs systems, it presents, qualitatively, the same physical results on the stability and electronic properties of our studied systems with PBE functional. According to our results, two-dimensional buckled gallium arsenide is a good candidate that can be synthesized by hydrogen*

surface passivation as its group III–V partners two-dimensional buckled gallium nitride and boron nitride. The hydrogenation of 2D-GaAs tunes the bandgap of pristine 2D-GaAs, which makes it a potential candidate for optoelectronic applications in the blue and violet ranges of the visible electromagnetic spectrum.

## 5.1 Introduction

Electronic properties of 2D materials can be tuned by chemical functionalization [173, 248]. When radical atoms are adsorbed on the 2D surface they can form covalent, ionic or van der Waals bonds with the in-plane atoms. These atoms change the 2D-material hybridization from  $sp^2$  to  $sp^3$ , which leads to the opening of a bandgap, e.g., graphene, a gapless semimetal, becomes a wide bandgap semiconductor when it is fully hydrogenated [249]. Furthermore, adsorption of hydrogen on 2D materials modifies their structural, optical, magnetic and mechanical properties [48, 100].

Chemical adsorption of hydrogen atoms on two-dimensional materials generates other new crystals with different geometries. Therefore, new hydrogen-based two-dimensional crystals are built with different physical properties from their pristine parent material. Among the several ordering patterns of adatoms on the pristine 2D-material, the most studied metastable geometries are chair, zigzag-line and boat [48, 98, 173, 250, 251]. As shown in Figure 5-1, in the chair (boat) geometry the hydrogen atoms alternate singly (pairwise) on either side of the GaAs plane, while in the zigzag-line configuration the hydrogen atoms of one hexagon alternate three-up and three-down on the GaAs plane. For the chair configuration the unit cell is hexagonal, while for the other two cases the unit cell is rectangular.

Shu *et al* [48] found that hydrogenated germanene tends to form chair and zigzag-line configurations, where its electronic and optical properties show close geometry dependence. They also reported that chair (zigzag-line) hydrogenated configuration is a direct (indirect) bandgap semiconductor. The authors highlight that the zigzag-line germanane could be used as a good optical linear polarizer due to highly anisotropic optical responses. In other theoretical study of germanane, Rivera–Julio *et al* [173] reported that the presence of various isomers in a mostly chair conforma-

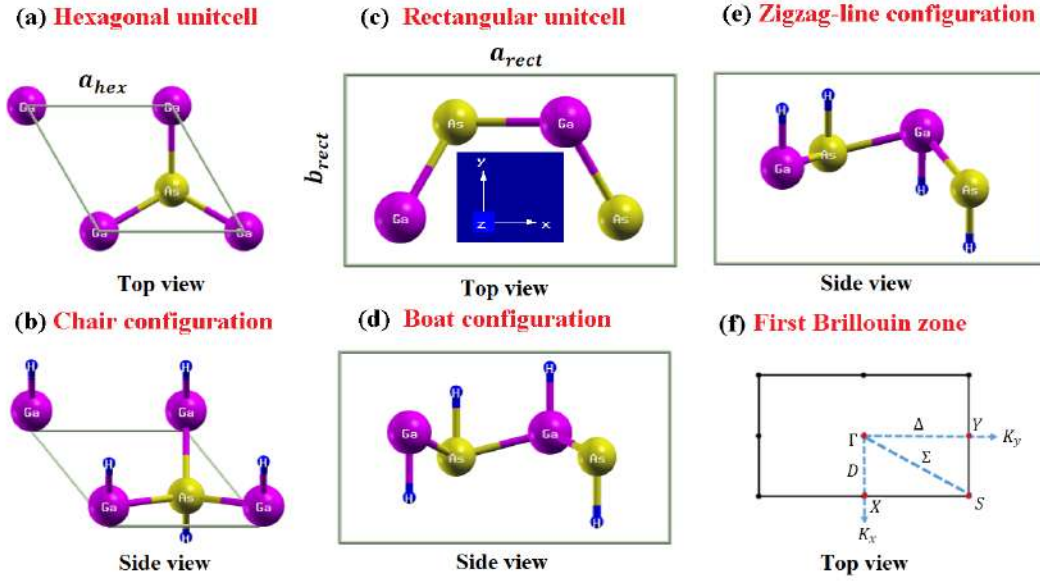


Figure 5-1: Schematic representation for : (a) 2D-GaAs hexagonal unit cell, (b) 2D H-GaAs chair configuration, (c) 2D H-GaAs rectangular unit cell, (d) 2D H-GaAs boat configuration, (e) 2D H-GaAs zigzag-line configuration, and (f) high symmetry points in the Brillouin zone for the rectangular unit cell of 2D H-GaAs.

tion material is expected due to the very small energy difference between the chair, z-line, and boat configurations. Sofo *et al* reported that graphene has two favorable conformations: a chair and boat geometry. Both of them present a direct bandgap at the gamma point with 3.5 eV (3.7 eV) for the chair (boat) configuration [249].

The surface of 2D group III-V materials could be chemically modified by hydrogenation [48, 100, 101]. It has been found both theoretically and experimentally that hydrogen passivation stabilizes two dimensional buckled III-V sheets [102]. Recently, two-dimensional buckled gallium nitride was synthesized by hydrogen surface passivation and graphene encapsulation [102]. Chen *et al* reported that surface hydrogenation tunes the electronic and magnetic properties of 2D-BN [103]. Hydrogenation causes the 2D-BN sheet to have a smaller energy bandgap than the pristine one, while semihydrogenated BN is a ferromagnetic metal [104]. The configuration in which the hydrogen atoms are adsorbed on III-V devices plays an important role in their electronic properties. The fully hydrogenated 2D-BN prefers the zigzag-line configuration rather than the boat or chair configuration [252, 253]. All three hy-

drogenated 2D-BN geometries: chair, zigzag-line and boat, are direct wide-bandgap semiconductors, where, their bandgap sizes are also hydrogen geometry dependent. The hydrogenation of 2D III-V materials could be of great interest not only to be stabilized and synthesized [102] but also to be used in a wide range of applications such as hydrogen storage, biosensors and bandgap tuning for manufacturing nanoelectronic devices [100].

Recently, 2D GaAs has been theoretically predicted to be a mechanically and dynamically stable semiconductor with buckled geometry not only in its pristine hexagonal unit cell but also forming a graphene-GaAs van der Waals heterostructure [123, 169, 171]. The authors also reported that electronic properties of GaAs and graphene can be modulated in a graphene-GaAs heterostructure [169]. In addition, some theoretical and experimental research highlight the importance of graphene/-GaAs systems for future practical applications in plasmonic and photonic technology [230, 231, 232, 233, 234]. However, to the best of our knowledge, there are no previous studies about two-dimensional hydrogenated buckled GaAs system.

Although the dynamical stability of pristine 2D-GaAs has already been studied theoretically by first-principles calculations [123, 169, 171], this material has never been synthesized. The fact that some two-dimensional group III-V materials have been grown by functionalization with hydrogen passivation [102, 254, 255], motivated us to study the stability of two-dimensional hydrogenated buckled gallium arsenide. Thus, in order to explore a possible path towards the synthesis of 2D-GaAs, we have studied the dynamic stability of 2D-GaAs when it is functionalized with hydrogen. We have also determined the structural, mechanical and electronic properties of both materials to evaluate if hydrogen passivation improves these properties with respect to the pristine material. We will also contrast our results with other ab-initio theoretical studies of two-dimensional hydrogenated materials that have already been synthesized; indeed some of their physical properties are similar to those displayed by 2D-HGaAs, such as 2D-HBN and 2D-germanane. Finally, we will present potential applications for 2D-HGaAs taking into account the physical properties found in this study.

Therefore, the structural and electronic properties, as well as the energy and dy-

namical stability of 2D hydrogenated GaAs sheets will be studied in this work taking into account three different geometric configurations: chair, zigzag-line and boat using the Perdew-Burke-Ernzerhof functional (PBE) [142] within DFT framework [135, 136]. Furthermore, in order to study the effect of van der Waals interactions on energy stability, and both structural and electronic properties of 2D hydrogenated GaAs, long range electronic correlations will be treated by the Grimme's method (DFT-D2) [256].

## 5.2 Computational details

The calculations were performed using *Vienna Ab-initio Simulation Package* (VASP) [152, 153] employing the first principles projected augmented wave (PAW) method in the framework of the DFT [135, 136]. Exchange and correlation effects were treated with the generalized gradient approximation (GGA) implemented in the Perdew-Burke-Ernzerhof functional (PBE) [142]. Core electrons were described by the projector augmented wave (PAW) method [151, 182] wherein  $d$  states for Ga and As were included as valence electrons in their PAW pseudo-potentials. The valence electron configurations for H, Ga and As are  $1s^1$ ,  $3d^{10}4s^24p^1$  and  $3d^{10}4s^24p^3$ , respectively. The 2D-GaAs buckled hexagonal primitive cell, with one Ga atom and one As atom, see Figure 5-1(a), was constructed from the zinc-blende structure in the (111) plane [171]. The electron wave function was expanded in plane waves up to a cutoff energy of 500 eV for all the calculations. A gamma-centered grid of  $25 \times 25 \times 1$   $k$ -point has been used to sample the irreducible Brillouin zone in the Monkhorst-Pack special scheme for calculations [146]. Phonon calculations have been performed by taking into account the interactions in a  $8 \times 8 \times 1$  2D H-GaAs supercell [166]. The PYPROCAR code was used to plot the electronic bands of 2D H-GaAs [236]. In addition, a 20 Å vacuum spacing between the adjacent supercells is kept to avoid interactions. For comparison, in order to study the effect of van der Waals interactions on energy stability, and both structural and electronic properties of 2D H-GaAs systems, calculations were also performed using Grimme's method (DFT-D2) [256]. To correct the bandgap values obtained by GGA-PBE and DFT-D2, hybrid func-

tional Heyd-Scuseria-Ernzerhof (HSE) [143] band-calculations are carried out on the relaxed structures obtained with GGA-PBE and DFT-D2, respectively.

## 5.3 Results and discussion

### 5.3.1 Energetic and dynamic stability

In order to study the 2D hydrogenated GaAs stability in the chair, boat and zigzag-line configurations, the adsorption energy was calculated. The adsorption energy is defined by:

$$E_{ad} = E_{H-GaAs} - E_{GaAs} - n_H E_H, \quad (5.1)$$

where  $E_{H-GaAs}$  and  $E_{GaAs}$  are the energies of the hydrogenated and pristine 2D-GaAs layers,  $n_H$  is the number of isolated spin-polarized hydrogen atoms, and  $E_H$  is the energy of a single isolated H atom. Table 5.1 displays these energies for comparison. The values obtained for chair, boat and zigzag-line configurations are -1.180 eV/atom (-1.200 eV/atom), -1.179 eV/atom (-1.204 eV/atom) and -1.182 eV/atom (-1.214 eV/atom), respectively, with PBE (DFT-D2) functional. We can see that all configurations are energetically stable with both PBE and DFT-D2 functionals. The adsorption energy value found for the chair geometry is of the same order of that reported for H-BN (-1.04 eV/atom) in the same geometry [104]. As H-BN chair configuration, the 2D hydrogenated GaAs presents an exothermic reaction and it could be obtained by the reaction of GaAs layers with H atoms. The zigzag-line configuration is energetically more favorable than the chair and the boat by 2 meV (14 meV) and 3 meV (4 meV), respectively, with PBE (DFT-D2) functional. These tiny energy differences with both PBE and DFT-D2 indicate the metastability of 2D hydrogenated GaAs system. We can see that the adsorption energy is more negative with DFT-D2 when compared to that of PBE functional for each configuration by 20 meV (chair), 25 meV (boat) and 32 meV (zigzag-line). Using first principles density functional calculations, Bhattacharya *et al* reported that 2D hydrogenated BN prefers the zigzag-line configuration rather than the boat or chair configuration

[252]. Tang *et al* found similar results for H-BN by dispersion-corrected density functional theory computations (DFT-D2) [253]. Regarding graphane, theoretical studies found that the chair configuration is the most stable one [98, 251, 257]. The energy stability order of our studied configurations was zigzag-line (zigzag-line), chair (boat) and boat (chair) with PBE (PBE-D2) functional. The reported energy stability order for H-BN and H-Ge was zigzag-line, boat and chair [173, 252, 253]. Authors also stated the metastability of these systems. For graphane, the reported configurations order was chair, zigzag-line and boat [257].

Table 5.1: Structural parameters for the pristine 2D-GaAs and three different configurations of 2D H-GaAs obtained by using PBE and vdW-Grimme method (DFT-D2) for comparison. The bandgap ( $E_g$ (eV)) was calculated with PBE and HSE functional. The adsorption ( $E_{ad}$ (eV/atom)) and formation ( $E_f$ (eV/atom)) energies were calculated with PBE functional and vdW-Grimme method (DFT-D2) for comparison.

	Hex-unit cell		Rect-unit cell		GaAsH-Configurations					
	$T_{eo}$	$T_{eo}$ <i>vdW</i>	$T_{eo}$	$T_{eo}$ <i>vdW</i>	<i>Chair</i>	<i>Chair</i> <i>vdW</i>	Boat	Boat <i>vdW</i>	Zigzag-line	Zigzag-line <i>vdW</i>
$a_{hex}$ (Å)	4.05 3.97 [123] 4.05 [171]	4.00	-	-	4.08	4.01	-	-	-	-
$a_{rect}$ (Å)	-	-	7.01	6.93	-	-	6.74	6.49	5.96	5.55
$b_{rect}$ (Å)	-	-	4.04	4.00	-	-	4.06	3.99	4.06	3.99
$d_{Ga-As}$ (Å)	2.41	2.39	2.41	2.39	2.48	2.45	2.49	2.46	2.48	2.45
$d_{Ga-H}$ (Å)	-	-	-	-	1.56	1.56	1.56	1.56	1.56	1.55
$d_{As-H}$ (eV)	-	-	-	-	1.52	1.51	1.52	1.51	1.52	1.51
buckling(Å)	0.58 0.55 [123] 0.58 [169]	0.60	0.51	0.60	0.79	0.80	0.88	0.92	0.86	0.86
$E_{gPBE}$ (eV)	1.09 $\Gamma K$ 1.29 $\Gamma K$ [123] 1.08 $\Gamma K$ [171]	1.35 $\Gamma K$	-	-	1.68 $\Gamma\Gamma$	1.87 $\Gamma\Gamma$	2.16 $\Gamma\Gamma$	2.20 $\Gamma\Gamma$	2.23 $\Gamma D$	2.30 $\Gamma D$
$E_{gHSE}$ (eV)	1.89 $\Gamma K$	2.18 $\Gamma K$	-	-	2.51 $\Gamma\Gamma$	2.73 $\Gamma\Gamma$	2.98 $\Gamma\Gamma$	3.00 $\Gamma\Gamma$	3.19 $\Gamma D$	3.32 $\Gamma D$
$E_{adPBE}$ (eV/atom)	-	-	-	-	-1.180	-1.200	-1.179	-1.204	-1.182	-1.214
$E_{fPBE}$ (eV/atom)	-	-	-	-	-0.046	-0.066	-0.045	-0.070	-0.048	-0.080

In order to compare the stability of H-GaAs with respect to other hydrogenated 2D systems, we calculated the 2D H-GaAs formation energies by the following mathematical expression:

$$E_f = E_{H-GaAs} - E_{GaAs} - n_H E_H^*, \quad (5.2)$$

where  $E_{H-GaAs}$  and  $E_{GaAs}$  are the energies of the hydrogenated and pristine 2D-GaAs layers,  $n_H$  is the number of hydrogen atoms, and  $E_H^*$  is the energy of a  $H_2$  molecule divided by two. From Table 5.1, the energy values obtained for the chair, boat and zigzag-line configurations are, respectively, -0.046 eV/atom (-0.066

eV/atom), -0.045 eV/atom (-0.070 eV/atom) and -0.048 eV/atom (-0.080 eV/atom) with PBE (DFT-D2) functional. The formation energies of our systems are negative, which physically means that hydrogenation of 2D-GaAs is feasible to occur. Sofo *et al* [249] reported a formation energy of -0.15 eV/atom and -0.10 eV/atom for graphane chair and boat configurations, respectively. Indeed, graphane has already been experimentally synthesized by various methods such as hydrogen plasma exposure of graphene, thermal exfoliation of graphene oxides, STM-assisted hydrogenation of graphene, plasma-enhanced CVD and electron-induced dissociation of HSQ on graphene [257, 258]. In addition, the fact that both thermal stability of hydrogenated boron nitride adsorbed on Ni(111) has been found experimentally [254, 255] and two-dimensional buckled gallium nitride has been synthesized by hydrogen surface passivation and graphene encapsulation on SiC(0001) [102], paves the way for the synthesis of other potential 2D group III–V materials such as buckled 2D-GaAs.

In order to study the dynamical stability of our systems, we have calculated the phonon dispersion around the  $\Gamma$  point by a frozen phonon approach. Figure 5-2 displays the phonon dispersion curves for pristine 2D-GaAs, and chair, boat and zigzag-line configurations with DFT-PBE functional. It proves the dynamical stability of the studied system, since there are no imaginary frequencies in the phonon dispersion. Some negative frequencies, i.e., they are actually imaginary frequency, near the  $\Gamma$  point are visible as well. This feature has been found in other 2D-systems [211, 239, 241, 242, 243] and highlights the flexural acoustic mode of 2D-systems. They are often present in theoretical calculations due to finite numerical and convergence accuracy close to the  $\Gamma$  point [239]. The highest frequency modes, corresponding to H bond stretching modes, occur at 65.1 THz ( $2170\text{ cm}^{-1}$ ) for the boat configuration, and at 64.8 THz ( $2160\text{ cm}^{-1}$ ) and 64.7 THz ( $2157\text{ cm}^{-1}$ ) for the chair and zigzag-line configurations, respectively. These results are in accordance with those found for the energy stability of our systems. The vibrational frequency is lowest (highest) for the most (less) stable configuration. Therefore, the zigzag-line (boat) configuration has the highest (lowest) stability and the lowest (highest) mode of vibration. The reported highest frequency modes for graphane in the boat (3026

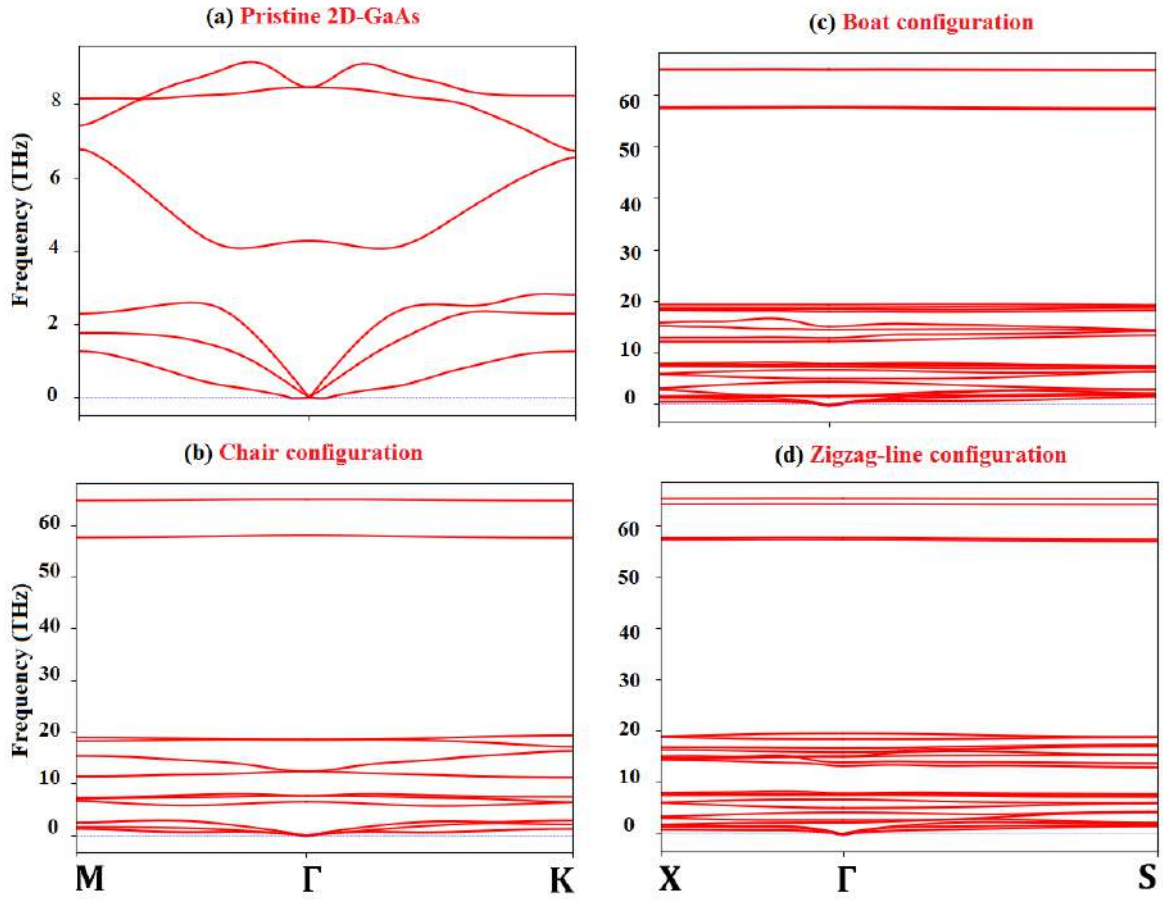


Figure 5-2: Phonon dispersion curves for (a) pristine 2D-GaAs, (b) 2D H-GaAs chair configuration, (c) 2D H-GaAs boat configuration, and (d) 2D H-GaAs zigzag-line configurations with DFT-PBE functional.

$cm^{-1}$ ) and chair ( $2919\text{ cm}^{-1}$ ) configurations are larger than those reported in this work. This suggests a more covalent character for the H-C bond in graphene as compared to that of H-GaAs.

### 5.3.2 Structural properties

To study the structural properties of pristine 2D-GaAs, and compare them to those found for chair, boat and zigzag-line configurations, we have first optimized the structural parameters of 2D-GaAs hexagonal primitive cell. Then, from the obtained values, the 2D-GaAs rectangular unit cell has been constructed and relaxed (Figure 5-2(c)). The longer side length ( $a_{rect}$ ) of this latter unit cell is three times

the Ga-As shortest distance ( $d_{Ga-As}$ ) of the hexagonal unit cell, while the other side ( $b_{rect}$ ) is equal to the lattice parameter of the hexagonal primitive cell ( $a_{hex}$ ). Finally, from these optimized hexagonal and rectangular unit cells, the chair (Figure 5-2(b)), and boat (Figure 5-2(c)) and zigzag-line (Figure 5-2(d)) configurations were built and relaxed, respectively.

The optimized parameters for 2D-GaAs monolayers: hexagonal and rectangular unit cells, and chair, boat and zigzag-line configurations are depicted in Table 5.1. Our results for hexagonal 2D-GaAs unit cell are in good agreement with previous theoretical ones reported by DFT. Although the average Ga-As distance is almost the same for the three configurations, a slight difference in H atoms bonding of the chair, boat and zigzag-line configurations is found. Different from chair configuration, both boat and zigzag-line have two different GaAs bond lengths. In the former configuration, the GaAs distances are equal because all GaAs bonds connect with H atoms attached at opposite sides of the sheet. On the contrary, for both latter configurations, the length of the GaAs distance, where Ga and As bonding the H atoms lying on the opposite side of the plane, is shorter than those ones bonding the H atoms on the same side of the plane. For boat (zigzag-line) configuration the shortest Ga-As distance was 2.483 Å (2.483 Å); while the largest, due to H-H repulsion, was 2.493 Å (2.485 Å). Regarding to GaH and AsH bonds, we can see that, due to the charge repulsion, GaH bond lengths are larger than those of AsH in all three configurations. The GaH (AsH) bond lengths in all three configurations are almost the same, but larger than those found for BH (NH) in H-BN [252] and CH in graphane [249].

A comparison of structural results shows that both unit cell lattice parameters (hexagonal and rectangular) and cation-anion distance ( $d_{Ga-As}$  and  $d_{As-H}$ ) decrease when we go from the DFT-D2 functional to PBE, while cation-cation distance ( $d_{Ga-H}$ ) is the same for both functionals.

The average Ga-As distance ( $d_{Ga-As}$ ) for chair, boat and zigzag-line configurations are larger than the one found for pristine 2D-GaAs by 2.90% (2.51%), 3.32% (2.93%) and 2.90% (2.51%), respectively, when using PBE (vdW) functional, as shown in Table 5.1. In order to get physical insight on the plasticity and stiffness

of pristine 2D-GaAs when hydrogenated, the mechanical properties for hexagonal pristine 2D-GaAs and hexagonal 2D-HGaAs chair configuration are compared. We found that in-plane Young's modulus (Poisson's ratio) for pristine 2D-GaAs is larger (smaller) than that of 2D-HGaAs chair configuration when using PBE functional by 125% (31.92%), which means that the pristine 2D-GaAs material displays less stiffness and more plasticity when hydrogenated. The values found for the in-plane Young's modulus (Poisson's ratio) for pristine 2D-GaAs and 2D-HGaAs materials are  $44.4 \text{ Jm}^{-2}$  (0.32) and  $19.7 \text{ Jm}^{-2}$  (0.47), respectively. The Poisson's ratio  $\nu$  and the in-plane Young's modulus  $Y$  are obtained from the calculated  $C_{11}$  and  $C_{12}$  elastic constants and multiplied later by the corresponding optimized unit-cell  $z$  distance. Their respective definitions are [237]:

$$\nu = C_{12}/C_{11}, \quad (5.3)$$

$$Y = (C_{11}^2 - C_{12}^2)/C_{11}, \quad (5.4)$$

### 5.3.3 Electronic structure and Bader charge transfer analysis

The electronic band structures for the pristine 2D-GaAs sheet, and chair, boat and zigzag-line configurations for 2D H-GaAs obtained with the PBE functional are displayed in Figure 5-3. The red lines represent the contributions of GaAs- $4p_z$  orbitals, the black lines represent the contributions of GaAs- $4p_{xy}$  mixed orbitals, while the yellow ones the contribution of either GaAs- $4s$  (pristine 2D-GaAs) or GaAs- $4s$  and H- $1s$  mixed orbitals (2D H-GaAs). We can see in Figure 5-3(a), for the pristine 2D-GaAs sheet, that hybridized  $4p_z$  and  $4p_{xy}$  orbitals are near the Fermi level in the valence bands, and  $4s$  and  $4p$  mixed unoccupied orbitals in the conduction bands. In addition,  $4s$  orbital can be seen at the bottom of the conduction band. From band structures for the chair, boat and zigzag-line configurations (Figure 5-3(b), Figure 5-3(c) and Figure 5-3(d), respectively) we can see in the valence bands an increased overlap between  $p_z$  and both planar  $p_{xy}$  and  $s$  orbitals when compared to the ones for pristine 2D-GaAs sheet (Figure 5-3(a)). As a result, the  $sp^2$  hybridization

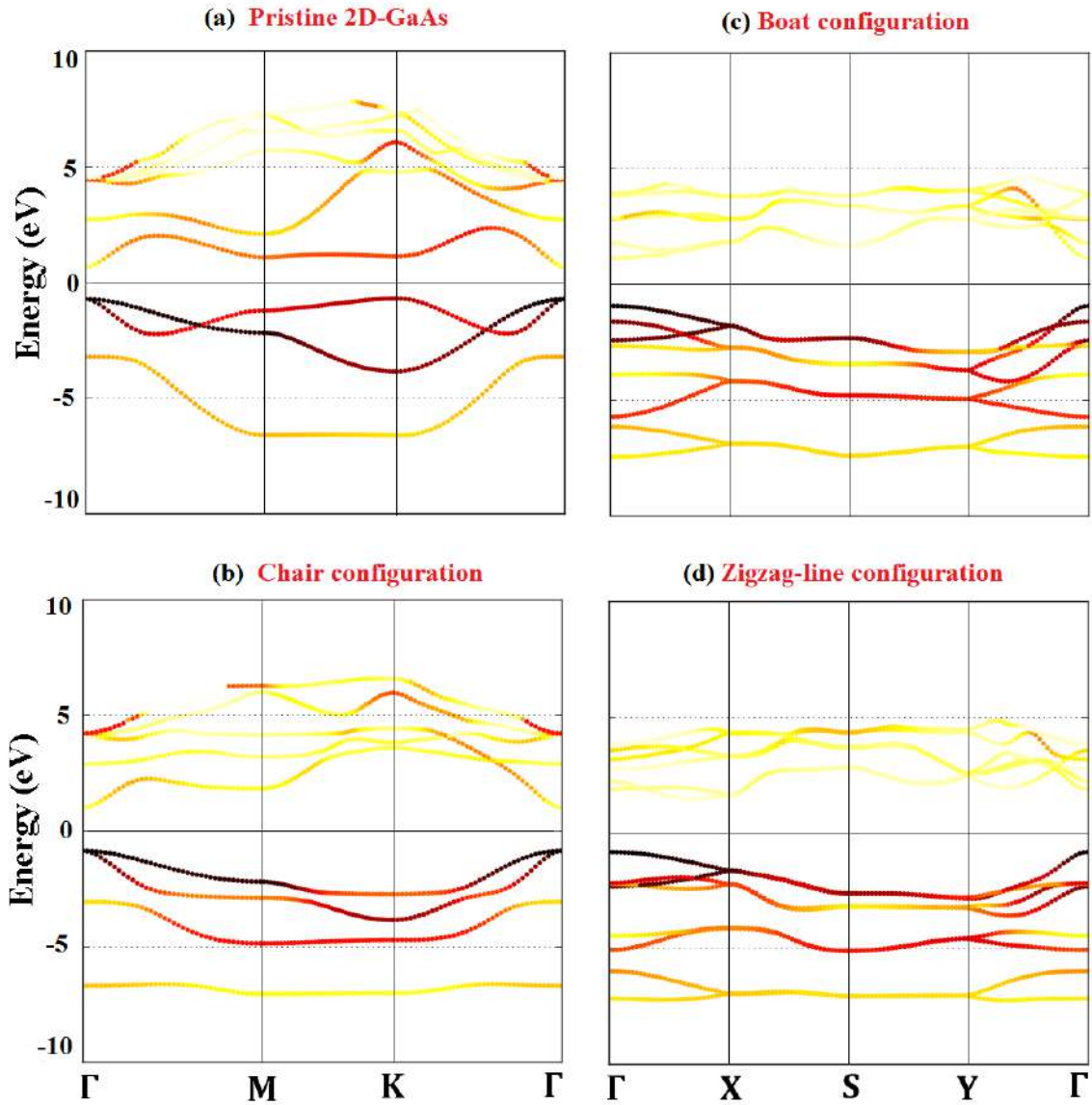


Figure 5-3: Electronic band structure for (a) the pristine 2D-GaAs sheet, and (b) chair, (c) boat, and (d) zigzag-line configurations for 2D H-GaAs, with DFT-PBE functional. The red lines represent the contributions of GaAs-4 $p_z$  orbitals, the black lines the contributions of GaAs-4 $p_{xy}$  mixed orbitals, and the yellow lines represent the contributions either of the GaAs-4s orbitals (pristine 2D-GaAs) or GaAs-4s and H-1s mixed orbitals (2D H-GaAs).

becomes weaker, and the  $sp^3$  one, stronger. Therefore, the average Ga-As atoms bond length ( $d_{Ga-As}$ ) for all three configurations is much larger than that of pristine 2D-GaAs, as shown in Table 5.1. Furthermore, in comparison to pristine 2D-GaAs band structure, an extra  $s$  orbital, due to H contribution, is shown in the bottom of

the valence bands for all three configurations.

From Figure 5-3(a), Figure 5-3(d) and Figure 5-1(f), we can see that pristine 2D-GaAs and zigzag-line configurations are  $\Gamma$ - $K$  and  $\Gamma$ - $D$  indirect semiconductors, respectively; while, from Figure 5-3(b) and Figure 5-3(c), the chair and boat configurations display a  $\Gamma$ - $\Gamma$  direct bandgap nature. As shown in Table 5.1, the corrected bandgap values for chair, boat and z-line configurations with HSE method are larger than those ones found by DFT-PBE (DFT-D2) for chair, boat and z-line, by 49.40% (46.00%), 37.96% (36.36%) and 43.05% (44.35%), respectively. The bandgap sizes of all studied configurations are also hydrogen dependent, and wider than that of pristine 2D-GaAs with PBE, PBE-vdW and HSE functionals, as shown in Table 5.1. Thus, the presence of H on 2D-GaAs layer opens the bandgap of 2D-GaAs layer, which makes it a potential candidate for optoelectronic applications in the visible range. A qualitatively similar bandgap opening effect of H on graphene has been reported by Sofo *et al* [249]. On the contrary, hydrogenation of 2D-BN sheet leads to a smaller bandgap than the pristine one [104].

The bandgap energy for pristine 2D-GaAs changes from 1.89 eV (red light) to 2.51 eV (blue light), 2.98 eV (violet light), and 3.19 eV (violet light) for chair, boat, and zigzag configurations, respectively, with the HSE approach when hydrogenated. It can be noticed from Table 5.1 that hydrogen tunes the  $\Gamma$ - $K$  indirect bandgap of pristine 2D-GaAs to  $\Gamma$ - $\Gamma$  direct one for both chair and boat configurations, while the zigzag configuration remains indirect. Moreover, given that the energy differences for all three configurations are tiny,  $\sim 2$ -3 meV with PBE functional, our results indicate that 2D-HGaAs is metastable in the chair, boat, and zigzag-line configurations, and thus the synthesis of these phases could be feasible by using the appropriate growth conditions and/or a specific substrate. Hence, the hydrogenation of 2D-GaAs tunes the bandgap of 2D-GaAs, which makes it a potential candidate for optoelectronic applications in the blue and violet ranges of the visible electromagnetic spectrum.

In order to get physical insight about the direction of charge transfer and ionicity of the studied 2D H-GaAs configurations, we have calculated the charge transference by Bader analysis [195]. For pristine 2D-GaAs a charge transfer of  $-0.60e$  ( $-0.59e$ ) from Ga to As atoms with PBE (DFT-vdW) functional was found, as shown in

Table 5.2: Bader charge state of Ga, As,  $H_{Ga}$  and  $H_{As}$  atoms in chair, boat and zigzag-line configurations for 2D H-GaAs systems with PBE and DFT-D2 functionals.

	Bader charge state			
	Pristine 2D-GaAs	Chair	Boat	Zigzag-line
	(e)	(e)	(e)	(e)
Ga	+0.60	+0.84	+0.72	+0.70
vdW	+0.59	+0.84	+0.70	+0.67
As	-0.60	-0.21	-0.23	-0.20
vdW	-0.59	-0.20	-0.20	-0.16
$H_{Ga}$	-	-0.37	-0.32	-0.31
vdW	-	-0.37	-0.31	-0.31
$H_{As}$	-	-0.26	-0.17	-0.19
vdW	-	-0.26	-0.17	-0.19

Table 5.2. This charge transference is larger than that of  $-0.34e$  found in 2D H-BN [252], which means that our system is more ionic. For other configurations of H atoms, due to the charge conservation principle, the electron lost by the Ga atoms is gained by As,  $H_{Ga}$  and  $H_{As}$  atoms of the corresponding unit cell. For instance, we see in Table 5.2, for the chair configuration, a positive charge for Ga of  $+0.84e$ , while the net negative charge for As ( $-0.21e$ ),  $H_{Ga}$  ( $-0.37e$ ) and  $H_{As}$  ( $-0.26e$ ) atoms is  $-0.84e$ .

The Bader analysis of Ga, As and H atoms in the three 2D H-GaAs configurations displays that in all configurations As,  $H_{As}$  and  $H_{Ga}$  acquire a negative charge state, gain electrons, while Ga acquires a positive charge state, loses electrons, as shown in Table 5.2. Physically, this takes place due to the electronegative difference between Ga, As and H atoms. We can also see that in all configurations the charge transference is larger than that of pristine 2D-GaAs sheet, which means that ionicity increases. This result agrees with the increased  $sp^3$  hybridization found in the band structure analysis for all configurations. The charge transference order for our systems is chair > boat > zigzag-line. Table 5.2 also shows that the charge transference in all configurations is slightly minor with DFT-vdW when compared to that with PBE functional, but follow the same qualitative trend. This effect cannot be directly attributed to van der Waals interactions since the DFT-D2 method is not self-consistent; rather, it is due to both the small change in atomic positions with respect to the ones obtained from PBE and the short range electronic interactions.

## 5.4 Conclusions

The ground state structure, stability, structural and electronic properties of two-dimensional hydrogenated GaAs with chair, boat and zigzag configurations have been studied by first-principles calculations with PBE and DFT-vdW functionals. To correct the bandgap values obtained by GGA-PBE, calculations with the hybrid functional Heyd-Scuseria-Ernzerhof (HSE) are carried out. The formation energy and phonon dispersion analysis display that all three hydrogenated configurations are stable semiconductors, where the most stable configuration is the zigzag, followed with a slight energy difference by chair (boat) and boat (chair) configurations with PBE (DFT-vdW) functional. Our results indicate that 2D-HGaAs is metastable in the chair, boat and zigzag-line configurations, and thus the synthesis of these phases could be feasible by using the appropriate growth conditions and/or a specific substrate. On the other hand, DFT-vdW interactions increase the adsorption energies and reduce the equilibrium distances when compared with PBE functional for the three configurations, but display qualitatively the same physical results on their stability and electronic properties. The calculated mechanical properties indicate that pristine 2D-GaAs displays less stiffness and more plasticity when it is hydrogenated. Electronic structure analysis shows that hydrogen reduces the in-plane  $sp^2$  ( $\sigma$  bonding) hybridization, and increases the  $sp^3$  hybridization when compared with pristine sheet. As a result, the 2D hydrogenated GaAs layers have a larger bandgap than the pristine one with both PBE and HSE functionals. In addition, zigzag is a  $\Gamma-D$  indirect semiconductor, while chair and boat are  $\Gamma-\Gamma$  direct semiconductors.

The bandgap energy for pristine 2D-GaAs changes from red to violet (blue) range for boat and zigzag (chair) configurations, with the HSE approach when hydrogenated. Our findings indicate that the presence of H on 2D-GaAs tunes the bandgap of pristine 2D-GaAs, which makes 2D-HGaAs a potential candidate for optoelectronic applications in the blue and violet ranges of the visible electromagnetic spectrum. Moreover, they suggest that 2D buckled-GaAs could be a good candidate to be synthesized by hydrogen surface passivation.

## 5.5 Publication

Chapter 5 was published as:

A González-García, W López-Pérez, R González-Hernández, J Rivera-Julio, C Espejo, MV Milošević, and FM Peeters. *Two-dimensional hydrogenated buckled gallium arsenide: an ab-initio study*. Journal of Physics: Condensed Matter, 32(14):145502, 2020.

# Chapter 6

## Transition-metal adatoms on 2D-GaAs: a route to chiral magnetic 2D materials by design

*Using relativistic density-functional calculations, we examine the magneto-crystalline anisotropy and exchange properties of transition-metal atoms adsorbed on 2D-GaAs. We show that single Mn and Mo atoms (Co and Os) strongly bind on 2D-GaAs, and induce local out-of-plane (in-plane) magnetic anisotropy. When a pair of TM atoms is adsorbed on 2D-GaAs in a close range from each other, magnetisation properties change (become tunable) depending on concentration and ordering of the adatoms. In all cases, we reveal the presence of strong Dzyaloshinskii-Moriya interaction (DMI). These results indicate novel pathways towards 2D chiral magnetic materials by design, tailored for desired applications in magneto-electronics.*

### 6.1 Introduction

Two-dimensional (2D) materials are nowadays being intensely studied both theoretically and experimentally due to their unique physical properties [9, 10, 54, 169, 170, 171, 172, 173]. Most of them are nonmagnetic in their pristine form, which restricts their applicability in magneto-electronics. According to the Mermin-Wagner-Hohenberg theorem [168, 259], thermal fluctuations strongly suppress long-

range magnetic order in two-dimensional materials at any non-zero temperature, even if those materials are intrinsically magnetic in 3D bulk form; nonetheless, such detrimental effect of fluctuations can be neutralized by the presence of magnetic anisotropy (MA). The pioneering experimental confirmations of magnetism in  $\text{CrI}_3$  [132] and  $\text{CrGeTe}_3$  [69] in 2017 opened an entirely new field of atomically-thin magnetic crystals, that does not cease to surprise [70]. For example, the critical temperature of  $\text{CrGeTe}_3$  tends to zero when material is reduced in thickness to the monolayer limit. However, when anisotropy is introduced in the  $\text{CrGeTe}_3$  system, by application of an (even tiny) external magnetic field, a non-zero magnetisation establishes at finite temperature [69, 70]. Zhang *et al.* reported robust intrinsic ferromagnetism and half semi-conductivity in two-dimensional single-layer chromium trihalides. They found a magnetocrystalline anisotropy energy (MAE) of  $685.5 \mu\text{eV}$  and  $185.5 \mu\text{eV}$  for 2D- $\text{CrI}_3$  and 2D- $\text{CrB}_3$  [260], respectively. The authors state that 2D-chromium trihalides systems are promising candidates for low-dimensional magneto-electronic applications. For comparison, these values of MAE are higher than those found for ferromagnetic materials such as bulk Fe, Ni and Co, which present a MAE per atom of  $1.4 \mu\text{eV}$ ,  $2.7 \mu\text{eV}$  and  $65 \mu\text{eV}$  [261], but lower for transition metal monolayers [262], magnetic atoms on metal surface [263] and ferromagnetic-semiconductor interface [264], whose MAE per atom are on the order of meV.

The spin-orbit coupling (SOC) is the microscopic source of magnetic anisotropy. Hence, tuning the orbital and spin moment of a crystal is fundamental; as an illustration, the magnetic anisotropy in a 2D material can be induced by doping with transition metals, among other ways of manipulating the SOC of a crystal [58, 59, 60, 61]. Long-range ferromagnetic ordering and high magnetic anisotropy have been found in manganese-doped 2D systems [260, 265, 266]. Using density functional theory (DFT) calculations, Mishra *et al.* reported long-range ferromagnetic ordering in Mn-doped two-dimensional dichalcogenides [265]. Sun *et al.* demonstrated that the  $\text{MnX}_3$  ( $X = \text{F}, \text{Cl}, \text{Br}, \text{I}$ ) are dynamically and thermodynamically stable up to high temperatures, and exhibit large magnetic moments ( $4 \mu_B$ ), high Curie temperatures, and large in-plane magnetic anisotropy energies [266].

On the other hand, diluted magnetic semiconductors (DMSs) based on III–V group materials have been of great interest in 3D systems due to their potential applications in spintronic devices [267, 268, 269, 270, 271]; in particular bulk Mn-doped GaAs has attracted significant interest in that respect [269, 270, 271]. The question arises: how the magnetic anisotropy properties of the Mn-GaAs system evolve in the ultrathin limit of that material? Lan *et al.* investigated from first principles the magnetic properties of 2D (Ga,Mn)As but did not study the magnetic anisotropy of this material, nor covered the magnetic exchange in sufficient detail. [272].

Recent theoretical [61, 273] and experimental [274] works have reported that the adsorption or doping of Os and Co on/in 2D monolayer systems can induce a large magnetic anisotropy (MA). Sivek *et al.* showed by an *ab-initio* study that transition-metal atoms (Os and Co) adsorbed on MoS<sub>2</sub> and fluorographene monolayers can cause a huge magnetocrystalline anisotropy to arise [273]. Furthermore, Torun *et al.* found a high MAE in Co on graphene and Os-doped MoTe<sub>2</sub>. They reported an out-of-plane and in-plane easy-axis direction of Co-on-graphene and Os-doped MoTe<sub>2</sub> systems, respectively [61].

Another important consequence of relativistic effects i.e., spin-orbit coupling combined with a broken spatial inversion symmetry, is the appearance of Dzyaloshinskii-Moriya interaction (DMI) [174, 175]. DMI, characterized by a Dzyaloshinskii-Moriya vector  $\mathbf{D}$  acting on a pair of spins, is an antisymmetric magnetic exchange interaction that aligns the neighbouring spins orthogonally to each other, with a unique sense of rotation, instead of the parallel or antiparallel spin alignments obtained by the usual Heisenberg exchange interaction [176]. DMI is essential for creating non-collinear long-range spin order in ultra-thin magnetic films, and is responsible for the creation, stabilisation and manipulation of skyrmions and chiral domain walls as bearers of attractive applications in novel spintronic, memory and logic devices [15, 177]. Thin-film heterostructures consisting of transition metal layers have been investigated on the basis of first-principles calculations in combination with spin-polarised scanning tunnelling microscopy (SP-STM), to report how DMI influences their magnetic structure, and changes standard perception of magnetic properties

[178, 275, 276, 277].

Motivated by the above developments, and by recent theoretical reports about the dynamical and mechanical stability of 2D-GaAs semiconductor [123, 171], here we investigate both the magnetic anisotropy and Dzyaloshinskii-Moriya interaction induced by transition metals adsorbed on two-dimensional gallium arsenide (TM=Mn, Co, Mo and Os). Experimental and theoretical studies of induced MA and DMI in such systems are entirely lacking at present, despite the materials in question being rather accessible and readily used in technological applications. The understanding of physical conditions for a given TM adatom to induce magnetic anisotropy, exchange and DMI in a given 2D material will pave the way for the creation of 2D magnetic materials at will, as required for a specific application in magneto-electronic technologies.

## 6.2 Computational and theoretical details

The calculations were performed using Vienna Ab-initio Simulation Package (VASP) [152, 153] employing the first-principles pseudo-potential method in the framework of the DFT [135, 136]. Exchange and correlation effects were treated with the generalized-gradient approximation implemented in the Perdew–Burke–Ernzerhof functional [142]. The core electrons were described by the projector augmented wave (PAW) method [151, 182] wherein the  $d$  states for Ga and As were included as valence electrons in their PAW pseudo-potentials. The hexagonal primitive cell, with one Ga atom and one As atom was constructed from the zinc-blende structure in the (111) plane [171]. The systems under study are composed of a 551–GaAs supercell in which a single transition metal atom (Mn, Co, Mo and Os) is adsorbed on top of the hexagonal Ga-As tile, as shown in Figure 6-1(a). This is equivalent to 4% coverage of TM atoms per Ga or As atoms. This supercell was constructed using the optimised 2D-GaAs unit-cell, and then relaxed. The optimised placements for Mn, Co, Mo and Os atoms are shown in Figure 6-1(b), Figure 6-1(c), Figure 6-1(e), and Figure 6-1(f), respectively.

In order to study the magnetic interaction between neighbouring TM atoms,

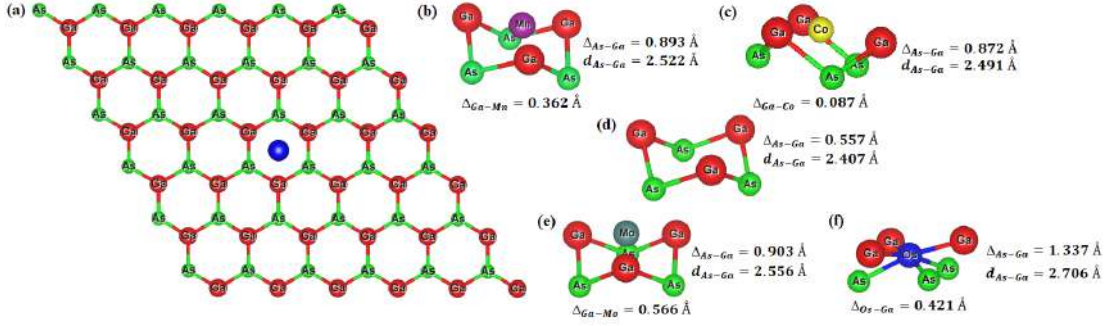


Figure 6-1: Oblique view of the considered systems: (a) top view of a transition-metal adatom at the hollow site of 551–GaAs supercell, and side views of the optimised placements for the adsorbed (b) Mn, (c) Co, (e) Mo, and (f) Os atoms at such a site. For comparison, panel (d) shows relaxed buckling of 551–GaAs at the hollow site in absence of an adatom.

identical TM atoms were considered adsorbed on 2D-GaAs in close proximity to each other, as shown in Figure 6-5.

The electron wave function was expanded in plane waves up to a cutoff energy of 500 eV in all the calculations. A  $\Gamma$ -centered grid of  $25 \times 25 \times 1$   $k$ -points was used to sample the irreducible Brillouin zone in the Monkhorst–Pack special scheme [146], except for the 551–GaAs supercell where a  $8 \times 8 \times 1$   $k$ -point grid was used. Grimme’s method (DFT-D2) was implemented to treat long-range electronic correlations [256]. The PYPROCAR code was used to plot the electronic bands of both 2D-GaAs pristine unit-cell and TM on 551–GaAs supercell [236]. In addition, a 20 Å vacuum was kept as vertical spacing between the adjacent supercells to avoid interactions. The optimised parameters for 2D-GaAs monolayer, and the TM adsorbed on 551–GaAs are given in Table 6.1. We have calculated the charge transference by Bader analysis [195]. In our study, the spin-orbit interaction for TM on 551–GaAs supercell has been taken into account. Spin-orbit coupling is a relativistic interaction between moving electrons and a local electric field  $\mathbf{E}$  created in their rest frame. From special relativity we know that in the electron frame a magnetic field  $\mathbf{B}$  is created. Due to the interaction of  $\mathbf{B}$  with the electron intrinsic magnetic moment, and the Zeeman effect, the orbital energy levels are split, which can lead to different transition levels with energy:

$$H_{so} = \xi(r)\mathbf{L} \cdot \mathbf{S}, \quad (6.1)$$

Table 6.1: Calculated lattice constant ( $a_0$  (Å)), angle between neighbouring bonds ( $\theta$ ), buckling parameter ( $\Delta_{As-Ga}$  (Å)), vertical Ga–TM distance ( $\Delta_{Ga-TM}$  (Å)), adsorption energy per TM atom ( $E_{ads}$ ), bandgap value ( $E_G$ ), magnetic moment per TM atom ( $\mu$ ), charge located on the adatom ( $\Delta\rho$ ), and magnetocrystalline anisotropy energy (MAE) per TM atom, for 2D-GaAs monolayers and TM on 551–GaAs supercell (TM = Mn, Co, Mo and Os). The positive (negative) value of the MAE implies that the easy magnetisation axis is out-of-plane (in-plane) to the surface of the 2D structure.

	$a_0$ (Å)	$\theta$ (°)	$d_{As-Ga}$ (Å)	$\Delta_{As-Ga}$ (Å)	$\Delta_{As-MT}$ (Å)	$E_{ads}$ (eV)	$E_G$ (eV)	$\mu$ ( $\mu_B$ )	$\Delta\rho$ (e)	MAE (meV)
2D-GaAs	4.048	114.4	2.407	0.577	–	–	1.060 $\Gamma K$	–	–	–
	(4.050)[171]	114.3	2.410	0.550	–	–	1.080 $\Gamma K$	–	–	–
	(3.970)[123]	114.7	2.380	0.550	–	–	1.290 $\Gamma K$	–	–	–
Mn	3.999	114.6	2.522	0.893	1.255	2.166	0.583 $\Gamma \Gamma$	3.000	0.532	0.530
Co	3.997	111.8	2.491	0.872	0.959	3.539	0.672 $\Gamma M$	1.000	0.043	–0.950
Mo	4.000	117.6	2.556	0.903	1.469	2.799	Halfmetal	4.000	0.427	3.460
Os	3.991	100.8	2.706	1.337	0.916	4.967	0.156 MM	2.000	–0.411	–6.930

where  $\xi(\mathbf{r}) = e^2/2m_e^2c^2r^3$  contains the entire radial dependence of the SOC Hamiltonian operator [154, 155].  $\mathbf{L}$  and  $\mathbf{S}$  are the electron orbital and spin angular momentum, respectively.

The magnetocrystalline anisotropy energy (MAE) of single TM on 551–GaAs was calculated using the following expression

$$MAE = E_{\parallel} - E_{\perp}, \quad (6.2)$$

where  $E_{\parallel}$  and  $E_{\perp}$  are total energies for the in-plane and out-of-plane magnetisation directions with respect to the surface of the 2D crystal, respectively [61]. Table 6.1 displays the calculated magnetocrystalline anisotropy energy (MAE) per TM atom of our systems.

To obtain magnetic exchange interactions between two adsorbed metal atoms, we employed the four-state energy mapping methodology [179, 180]. Heisenberg spin Hamiltonian is considered in the form:

$$H = \frac{1}{2} \sum_{i,j} \mathbf{S}_i \mathbf{J}_{ij} \mathbf{S}_j, \quad (6.3)$$

where  $\mathbf{S}_i = (S_i^x, S_i^y, S_i^z)$  is a vector.  $\mathbf{J}_{ij}$  is  $3 \times 3$  matrix describing the magnetic exchange interaction between two magnetic sites.  $\mathbf{J}_{ij}$  may be formally decomposed into 3 components: the diagonal part, i.e. the isotropic exchange; the antisymmetric component, also known as the Dzyaloshinskii–Moriya interaction (DMI), whose

vector  $\mathbf{D}$  is made from off-diagonal elements of the antisymmetric exchange, and the off-diagonal elements of the isotropic exchange. Since off-diagonal elements of the isotropic exchange part are small, in this work, we will focus on the two first components: the isotropic exchange and DMI. The DMI components, i.e.,  $D_{12}^x$ ,  $D_{12}^y$  and  $D_{12}^z$ , were calculated by the following equations:  $D_{12}^x = \frac{1}{2}(J_{12}^{yz} - J_{12}^{zy})$ ,  $D_{12}^y = \frac{1}{2}(J_{12}^{zx} - J_{12}^{xz})$ , and  $D_{12}^z = \frac{1}{2}(J_{12}^{xy} - J_{12}^{yx})$ . All nine elements of the matrix ( $J_{12}^{ij}$ ), as well as the DMI parameters, are listed in [Table 6.2](#). In order to obtain the ground state spin configuration of two adatom cases, the Heisenberg spin Hamiltonian, which is constructed with the obtained magnetic exchange interaction via DFT, is solved iteratively.

Literature suggests an alternative (LKAG) approach to find the magnetic exchange parameter for ferromagnetic metals and alloys [278], however this method does not yield information about anisotropic interactions and DMI. We therefore use 4SM method, due to our interest extended beyond the isotropic magnetic exchange interactions, also to the induced DMI when TM adatoms are adsorbed on 2D-GaAs semiconductor and inversion symmetry is broken. 4SM method has been shown to be particularly effective for this purpose [279].

## 6.3 Results and discussion

### 6.3.1 Energetic stability and structural properties

We first calculated the adsorption energy of a single TM adatom (Mn, Co, Mo and Os) on a 551-GaAs supercell and examined the stability of our systems using the following expression

$$E_{ad} = E^{(GaAs)} + E^{(TM)} - E^{(TM-GaAs)}, \quad (6.4)$$

where  $E^{(TM-GaAs)}$  and  $E^{(GaAs)}$  are the total energies of the system with adsorbed TM atom and 551-GaAs supercell respectively, and  $E^{(TM)}$  is the energy of a single isolated TM atom. More stable structures have a larger adsorption energy. We found that the preferential location of all the TM adatoms studied in our work is the hollow

site (within the hexagonal Ga-As tile), followed by the site on top of As as the second most favourable. Os atom is metastable on both sites, with an energy difference of  $\sim 284$  meV. We have chosen the hollow site as the location for adsorption of the TM atoms, because it combines the best energetic and structural stability. Table 6.1 displays the adsorption energies on hollow site for comparison. The energy stability order of our studied configurations is as follows: Os (4.967 eV/adatom), Co (3.539 eV/adatom), Mo (2.799 eV/adatom), and Mn (2.166 eV/adatom). We note that all configurations exhibit comfortably large energetic stability.

Subsequently, we investigated the local structural distortions introduced by the adatom in the supercell. The optimised structural parameters for pristine 2D-GaAs crystal structure and TM on 551-GaAs are given in Table 6.1. In addition, Figure 6-1 depicts a top view for TM centred above one hollow site (middle of Ga-As hexagonal tile) of the 551-GaAs supercell (Figure 6-1(a)), as well as the side view of the relaxed buckling for Ga and As atoms ( $\Delta_{As-Ga}$ ) located at the hollow site for 551-GaAs supercell in absence of any adatom (Figure 6-1(d)). Furthermore, the optimised placements for Mn, Co, Mo and Os atoms ( $\Delta_{Ga-TM}$ ) are shown in Figure 6-1(b), Figure 6-1(c), Figure 6-1(e), and Figure 6-1(f), respectively. One sees from Table 6.1 that the optimised structural parameters for pristine 2D-GaAs ( $a_0$ ) are in good agreement with previous theoretical reports [123, 171]. When one TM atom is adsorbed on the 551-GaAs supercell, the relaxed unit-cell lattice parameter of TM on 551-GaAs system ( $a'_0 = a_{sup}/5$ ) is reduced slightly when compared with the one of pristine unit-cell, i.e. by 1.21, 1.26, 1.19, and 1.41 %, for Mn, Co, Mo and Os adatom, respectively. This can be explained by the larger buckling parameter ( $\Delta_{As-Ga}$ ) for TM adsorbed on 551-GaAs when compared with the one of pristine 2D-GaAs. The nearest As-Ga bond ( $d_{As-Ga}$ ) is larger for TM on 551-GaAs than the one in pristine 2D-GaAs by 4.78, 3.94, 6.19, and 12.42 %, for Mn, Co, Mo and Os atom, respectively.

From the analysis above, one can see that Os ( $Z=76$ ) and Mo ( $Z=42$ ) atoms, which have higher atomic numbers and are larger, result in a larger buckling ( $\Delta_{As-Ga}$ ) and extend As-Ga bonding length ( $d_{As-Ga}$ ) compared to the cases of Mn ( $Z=25$ ) and Co ( $Z=27$ ). The optimised placements for Mn, Co, Mo and Os atoms ( $\Delta_{Ga-TM}$ )

are shown in Figure 6-1(b), Figure 6-1(c), Figure 6-1(e), and Figure 6-1(f), respectively. The Mn and Mo atoms remain above the hollow site at a vertical distance of, respectively, 0.362 Å and 0.566 Å from the Ga-plane, while Co is almost in the Ga-plane (0.087 Å from Ga-plane) and Os is located between As-plane and Ga-plane, nearer to the Ga-plane ( $\Delta_{Os-Ga}=0.421$  Å and  $\Delta_{As-Os}=0.916$  Å). These differences in TM distance from Ga-plane (As-plane) can be intuitively explained by the electronegativity difference between TM and Ga (As) atoms. Mo (Os) and Mn (Co) are the most (least) electropositive atoms, thus Ga-Ga (As-As) in-plane distance increases (decreases) due to charge repulsion (attraction) when a more electropositive atom is adsorbed. This expansion (contraction) of Ga-Ga (As-As) in-plane distance can be evidenced by the increase (decrease) of the angle between neighbouring bonds ( $\theta_{GaAsGa}$ ) for Mo (2.797 %) and Mn (0.175 %) (Os: -11.888 % and Co: -2.797 %) when compared to the one of the pristine system, as shown in Table 6.1. As a result, Mo and Mn atoms experience a lower net electrostatic force towards the Ga-plane (As-plane) when compared to Co and Os atoms. In Table 6.1 we also give the charge located on the TM adatom ( $\Delta\rho$ ), which is consistent with the difference of electronegativity between the constituent elements.

### 6.3.2 MAE and electronic properties

As shown in Table 6.1, the adsorbed single adatom induces a magnetic ground state in the nonmagnetic 2D-GaAs system, with a net magnetic moment of 3.0  $\mu_B$ , 1.0  $\mu_B$ , 4.0  $\mu_B$ , and 2.0  $\mu_B$  per TM atom for the case of Mn, Co, Mo and Os adatom, respectively. Table 6.1 also shows the calculated magnetocrystalline anisotropy energy (MAE) per TM atom of our systems. The positive (negative) value of the MAE implies that the easy magnetisation axis is out-of-plane (in-plane) to the surface of the 2D structures. One sees that Os atom induces the largest MAE (-6.930 meV), followed by Mo (3.460 meV), Co (-0.950 meV), and Mn (0.530 meV). However, as would be expected, we find that a higher magnetic moment does not necessarily lead to a higher MAE, e.g., Os with a moment of 2.00  $\mu_B$  has a higher MAE than Mo (4.00  $\mu_B$ ) and Mn (3.00  $\mu_B$ ). The physical reasons that lead to MA in 2D TM-adsorbed GaAs will be analyzed in the next paragraphs. For Os adsorbed

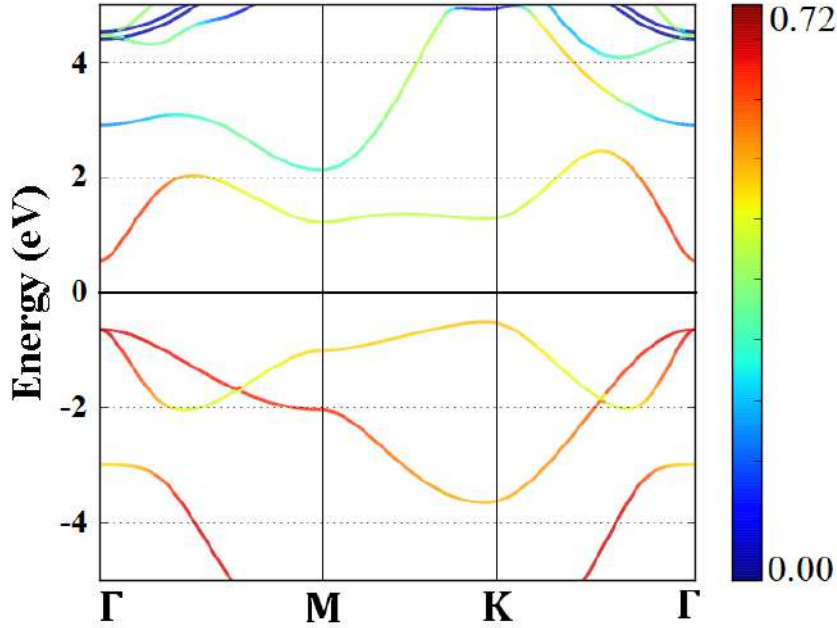


Figure 6-2: Parametric orbital projected band structure of pristine 2D-GaAs. The colour intensity corresponds to the degree of overlap of  $sp$  orbitals between Ga and As atoms. Fermi energy is set to 0 eV.

on the metastable As-top site, we found a strikingly large MAE of -28 meV.

In order to provide fundamental insights into the interaction of a TM adatom with the 2D-GaAs host semiconductor (TM = Mn, Co, Mo and Os), and how those interactions can induce magnetocrystalline anisotropy, both the electronic band structure of pristine 2D-GaAs, and the ones of Mn, Co, Mo and Os adsorbed on the hollow site of 2D-GaAs were calculated for comparison. The parametric projected electronic band structures for both the pristine 2D-GaAs sheet and the adsorbed TM on 2D-GaAs are shown in [Figure 6-2](#) and [Figure 6-3](#), respectively. Notice in [Figure 6-2](#) that 2D-GaAs has a K– $\Gamma$  indirect band gap of 1.06 eV. In the projected plots, the colour intensity corresponds to the degree of overlapping of  $sp$  orbitals between Ga and As atoms. The yellow lines, near and below the Fermi level, represent the contributions of As-4 $p_z$  orbitals. The empty band, near and above the Fermi level (green lines), represents the contribution of Ga-4 $p_z$  and Ga-4s orbitals. The buckling reduces the  $sp^2$  ( $p_z$  orbitals) hybridization, and increases the  $sp^3$  one ( $p_z$  and planar  $s$ ). [Figure 6-3](#) displays the parametric orbital projected electronic

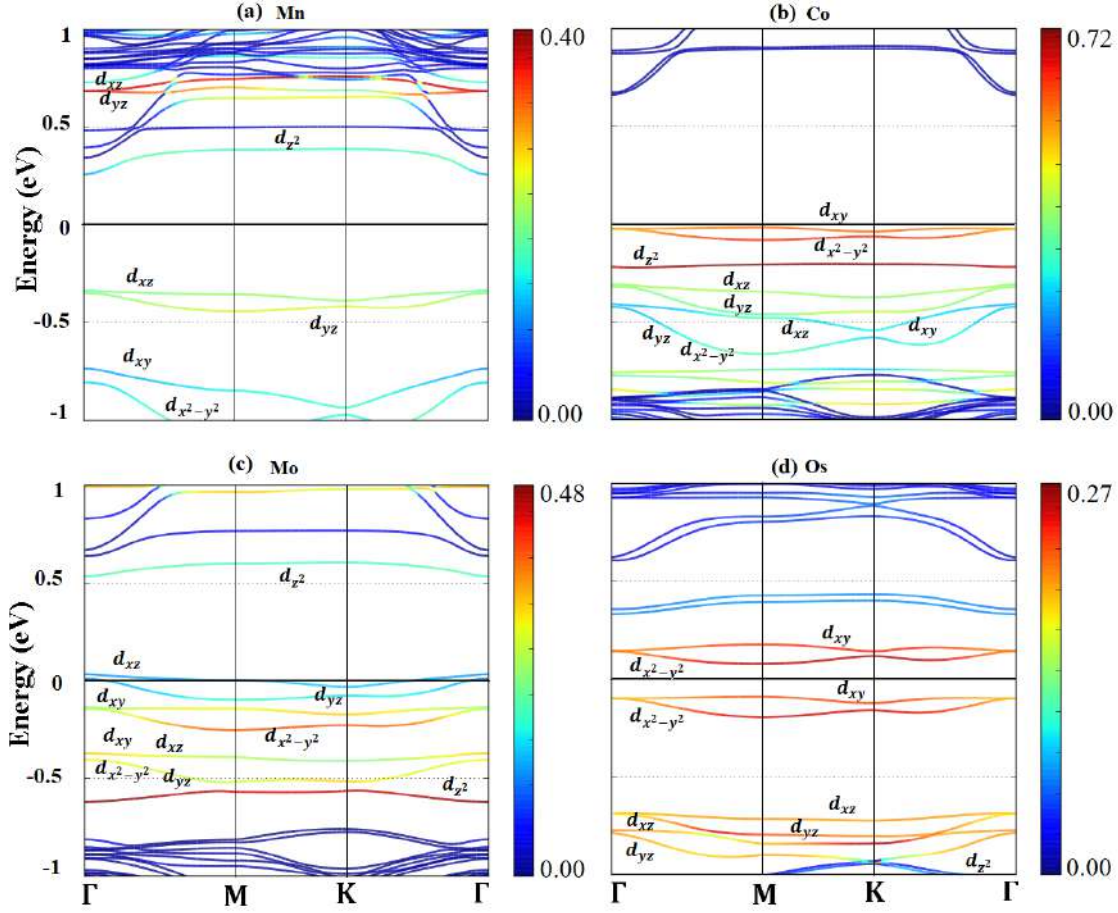


Figure 6-3: Parametric orbital projected band structure of TM on 2D-GaAs, calculated with SOC included. The colour intensity corresponds to the degree of contribution of the  $d$  orbital of a TM adatom. Fermi energy is set to 0 eV.

structure for TM on 2D-GaAs (TM = Mn (a), Co (b), Mo (c) and Os (d)). Electronic structure analysis shows that the semiconducting nature of pristine 2D-GaAs is retained by Mn ( $\Gamma - \Gamma$ ), Co ( $M - \Gamma$ ) and Os ( $M - M$ ) systems, with bandgap energy reduced by 45%, 37 % and 85 %, respectively. On the other hand, adsorption of Mo on 2D-GaAs changes its nature to a half-metallic one. One sees in Figure 6-3 that the TM adatom creates localised states near the Fermi level. In the projected plots, the colour intensity corresponds to the degree of contribution of the  $d$ -electrons of the TM adatom. The Ga and As atoms surrounding the adatom lead to a crystal field splitting of the  $d$  orbitals of the TM adatom. Due to the buckling of 2D-GaAs, and the different electronegativities and atomic numbers between TM, Ga and As atoms, the crystal-field splitting of the  $d$  orbitals of the TM on 2D-GaAs deviates

from the known planar trigonal-level splitting. In the case of crystal-field splitting of trigonal planar geometry, if the ligand atoms lie in the  $x - y$  plane, the  $d_{xy}$  and  $d_{x^2-y^2}$  orbitals have the highest energy because their electron density is concentrated in the  $x - y$  plane. The  $d_{z^2}$  orbital has higher energy than the  $d_{xz}$  and  $d_{yz}$  orbitals. The physical reason of this feature is the ring of electron density that  $d_{z^2}$  orbital has in the  $x - y$  plane. The  $d_{xz}$  and  $d_{yz}$  orbitals of the central TM adatom have the lowest energies because they have all their electron density out-of-plane.

For the cases of Co and Os, which exhibit magnetisation in the in-plane direction, the orbitals of higher energy levels are  $d_{xy}$  and  $d_{x^2-y^2}$ , as shown in Figure 6-3(b) and Figure 6-3(d), respectively. Due to different vertical position of Co and Os adatom with respect to the Ga-plane and As-plane, see Figure 6-1(c) and Figure 6-1(f), respectively, the energies for  $d_{z^2}$  and  $d_{xz}$  ( $d_{yz}$ ) orbitals differ. While the  $d_{z^2}$  orbital for Co has a somewhat higher energy than that of the  $d_{xz}$  and  $d_{yz}$  orbitals, for Os we find the opposite, the energies for  $d_{xz}$  and  $d_{yz}$  orbitals are higher than that of  $d_{z^2}$ . Another difference between these cases is the large overlap among the  $d_{xz}$  and  $d_{yz}$  orbitals of Co and 4- $p_x p_y p_z$ -GaAs orbitals as compared with those for Os, as shown in Figure 6-3(b) by green lines. This can be explained by the closer distance between Co and Ga-planes as compared to the distance of Os to the Ga-plane. Regarding the electronic structure of Mn and Mo on 2D-GaAs, one notices in Figure 6-3(a) and Figure 6-3(c), respectively, that  $d_{xz}$  and  $d_{yz}$  are the occupied states of higher energy, followed by  $d_{xy}$  and  $d_{x^2-y^2}$ . This can explain the out-of-plane magnetisation axis for both those TM adatoms on 2D-GaAs.

SOC plays a fundamental role in the magnetic behavior of the TM-adsorbed on 2D-GaAs semiconductor. The SOC mechanism works as follows: Figure 6-2 displays  $s$  and  $p$  mixed orbitals of pristine 2D-GaAs near the Fermi level, both in the valence and in the conduction bands. Structural buckling reduces the overlap between  $p_z$  orbitals. As a result, the  $sp^3$  hybridization near Fermi level becomes stronger than  $sp^2$ . On the other hand, the outermost  $d$ -orbital of TM ions are half-filled and, by Hund's rule, they are aligned parallel. When TM ion is adsorbed on 2D-GaAs semiconductor, the local magnetic moment of  $d$ -TM states hybridizes with the  $sp$  bands near the Fermi level of 2D-GaAs (spin-orbit interaction). Therefore, the  $sp-d$

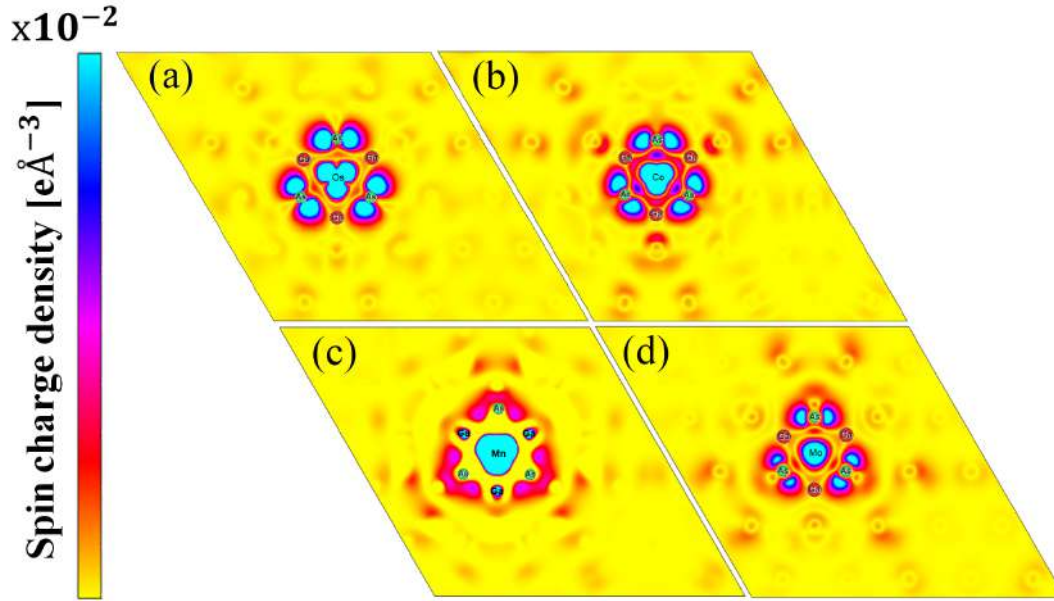


Figure 6-4: Calculated electronic spin-charge density for systems with the easy magnetisation axis in-plane ((a) Os and (b) Co) or out-of-plane ((c) Mn and (d) Mo) to the surface of the 2D structure. The colour intensity represents the spin-charge density, where blue and red indicate high and low electronic spin-charge density, respectively.

exchange interaction between the  $sp$  band electrons of 2D-GaAs and the  $d$  electrons associated with the TM atoms, as well as the lack of inversion symmetry of the crystal environment, are responsible for the magnetic behavior of TM-adsorbed on 2D-GaAs semiconductor.

The calculated electronic spin-charge density for systems with the easy magnetisation axis parallel ((a) Os and (b) Co) and perpendicular ((c) Mn and (d) Mo) to the surface of the considered 2D structures is shown in Figure 6-4. The colour intensity represents the spin-charge density, where blue and red indicate high and low density, respectively. The magnetic moment in each of these systems mainly originates from the adatom, i.e. 63, 95, 68 and 53 % of total magnetisation for Mn, Co, Mo and Os atom, respectively. Conversely, the magnetic moment stemming from the nearest neighbours at the hexagonal Ga-As tile where adatom resides is smaller than that found in adatom case, i.e. 4.9, 4.5, 10 and 37 % of total magnetisation for Mn, Co, Mo and Os system, respectively. Thus, according to our results, the MA of TM on 2D-GaAs system depends robustly on the broken crystal symmetry, the

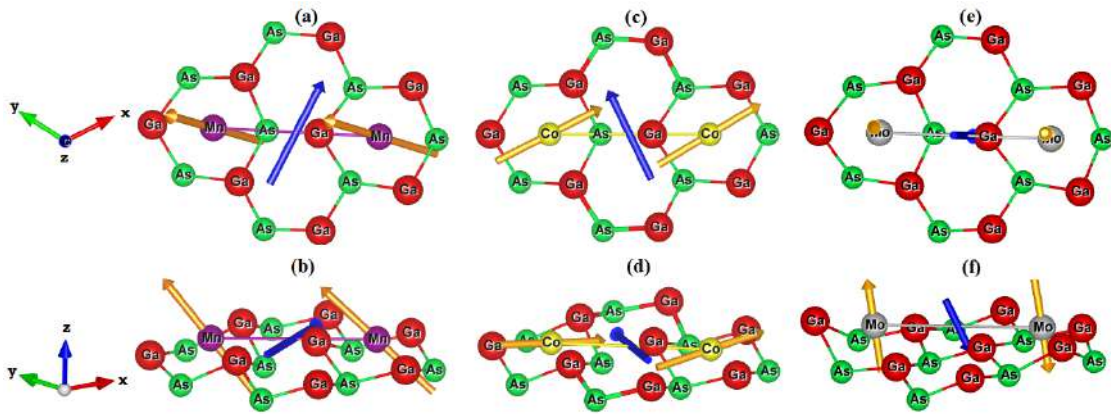


Figure 6-5: Top and side view of interacting TM adatoms on 2D-GaAs: Mn (a,b), Co (c,d), and Mo (e,f) atoms, located at the hollow sites of a  $5 \times 5$ –GaAs supercell. DMI vector  $\mathbf{D}_{12}$  (blue), showing non-trivial magnetic exchange interaction between the two TM adatoms is also shown, together with their spins (vectors in gold) at ground state for facilitated sense of orientation.

orbital character of the states in the vicinity of the Fermi level, and the magnitude of the interaction of the spins with the field generated by the electron orbital motion in the crystal.

### 6.3.3 Magnetic Exchange Interaction

During experimentally performed adsorption, one expects multiple adatoms to reside in close proximity to each other. The study of small clusters is of special scientific interest due to their unique magnetic properties that can be tailored for desired applications in magneto-electronics by choosing a special size or composition of the cluster. That in turn opens questions about the nature of magnetic interaction arising between the adsorbed atoms in a close range from each other.

Modern DFT-based calculations are able to describe the electronic and magnetic properties of the transition metal clusters in excellent agreement with the value obtained from the experimental ones. For instance, the experimental study of magnetic properties of Co atoms adsorbed on graphene [280] agrees very well with the ones predicted by DFT [281]. In addition, A. Stroppa *et al.* reported that computational images of Mn defects on GaAs predicted by DFT are consistent with the experimental ones [282].

Table 6.2: Calculated exchange matrix parameters ( $J_{12}^{ij}$ ) between two TM atoms of the same type adsorbed on a 2D-GaAs (TM = Mn, Co and Mo), as well as the DMI components  $D_{12}^x$ ,  $D_{12}^y$ ,  $D_{12}^z$ , the total DMI parameter  $|D|$ , the ratio between  $|D|$  and the average of diagonal exchange parameters  $J_{12}^{xx}$ ,  $J_{12}^{yy}$  and  $J_{12}^{zz}$ , and the calculated magnetocrystalline anisotropy energy (MAE), all defined with respect to the TM pair. The positive (negative) value of the MAE implies that the easy magnetisation axis is out-of-plane (in-plane) to the surface of the 2D structures.

	$J_{12}^{xx}$ (meV)	$J_{12}^{yy}$ (meV)	$J_{12}^{zz}$ (meV)	$J_{12}^{yz}$ (meV)	$J_{12}^{zy}$ (meV)	$J_{12}^{zx}$ (meV)	$J_{12}^{xz}$ (meV)	$J_{12}^{xy}$ (meV)	$J_{12}^{yx}$ (meV)	$D_{12}^x$ (meV)	$D_{12}^y$ (meV)	$D_{12}^z$ (meV)	$ D $ (meV)	$ D / J_{diag} $	MAE (meV)
Mn	-4.54	-4.55	-4.56	-0.27	-1.56	1.46	0.55	-0.04	0.04	0.64	0.46	-0.04	0.79	0.17	1.03
Co	-8.05	-0.01	-6.73	-0.22	-0.53	2.08	-2.04	-0.20	0.47	0.15	2.06	-0.33	2.09	0.42	-0.54
Mo	3.50	3.49	3.54	0.11	-0.09	-0.07	0.06	-0.28	0.27	0.10	-0.06	-0.27	0.30	0.09	2.89

We therefore set out to determine the magnetic exchange interaction between two neighbouring transition-metal adatoms on 2D-GaAs, by calculating the generalised  $3 \times 3$  matrix according to equation (6.3). We will primarily focus on two components of the magnetic exchange interaction: the isotropic exchange and the DMI.

In order to examine the magnetic exchange interaction between two adsorbed transition metal atoms in close proximity to each other, we first relaxed the structures for the first (4.05 Å) and second nearest distance (7.01 Å) between TM atoms (MnMn, CoCo, and MoMo) adsorbed on 2D-GaAs. The second nearest distance was chosen as subject of this study, as shown in Figure 6-5, instead of the nearest one, because its geometry was not distorted at the hexagon site after relaxation as for the nearest case. Then, we calculate the magnetic exchange parameters for the most stable geometry ( $J_{12}^{ij}$ ) using DFT methodology described in Section II. All nine elements of the matrix ( $J_{12}^{ij}$ ), as well as the DMI parameters  $D_{12}^x$ ,  $D_{12}^y$ ,  $D_{12}^z$ , the total DMI parameter  $|D|$ , and the ratio between  $|D|$  and the average of the diagonal exchange parameters  $J_{12}^{xx}$ ,  $J_{12}^{yy}$  and  $J_{12}^{zz}$ , are listed in Table 6.2. Ratio  $|D|/|J_{diag}|$  gives one insight in how strong  $\mathbf{D}$  is as compared to the isotropic exchange  $\mathbf{J}$  (yielding standard (A)FM behaviour).

Our results show that the total magnetisation obtained for Co (1  $\mu_B$ /adatom) is smaller than those for Mn (3  $\mu_B$ /adatom) and Mo (4  $\mu_B$ /adatom) atoms. The pairwise distances between Co, Mn and Mo adatoms after relaxation are, respectively, 6.68 Å, 6.77 Å, and 7.16 Å. One can see that for our three magnetic systems, the magnetic exchange interaction is stronger as the TM adatoms reside closer to each other. The optimised position of the two adatoms has the same physical ten-

dency as for the single adatom cases. The Mn and Mo atoms remain above the hollow site to a vertical distance of 0.469 Å (0.362 Å) and 0.611 (0.566 Å) from the Ga-plane, respectively, while Co resides in the Ga-plane (0.087 Å from Ga-plane). The values given in parenthesis represent the corresponding distances for the case of a single adatom, for comparison. When two TM atoms are adsorbed on the 551–GaAs supercell, the relaxed unit-cell lattice parameter of TM on 551–GaAs system ( $a'_0 = a_{sup}/5$ ) is reduced slightly when compared with the one of the pristine unit-cell, i.e. by 1.48 (1.21), 1.58 (1.26) and 1.24 (1.19) %, for Mn, Co and Mo atoms, respectively (the values in parenthesis are for single adatom cases). The optimised structural parameters for a pair of adatoms therefore exhibit the same physical tendencies as the previous single-adatom cases.

As shown in [Table 6.2](#), the magnetic interaction between adjacent TM adatoms significantly changes the emergent magnetic properties. One sees that Co prefers the FM ground state, with the magnetisation along the x-axis, and exhibits a strong FM interaction in both x and z directions, as  $J_{12}^{xx} = -8.05$  meV and  $J_{12}^{zz} = -6.73$  meV. Such difference of diagonal elements points to strong anisotropy. Regarding the Mn system, FM interaction is also found. The difference between all diagonal elements differs only by 0.01 meV, meaning there is almost no anisotropy. On the other hand, there is an AFM interaction found between two Mo atoms on 2D-GaAs, with a slight anisotropy favouring the z-(out-of-plane)direction. We found for all three systems that  $J_{12}^{xy} \neq J_{12}^{yx}$ ,  $J_{12}^{yz} \neq J_{12}^{zy}$ , and  $J_{12}^{xz} \neq J_{12}^{zx}$ , which indicates that the matrix  $J_{12}$  is antisymmetric. Furthermore, the off-diagonal elements of the exchange matrix are all different from zero, in agreement with the antisymmetry considerations by Moriya [175]. The consequent magnitudes of  $|D|$  for Mn, Co, and Mo pairs of adatoms are, respectively,  $\sim 17\%$ ,  $\sim 42\%$ , and  $\sim 9\%$  of the average symmetric exchange interaction, as shown in [Table 6.2](#). Hence, DMI is both stronger and more influential in the case of Co adatoms, compared to Mn and Mo adatoms. While having a weaker magnetic moment, Co hosts larger spin-orbit coupling and therefore enhances the DMI interaction. [Table 6.2](#) also displays the calculated MAE with respect to the TM pair of our systems. The positive (negative) value of the MAE implies that the easy magnetization axis is out-of-plane (in-plane) to the surface of the 2D structures. We

can see that Mo atom induces the largest MAE (2.89 meV), followed by Mn (1.03 meV) and Co (-0.54 meV). As for the single adatom cases, the easy magnetization axis of Co and Mo (Mn) atoms in two adatom cases remains in-plane and out-of-plane, respectively. [Figure 6-5](#) depicts orientation vectors for both the spins at ground state (gold color) and DMI (blue color) of the magnetic exchange interaction for each studied pair of TM atoms adsorbed on 2D-GaAs. The ground state spin configurations are obtained by solving Heisenberg spin Hamiltonian iteratively. We note once more that  $\mathbf{D}$  vector tends to align the neighbouring spins orthogonally to each other, instead of the parallel or antiparallel spin alignments obtained by the usual Heisenberg exchange interaction. The direction of the induced magnetisation on 2D-GaAs semiconductor can be selectively manipulated depending on chosen TM adatoms. The induced DMI in the TM-adsorbed GaAs monolayer causes spins of adjacent TM atoms to deviate from perfect (anti)ferromagnetic alignment. As a consequence, spins prefer non-collinear, chiral magnetic ordering, enabling spin textures unattainable otherwise. That is in turn attractive for the development of spintronic devices, for example those based on special properties of spin-waves, with dispersion tailored by local DMI

Finally we observe that Os adatoms in close proximity to each other the magnetisation vanishes on each Os atom, and the system goes to a non-magnetic state. Therefore, Os atoms coupling neither FM nor AFM in a close range from each other. This result strongly differs from our calculations for single Os adatom, where the system is comfortably magnetic with  $2 \mu_B$  magnetisation. It is therefore clear from these results that magnetic properties of adatoms strongly depend on the density of adatoms, and that more studies are needed to fully characterize the magnetic properties of specific patterns and densities of TM adatoms on 2D-GaAs. Furthermore, taking into consideration that the magnetic interactions may change drastically with distance [283], the study of the distance dependent magnetic exchange interaction of TM-adsorbed 2D-GaAs will be explored in further research.

## 6.4 Conclusions

We investigated the structural and electronic properties, as well as the magneto-crystalline anisotropy energy and magnetic exchange interactions of different transition metal adatoms (Mn, Co, Mo and Os) on 2D-GaAs using first-principles and the four-state energy mapping methodologies based on DFT. Electronic structures analysis upon structural relaxation revealed that the indirect K– $\Gamma$  semiconducting nature of the pristine 2D-GaAs can be tuned by adsorption of transition metal atoms. We also found that the transition metal adatom leads to a magnetic ground state in otherwise nonmagnetic 2D-GaAs system. More specifically, even a single TM adatom gives rise to high magneto-crystalline anisotropy energy, exhibiting either in-plane (e.g. Os, 6.93 meV) or out-of-plane MAE (e.g. Mo, 3.46 meV) for TM adsorbed on the central site above a hexagonal Ga-As tile. MAE can increase dramatically for TM adatoms trapped at a metastable site, as demonstrated in case of Os on As–top site leading to a giant in-plane MAE of 28 meV. According to our results the arising magnetic anisotropy of TM on 2D-GaAs stems from the broken crystal symmetry, the orbital character of the states in the vicinity of the Fermi level and the spin–orbit interactions in the crystal. One notices however that same arguments can be put forward to justify the appearance of the Dzyaloshinskii-Moriya interaction (DMI), crucial for the appearance of non-collinear magnetic textures beyond the standard ferro-antiferro dichotomy. For that reason, we examined in detail the magnetic interactions between a pair of identical transition-metal atoms adsorbed on 2D-GaAs. For Co adatoms, we found a FM ground state with in-plane magnetic anisotropy, as well as strong DMI. For either Mn and Mo adatoms placed on adjacent adsorption sites, almost no anisotropy is found. Still, Mn retains FM interaction, while Mo adatoms exhibit AFM interaction. On the other hand, a pair of Os adatoms, in same locations as other TM pairs, fall into a non-magnetic ground state (despite the single adatoms being strongly magnetic). This clearly indicates that both the concentration and ordering of TM adatoms play a crucial role in their induced magnetic features in 2D-GaAs. Bearing in mind the versatility of magnetic features we reported in the case of different TMs, and the need for magnetic

textures by design for applications in e.g. magnonics, our findings provide a useful foundation for further theoretical and experimental tuning of 2D magnetic materials based on III-V systems (the latter already being a proven commodity in spintronic applications).

## 6.5 Publication

**Chapter 6** was published as:

**A González-García**, W López-Pérez, R González-Hernández, C Bacaksiz, D Šabani, MV Milošević, and FM Peeters. *Transition-metal adatoms on 2d-GaAs: a route to chiral magnetic 2d materials by design*. Journal of Physics: Condensed Matter, 33(14):145803, 2021.

# Chapter 7

## Summary and outlook

### 7.1 Summary

The aim of this thesis is to tune the physical properties of the materials of group III-As in the thinnest limit by *ab initio* DFT-based calculations. Besides, it is expected that the results obtained in this study bring new theoretical insights to the research of 2D group III-V semiconductors for future electronic applications.

To accomplish this goal, this work has been organized into seven chapters, including this section. The first and second chapters, respectively, are devoted to highlighting the growing impact of two-dimensional materials in the nano- technological revolution of the 21st century, as well as providing readers with physical insights into the theoretical foundations that supported this research. In the first chapter is also pointed out the scarce research in the literature about the study of group III-As at the atomic level, which is contradicted with the applications of 3D group III-As materials in the engineering science.

Chapters three to six are dedicated to presenting the results related to the tuning of the mechanical, electronic and magnetic properties of these group III-As materials in the atomic level using nano-multilayers, straintronics, hydrogen functionalization, and transition metal adsorption.

As a platform to build the entire scaffolding of this research, a complete characterization of the structural, electronic, mechanical and vibrational properties of the pristine monolayers for two-dimensional group III-V semiconductors (BAs, GaAs,

and InAs), was carried out in chapter 3. Moreover, the structural and electronic properties of few-layer  $h$ -IIIAs structures have been studied and compared to those of pristine monolayers.

Our initial findings reveal the mechanical and dynamical stability of 2D  $h$ -IIIAs systems (III = B, Ga and In). They also show the tunability of their mechanical properties by varying the bond length between the neighboring cation-anion atoms. As the bond length between the neighboring cation-anion atoms increases, the 2D  $h$ -IIIAs binary compounds display less stiffness and more plasticity. Moreover, our results indicate the semiconducting nature of these systems, like their 3D counterpart, and give physical insights about the contribution of the  $\sigma$  and  $\pi$  bonding in their most stable geometry (planar for BAs and buckled for GaAs and InAs).

In our results, the  $\Gamma$ - $\Delta_{min}$  indirect semiconducting nature of 3D-BAs (0.67 eV) is tuned to  $K$ - $K$  direct bandgap (1.15 eV) for its 2D-BAs counterpart. Similarly, the  $\Gamma$ - $\Gamma$  direct semiconducting nature of 3D-GAs (1.42 eV) is tuned to  $\Gamma$ - $K$  indirect bandgap (1.87 eV) for its 2D-GAs counterpart. While the  $\Gamma$ - $\Gamma$  direct semiconducting nature of 3D-InAs (0.42 eV) is retained for its 2D-InAs counterpart (1.46 eV).

On the other hand, it is found that when increasing the numbers of layers,  $h$ -BAs keeps its planar geometry, while both  $h$ -GAs and  $h$ -InAs retain their buckled ones obtained by their single layers. Bilayer  $h$ -IIIAs present the same bandgap nature of their counterpart in 3D. As the number of layers increase from 2 to 4, the bandgap width for layered  $h$ -IIIAs decreases until they become semimetal or metal.

The findings found in chapter 3 motivated us to continue exploring the tunability of the properties of III-As systems at the atomic level for nanoelectronic applications. Furthermore, taking into account that Graphene-group III-V heterostructures have been studied in bilayer [129] and multilayer systems [130, 131], in order to tune the graphene band gap for optoelectronic applications, in chapter 4, the structural, mechanical and vibrational properties of graphene/GaAs bilayer are investigated; as well as the effect of both uniaxial stress along  $c$  axis and different planar strain distributions on the electronic properties.

The analysis of the results found in chapter 4 lead to the dynamical and mechanical stability of the graphene/GaAs system. Electronic structure analysis after

structural relaxation revealed that the indirect  $\Gamma$ - $K$  semiconducting nature of pristine 2D-GaAs can be tuned to  $\Gamma$ - $\Gamma$  direct in Graphene/GaAs bilayer heterostructure. Under the same latter physical conditions, graphene displays a bandgap of 5.0 meV. In addition, our results show that the uniaxial stress strongly affects the graphene electronic bandgap, while symmetric in-plane strain does not open a bandgap in graphene. Nevertheless, it induces remarkable changes on the GaAs bandgap-width around the Fermi level. However, when applying asymmetric in-plane strain to graphene/GaAs, the graphene sublattice symmetry is broken, and the graphene bandgap is opened at the Fermi level to a maximum width of 814 meV. This value is much larger than that reported for just graphene under asymmetric strain. The  $\Gamma$ - $\Gamma$  direct nature of GaAs remains unchanged in graphene/GaAs under different types of applied strain. It is also found that the mechanical properties for bilayer heterostructure are better than those of their constituent monolayers. This finding, together with the tunable graphene bandgap not only by the strength but also by the direction of the strain, enhances the potential for strain engineering of ultrathin group-III-V electronic devices hybridized by graphene. It is important to highlight that the lattice mismatch between two different bilayers causes elastic strains, which significantly affects their electronic properties. Therefore, the electronic structure of the graphene/GaAs bilayer will be sensitive to the chosen supercells for graphene and GaAs.

Motivated by recent reports in the literature about the tuning of the structural, optical, magnetic and mechanical properties of pristine 2D materials by hydrogen adsorption [48, 100], and the fact that hydrogen passivation stabilizes two dimensional buckled III-V sheets [102], in chapter 5, the stability, structural and electronic properties of two-dimensional (2D) hydrogenated GaAs with three possible geometries: chair, zigzag-line and boat configurations were analyzed. The results found in chapter 5, reveal that the hydrogenation of 2D-GaAs tunes the bandgap of pristine 2D-GaAs, which makes it a potential candidate for optoelectronic applications in the blue and violet ranges of the visible electromagnetic spectrum.

Finally, motivated by the recent experimental confirmation of magnetism in atomically thin magnetic crystals, which took place in 2017 [69, 132], and the fact

that chiral magnetism can be induced in a 2D material by doping with transition metals [58, 59, 60, 61], in chapter 6, the physical effect of spin-orbit coupling on both magnetic anisotropy and Dzyaloshinskii-Moriya interaction in two-dimensional gallium arsenide when single and pair TMs are adsorbed (TM: Mn, Co, Mo and Os), is investigated. The results found in chapter 6 show that single Mn and Mo atom (Co and Os) strongly bind on 2D-GaAs, and induce local out-of-plane (in-plane) magnetic anisotropy. When a pair of TM atoms is adsorbed on 2D-GaAs at close range from each other, magnetisation properties change (become tunable) depending on concentration and ordering of the adatoms. In all cases, we reveal the presence of strong Dzyaloshinskii-Moriya interaction (DMI). These results indicate novel pathways towards 2D chiral magnetic materials by design, tailored for desired applications in magneto-electronics.

## 7.2 Outlook

As mentioned in chapter 1, our initial aim of tuning the properties of group III-As (III=B, Ga and In) in the thinnest limit was too ambitious to be covered in four years. Even though, in chapter 3, we studied the structural, mechanical, electronic, and vibrational properties of 2D single-layer *h*-IIIAs (BAs, GaAs, and InAs) systems, as well as the structural and electronic properties of few-layer *h*-IIIAs structures; from chapter 4 on, we only focused our attention in tuning the mechanical, electronic and magnetic properties of 2D-GaAs semiconductor system by using 2D-multilayers, straintronics, hydrogen functionalization, and transition metal adsorption approaches, respectively. Thus, now, after finishing the study of 2D-GaAs system, and with the knowledge and expertise obtained during this process, we will continue our research to tune the physical properties of group IIIAs at the atomic level, but now focusing our attention on 2D-BAs and InAs. It could be interesting to contrast the physical results obtained for planar 2D-BAs structure to those of buckled 2D-GaAs and InAs structures. Moreover, the fact that BAs, GaAs and InAs have a different semiconducting nature, makes the research more interesting from the point of view of their physical properties and their potential

applications in nano-electronics.

As shown in the introduction section of this thesis, 2D-heterostructures are an efficient way of tuning the bandgap width of semiconductors, which makes them promising candidates for the manufacture of solar cells due to the complete adsorption of light by successive layers. The remarkable tunable properties of 2D-heterostructures, together with the development of experimental and computational methods for their synthesis and characterization, makes them attractive materials for technological and industrial applications.

The study of 2D-heterostructures based on BAs, GaAs and InAs layered materials could be of great interest due to their tunable bandgaps, which makes them potential candidates for different functional optoelectronic devices. In addition, the assembly of hybrid multilayer using different stacking possibilities of BAs, GaAs, InAs and graphene layers, could be technologically interesting due to the large optical window in 2D atomic scale thickness. We will conduct these studies taking into account the dipolar corrections for comparison.

On the other hand, we consider that more work must be done in the study of magnetic properties of TM on/in III-V ultrathin limit. In chapter 6 the presence of strong Dzyaloshinskii-Moriya interaction (DMI) in transition-metal atoms adsorbed on 2D-GaAs was revealed, indicating novel pathways towards 2D chiral magnetic materials by design, tailored for desired applications in magneto-electronics. Furthermore, recent studies have shown that ultrathin ferromagnets sandwiched between normal metals can have chiral domain walls, which move surprisingly quickly in response to currents. This finding could be used in magnetic memory devices, spin logic devices and nanoscale magnetic spin-torque oscillators [284, 285].

Taking into account our findings and those of references [284, 285], our results can be considered as the starting point for a detailed analysis of nonconventional magnetism in nano-multilayer systems using ferromagnetic monolayers and group III-V single layers.

Finally, I will continue researching into the fascinating field of ultrathin materials, doing my best to find and theoretically characterize new nanomaterials, providing theoretical insights into their potential nanotechnological applications.

# Bibliography

- [1] A. C. Neto, F. Guinea, N. M. Peres, K. S. Novoselov, and A. K. Geim, “The electronic properties of graphene,” *Reviews of Modern Physics*, vol. 81, no. 1, p. 109, 2009.
- [2] S. Reich, C. Thomsen, and J. Maultzsch, *Carbon nanotubes: basic concepts and physical properties*. John Wiley & Sons, 2008.
- [3] K. Shavanova, Y. Bakakina, I. Burkova, I. Shtepliuk, R. Viter, A. Ubelis, V. Beni, N. Starodub, R. Yakimova, and V. Khranovskyy, “Application of 2D non-graphene materials and 2D oxide nanostructures for biosensing technology,” *Sensors*, vol. 16, no. 2, p. 223, 2016.
- [4] A. J. Mannix, B. Kiraly, M. C. Hersam, and N. P. Guisinger, “Synthesis and chemistry of elemental 2D materials,” *Nature Reviews Chemistry*, vol. 1, no. 2, p. 0014, 2017.
- [5] G. Faraji, H. S. Kim, and H. T. Kashi, *Severe plastic deformation: methods, processing and properties*. Elsevier, 2018.
- [6] N. A. Poklonski, E. F. Kislyakov, S. A. Vyrko, O. N. Bubel, and S. V. Ratkevich, “Electronic band structure and magnetic states of zigzag graphene nanoribbons: quantum chemical calculations,” *Journal of Nanophotonics*, vol. 6, no. 1, p. 061712, 2012.
- [7] A. K. Geim and I. V. Grigorieva, “Van der Waals heterostructures,” *Nature*, vol. 499, no. 7459, p. 419, 2013.
- [8] K. Novoselov and A. C. Neto, “Two-dimensional crystals-based heterostructures: materials with tailored properties,” *Physica Scripta*, vol. 2012, no. T146, p. 014006, 2012.
- [9] A. C. Ferrari, F. Bonaccorso, V. FalKo, K. S. Novoselov, S. Roche, P. Bøggild, S. Borini, F. H. Koppens, V. Palermo, N. Pugno *et al.*, “Science and technology roadmap for graphene, related two-dimensional crystals, and hybrid systems,” *Nanoscale*, vol. 7, no. 11, pp. 4598–4810, 2015.
- [10] F. Bonaccorso, L. Colombo, G. Yu, M. Stoller, V. Tozzini, A. C. Ferrari, R. S. Ruoff, and V. Pellegrini, “Graphene, related two-dimensional crystals, and hybrid systems for energy conversion and storage,” *Science*, vol. 347, no. 6217, p. 1246501, 2015.

- [11] J. Miao, X. Liu, K. Jo, K. He, R. Saxena, B. Song, H. Zhang, J. He, M.-G. Han, W. Hu *et al.*, “Gate-tunable semiconductor heterojunctions from 2D/3D van der Waals interfaces,” *Nano Letters*, vol. 20, no. 4, pp. 2907–2915, 2020.
- [12] Y. Lee, S. B. Cho, and Y.-C. Chung, “Tunable indirect to direct band gap transition of monolayer  $\text{Sc}_2\text{CO}_2$  by the strain effect,” *ACS Applied Materials & Interfaces*, vol. 6, no. 16, pp. 14724–14728, 2014.
- [13] A. Brataas, “Chiral domain walls move faster,” *Nature Nanotechnology*, vol. 8, no. 7, pp. 485–486, 2013.
- [14] K. Everschor, “Current-induced dynamics of chiral magnetic structures: skyrmions, emergent electrodynamics and spin-transfer torques,” Ph.D. dissertation, Universität zu Köln, 2012.
- [15] A. Fert, V. Cros, and J. Sampaio, “Skyrmions on the track,” *Nature Nanotechnology*, vol. 8, no. 3, pp. 152–156, 2013.
- [16] A. K. Geim and K. S. Novoselov, “The rise of graphene,” in *Nanoscience and technology: a collection of reviews from nature journals*. World Scientific, 2010, pp. 11–19.
- [17] A. Geim, “Graphene prehistory,” *Physica Scripta*, vol. 2012, no. T146, p. 014003, 2012.
- [18] P. R. Wallace, “The band theory of graphite,” *Physical Review*, vol. 71, no. 9, p. 622, 1947.
- [19] G. Ruess and F. Vogt, “Höchstlamellarer kohlenstoff aus graphitoxhydroxyd.” *Monatshefte für Chemie und verwandte Teile anderer Wissenschaften*, vol. 78, no. 3-4, pp. 222–242, 1948.
- [20] H.-P. Boehm, A. Clauss, G. Fischer, and U. Hofmann, “Das adsorptionsverhalten sehr dünner kohlenstoff-folien,” *Zeitschrift für anorganische und allgemeine Chemie*, vol. 316, no. 3-4, pp. 119–127, 1962.
- [21] H. Boehm, R. Setton, and E. Stumpp, *Nomenclature and terminology of graphite intercalation compounds*. Pergamon, 1986.
- [22] H.-P. Boehm and E. Stumpp, “Citation errors concerning the first report on exfoliated graphite,” *Carbon*, vol. 7, no. 45, pp. 1381–1383, 2007.
- [23] C. Schafhaeutl, “LXXXVI. on the combinations of carbon with silicon and iron, and other metals, forming the different species of cast iron, steel, and malleable iron,” *The London, Edinburgh, and Dublin Philosophical Magazine and Journal of Science*, vol. 16, no. 106, pp. 570–590, 1840.
- [24] J. Blakely, J. Kim, and H. Potter, “Segregation of carbon to the (100) surface of nickel,” *Journal of Applied Physics*, vol. 41, no. 6, pp. 2693–2697, 1970.

- [25] J. Grant and T. Haas, "A study of Ru (0001) and Rh (111) surfaces using LEED and Auger electron spectroscopy," *Surface Science*, vol. 21, no. 1, pp. 76–85, 1970.
- [26] R. Rosei, M. De Crescenzi, F. Sette, C. Quaresima, A. Savoia, and P. Perfetti, "Structure of graphitic carbon on Ni (111): A surface extended-energy-loss fine-structure study," *Physical Review B*, vol. 28, no. 2, p. 1161, 1983.
- [27] C. McConville, D. Woodruff, S. Kevan, M. Weinert, and J. Davenport, "Electronic structure of the  $(2 \times 2)C$   $\rho 4g$  carbidic phase on Ni{100}," *Physical Review B*, vol. 34, no. 4, p. 2199, 1986.
- [28] T. Land, T. Michely, R. Behm, J. Hemminger, and G. Comsa, "STM investigation of single layer graphite structures produced on Pt (111) by hydrocarbon decomposition," *Surface Science*, vol. 264, no. 3, pp. 261–270, 1992.
- [29] A. Van Bommel, J. Crombeen, and A. Van Tooren, "LEED and Auger electron observations of the SiC (0001) surface," *Surface Science*, vol. 48, no. 2, pp. 463–472, 1975.
- [30] A. Nagashima, K. Nuka, K. Satoh, H. Itoh, T. Ichinokawa, C. Oshima, and S. Otani, "Electronic structure of monolayer graphite on some transition metal carbide surfaces," *Surface Science*, vol. 287, pp. 609–613, 1993.
- [31] M. Terai, N. Hasegawa, M. Okusawa, S. Otani, and C. Oshima, "Electronic states of monolayer micrographite on TiC (111)-faceted and TiC (410) surfaces," *Applied Surface Science*, vol. 130, pp. 876–882, 1998.
- [32] K. Seibert, G. Cho, W. Kütt, H. Kurz, D. Reitze, J. Dadap, H. Ahn, M. Downer, and A. Malvezzi, "Femtosecond carrier dynamics in graphite," *Physical Review B*, vol. 42, no. 5, p. 2842, 1990.
- [33] T. W. Ebbesen and H. Hiura, "Graphene in 3-dimensions: Towards graphite origami," *Advanced Materials*, vol. 7, no. 6, pp. 582–586, 1995.
- [34] X. Lu, M. Yu, H. Huang, and R. S. Ruoff, "Tailoring graphite with the goal of achieving single sheets," *Nanotechnology*, vol. 10, no. 3, p. 269, 1999.
- [35] Y. Gan, W. Chu, and L. Qiao, "STM investigation on interaction between superstructure and grain boundary in graphite," *Surface Science*, vol. 539, no. 1-3, pp. 120–128, 2003.
- [36] H. Beyer, M. Müller, and T. Schimmel, "Monolayers of graphite rotated by a defined angle: hexagonal superstructures by STM." *Applied Physics A: Materials Science & Processing*, vol. 68, no. 2, 1999.
- [37] J. McClure, "Diamagnetism of graphite," *Physical Review*, vol. 104, no. 3, p. 666, 1956.
- [38] J. Slonczewski and P. Weiss, "Band structure of graphite," *Physical Review*, vol. 109, no. 2, p. 272, 1958.

- [39] G. W. Semenoff, "Condensed-matter simulation of a three-dimensional anomaly," *Physical Review Letters*, vol. 53, no. 26, p. 2449, 1984.
- [40] F. D. M. Haldane, "Model for a quantum Hall effect without Landau levels: Condensed-matter realization of the "parity anomaly"," *Physical Review Letters*, vol. 61, no. 18, p. 2015, 1988.
- [41] R. Saito, M. Fujita, G. Dresselhaus, and M. Dresselhaus, "Electronic structure of chiral graphene tubules," *Applied Physics Letters*, vol. 60, no. 18, pp. 2204–2206, 1992.
- [42] E. Gorbar, V. Gusynin, V. Miransky, and I. Shovkovy, "Magnetic field driven metal-insulator phase transition in planar systems," *Physical Review B*, vol. 66, no. 4, p. 045108, 2002.
- [43] S. Z. Butler, S. M. Hollen, L. Cao, Y. Cui, J. A. Gupta, H. R. Gutiérrez, T. F. Heinz, S. S. Hong, J. Huang, A. F. Ismach *et al.*, "Progress, challenges, and opportunities in two-dimensional materials beyond graphene," *ACS Nano*, vol. 7, no. 4, pp. 2898–2926, 2013.
- [44] P. K. Nayak, *Two-dimensional Materials: Synthesis, Characterization and Potential Applications*. BoD–Books on Demand, 2016.
- [45] S. J. Kim, K. Choi, B. Lee, Y. Kim, and B. H. Hong, "Materials for flexible, stretchable electronics: graphene and 2D materials," *Annual Review of Materials Research*, vol. 45, pp. 63–84, 2015.
- [46] K. S. Novoselov, V. Fal, L. Colombo, P. Gellert, M. Schwab, K. Kim *et al.*, "A roadmap for graphene," *Nature*, vol. 490, no. 7419, pp. 192–200, 2012.
- [47] L. Liao, H. Peng, and Z. Liu, "Chemistry makes graphene beyond graphene," *Journal of the American Chemical Society*, vol. 136, no. 35, pp. 12 194–12 200, 2014.
- [48] H. Shu, Y. Li, S. Wang, and J. Wang, "Quasi-particle energies and optical excitations of hydrogenated and fluorinated germanene," *Physical Chemistry Chemical Physics*, vol. 17, no. 6, pp. 4542–4550, 2015.
- [49] Y. Liu, N. O. Weiss, X. Duan, H.-C. Cheng, Y. Huang, and X. Duan, "Van der Waals heterostructures and devices," *Nature Reviews Materials*, vol. 1, no. 9, p. 16042, 2016.
- [50] T. Niu and A. Li, "From two-dimensional materials to heterostructures," *Progress in Surface Science*, vol. 90, no. 1, pp. 21–45, 2015.
- [51] A. Molle, J. Goldberger, M. Houssa, Y. Xu, S.-C. Zhang, and D. Akinwande, "Buckled two-dimensional Xene sheets," *Nature Materials*, vol. 16, no. 2, p. 163, 2017.

- [52] Z. A. Piazza, H.-S. Hu, W.-L. Li, Y.-F. Zhao, J. Li, and L.-S. Wang, "Planar hexagonal B 36 as a potential basis for extended single-atom layer boron sheets," *Nature Communications*, vol. 5, p. 3113, 2014.
- [53] P. Vogt, P. De Padova, C. Quaresima, J. Avila, E. Frantzeskakis, M. C. Asensio, A. Resta, B. Ealet, and G. Le Lay, "Silicene: compelling experimental evidence for graphenelike two-dimensional silicon," *Physical Review Letters*, vol. 108, no. 15, p. 155501, 2012.
- [54] Z. Liu, Y. Gong, W. Zhou, L. Ma, J. Yu, J. C. Idrobo, J. Jung, A. H. MacDonald, R. Vajtai, J. Lou *et al.*, "Ultrathin high-temperature oxidation-resistant coatings of hexagonal boron nitride," *Nature Communications*, vol. 4, p. 2541, 2013.
- [55] B. Van den Broek, M. Houssa, E. Scalise, G. Pourtois, V. Afanasev, and A. Stesmans, "Two-dimensional hexagonal tin: ab initio geometry, stability, electronic structure and functionalization," *2D Materials*, vol. 1, no. 2, p. 021004, 2014.
- [56] H. Liu, A. T. Neal, Z. Zhu, Z. Luo, X. Xu, D. Tománek, and P. D. Ye, "Phosphorene: an unexplored 2D semiconductor with a high hole mobility," *ACS Nano*, vol. 8, no. 4, pp. 4033–4041, 2014.
- [57] Y. Lu, W. Xu, M. Zeng, G. Yao, L. Shen, M. Yang, Z. Luo, F. Pan, K. Wu, T. Das *et al.*, "Topological properties determined by atomic buckling in self-assembled ultrathin Bi(110)," *Nano Letters*, vol. 15, no. 1, pp. 80–87, 2014.
- [58] W. Cong, Z. Tang, X. Zhao, and J. Chu, "Enhanced magnetic anisotropies of single transition-metal adatoms on a defective MoS<sub>2</sub> monolayer," *Scientific Reports*, vol. 5, p. 9361, 2015.
- [59] S. Gong, C.-G. Duan, Z.-Q. Zhu, and J.-H. Chu, "Manipulation of magnetic anisotropy of Fe/graphene by charge injection," *Applied Physics Letters*, vol. 100, no. 12, p. 122410, 2012.
- [60] P. Ong, N. Kioussis, P. K. Amiri, J. Alzate, K. Wang, G. P. Carman, J. Hu, and R. Wu, "Electric field control and effect of Pd capping on magnetocrystalline anisotropy in FePd thin films: A first-principles study," *Physical Review B*, vol. 89, no. 9, p. 094422, 2014.
- [61] E. Torun, H. Sahin, C. Bacaksiz, R. T. Senger, and F. M. Peeters, "Tuning the magnetic anisotropy in single-layer crystal structures," *Physical Review B*, vol. 92, no. 10, p. 104407, 2015.
- [62] Q. Tang, Z. Zhou, and Z. Chen, "Graphene-related nanomaterials: tuning properties by functionalization," *Nanoscale*, vol. 5, no. 11, pp. 4541–4583, 2013.
- [63] M. Lotya, Y. Hernandez, P. J. King, R. J. Smith, V. Nicolosi, L. S. Karlsson, F. M. Blighe, S. De, Z. Wang, I. McGovern *et al.*, "Liquid phase production

- of graphene by exfoliation of graphite in surfactant/water solutions,” *Journal of the American Chemical Society*, vol. 131, no. 10, pp. 3611–3620, 2009.
- [64] S. Johal, “Chemical exfoliation of graphene and other 2D-materials,” Ph.D. dissertation, The University of Manchester (United Kingdom), 2013.
- [65] M. Ohring, “Chapter 6 - chemical vapor deposition,” in *Materials Science of Thin Films*, Second Edition ed., M. Ohring, Ed. San Diego: Academic Press, 2002, pp. 277 – 355. [Online]. Available: <http://www.sciencedirect.com/science/article/pii/B9780125249751500094>
- [66] A. S. H. Makhlouf and I. Tiginyanu, *Nanocoatings and ultra-thin films: technologies and applications*. Elsevier, 2011.
- [67] J. Yu, J. Li, W. Zhang, and H. Chang, “Synthesis of high quality two-dimensional materials via chemical vapor deposition,” *Chemical Science*, vol. 6, no. 12, pp. 6705–6716, 2015.
- [68] X. Li, W. Cai, J. An, S. Kim, J. Nah, D. Yang, R. Piner, A. Velamakanni, I. Jung, E. Tutuc *et al.*, “Large-area synthesis of high-quality and uniform graphene films on copper foils,” *Science*, vol. 324, no. 5932, pp. 1312–1314, 2009.
- [69] C. Gong, L. Li, Z. Li, H. Ji, A. Stern, Y. Xia, T. Cao, W. Bao, C. Wang, Y. Wang *et al.*, “Discovery of intrinsic ferromagnetism in two-dimensional van der Waals crystals,” *Nature*, vol. 546, no. 7657, p. 265, 2017.
- [70] M. Gibertini, M. Koperski, A. Morpurgo, and K. Novoselov, “Magnetic 2D materials and heterostructures,” *Nature Nanotechnology*, vol. 14, no. 5, pp. 408–419, 2019.
- [71] M. Velický and P. S. Toth, “From two-dimensional materials to their heterostructures: an electrochemist’s perspective,” *Applied Materials Today*, vol. 8, pp. 68–103, 2017.
- [72] J. Li, Z. Wei, and J. Kang, *Two-Dimensional Semiconductors: Synthesis, Physical Properties and Applications*. John Wiley & Sons, 2020.
- [73] Y. Guo, W. Guo, and C. Chen, “Semiconducting to half-metallic to metallic transition on spin-resolved zigzag bilayer graphene nanoribbons,” *The Journal of Physical Chemistry C*, vol. 114, no. 30, pp. 13 098–13 105, 2010.
- [74] M. Y. Han, B. Özyilmaz, Y. Zhang, and P. Kim, “Energy band-gap engineering of graphene nanoribbons,” *Physical Review Letters*, vol. 98, no. 20, p. 206805, 2007.
- [75] Y.-W. Son, M. L. Cohen, and S. G. Louie, “Energy gaps in graphene nanoribbons,” *Physical Review Letters*, vol. 97, no. 21, p. 216803, 2006.

- [76] R. R. King, A. Boca, W. Hong, X. Liu, D. Bhusari, D. Larrabee, K. Edmondson, D. Law, C. Fetzer, S. Mesropian *et al.*, “Band-gap-engineered architectures for high-efficiency multijunction concentrator solar cells,” in *24th European Photovoltaic Solar Energy Conference and Exhibition, Hamburg, Germany*, vol. 21, 2009, p. 55.
- [77] A. Bablich, S. Kataria, and M. C. Lemme, “Graphene and two-dimensional materials for optoelectronic applications,” *Electronics*, vol. 5, no. 1, p. 13, 2016.
- [78] Y. Zhang, T.-T. Tang, C. Girit, Z. Hao, M. C. Martin, A. Zettl, M. F. Crommie, Y. R. Shen, and F. Wang, “Direct observation of a widely tunable bandgap in bilayer graphene,” *Nature*, vol. 459, no. 7248, pp. 820–823, 2009.
- [79] L. Britnell, R. Ribeiro, A. Eckmann, R. Jalil, B. Belle, A. Mishchenko, Y.-J. Kim, R. Gorbachev, T. Georgiou, S. Morozov *et al.*, “Strong light-matter interactions in heterostructures of atomically thin films,” *Science*, vol. 340, no. 6138, pp. 1311–1314, 2013.
- [80] Y. Li, Z. Wei, and J. Li, “Modulation of the electronic property of phosphorene by wrinkle and vertical electric field,” *Applied Physics Letters*, vol. 107, no. 11, p. 112103, 2015.
- [81] L. Yu, A. Ruzsinszky, and J. P. Perdew, “Bending two-dimensional materials to control charge localization and Fermi-level shift,” *Nano Letters*, vol. 16, no. 4, pp. 2444–2449, 2016.
- [82] S. Manzeli, A. Allain, A. Ghadimi, and A. Kis, “Piezoresistivity and strain-induced band gap tuning in atomically thin MoS<sub>2</sub>,” *Nano Letters*, vol. 15, no. 8, pp. 5330–5335, 2015.
- [83] C. Lee, X. Wei, J. W. Kysar, and J. Hone, “Measurement of the elastic properties and intrinsic strength of monolayer graphene,” *Science*, vol. 321, no. 5887, pp. 385–388, 2008.
- [84] F. Ding, H. Ji, Y. Chen, A. Herklotz, K. Dorr, Y. Mei, A. Rastelli, and O. G. Schmidt, “Stretchable graphene: a close look at fundamental parameters through biaxial straining,” *Nano Letters*, vol. 10, no. 9, pp. 3453–3458, 2010.
- [85] M. Huang, H. Yan, C. Chen, D. Song, T. F. Heinz, and J. Hone, “Phonon softening and crystallographic orientation of strained graphene studied by Raman spectroscopy,” *Proceedings of the National Academy of Sciences*, vol. 106, no. 18, pp. 7304–7308, 2009.
- [86] N. Ferralis, R. Maboudian, and C. Carraro, “Evidence of structural strain in epitaxial graphene layers on 6H-SiC (0001),” *Physical Review Letters*, vol. 101, no. 15, p. 156801, 2008.
- [87] C. Si, Z. Sun, and F. Liu, “Strain engineering of graphene: a review,” *Nanoscale*, vol. 8, no. 6, pp. 3207–3217, 2016.

- [88] A. C. Ferrari, “Raman spectroscopy of graphene and graphite: Disorder, electron–phonon coupling, doping and nonadiabatic effects,” *Solid State Communications*, vol. 143, no. 1-2, pp. 47–57, 2007.
- [89] G. Cocco, E. Cadelano, and L. Colombo, “Gap opening in graphene by shear strain,” *Physical Review B*, vol. 81, no. 24, p. 241412, 2010.
- [90] Q. Yue, S. Chang, J. Kang, X. Zhang, Z. Shao, S. Qin, and J. Li, “Bandgap tuning in armchair MoS<sub>2</sub> nanoribbon,” *Journal of Physics: Condensed Matter*, vol. 24, no. 33, p. 335501, 2012.
- [91] E. J. Santos and E. Kaxiras, “Electric-field dependence of the effective dielectric constant in graphene,” *Nano Letters*, vol. 13, no. 3, pp. 898–902, 2013.
- [92] G. Giovannetti, P. A. Khomyakov, G. Brocks, V. v. Karpan, J. Van den Brink, and P. J. Kelly, “Doping graphene with metal contacts,” *Physical Review Letters*, vol. 101, no. 2, p. 026803, 2008.
- [93] S. Y. Zhou, G.-H. Gweon, A. Fedorov, d. First, PN, W. De Heer, D.-H. Lee, F. Guinea, A. C. Neto, and A. Lanzara, “Substrate-induced bandgap opening in epitaxial graphene,” *Nature Materials*, vol. 6, no. 10, pp. 770–775, 2007.
- [94] C. Attaccalite, L. Wirtz, M. Lazzeri, F. Mauri, and A. Rubio, “Doped graphene as tunable electron-phonon coupling material,” *Nano Letters*, vol. 10, no. 4, pp. 1172–1176, 2010.
- [95] J. A. Rodriguez-Manzo, O. Cretu, and F. Banhart, “Trapping of metal atoms in vacancies of carbon nanotubes and graphene,” *ACS Nano*, vol. 4, no. 6, pp. 3422–3428, 2010.
- [96] Z. Sun, Z. Yan, J. Yao, E. Beitler, Y. Zhu, and J. M. Tour, “Growth of graphene from solid carbon sources,” *Nature*, vol. 468, no. 7323, pp. 549–552, 2010.
- [97] I. Gierz, C. Riedl, U. Starke, C. R. Ast, and K. Kern, “Atomic hole doping of graphene,” *Nano Letters*, vol. 8, no. 12, pp. 4603–4607, 2008.
- [98] O. Leenaerts, H. Peelaers, A. Hernández-Nieves, B. Partoens, and F. Peeters, “First-principles investigation of graphene fluoride and graphane,” *Physical Review B*, vol. 82, no. 19, p. 195436, 2010.
- [99] H. González-Herrero, J. M. Gómez-Rodríguez, P. Mallet, M. Moaied, J. J. Palacios, C. Salgado, M. M. Ugeda, J.-Y. Veuillen, F. Yndurain, and I. Brihuega, “Atomic-scale control of graphene magnetism by using hydrogen atoms,” *Science*, vol. 352, no. 6284, pp. 437–441, 2016.
- [100] Y. I. Chen, *Nanotubes and nanosheets: functionalization and applications of boron nitride and other nanomaterials*. CRC Press, 2015.
- [101] R. González-Ariza, O. Martínez-Castro, M. G. Moreno-Armenta, A. Gonzalez-Garcia, W. Lopez-Perez, and R. Gonzalez-Hernandez, “Tuning the electronic and magnetic properties of 2D g-GaN by H adsorption: An ab-initio study,” *Physica B: Condensed Matter*, vol. 569, pp. 57–61, 2019.

- [102] Z. Y. Al Balushi, K. Wang, R. K. Ghosh, R. A. Vilá, S. M. Eichfeld, J. D. Caldwell, X. Qin, Y.-C. Lin, P. A. DeSario, G. Stone *et al.*, “Two-dimensional gallium nitride realized via graphene encapsulation,” *Nature Materials*, vol. 15, no. 11, p. 1166, 2016.
- [103] W. Chen, Y. Li, G. Yu, C.-Z. Li, S. B. Zhang, Z. Zhou, and Z. Chen, “Hydrogenation: a simple approach to realize semiconductor- half-metal- metal transition in boron nitride nanoribbons,” *Journal of the American Chemical Society*, vol. 132, no. 5, pp. 1699–1705, 2010.
- [104] Y. Wang, “Electronic properties of two-dimensional hydrogenated and semi-hydrogenated hexagonal boron nitride sheets,” *Physica Status Solidi (RRL)– Rapid Research Letters*, vol. 4, no. 1-2, pp. 34–36, 2010.
- [105] J. Bardeen and W. H. Brattain, “The transistor, a semi-conductor triode,” *Physical Review*, vol. 74, no. 2, p. 230, 1948.
- [106] W. Shockley, G. Pearson, and J. Haynes, “Hole injection in germanium—quantitative studies and filamentary transistors,” *Bell System Technical Journal*, vol. 28, no. 3, pp. 344–366, 1949.
- [107] R. Zhang and R. Cheung, “Mechanical properties and applications of two-dimensional materials,” *Two-dimensional Materials-Synthesis, Characterization and Potential Applications. Rijeka, Croatia: InTech*, pp. 219–246, 2016.
- [108] Y. Cao, V. Fatemi, A. Demir, S. Fang, S. L. Tomarken, J. Y. Luo, J. D. Sanchez-Yamagishi, K. Watanabe, T. Taniguchi, E. Kaxiras *et al.*, “Correlated insulator behaviour at half-filling in magic-angle graphene superlattices,” *Nature*, vol. 556, no. 7699, pp. 80–84, 2018.
- [109] Y. Cao, V. Fatemi, S. Fang, K. Watanabe, T. Taniguchi, E. Kaxiras, and P. Jarillo-Herrero, “Unconventional superconductivity in magic-angle graphene superlattices,” *Nature*, vol. 556, no. 7699, pp. 43–50, 2018.
- [110] L. Wang, E.-M. Shih, A. Ghiotto, L. Xian, D. A. Rhodes, C. Tan, M. Claassen, D. M. Kennes, Y. Bai, B. Kim *et al.*, “Correlated electronic phases in twisted bilayer transition metal dichalcogenides,” *Nature Materials*, pp. 1–6, 2020.
- [111] Z. Zhang, Y. Wang, K. Watanabe, T. Taniguchi, K. Ueno, E. Tutuc, and B. J. LeRoy, “Flat bands in twisted bilayer transition metal dichalcogenides,” *Nature Physics*, vol. 16, no. 11, pp. 1093–1096, 2020.
- [112] Y. Tang, L. Li, T. Li, Y. Xu, S. Liu, K. Barmak, K. Watanabe, T. Taniguchi, A. H. MacDonald, J. Shan *et al.*, “Simulation of hubbard model physics in WSe<sub>2</sub>/WS<sub>2</sub> moiré superlattices,” *Nature*, vol. 579, no. 7799, pp. 353–358, 2020.
- [113] Y. Shimazaki, I. Schwartz, K. Watanabe, T. Taniguchi, M. Kroner, and A. Imamoglu, “Strongly correlated electrons and hybrid excitons in a moiré heterostructure,” *Nature*, vol. 580, no. 7804, pp. 472–477, 2020.

- [114] S. Mitra, D. Srivastava, S. S. Singha, S. Dutta, B. Satpati, M. Karppinen, A. Ghosh, and A. Singha, “Tailoring phonon modes of few-layered MoS<sub>2</sub> by in-plane electric field,” *npj 2D Materials and Applications*, vol. 4, no. 1, pp. 1–7, 2020.
- [115] R. Ahmed, S. J. Hashemifar, H. Akbarzadeh, M. Ahmed *et al.*, “Ab initio study of structural and electronic properties of III-arsenide binary compounds,” *Computational Materials Science*, vol. 39, no. 3, pp. 580–586, 2007.
- [116] S. Adachi, *Properties of semiconductor alloys: group-IV, III-V and II-VI semiconductors*. John Wiley & Sons, 2009, vol. 28.
- [117] H. Bross and R. Bader, “Calculation of the ground state properties of diamond and cubic boron nitride,” *Physica Status Solidi (b)*, vol. 191, no. 2, pp. 369–385, 1995.
- [118] H. Warlimont, “Ceramics,” *Springer Handbook of Condensed Matter and Materials Data*, pp. 431–476, 2005.
- [119] I. Vurgaftman, J. Meyer, and L. Ram-Mohan, “Band parameters for III–V compound semiconductors and their alloys,” *Journal of applied physics*, vol. 89, no. 11, pp. 5815–5875, 2001.
- [120] S. Adachi, “Material parameters of In<sub>1-x</sub>Ga<sub>x</sub>As<sub>y</sub>P<sub>1-y</sub> and related binaries,” *Journal of Applied Physics*, vol. 53, no. 12, pp. 8775–8792, 1982.
- [121] A. González-García, W. López-Pérez, R. Palacio-Mozo, and R. González-Hernández, “Thermodynamic properties of In<sub>1-x</sub>B<sub>x</sub>P semiconducting alloys: A first-principles study,” *Computational Materials Science*, vol. 91, pp. 279–284, 2014.
- [122] T. Rieger and D. Grützmacher, “Growth and structural characterization of III-V semiconductor nanowires,” Fachgruppe Physik, Tech. Rep., 2015.
- [123] H. Şahin, S. Cahangirov, M. Topsakal, E. Bekaroglu, E. Akturk, R. T. Senger, and S. Ciraci, “Monolayer honeycomb structures of group-IV elements and III-V binary compounds: First-principles calculations,” *Physical Review B*, vol. 80, no. 15, p. 155453, 2009.
- [124] A. Onen, D. Kecik, E. Durgun, and S. Ciraci, “GaN: From three-to two-dimensional single-layer crystal and its multilayer van der Waals solids,” *Physical Review B*, vol. 93, no. 8, p. 085431, 2016.
- [125] S.-H. Bae, H. Kum, W. Kong, Y. Kim, C. Choi, B. Lee, P. Lin, Y. Park, and J. Kim, “Integration of bulk materials with two-dimensional materials for physical coupling and applications,” *Nature Materials*, vol. 18, no. 6, pp. 550–560, 2019.
- [126] A. McCreary, O. Kazakova, D. Jariwala, and Z. Y. Al Balushi, “An outlook into the flat land of 2D materials beyond graphene: synthesis, properties and device applications,” *2D Materials*, vol. 8, no. 1, p. 013001, 2020.

- [127] C. R. Dean, A. F. Young, I. Meric, C. Lee, L. Wang, S. Sorgenfrei, K. Watanabe, T. Taniguchi, P. Kim, K. L. Shepard *et al.*, “Boron nitride substrates for high-quality graphene electronics,” *Nature Nanotechnology*, vol. 5, no. 10, p. 722, 2010.
- [128] J. H. Edgar, T. B. Hoffman, B. Clubine, M. Currie, X. Du, J. Lin, and H. Jiang, “Characterization of bulk hexagonal boron nitride single crystals grown by the metal flux technique,” *Journal of Crystal Growth*, vol. 403, pp. 110–113, 2014.
- [129] G. Giovannetti, P. A. Khomyakov, G. Brocks, P. J. Kelly, and J. Van Den Brink, “Substrate-induced band gap in graphene on hexagonal boron nitride: Ab initio density functional calculations,” *Physical Review B*, vol. 76, no. 7, p. 073103, 2007.
- [130] T. P. Kaloni, Y. Cheng, and U. Schwingenschlögl, “Electronic structure of superlattices of graphene and hexagonal boron nitride,” *Journal of Materials Chemistry*, vol. 22, no. 3, pp. 919–922, 2012.
- [131] X. Zhong, R. G. Amorim, R. H. Scheicher, R. Pandey, and S. P. Karna, “Electronic structure and quantum transport properties of trilayers formed from graphene and boron nitride,” *Nanoscale*, vol. 4, no. 17, pp. 5490–5498, 2012.
- [132] B. Huang, G. Clark, E. Navarro-Moratalla, D. R. Klein, R. Cheng, K. L. Seyler, D. Zhong, E. Schmidgall, M. A. McGuire, D. H. Cobden *et al.*, “Layer-dependent ferromagnetism in a van der Waals crystal down to the monolayer limit,” *Nature*, vol. 546, no. 7657, pp. 270–273, 2017.
- [133] M. Born and R. Oppenheimer, “Zur quantentheorie der molekeln,” *Annalen der Physik*, vol. 389, no. 20, pp. 457–484, 1927.
- [134] J. G. Lee, *Computational materials science: an introduction*. CRC Press, 2016.
- [135] P. Hohenberg and W. Kohn, “Inhomogeneous electron gas,” *Physical Review*, vol. 136, no. 3B, p. B864, 1964.
- [136] W. Kohn and L. J. Sham, “Self-consistent equations including exchange and correlation effects,” *Physical Review*, vol. 140, no. 4A, p. A1133, 1965.
- [137] J. Kohanoff, *Electronic structure calculations for solids and molecules: theory and computational methods*. Cambridge University Press, 2006.
- [138] J. Bekaert, “Ab initio description of multicomponent superconductivity in bulk to atomically thin materials,” Ph.D. dissertation, University of Antwerp, 2018.
- [139] P. A. Dirac, “Note on exchange phenomena in the Thomas atom,” in *Mathematical Proceedings of the Cambridge Philosophical Society*, vol. 26, no. 3. Cambridge University Press, 1930, pp. 376–385.

- [140] D. M. Ceperley and B. Alder, “Ground state of the electron gas by a stochastic method,” *Physical Review Letters*, vol. 45, no. 7, p. 566, 1980.
- [141] J. P. Perdew and A. Zunger, “Self-interaction correction to density-functional approximations for many-electron systems,” *Physical Review B*, vol. 23, no. 10, p. 5048, 1981.
- [142] J. P. Perdew, K. Burke, and M. Ernzerhof, “Generalized gradient approximation made simple,” *Physical Review Letters*, vol. 77, no. 18, p. 3865, 1996.
- [143] J. Heyd, G. E. Scuseria, and M. Ernzerhof, “Hybrid functionals based on a screened Coulomb potential,” *The Journal of Chemical Physics*, vol. 118, no. 18, pp. 8207–8215, 2003.
- [144] F. Bloch, “Quantum mechanics of electrons in crystal lattices,” *Z. Phys*, vol. 52, pp. 555–600, 1928.
- [145] G. Kresse and J. Hafner, “VASP the Guide, University of Vienna, 2007.”
- [146] H. J. Monkhorst and J. D. Pack, “Special points for Brillouin-zone integrations,” *Physical Review B*, vol. 13, no. 12, p. 5188, 1976.
- [147] W. Kohn and N. Mermin, “in “Strongly Coupled Coulomb Systems,” ed. by GJ Kalman, JM Rommel, and K. Blagojev, Plenum, New York, 1998, pg. 9,” *Phys. Rev.*, vol. 137, p. 1441, 1965.
- [148] A. De Vita, “The energetics of defects and impurities in metals and ionic materials from first principles.” Ph.D. dissertation, University of Keele, 1992.
- [149] M. Methfessel and A. Paxton, “High-precision sampling for Brillouin-zone integration in metals,” *Physical Review B*, vol. 40, no. 6, p. 3616, 1989.
- [150] J. C. Phillips and L. Kleinman, “New method for calculating wave functions in crystals and molecules,” *Physical Review*, vol. 116, no. 2, p. 287, 1959.
- [151] P. E. Blöchl, “Projector augmented-wave method,” *Physical Review B*, vol. 50, no. 24, p. 17953, 1994.
- [152] G. Kresse and J. Furthmüller, “Efficiency of ab-initio total energy calculations for metals and semiconductors using a plane-wave basis set,” *Computational Materials Science*, vol. 6, no. 1, pp. 15–50, 1996.
- [153] G. Kresse and J. Furthmüller, “Efficient iterative schemes for ab initio total-energy calculations using a plane-wave basis set,” *Physical Review B*, vol. 54, no. 16, p. 11169, 1996.
- [154] C. Cohen-Tannoudji, B. Diu, and F. Laloe, *Quantum Mechanics, Volume 2*. Wiley-VCH, 1986.
- [155] L. E. F. Torres, S. Roche, and J.-C. Charlier, *Introduction to graphene-based nanomaterials: from electronic structure to quantum transport*. Cambridge University Press, 2020.

- [156] D. Stein, K. v. Klitzing, and G. Weimann, “Electron spin resonance on GaAs-Al<sub>x</sub>Ga<sub>1-x</sub>As heterostructures,” *Physical Review Letters*, vol. 51, no. 2, p. 130, 1983.
- [157] H. Stormer, Z. Schlesinger, A. Chang, D. Tsui, A. Gossard, and W. Wiegmann, “Energy structure and quantized Hall effect of two-dimensional holes,” *Physical Review Letters*, vol. 51, no. 2, p. 126, 1983.
- [158] P. Pyykko, “Relativistic effects in structural chemistry,” *Chemical Reviews*, vol. 88, no. 3, pp. 563–594, 1988.
- [159] C. Huan, “Spin Current, edited by Sadamichi Maekawa, Sergio O. Valenzuela, Eiji Saitoh, and Takashi Kimura: Scope: monograph, review. level: postgraduate, advanced undergraduate, early career researcher, researcher, teacher, specialist, scientist,” 2014.
- [160] N. W. Ashcroft, N. D. Mermin *et al.*, *Solid state physics*. New York: Holt, Rinehart and Winston, 1976.
- [161] G. Kresse, J. Furthmüller, and J. Hafner, “Ab initio force constant approach to phonon dispersion relations of diamond and graphite,” *EPL (Europhysics Letters)*, vol. 32, no. 9, p. 729, 1995.
- [162] K. Parlinski, Z. Li, and Y. Kawazoe, “First-principles determination of the soft mode in cubic ZrO<sub>2</sub>,” *Physical Review Letters*, vol. 78, no. 21, p. 4063, 1997.
- [163] P. Giannozzi, S. De Gironcoli, P. Pavone, and S. Baroni, “Ab initio calculation of phonon dispersions in semiconductors,” *Physical Review B*, vol. 43, no. 9, p. 7231, 1991.
- [164] H. Hellman, “Einführung in die quantenchemie,” *Franz Deuticke, Leipzig*, p. 285, 1937.
- [165] R. P. Feynman, “Forces in molecules,” *Physical Review*, vol. 56, no. 4, p. 340, 1939.
- [166] A. Togo and I. Tanaka, “First principles phonon calculations in materials science,” *Scripta Materialia*, vol. 108, pp. 1–5, 2015.
- [167] M. Born and T. Von Karman, *Über Schwingungen in Raumgittern*, *Physik. Z.*, 1912.
- [168] N. D. Mermin and H. Wagner, “Absence of ferromagnetism or antiferromagnetism in one-or two-dimensional isotropic Heisenberg models,” *Physical Review Letters*, vol. 17, no. 22, p. 1133, 1966.
- [169] A. González-García, W. López-Pérez, R. González-Hernández, J. Rodríguez, M. Milošević, and F. Peeters, “Tunable 2D-gallium arsenide and graphene bandgaps in a graphene/GaAs heterostructure: an ab initio study,” *Journal of Physics: Condensed Matter*, vol. 31, no. 26, p. 265502, 2019.

- [170] M. Acerce, D. Voiry, and M. Chhowalla, “Metallic 1T phase MoS<sub>2</sub> nanosheets as supercapacitor electrode materials,” *Nature Nanotechnology*, vol. 10, no. 4, p. 313, 2015.
- [171] A. González-García, W. López-Pérez, J. Rivera-Julio, F. Peteers, V. Mendoza-Estrada, and R. González-Hernández, “Structural, mechanical and electronic properties of two-dimensional structure of III-arsenide (111) binary compounds: An ab-initio study,” *Computational Materials Science*, vol. 144, pp. 285–293, 2018.
- [172] C. Tan, Z. Liu, W. Huang, and H. Zhang, “Non-volatile resistive memory devices based on solution-processed ultrathin two-dimensional nanomaterials,” *Chemical Society Reviews*, vol. 44, no. 9, pp. 2615–2628, 2015.
- [173] J. Rivera-Julio, A. González-García, R. González-Hernández, W. López-Pérez, F. M. Peeters, and A. D. Hernández-Nieves, “Vibrational properties of germanane and fluorinated germanene in the chair, boat, and zigzag-line configurations,” *J. Phys.: Condens. Matter*, vol. 31, no. 075301, p. 10pp, 2019.
- [174] I. Dzyaloshinsky, “A thermodynamic theory of “weak” ferromagnetism of antiferromagnetics,” *Journal of Physics and Chemistry of Solids*, vol. 4, no. 4, pp. 241–255, 1958.
- [175] T. Moriya, “Anisotropic superexchange interaction and weak ferromagnetism,” *Physical Review*, vol. 120, no. 1, p. 91, 1960.
- [176] M. Hervé, B. Dupé, R. Lopes, M. Böttcher, M. D. Martins, T. Balashov, L. Gerhard, J. Sinova, and W. Wulfhekel, “Stabilizing spin spirals and isolated skyrmions at low magnetic field exploiting vanishing magnetic anisotropy,” *Nature Communications*, vol. 9, no. 1, pp. 1–8, 2018.
- [177] H. Yang, G. Chen, A. A. Cotta, A. T. N’Diaye, S. A. Nikolaev, E. A. Soares, W. A. Macedo, K. Liu, A. K. Schmid, A. Fert *et al.*, “Significant Dzyaloshinskii–Moriya interaction at graphene–ferromagnet interfaces due to the Rashba effect,” *Nature Materials*, vol. 17, no. 7, pp. 605–609, 2018.
- [178] S. Heinze, K. Von Bergmann, M. Menzel, J. Brede, A. Kubetzka, R. Wiesendanger, G. Bihlmayer, and S. Blügel, “Spontaneous atomic-scale magnetic skyrmion lattice in two dimensions,” *Nature Physics*, vol. 7, no. 9, pp. 713–718, 2011.
- [179] H. Xiang, C. Lee, H.-J. Koo, X. Gong, and M.-H. Whangbo, “Magnetic properties and energy-mapping analysis,” *Dalton Transactions*, vol. 42, no. 4, pp. 823–853, 2013.
- [180] D. Šabani, C. Bacaksiz, and M. Milošević, “Ab initio methodology for magnetic exchange parameters: Generic four-state energy mapping onto a Heisenberg spin hamiltonian,” *Physical Review B*, vol. 102, no. 1, p. 014457, 2020.

- [181] R. John and B. Merlin, "Theoretical investigation of structural, electronic, and mechanical properties of two dimensional C, Si, Ge, Sn," *Crystal Structure Theory and Applications*, vol. 5, no. 03, p. 43, 2016.
- [182] G. Kresse and D. Joubert, "From ultrasoft pseudopotentials to the projector augmented-wave method," *Physical Review B*, vol. 59, no. 3, p. 1758, 1999.
- [183] Y. Le Page and P. Saxe, "Symmetry-general least-squares extraction of elastic data for strained materials from ab initio calculations of stress," *Physical Review B*, vol. 65, no. 10, p. 104104, 2002.
- [184] O. Nielsen and R. M. Martin, "First-principles calculation of stress," *Physical Review Letters*, vol. 50, no. 9, p. 697, 1983.
- [185] R. M. Martin, *Electronic structure: basic theory and practical methods*. Cambridge university press, 2020.
- [186] Q. Hu, Q. Wu, Y. Ma, L. Zhang, Z. Liu, J. He, H. Sun, H.-T. Wang, and Y. Tian, "First-principles studies of structural and electronic properties of hexagonal BC<sub>5</sub>," *Physical Review B*, vol. 73, no. 21, p. 214116, 2006.
- [187] X. Wu, Y. Pei, and X. C. Zeng, "B<sub>2</sub>C graphene, nanotubes, and nanoribbons," *Nano Letters*, vol. 9, no. 4, pp. 1577–1582, 2009.
- [188] V. V. Bannikov, I. R. Shein, and A. L. Ivanovskii, "Elastic and electronic properties of hexagonal rhenium sub-nitrides Re<sub>3</sub>N and Re<sub>2</sub>N in comparison with hcp-Re and wurtzite-like rhenium mononitride ReN," *Physica Status Solidi (b)*, vol. 248, no. 6, pp. 1369–1374, 2011.
- [189] K. Kawahara, T. Shirasawa, R. Arafune, C.-L. Lin, T. Takahashi, M. Kawai, and N. Takagi, "Determination of atomic positions in silicene on Ag (111) by low-energy electron diffraction," *Surface Science*, vol. 623, pp. 25–28, 2014.
- [190] R. Wyckoff, *Crystal Structures, second ed.* Krieger, Malabar, 1986.
- [191] D. Jose and A. Datta, "Understanding of the buckling distortions in silicene," *The Journal of Physical Chemistry C*, vol. 116, no. 46, pp. 24 639–24 648, 2012.
- [192] F. Song and X. Hu, "Exfoliation of layered double hydroxides for enhanced oxygen evolution catalysis," *Nature Communications*, vol. 5, p. 4477, 2014.
- [193] H. Wang, Y. Zhao, Y. Xie, X. Ma, and X. Zhang, "Recent progress in synthesis of two-dimensional hexagonal boron nitride," *Journal of Semiconductors*, vol. 38, no. 3, p. 031003, 2017.
- [194] G. Henkelman, A. Arnaldsson, and H. Jónsson, "A fast and robust algorithm for Bader decomposition of charge density," *Computational Materials Science*, vol. 36, no. 3, pp. 354–360, 2006.
- [195] E. Sanville, S. D. Kenny, R. Smith, and G. Henkelman, "Improved grid-based algorithm for Bader charge allocation," *Journal of Computational Chemistry*, vol. 28, no. 5, pp. 899–908, 2007.

- [196] S. Tang, G. Ding, X. Xie, J. Chen, C. Wang, X. Ding, F. Huang, W. Lu, and M. Jiang, "Nucleation and growth of single crystal graphene on hexagonal boron nitride," *Carbon*, vol. 50, no. 1, pp. 329–331, 2012.
- [197] N. Ooi, V. Rajan, J. Gottlieb, Y. Catherine, and J. Adams, "Structural properties of hexagonal boron nitride," *Modelling and Simulation in Materials Science and Engineering*, vol. 14, no. 3, p. 515, 2006.
- [198] C. Bacaksiz, H. Sahin, H. Ozaydin, S. Horzum, R. T. Senger, and F. M. Peeters, "Hexagonal AlN: Dimensional-crossover-driven band-gap transition," *Physical Review B*, vol. 91, no. 8, p. 085430, 2015.
- [199] M. A. Lukowski, A. S. Daniel, F. Meng, A. Forticaux, L. Li, and S. Jin, "Enhanced hydrogen evolution catalysis from chemically exfoliated metallic MoS<sub>2</sub> nanosheets," *Journal of the American Chemical Society*, vol. 135, no. 28, pp. 10 274–10 277, 2013.
- [200] Y. Chen, C. Tan, H. Zhang, and L. Wang, "Two-dimensional graphene analogues for biomedical applications," *Chemical Society Reviews*, vol. 44, no. 9, pp. 2681–2701, 2015.
- [201] F. Schedin, A. Geim, S. Morozov, E. Hill, P. Blake, M. Katsnelson, and K. Novoselov, "Detection of individual gas molecules adsorbed on graphene," *Nature Materials*, vol. 6, no. 9, p. 652, 2007.
- [202] B. Lalmi, H. Oughaddou, H. Enriquez, A. Kara, S. Vizzini, B. Ealet, and B. Aufray, "Epitaxial growth of a silicene sheet," *Applied Physics Letters*, vol. 97, no. 22, p. 223109, 2010.
- [203] H. Liu, Y. Du, Y. Deng, and D. Y. Peide, "Semiconducting black phosphorus: synthesis, transport properties and electronic applications," *Chemical Society Reviews*, vol. 44, no. 9, pp. 2732–2743, 2015.
- [204] M. Naguib, V. N. Mochalin, M. W. Barsoum, and Y. Gogotsi, "25th anniversary article: MXenes: a new family of two-dimensional materials," *Advanced Materials*, vol. 26, no. 7, pp. 992–1005, 2014.
- [205] Y. Lin, T. V. Williams, and J. W. Connell, "Soluble, exfoliated hexagonal boron nitride nanosheets," *The Journal of Physical Chemistry Letters*, vol. 1, no. 1, pp. 277–283, 2009.
- [206] M. Chhowalla, H. S. Shin, G. Eda, L.-J. Li, K. P. Loh, and H. Zhang, "The chemistry of two-dimensional layered transition metal dichalcogenide nanosheets," *Nature Chemistry*, vol. 5, no. 4, p. 263, 2013.
- [207] X. Huang, Z. Zeng, and H. Zhang, "Metal dichalcogenide nanosheets: preparation, properties and applications," *Chemical Society Reviews*, vol. 42, no. 5, pp. 1934–1946, 2013.
- [208] M. Xu, T. Liang, M. Shi, and H. Chen, "Graphene-like two-dimensional materials," *Chemical Reviews*, vol. 113, no. 5, pp. 3766–3798, 2013.

- [209] M. Chhowalla, Z. Liu, and H. Zhang, “Two-dimensional transition metal dichalcogenide (TMD) nanosheets,” *Chemical Society Reviews*, vol. 44, no. 9, pp. 2584–2586, 2015.
- [210] M. Osada and T. Sasaki, “Exfoliated oxide nanosheets: new solution to nano-electronics,” *Journal of Materials Chemistry*, vol. 19, no. 17, pp. 2503–2511, 2009.
- [211] Q. Wang and D. O’Hare, “Recent advances in the synthesis and application of layered double hydroxide (LDH) nanosheets,” *Chemical Reviews*, vol. 112, no. 7, pp. 4124–4155, 2012.
- [212] Y. Peng, Y. Li, Y. Ban, H. Jin, W. Jiao, X. Liu, and W. Yang, “Metal-organic framework nanosheets as building blocks for molecular sieving membranes,” *Science*, vol. 346, no. 6215, pp. 1356–1359, 2014.
- [213] T. Rodenas, I. Luz, G. Prieto, B. Seoane, H. Miro, A. Corma, F. Kapteijn, F. X. L. i Xamena, and J. Gascon, “Metal–organic framework nanosheets in polymer composite materials for gas separation,” *Nature Materials*, vol. 14, no. 1, p. 48, 2015.
- [214] J. W. Colson, A. R. Woll, A. Mukherjee, M. P. Levendorf, E. L. Spitler, V. B. Shields, M. G. Spencer, J. Park, and W. R. Dichtel, “Oriented 2D covalent organic framework thin films on single-layer graphene,” *Science*, vol. 332, no. 6026, pp. 228–231, 2011.
- [215] M. J. Kory, M. Wörle, T. Weber, P. Payamyar, S. W. Van De Poll, J. Dshemuchadse, N. Trapp, and A. D. Schlüter, “Gram-scale synthesis of two-dimensional polymer crystals and their structure analysis by X-ray diffraction,” *Nature Chemistry*, vol. 6, no. 9, p. 779, 2014.
- [216] P. Kissel, D. J. Murray, W. J. Wulftange, V. J. Catalano, and B. T. King, “A nanoporous two-dimensional polymer by single-crystal-to-single-crystal photopolymerization,” *Nature Chemistry*, vol. 6, no. 9, p. 774, 2014.
- [217] C. Tan, X. Qi, X. Huang, J. Yang, B. Zheng, Z. An, R. Chen, J. Wei, B. Z. Tang, W. Huang *et al.*, “Single-layer transition metal dichalcogenide nanosheet-assisted assembly of aggregation-induced emission molecules to form organic nanosheets with enhanced fluorescence,” *Advanced Materials*, vol. 26, no. 11, pp. 1735–1739, 2014.
- [218] Z. Fan, X. Huang, C. Tan, and H. Zhang, “Thin metal nanostructures: synthesis, properties and applications,” *Chemical Science*, vol. 6, no. 1, pp. 95–111, 2015.
- [219] X. Huang, S. Li, Y. Huang, S. Wu, X. Zhou, S. Li, C. L. Gan, F. Boey, C. A. Mirkin, and H. Zhang, “Synthesis of hexagonal close-packed gold nanostructures,” *Nature Communications*, vol. 2, p. 292, 2011.

- [220] X. Huang, S. Tang, X. Mu, Y. Dai, G. Chen, Z. Zhou, F. Ruan, Z. Yang, and N. Zheng, “Freestanding palladium nanosheets with plasmonic and catalytic properties,” *Nature Nanotechnology*, vol. 6, no. 1, p. 28, 2011.
- [221] H. Duan, N. Yan, R. Yu, C.-R. Chang, G. Zhou, H.-S. Hu, H. Rong, Z. Niu, J. Mao, H. Asakura *et al.*, “Ultrathin rhodium nanosheets,” *Nature Communications*, vol. 5, p. 3093, 2014.
- [222] A. S. Mayorov, R. V. Gorbachev, S. V. Morozov, L. Britnell, R. Jalil, L. A. Ponomarenko, P. Blake, K. S. Novoselov, K. Watanabe, T. Taniguchi *et al.*, “Micrometer-scale ballistic transport in encapsulated graphene at room temperature,” *Nano Letters*, vol. 11, no. 6, pp. 2396–2399, 2011.
- [223] R. Balog, B. Jørgensen, L. Nilsson, M. Andersen, E. Rienks, M. Bianchi, M. Fanetti, E. Lægsgaard, A. Baraldi, S. Lizzit *et al.*, “Bandgap opening in graphene induced by patterned hydrogen adsorption,” *Nature Materials*, vol. 9, no. 4, p. 315, 2010.
- [224] A. Ebnoungassir, B. Narayanan, S. Kodambaka, and C. V. Ciobanu, “Tunable MoS<sub>2</sub> bandgap in MoS<sub>2</sub>-graphene heterostructures,” *Applied Physics Letters*, vol. 105, no. 3, p. 031603, 2014.
- [225] S. Haigh, A. Gholinia, R. Jalil, S. Romani, L. Britnell, D. Elias, K. Novoselov, L. Ponomarenko, A. Geim, and R. Gorbachev, “Cross-sectional imaging of individual layers and buried interfaces of graphene-based heterostructures and superlattices,” *Nature Materials*, vol. 11, no. 9, p. 764, 2012.
- [226] M. Son, H. Lim, M. Hong, and H. C. Choi, “Direct growth of graphene pad on exfoliated hexagonal boron nitride surface,” *Nanoscale*, vol. 3, no. 8, pp. 3089–3093, 2011.
- [227] A. Ramasubramaniam, D. Naveh, and E. Towe, “Tunable band gaps in bilayer graphene-BN heterostructures,” *Nano Letters*, vol. 11, no. 3, pp. 1070–1075, 2011.
- [228] Y.-J. Li, Q.-Q. Sun, L. Chen, P. Zhou, P.-F. Wang, S.-J. Ding, and D. W. Zhang, “Hexagonal boron nitride intercalated multi-layer graphene: a possible ultimate solution to ultra-scaled interconnect technology,” *AIP Advances*, vol. 2, no. 1, p. 012191, 2012.
- [229] Y. A. Bychkov and E. I. Rashba, “Oscillatory effects and the magnetic susceptibility of carriers in inversion layers,” *Journal of Physics C: Solid State Physics*, vol. 17, no. 33, p. 6039, 1984.
- [230] A. Gamucci, D. Spirito, M. Carrega, B. Karmakar, A. Lombardo, M. Bruna, L. Pfeiffer, K. West, A. C. Ferrari, M. Polini *et al.*, “Anomalous low-temperature Coulomb drag in graphene-GaAs heterostructures,” *Nature Communications*, vol. 5, p. 5824, 2014.

- [231] S.-S. Lin, Z.-Q. Wu, X.-Q. Li, Y.-J. Zhang, S.-J. Zhang, P. Wang, R. Panneerselvam, and J.-F. Li, “Stable 16.2% efficient surface plasmon-enhanced graphene/GaAs heterostructure solar cell,” *Advanced Energy Materials*, vol. 6, no. 21, p. 1600822, 2016.
- [232] Y. Lu, S. Feng, Z. Wu, Y. Gao, J. Yang, Y. Zhang, Z. Hao, J. Li, E. Li, H. Chen *et al.*, “Broadband surface plasmon resonance enhanced self-powered graphene/GaAs photodetector with ultrahigh detectivity,” *Nano Energy*, vol. 47, pp. 140–149, 2018.
- [233] N. Van Men and N. Q. Khanh, “Plasmon modes in graphene–GaAs heterostructures,” *Physics Letters A*, vol. 381, no. 44, pp. 3779–3784, 2017.
- [234] N. V. Men and D. T. K. Phuong, “Plasmon modes in bilayer-graphene–GaAs heterostructures including layer-thickness and exchange-correlation effects,” *International Journal of Modern Physics B*, vol. 32, no. 23, p. 1850256, 2018.
- [235] A. Tkatchenko and M. Scheffler, “Accurate molecular van der Waals interactions from ground-state electron density and free-atom reference data,” *Physical Review Letters*, vol. 102, no. 7, p. 073005, 2009.
- [236] U. Herath, P. Tavadze, X. He, E. Bousquet, S. Singh, F. Munoz, and A. H. Romero, “Pyprocar: A python library for electronic structure pre/post-processing,” *Computer Physics Communications*, vol. 251, p. 107080, 2020.
- [237] R. C. Andrew, R. E. Mapasha, A. M. Ukpong, and N. Chetty, “Mechanical properties of graphene and boronitrene,” *Physical Review B*, vol. 85, no. 12, p. 125428, 2012.
- [238] H. Kumar, D. Er, L. Dong, J. Li, and V. B. Shenoy, “Elastic deformations in 2D van der Waals heterostructures and their impact on optoelectronic properties: predictions from a multiscale computational approach,” *Scientific Reports*, vol. 5, p. 10872, 2015.
- [239] S. Singh, C. Espejo, and A. H. Romero, “Structural, electronic, vibrational, and elastic properties of graphene/MoS<sub>2</sub> bilayer heterostructures,” *Physical Review B*, vol. 98, no. 15, p. 155309, 2018.
- [240] D. Pierucci, H. Henck, J. Avila, A. Balan, C. H. Naylor, G. Patriarche, Y. J. Dappe, M. G. Silly, F. Sirotti, A. C. Johnson *et al.*, “Band alignment and minigaps in monolayer MoS<sub>2</sub>-graphene van der Waals heterostructures,” *Nano Letters*, vol. 16, no. 7, pp. 4054–4061, 2016.
- [241] S. Singh and A. H. Romero, “Giant tunable Rashba spin splitting in a two-dimensional BiSb monolayer and in BiSb/AlN heterostructures,” *Physical Review B*, vol. 95, no. 16, p. 165444, 2017.
- [242] W. Yu, C.-Y. Niu, Z. Zhu, X. Wang, and W.-B. Zhang, “Atomically thin binary V–V compound semiconductor: a first-principles study,” *Journal of Materials Chemistry C*, vol. 4, no. 27, pp. 6581–6587, 2016.

- [243] H. Zheng, X.-B. Li, N.-K. Chen, S.-Y. Xie, W. Q. Tian, Y. Chen, H. Xia, S. Zhang, and H.-B. Sun, "Monolayer II-VI semiconductors: A first-principles prediction," *Physical Review B*, vol. 92, no. 11, p. 115307, 2015.
- [244] B. Sachs, T. Wehling, M. Katsnelson, and A. Lichtenstein, "Adhesion and electronic structure of graphene on hexagonal boron nitride substrates," *Physical Review B*, vol. 84, no. 19, p. 195414, 2011.
- [245] P. San-Jose, A. Gutiérrez-Rubio, M. Sturla, and F. Guinea, "Spontaneous strains and gap in graphene on boron nitride," *Physical Review B*, vol. 90, no. 7, p. 075428, 2014.
- [246] H. Shi, H. Pan, Y.-W. Zhang, and B. I. Yakobson, "Quasiparticle band structures and optical properties of strained monolayer MoS<sub>2</sub> and WS<sub>2</sub>," *Physical Review B*, vol. 87, no. 15, p. 155304, 2013.
- [247] G. Gui, J. Li, and J. Zhong, "Band structure engineering of graphene by strain: first-principles calculations," *Physical Review B*, vol. 78, no. 7, p. 075435, 2008.
- [248] D. Boukhvalov and M. Katsnelson, "Chemical functionalization of graphene," *Journal of Physics: Condensed Matter*, vol. 21, no. 34, p. 344205, 2009.
- [249] J. O. Sofo, A. S. Chaudhari, and G. D. Barber, "Graphane: A two-dimensional hydrocarbon," *Physical Review B*, vol. 75, no. 15, p. 153401, 2007.
- [250] J.-C. Charlier, X. Gonze, and J.-P. Michenaud, "First-principles study of graphite monofluoride (CF)<sub>n</sub>," *Physical Review B*, vol. 47, no. 24, p. 16162, 1993.
- [251] M. H. Sluiter and Y. Kawazoe, "Cluster expansion method for adsorption: Application to hydrogen chemisorption on graphene," *Physical Review B*, vol. 68, no. 8, p. 085410, 2003.
- [252] A. Bhattacharya, S. Bhattacharya, C. Majumder, and G. Das, "First principles prediction of the third conformer of hydrogenated BN sheet," *Physica Status Solidi (RRL)–Rapid Research Letters*, vol. 4, no. 12, pp. 368–370, 2010.
- [253] Q. Tang, Z. Zhou, P. Shen, and Z. Chen, "Band gap engineering of BN sheets by interlayer dihydrogen bonding and electric field control," *ChemPhysChem*, vol. 14, no. 9, pp. 1787–1792, 2013.
- [254] F. Späth, J. Gebhardt, F. Düll, U. Bauer, P. Bachmann, C. Gleichweit, A. Görling, H. Steinrück, and C. Papp, "Hydrogenation and hydrogen intercalation of hexagonal boron nitride on Ni(111): reactivity and electronic structure," *2D Materials*, vol. 4, no. 3, p. 035026, 2017.
- [255] M. Ohtomo, Y. Yamauchi, X. Sun, A. A. Kuzubov, N. S. Mikhaleva, P. V. Avramov, S. Entani, Y. Matsumoto, H. Naramoto, and S. Sakai, "Direct observation of site-selective hydrogenation and spin-polarization in hydrogenated hexagonal boron nitride on Ni (111)," *Nanoscale*, vol. 9, no. 6, pp. 2369–2375, 2017.

- [256] S. Grimme, “Semiempirical gga-type density functional constructed with a long-range dispersion correction,” *Journal of Computational Chemistry*, vol. 27, no. 15, pp. 1787–1799, 2006.
- [257] H. Sahin, O. Leenaerts, S. Singh, and F. Peeters, “Graphane,” *Wiley Interdisciplinary Reviews: Computational Molecular Science*, vol. 5, no. 3, pp. 255–272, 2015.
- [258] D. C. Elias, R. R. Nair, T. Mohiuddin, S. Morozov, P. Blake, M. Halsall, A. C. Ferrari, D. Boukhvalov, M. Katsnelson, A. Geim *et al.*, “Control of graphene’s properties by reversible hydrogenation: evidence for graphane,” *Science*, vol. 323, no. 5914, pp. 610–613, 2009.
- [259] P. C. Hohenberg, “Existence of long-range order in one and two dimensions,” *Physical Review*, vol. 158, no. 2, p. 383, 1967.
- [260] W.-B. Zhang, Q. Qu, P. Zhu, and C.-H. Lam, “Robust intrinsic ferromagnetism and half semiconductivity in stable two-dimensional single-layer chromium trihalides,” *Journal of Materials Chemistry C*, vol. 3, no. 48, pp. 12 457–12 468, 2015.
- [261] G. Daalderop, P. Kelly, and M. Schuurmans, “First-principles calculation of the magnetocrystalline anisotropy energy of iron, cobalt, and nickel,” *Physical Review B*, vol. 41, no. 17, p. 11919, 1990.
- [262] P. Bruno, “Tight-binding approach to the orbital magnetic moment and magnetocrystalline anisotropy of transition-metal monolayers,” *Physical Review B*, vol. 39, no. 1, p. 865, 1989.
- [263] T. Balashov, T. Schuh, A. Takács, A. Ernst, S. Ostanin, J. Henk, I. Mertig, P. Bruno, T. Miyamachi, S. Suga *et al.*, “Magnetic anisotropy and magnetization dynamics of individual atoms and clusters of Fe and Co on Pt (111),” *Physical Review Letters*, vol. 102, no. 25, p. 257203, 2009.
- [264] G. Bayreuther, J. Prempfer, M. Sperl, and D. Sander, “Uniaxial magnetic anisotropy in Fe/GaAs (001): Role of magnetoelastic interactions,” *Physical Review B*, vol. 86, no. 5, p. 054418, 2012.
- [265] R. Mishra, W. Zhou, S. J. Pennycook, S. T. Pantelides, and J.-C. Idrobo, “Long-range ferromagnetic ordering in manganese-doped two-dimensional dichalcogenides,” *Physical Review B*, vol. 88, no. 14, p. 144409, 2013.
- [266] Q. Sun and N. Kioussis, “Prediction of manganese trihalides as two-dimensional Dirac half-metals,” *Physical Review B*, vol. 97, no. 9, p. 094408, 2018.
- [267] R. González-Hernández, A. González-García, and W. López-Pérez, “Ferromagnetism in Cu-doped polar and nonpolar GaN surfaces,” *Computational Materials Science*, vol. 83, pp. 217–221, 2014.

- [268] A. González-García, W. López-Pérez, and R. González-Hernández, “Theoretical study of magnetic ordering and electronic properties of  $\text{Ag}_x\text{Al}_{1-x}\text{N}$  compounds,” *Solid State Communications*, vol. 151, no. 23, pp. 1794–1797, 2011.
- [269] H. Ohno, A. Shen, F. Matsukura, A. Oiwa, A. Endo, S. Katsumoto, and Y. Iye, “(Ga, Mn)As: a new diluted magnetic semiconductor based on GaAs,” *Applied Physics Letters*, vol. 69, no. 3, pp. 363–365, 1996.
- [270] L. Chen, X. Yang, F. Yang, J. Zhao, J. Misuraca, P. Xiong, and S. von Molnár, “Enhancing the Curie temperature of ferromagnetic semiconductor (Ga, Mn)As to 200 K via nanostructure engineering,” *Nano Letters*, vol. 11, no. 7, pp. 2584–2589, 2011.
- [271] T. Dietl, H. Ohno, and F. Matsukura, “Ferromagnetic semiconductor heterostructures for spintronics,” *IEEE Transactions on Electron Devices*, vol. 54, no. 5, pp. 945–954, 2007.
- [272] M. Lan, G. Xiang, and X. Zhang, “Electronic structures and magnetic stabilities of 2D Mn-doped GaAs nanosheets: The role of long-range exchange interactions and doping strategies,” *Journal of Applied Physics*, vol. 116, no. 8, p. 083912, 2014.
- [273] J. Sivek, H. Sahin, B. Partoens, and F. Peeters, “Giant magnetic anisotropy in doped single layer molybdenum disulfide and fluorographene,” *Journal of Physics: Condensed Matter*, vol. 28, no. 19, p. 195301, 2016.
- [274] F. Donati, Q. Dubout, G. Autès, F. Patthey, F. Calleja, P. Gambardella, O. Yazyev, and H. Brune, “Magnetic moment and anisotropy of individual Co atoms on graphene,” *Physical Review Letters*, vol. 111, no. 23, p. 236801, 2013.
- [275] M. Heide, G. Bihlmayer, and S. Blügel, “Dzyaloshinskii-Moriya interaction accounting for the orientation of magnetic domains in ultrathin films: Fe/W (110),” *Physical Review B*, vol. 78, no. 14, p. 140403, 2008.
- [276] M. Bode, M. Heide, K. Von Bergmann, P. Ferriani, S. Heinze, G. Bihlmayer, A. Kubetzka, O. Pietzsch, S. Blügel, and R. Wiesendanger, “Chiral magnetic order at surfaces driven by inversion asymmetry,” *Nature*, vol. 447, no. 7141, pp. 190–193, 2007.
- [277] P. Ferriani, K. Von Bergmann, E. Vedmedenko, S. Heinze, M. Bode, M. Heide, G. Bihlmayer, S. Blügel, and R. Wiesendanger, “Atomic-scale spin spiral with a unique rotational sense: Mn monolayer on W (001),” *Physical Review Letters*, vol. 101, no. 2, p. 027201, 2008.
- [278] A. I. Liechtenstein, M. Katsnelson, V. Antropov, and V. Gubanov, “Local spin density functional approach to the theory of exchange interactions in ferromagnetic metals and alloys,” *Journal of Magnetism and Magnetic Materials*, vol. 67, no. 1, pp. 65–74, 1987.

- [279] C. Xu, J. Feng, H. Xiang, and L. Bellaiche, “Interplay between kitaev interaction and single ion anisotropy in ferromagnetic CrI<sub>3</sub> and CrGeTe<sub>3</sub> monolayers,” *npj Computational Materials*, vol. 4, no. 1, pp. 1–6, 2018.
- [280] F. Donati, L. Gragnaniello, A. Cavallin, F. Natterer, Q. Dubout, M. Pivetta, F. Patthey, J. Dreiser, C. Piamonteze, S. Rusponi *et al.*, “Tailoring the magnetism of Co atoms on graphene through substrate hybridization,” *Physical Review Letters*, vol. 113, no. 17, p. 177201, 2014.
- [281] T. Wehling, A. Balatsky, M. Katsnelson, A. Lichtenstein, and A. Rosch, “Orbitally controlled kondo effect of Co adatoms on graphene,” *Physical Review B*, vol. 81, no. 11, p. 115427, 2010.
- [282] A. Stroppa, X. Duan, M. Peressi, D. Furlanetto, and S. Modesti, “Computational and experimental imaging of Mn defects on GaAs (110) cross-sectional surfaces,” *Physical Review B*, vol. 75, no. 19, p. 195335, 2007.
- [283] P. Ruiz-Díaz, O. V. Stepanyuk, and V. S. Stepanyuk, “Effects of interatomic coupling on magnetic anisotropy and order of spins on metallic surfaces,” *The Journal of Physical Chemistry C*, vol. 119, no. 46, pp. 26 237–26 241, 2015.
- [284] S. Emori, U. Bauer, S.-M. Ahn, E. Martinez, and G. S. Beach, “Current-driven dynamics of chiral ferromagnetic domain walls,” *Nature Materials*, vol. 12, no. 7, pp. 611–616, 2013.
- [285] K.-S. Ryu, L. Thomas, S.-H. Yang, and S. Parkin, “Chiral spin torque at magnetic domain walls,” *Nature Nanotechnology*, vol. 8, no. 7, pp. 527–533, 2013.

# Appendix A

## Abbreviations

# Abbreviations

<b>2D</b>	Two-dimensional
<b>4SM</b>	Four-State energy Mapping
<b>III-V</b>	Elements from group III and V of the periodic table
<b>AE</b>	All Electron
<b>AES</b>	Auger Electron Spectroscopy
<b>AFM</b>	Atomic Force Microscopy
<b>AQHE</b>	Anomalous Quantum Hall Effect
<b>ARUPS</b>	Angle-Resolved Ultraviolet Photoelectron Spectroscopy
<b>BCN</b>	2D nanocomposites containing Boron, Carbon and Nitrogen
<b>BO</b>	Born-Oppenheimer
<b>BSCCO</b>	Bismuth Strontium Calcium Copper Oxide
<b>BZ</b>	Brillouin Zone
<b>CVD</b>	Chemical Vapor Deposition
<b>DFPT</b>	Density Functional Perturbation Theory
<b>DFT</b>	Density Functional Theory
<b>DMI</b>	Dzyaloshinskii-Moriya Interaction
<b>DOS</b>	Density Of States
<b>E<sub>xc</sub></b>	Exchange-correlation Energy Functional
<b>F<sub>HK</sub></b>	Universal Functional
<b>FDM</b>	Finite Displacement Method
<b>FFT</b>	Fast Fourier Transform
<b>GGA</b>	Generalized Gradient Approximation
<b>GNRs</b>	Graphene Nanoribbons
<b>h-BAs</b>	Hexagonal Boron Arsenide
<b>h-BN</b>	Hexagonal Boron Nitride
<b>HEG</b>	Homogeneous Electron Gas
<b>HF</b>	Hartree-Fock
<b>H-F</b>	Hellmann-Feynman
<b>h-GaAs</b>	Hexagonal Gallium Arsenide
<b>h-III-As</b>	Hexagonal III-Arsenide
<b>h-InAs</b>	Hexagonal Indium Arsenide
<b>HK</b>	Hohenberg-Kohn
<b>HOPG</b>	Highly Oriented Pyrolytic Graphite
<b>HSE</b>	Heyd-Scuseria-Ernzerhof
<b>IBZ</b>	Irreducible Brillouin Zone
<b>KS</b>	Kohn-Sham
<b>LDA</b>	Local Density Approximation
<b>LEED</b>	Low Energy Electron Diffraction

<b>MA</b>	Magnetic Anisotropy
<b>MAE</b>	Magnetocrystalline Anisotropy Energy
<b>MP</b>	Monkhorst Pack
<b>PAW</b>	Projector Augmented Wave
<b>PBC</b>	Periodic Boundary Conditions
<b>PBE</b>	Perdew-Burke-Ernzerof
<b>PDOS</b>	Projected Density Of States
<b>PES</b>	Potential Energy Surface
<b>PP</b>	Four-State energy Mapping
<b>PVD</b>	Physical Vapor Deposition
<b>PW</b>	Plane Wave
<b>QED</b>	Quantum Electrodynamics
<b>SDBS</b>	Sodium Dodecyl Benzene Sulfonate
<b>SDFT</b>	Spin Density Functional Theory
<b>SOC</b>	Spin-Orbit Coupling
<b>STM</b>	Scanning Tunneling Microscopy
<b>TEM</b>	Transmission Electron Microscopy
<b>TM</b>	Transition Metal
<b>TMDCs</b>	Transition Metal Dichalcogenides
<b>TMOs</b>	Transition Metal Oxides
<b>UPS</b>	Ultraviolet Photoelectron Spectroscopy
<b>VASP</b>	Vienna Ab-initio Simulation Package
<b>vdW</b>	Van der Waals
<b>X-anes</b>	X-ene system with adsorbed hydrogen
<b>X-enes</b>	Honeycomb structure similar to graphene
<b>XPS</b>	X-ray photoelectron spectroscopy

## Appendix B

### Curriculum vitae

# Curriculum Vitae

## Álvaro González García

Department of Physics  
Universidad del Norte  
Km 5 vía a Puerto Colombia  
Barranquilla, Atlántico. Colombia  
+57 5 3509509 ext 3162 (Office)  
[alvarogonzalez@uninorte.edu.co](mailto:alvarogonzalez@uninorte.edu.co)



## Research Interest

My research field is computational condensed matter physics: electronic, structural, optical, elastic, thermal, magnetic and vibrational properties of materials such as: Ternary semiconductors, simple metals, transition metal nitrides, metal-hydrogen system, rare-earth nitrides, hydrides and borides, pressure dependencies and 2D-materials. With theory and methods as Density Functional Theory (DFT), Density Functional Perturbation Theory (DFPT), Plane-wave pseudopotential method (PW-PP), Linearized augmented plane-wave method (LAPW). In addition, I am interested in Projector Augmented Wave Method (PAW), Time dependent Density Functional Theory (TDDFT), improved functional (LDA/GGA+U)

## Personal Information

Name: Alvaro González García.  
Date and place of birth: 28-08-1966, el Banco.  
Nationality: Colombian.  
Civil status: Married.  
E-mail: [alvarogonzalez@uninorte.edu.co](mailto:alvarogonzalez@uninorte.edu.co)

## Educational Background

2017 Ph. D. Physics candidate - Universidad del Norte, Barranquilla, Colombia.  
2010 Master of Science, State University Of New York  
2011 Master - Applied Physics. Universidad del Norte, Barranquilla, Colombia.  
1990 Bachelor - Physics. Universidad del Atlántico, Barranquilla, Colombia.  
1984 High School. Colegio José Eusebio Caro, Barranquilla, Colombia.

## Academics honor and awards

Scholarship at the University of Antwerp from 5 January 2021 to 4 July 2021.

Award for the implementation of Good Strategies for Teaching Physics in Difficult Times, Uninorte, November 2020

Admitted to the Joint-PhD program of the University of Antwerp 2017

Master Cum Laude Laureate Physics Thesis-Uninorte - December 2012

Pedagogic Innovation award, Universidad Del Norte - Uninorte - November 2014

Award for Teaching Excellence in the Classroom - Uninorte - October 2010

Research stay sponsored by DAAD, Helmholtz Zentrum Berlin - November 2009

## **Occupational History**

Since June 2013 Assistant Professor and Researcher, Departamento de Física, Universidad del Norte (Barranquilla, (Colombia).

2013-2015 Coordinator of Physics postgraduate program, Universidad del Norte, Barranquilla, Colombia.

2009-2013 Auxiliar Professor, Departamento de Física, Universidad del Norte (Barranquilla, Colombia).

2000-2010 Physics teacher in engineering, Universidad San Martín

2004-2012 High school teacher in physics at the Marymount High school, Barranquilla, Colombia.

1995-2003 High school teacher in physics at the Sagrado Corazón High school, Barranquilla, Colombia.

## **Workshops and Congress**

2019 First Caribbean Workshop on Frontiers in Functional Materials, Barranquilla, Colombia, Dec 5-6

2019 XXVIII National Physics Congress, Armenia, Colombia, September 9-12

2017 XXVII National Physics Congress, Cartagena, Colombia, October 3-6

2017 International congress: Physics of light-matter coupling in nanostructures PLMCN, Santa Marta, Colombia, May 23-26

2015 International congress: Physics of light-matter coupling in nanostructures PLMCN, Medellín, Colombia, February 3-8

2015 Hands-On workshop density functional theory and beyond, Harnack- Haus of the Max Planck Society, Berlin, Germany, July 13-23

2015 National Physics Congress, Manizales, Colombia, September 29- October 2

2015 Nano-science and Nano- technology week, Colombia, October 5-9

2014 Workshop en Procesamientos químicos físicos avanzados- Bucaramanga, Colombia, March 10-14

2012 Quantum Espresso 2012 Workshop - Pennsylvania State University, United State, June 25-29.

2012 Workshop en simulación computacional de nano estructuras, Universidad del Norte, Barranquilla, Colombia, June 10-15

2011 XXIV National Physics Congress, Bogotá, Colombia, October 1-5, 2011

2010 American School on Magnetism, Universidad Nacional, Manizalez, Colombia, July 24-25

2009 XXIII National Physics Congress, Universidad del Magdalena, Santa Marta, Colombia, October 1st

2008 Encuentro Regional de Física y Aplicaciones Tecnológica, Albania, Guajira, Colombia, June 10-15, 2008

## **International Research**

2021 Research activities, Antwerp University, Antwerp, Belgium, Jan 5- July 4

2019 Research activities, Antwerp University, Antwerp, Belgium, June 3- July 12

2018 Research activities, Antwerp University, Antwerp, Belgium, June 4- July 13

2017 Research activities, Antwerp University, Antwerp, Belgium, June 5- July 15.

2016 Research activities, Centro atómico de Bariloche, Argentina, June 6- July 30.

2015 Research activities, Technische Universitat Darmstadt, Darmstadt, Germany, June 6- July 30

2010 Research activities of the Helmholtz Berlin, Helmholtz Zentrum, Berlin, Germany, November-February

## **Languages**

Spanish (Mother language), English.